UNIVERSITAT DE BARCELONA

Deciphering the structure and dynamics of the vault particles

María González Álamos

Deciphering the structure and dynamics of vault particles

María González Álamos

Barcelona, 2023

Deciphering the structure and dynamics of vault particles

María González Álamos

2023

ibmb
Institut de Biologia Molecular de Barcelona
Molecular Biology Institute of Barcelona CSIC

UNIVERSITAT DE BARCELONA

UNIVERSITAT DE BARCELONA

FACULTAT DE FARMÀCIA I CIÈNCIES DE L'ALIMENTACIÓ

DECIPHERING THE STRUCTURE AND DYNAMICS OF VAULT PARTICLES

María González Álamos
2023

UNIVERSITAT DE BARCELONA

FACULTAT DE FARMÀCIA I CIÈNCIES DE L'ALIMENTACIÓ

PROGRAMA DE DOCTORAT DE BIOTECNOLOGÍA

DECIPHERING THE STRUCTURE AND DYNAMICS OF VAULT PARTICLES

Memòria presentada per María González Álamos per optar al títol de doctor per la Universitat de Barcelona

Directora: Prof. Núria Verdaguer Massana

Director: PhD Pablo Guerra Lahoz

Doctoranda: María González Álamos

Tutora: Prof. Josefa Badia Palacín

María González Álamos
2023

"Rodéate de lo que te enriquezca el alma"

No sé si lo he leído,
no sé si lo he pensado,
pero aquí os lo he dejado.

AGRADECIMIENTOS

¡Por fin! ¡Bienvenida, querida tesis! Ha costado, pero aquí está, para que la disfrutéis. Se podría decir que este apartado lo he dejado para el final (suena mejor para el final que ser el aparatado más procrastinado, y... ¡hay testigos de ello!). Y, quizá sea porque en la vida pocas veces se agradecen las cosas y menos a las personas, pero, ¡qué bonito es agradecer! Comenzaré sin preámbulos, pero seguramente no tenga palabras suficientes, y mientras lo escribo alguna lagrimilla caerá, suave, pero caerá, y tendré la piel de gallina, suave, pero a flor de piel.

Me gustaría comenzar con mi laboratorio, CRI6, donde compartir las horas es lo nuestro. En primer lugar, me gustaría darle las gracias a **Núria**, por darme la oportunidad de realizar el doctorado en su laboratorio, por su perseverancia constante en el proyecto y por las ganas transmitidas para crecer como científica. Sí, al final será que he crecido (de altura, no mucho) pero como persona e investigadora. También gracias Núria por formar este grupo de investigación, y darme la oportunidad de conocer a las personas que voy a mencionar a continuación. **Pablo**, mi mentor, por confiar en mi desde el primer momento, y por formar siempre un buen equipo, por la colección de libros que me llevo bajo el brazo: experimental, paternal, de la vida en general, de bares, de conciertos y de cerveza. Por tu paciencia (que no es poca), por las ganas de enseñarme, por los viajes a Grenoble y por las risas aseguradas. **Diego**, por tu constancia, por tu motivación por la ciencia, por todos los consejos científicos, por tu paciencia, ayuda y guía en este proyecto cuando estaba un poco perdida. Siempre se necesita una vista con perspectiva. **Omar**, ay Omar, que guapa ella, que maja ella, que todo ella. Gracias, por ser mi codo con codo, o mano con mano, o pie con pie (sí, también por enseñarme a bailar danzas valencias). Porque desde el momento que entraste, ya lo revolucionaste, por sacar lo mejor de cada uno y conocer a todo el edificio. Gracias amigo, por la sonrisita mañanera, la de después de comer y la de salir. Por nuestros cálculos y nuestras células, contigo siempre es un placer. **Cris**, gracias por compartir toda tu experiencia científica, por todos esos truquillos y por la organización (siempre es necesaria). Por las charlitas mañaneras con cuernitos de chocolate, por las charlitas al medio día, por las charlitas en la comida y las de después (sí, podríamos decir que nos encanta darle al pico y con algo de comer, siempre mejor). Por estar pendiente y por estar cada vez que necesitaba un cable fuerte. **Sergi**, gracias por el apoyo constante, y por todos esos consejitos para que esta tesis pareciera una tesis en

condiciones. Espero no volverte loco con tantas preguntas, no lo puedo evitar. **Víctor**, por acogerme como una más, por presentarme a los amigos (ya doctores) de otros laboratorios y por nuestro querido pasapalabra (A: alanina). Por todas las horas compartidas y momentos guardados bajo la bata del laboratorio. Siempre tendremos anécdotas que contar. A **Michela**, a **Nasty**, **Mònica** y a **Laia**, por las horas compartidas cada una con su huellita personal. Gracias familia CRI6.

Y si de compartir horas va el asunto, también me gustaría mencionar al laboratorio donde estuve seis meses de estancia. Bella Italia, Milano, Human Technopole. Thank you, **Philipp**, your first lab-day was my first stage-day. Thank you for welcoming and sharing your expertise knowledge. **Gaia**, la mia sorella, oh raga, no words for your support during the hole stage. **Roberta**, always with some advices, always with a smile. **Jas**, thank you for your constant attention. Madre mia **Michelangelo**, **Malan** and laughs, **Simona, Nik, Helen** and patience, **Irene** and wines, **Zawar, Giovanni** and smiles. Thank you Human Technopole for such a nice experience.

Aprovecho para mencionar a las Yamas italianas, lo que surge a partir de un: ¡que aproveche chicos! **Marta**, **Mario**, **Sandra**, **Ioanna**, y **Diego**, gracias por esas cervecitas compartidas en la Dársena (mejor no las contamos), nuestras horas en la vinería (si, nuestro lugar de confianza), nuestros bailoteos (en batukadas, en Leoncavallo..) y las escapaditas. Por ser la familia italiana que uno elige. Grazie mille, Yamas.

Y vuelvo a la carga con toda la gente del IBMB. Siempre parece que somos pocos, pero al final cundimos. Empezaré con los laboratorios vecinos. CRI7, gracias **Aleix**, por ser mi confidente, siempre con tu optimismo y con tu sonrisa. Anda que no nos hemos pasado horas contándonos la vida. Gracias **Elena**, por compartir el teatro (vaya par de actrices estamos hechas), por los ratitos de cotilleos y por los vermuts sin fin. A **Ramiro**, por el ánimo mutuo en esta etapa, por todos los consejos burocráticos y por todo lo compartido. A **Arkadius**, por sus bailes y a **Nord**. CRI3, gracias **Arturo** por las risas en purificación, a **Ulrich**, a las **Lauras**, a **Soraia** por los consejitos, y a **Juanse** por ser un buen vecino, la compañía en el bus siempre es buena. CRI4, gracias **Ira**, por nacer en la misma tierra, dos riojanas siempre mejor que una, por Makoki, y por las cervezas eternas compartidas. Lo que nos gusta un conciertito y un buen vermuteo. CRI0, nombre inventado, no hacen cristalografía, pero si hay muy buena gente que alegran las comidas: **Ofelia**, **Belén**, **Joanna** y **Toni**. Especial mención a **Silvia**, por ser uña y carne. Y pasarnos horas

hablando de nuestras vidas, es lo que mejor se nos da. También a **Alba**, por la nueva incorporación, y vaya incorporación cargada de vidilla. CRI1 y CRI2, gracias **Rosa** por los momentos en coles compartidos, y a **Adrià**, por empezar y acabar juntos esta etapa, y compartir con risas lo aprendido.

Y ahora, empiezo con el hélix mix. Un buen popurrí de buena gente por los pasillos de la segunda planta y ojo, de la tercera planta también. **Marcos**, por lo majo, por las coñas continuas y por todos los momentos desde la carrera hasta el doctorado. A **Mònica**, por conocernos en cultivos y no callar, por sacar energía de donde no la hay, por miradas telepáticas y por llenar de alegría allá donde pisas. Juntas durante esta etapa hasta el final (nunca mejor dicho, con birritas y abrazos mejor). Así es, nuestra querida Mònica. A **Blanca**, por mantener al IBMB activo, organizando mil actividades. Y por ser otra buena vecina. A **Alexis** y a **Alba**. A **Laura**, otro apoyo continuo en estos años y por ser casi miembro de nuestro laboratorio una temporada. Apuntadas quedan unas cuantas risas. A **Marta**, porque Cullera ha dado para mucho, la fallera más fallera. A **Marta V**, por los ratitos de cotilleo en cultivos, poniéndonos al día, y por los consejitos para algún experimento. A **Nùria**, **Mónica**, y a las **Cris**, por los buenos ratos en la sala amarilla, grabando videos, bailando, comiendo con anécdotas y con risas contagiosas. A **Alex**, por los buenos afterworks pandémicos. A **Mariajo**, por ser la gallega más andaluza, por las comidas del último año, por la ayuda con las imágenes (y con cualquier cosa), por el ánimo para cerrar la tesis y por la juventud. A **Jose**, por las risas bien compartidas y ese disfraz de Blancanieves. A **Paula**, por lo vivido en Milán. A **Yara**, such a cute and powerful girl. A **Pili**, ay mi Pili, la más intensa del pasillo, pero con el corazón más llenito. Que llega del sur y revoluciona el edificio. Con ella uno se jarta de reir (bueno bueno bueno). Por esos afterworks pandémicos, por las excursiones, y por el último añito de escalada, que vaya añito. Me la llevo. A **Mar**, por ser el ser de luz del pasillo, todo bondad y cariño. Por ser la amiga más atenta que uno puede tener, por sacar lo bonito de las entrañas y por empatizar. También por el añito de escalada. Gracias Mar por todo lo que he aprendido de ti. Te admiro. Me la llevo. Otro ser de luz es nuestra querida **Antonia**, por sus buenos días, que alegran el día a cualquiera. Con su sonrisa instaurada desde el minuto uno del día y durante todo el día. Es un placer tenerla cerca. Y su confianza. Ay mi querida Antonia, gracias por animarnos a todas horas.

Me dejo a una personita del edificio de enfrente, que también juntitos desde la carrera hasta el doctorado, y pasando por un máster. Gracias **Niko**, te espero otra vez en San

Mateo. Y hablando de gente de la carrera, aprovecho para mencionar a **Se la lleva**, gracias guapos, gracias por ser fieles a los contratos. Buscando próximo destino. Y a los supervivientes del máster, unos pocos, siempre me alegran más de un miércoles en el bar de Julio.

Uy Resa Lesseps, la gente de la resi, uy aquí tendría que mencionar a mucha gente. Porque lo bonito de las amistades es que se mantienen, aunque no haya vivido este periodo en una residencia, ellos siguen ahí, permanecen. Y que perduren los reencuentros: **Masvi**, **Borja**, **Juan**, **Jesús**… **Chula**, por ser como el agua y el aceite, la mejor compañera de habitación y de piso, por confiar en mi desde el principio y hasta el final. Te echo de menos. A mis queridas novatas, mis amigas a las que les doy la turra, y me llaman pesada. El Klaustro de Barcelona o el Tortato de Boquilla. Las que me dan vida en Barcelona. **Clara**, por ir siempre al grano y tener siempre razón. Por compartir buena música, por tus consejos de sabia o de maga. Porque, vasca y riojana, es buena combinación, el comer y el beber nos sienta bien. Uno, dos, ches y cuacho. **Marta**, la gallega imprescindible, te fuiste y volviste (¡y menos mal que volviste amiga!). Por tus verbos conjugados y tu acento, por las buenas vibras y las cervezas bien tomadas. Por tu estilo y compartir música a la moda. Otro viajecito ya. **Uxue**, por lo que nos gusta improvisar, dejarnos llevar y fluir. Por nuestro plan de futuro: el festival. Mucha música, muchas palmaditas, y alguna que otra cerveza. Por el añito de escalada, y ser mi escaladora favorita. Eso sí, una pena que sea debajo del Ebro. Siempre quedará pendiente un ruteo por los bares de tu querida Iruña. A **Maitane**, la bilbaína del grupo, que se fue a Japón

por amor. Aquí le echamos de menos. A **Marta Güell**, por las cenitas cuando vuelve, por la visita a Milán y por enseñarme Zürich. Aquí siempre te esperamos. A **Silvia**, nuestra matrona preferida, por sentirnos como en casa cuando vamos a verte. Gracias amigas, por no dudar de mí.

Hablando de amigas, gracias amigas, gracias a la cuadrilla de Logroño, por disfrutar de cada momento que nos juntamos, que todo nos viene bien. Que un conciertillo, que una subida a la peña de Islallana, que una comidita en el monte. Si, vosotras, gracias por sacar lo mejor de mí. Mención especial a **Iratxe**, por pasar una buena tarde diseñando la portada de esta tesis. Mencionar a la cuadrilla del Vuelo Madrid Manila, que los chicos siempre están ahí. **Javi**, por lo compartido en Barcelona. Y a **Edu**, también, y por ser amigos desde bebés.

Ahora ya solo queda hablar de mi familia. A mis padres, **Mamá** y **Papá** (**Jesús** y **Adita**), gracias por siempre hacernos ver la vida sin complicaciones, sacándole siempre el lado positivo, y por enseñarnos a saber disfrutar cada segundo de esta vida. Así, una tesis se lleva más fácil y se relativiza. Gracias con el corazón, por ser tan bonitos por dentro y por fuera. Y nos toca celebrarlo, tenemos que poner fecha. Vuestra hija mayor que os quiere. A mi hermana **Marta**, con ella me quedo sin palabras, porque yo no sé qué tipo de conexión nos une, pero siempre quiero estar a su lado. Aunque la odie a momentos, siempre me llena de vida. Por bugui, por el punch, por el baile de los sábados, por la música, por las cenitas, por las excursiones. En fin, por todo. Hermana de los pies a la cabeza. A **Nela**, por ser la tía que más nos soporta, por la confianza y la voz sabia, por saberme guiar. Y por siempre querer estar a nuestro lado. Por echar tanto de menos a los yayos como nosotras. **Yaya**, que orgullosa estarías. A toda mi familia de Valencia, por los veranitos en Cullera y a mis queridas amigas del pueblito pesquero. A todos mis tíos y primos de Logroño, a la familia Calleja y al gran abuelo. **Abuelo**, que orgulloso estarías.

A **Juan**, por El Juanish y la Marichi, por El Juanillo y la MariPili, por conocernos a la vez que empecé la tesis, por la conexión inmediata, por los viajes sin organizar, por hacerme feliz, por reírnos a carcajadas, por sacar lo bueno de todas las personas que te rodean. Gracias a toda tu familia, en especial a tu mami **Isabel**, a tu hermana **María**, a **Gonzalo**, y a nuestro sobrino **Felipe**. Gracias por compartir la vida conmigo, y por brindar siempre con el vaso lleno. Gracias por hacer que los km que no separan, no sean distancia. Gracias por ser mi apoyo incondicional. Ahora nos toca construir nuestra vida juntos.

ABSTRACT

The vault particle, with a mass of 10 MDa and dimensions of 70 nm x 40 nm x 40 nm, is the largest ribonucleoprotein described in the eukaryotic kingdom. The vault shell is organized in two identical moieties, each consisting of 39 copies of the major vault protein (MVP, 100 kDa), which assemble to form a barrel-like cage with an enormous interior volume. The telomerase associated protein 1 (TEP1, 290 kDa), the vault poly (ADP)-ribose polymerase (vPARP, 193 kDa), as well as several short untranslated RNAs (vRNA) are localized in the interior volume of the particle, as minor components. Vaults are present and widely conserved in most eukaryotes, suggesting an essential biological role, which, however, remains poorly understood.

In a previous work, using a combination of vault recombinant reconstitution, biophysics and cryo-electron microscopy (cryo-EM) techniques, we characterized the structural dynamics of rat vaults, suggesting a mechanistic model for the vault opening-closing cycle with functional implications for cargo encapsulation, transport, and delivery.

Dictyostelium discoideum is the only organism described so far possessing two closely related isoforms of MVP (MVPα and MVPβ), and our previous findings demonstrated that both isoforms are essential for vault assembly. Solving the structure of *Dictyostelium* vaults would shed new light on the evolutionary relationships between these singular particles among lower and higher eukaryotes. In this work, we solved the cryo-EM structures of recombinant *Dictyostelium* vaults, unbound (3.8 Å resolution) and bound to a nanobody (5.1 Å resolution), recognizing a myc-tag, artificially inserted in an exposed loop of the R6 repeat in MVPβ, to differentiate the two isoforms.

In parallel, with the aim of contributing to the understanding of the role of vaults in intracellular transport, we performed a preliminary characterization of the structure and interactions of vault particles in their native environment by *in situ* cryo-electron tomography (cryo-ET).

RESUMEN

La partícula vault, con una masa de 10 MDa y unas dimensiones de 40 nm x 40 nm x 70nm, es la mayor ribonucleoproteína descrita en el reino eucariota. La partícula está organizada en dos mitades idénticas, compuesta cada una por 39 copias de la *major vault protein* (MVP, 100 kDa), las cuales se ensamblan para formar una estructura en forma de barril con un voluminoso espacio en su interior. La *telomerase associated protein 1* (TEP1, 290 kDa) y la *vault poly (ADP)-ribose polimerasa* (vPARP, 193 kDa), además de algunos pequeños RNAs no traducidos (vRNA) se encuentran en el volumen interno de la vault como componentes minoritarios. Las vaults están presentes y conservadas en el reino eucariota, lo que sugiere una función biológica esencial, sin embargo, todavía no se conoce la función exacta de estas partículas.

En un estudio previo, caracterizamos la dinámica estructural de vaults de rata, mediante la combinación de técnicas biofísicas con la expresión recombinante de vaults con mutaciones en la región central de interacción entre las dos mitades, y crio microscopía electrónica (cryo-EM), proponiendo un modelo mecanicista del ciclo de apertura y cierre de la partícula vault con implicaciones funcionales como encapsulación de carga, transporte y entrega.

Dictyostelium discoideum es el único organismo descrito hasta ahora que presenta dos isoformas de la MVP similares en secuencia (MVPα y MVPβ). Previamente demostramos que las dos isoformas son esenciales para el ensamblaje de la vault. Resolver la estructura de las vaults de *Dictyostelium* arrojaría nueva luz sobre las relaciones evolutivas de estas singulares partículas entre eucariotas inferiores y superiores. En este trabajo hemos resuelto dos estructuras de vaults recombinantes de *Dictyostelium*, mediante técnicas de cryo-EM: una propia de las vaults (3.8 Å de resolución) y otra de vaults en complejo con un *nanobody* (5.1 Å de resolución) que reconoce un myc-tag insertado artificialmente en un bucle expuesto del dominio R6 de la MVPβ, con el objetivo de diferenciar ambas isoformas.

En paralelo, con el objetivo de contribuir a la comprensión del papel de las vaults en el transporte intracelular, realizamos la caracterización preliminar de la estructura y las interacciones de estas partículas en su entorno nativo, *in situ* mediante tomografía crioelectrónica (crio-ET).

TABLE OF CONTENTS

GLOSARY OF TERMS

Proteinogenic L-aminoacids list:

A (Ala): Alanine

C (Cys): Cysteine

D (Asp): Aspartate

E (Glu): Glutamate

F (Phe): Phenylalanine

G (Gly): Glycine

H (His): Histidine

I (Ile): Isoleucine

K (Lys): Lysine

L (Leu): Leucine

M (Met): Methionine

N (Asn): Asparagine

P (Pro): Proline

Q (Gln): Glutamine

R (Arg): Arginine

S (Ser): Serine

T (Thr): Threonine

V (Val): Valine

W (Trp): Tryptophan

Y (Tyr): Tyrosine

Other terms:

2D: Two dimensional

3D: Three dimensional

ADP: Adenosine Di-Phosphate

AKT: Protein kinase B

ATG8: Autophagy related family proteins

AFM: Atomic force microscopy

BL2: Burkitt lymphoma

COP1: Constitutive Photomorphogenic 1

CCD: Digital charge-couple device

CHX: Cycloheximide

CsCl: Cesium Chloride

DDM: N-Dodecyl-β-D-maltoside

Dictyostelium: *Dictyostelium discoideum*

DNA: Deoxyrubonucleic Acid

Dox: Doxycycline

DSF: Differential scanning fluorimetry

FRET: Fluorescence Resonance Energy Transfer

FSC: Fourier Shell Correlation

EBV: Epstein–Barr virus

E.coli: *Escherichia coli*

EGFR: Epidermal growth factor receptor

EGFP: Enhanced Green Fluorescence Protein

EM: Electron microscopy

ET: Electron tomography

ERK: Extracellular-regulated kinases

IMAC: immobilized metal affinity chromatography

INT: MVP-interacting

LA: lamin A

LC3: Light chain

LIR: LC3-interacting region

LRP: Lung resistance protein

mA: milliampere

MALS: Multi-angle light scattering analysis

MAPK: Mitogen-activated protein kinase

$MgCl_2$: Magnesium Chloride

mTOR: Mammalian target of rapamycin

MVP: Major vault protein

NaCl: Sodium Chloride

NLS: Nuclear localization sequence

NTPase: Nucleoside-triphosphatase

NPC: Nuclear pore complex

PBS: Phosphate-buffered saline

PC12: Pheochromocytoma cell line

PCR: Polimerase chain reaction

PKR: Protein kinase R

pFB: pFastBac Hta

PTEN: Tumor-suppressor phosphatase

rBV: Recombinant Baculoviruses

R3D: 3D refinements

Rapa: Rapamycin

RIP-qPCR: RNA immunoprecipitation quantitative PCR

RNA: Ribonucleic Acid

RNP: Ribonucleoprotein particle

SEC: Size exclusion chromatography

SCLC: Small cell lung cancer

SDS: Sodium dodecyl sulphate

SR-A: Class A scavenger receptor

SHP-2: Tyrosine phosphatase

SPA: Single particle analysis

TEM: Transmission electron microscopy

TEP1: Telomerase associated protein 1

TRIM5: Tripartite Motif Containing 5

TROVE: Telomerase, Ro and Vault

UBA: Ubiquitin-associated

vPARP: Vault poly (ADP)-ribose polimerasa

VIT: Vault inter-alpha-trypsin

VLPs: Vault-like particles

vtRNAs: vault RNAs

vWa: von Willebrand type A

Introduction

INTRODUCTION

1. Historical background

The vault complex, with a mass of 10 MDa and overall dimensions of 70 nm x 40 nm x 40 nm, is the largest ribonucleoprotein described in the eukaryotic kingdom (Kedersha et al., 1900; Hamill and Suprenant, 1997; Herrmann et al., 1997). Despite their widespread expression in human and animal tissues, vaults were not discovered until 1986 (Kedersha et al., 1986). This late appearance can be explained by the lack of visibility of proteins in standard electron microscopy preparations, where the stains depict primarily membranes and nucleic acids. However, once negative staining electron microscopy was introduced, vaults were easily recognized as contaminants in clathrin-coated vesicle preparations from rat liver tissues. The particles were named vault because of their symmetric barrel-shaped morphology, which resembled gothic cathedral ceilings (Rome et al., 1991) (Figure 1).

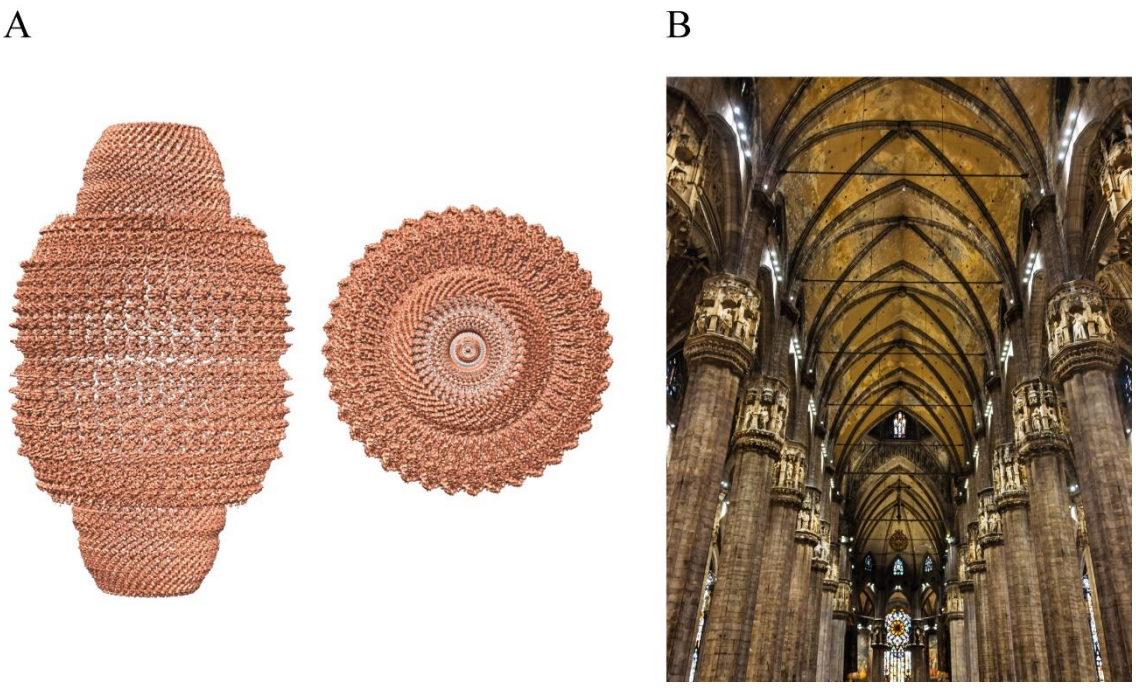

Figure 1. (**A**) Different views of a 3D reconstruction of the vault particle (Guerra et al., 2022). (**B**) Example of the gothic cathedral ceiling that inspired the name of vaults (Duomo di Milano cathedral, in Milan).

Introduction

In mammals, vaults are composed of three proteins: the 100 kDa major vault protein MVP (Kedersha and Rome, 1986), the 193 kDa vault poly(ADP-ribosyl)ating polymerase vPARP (Kickhoefer et al., 1999), the 240 kDa telomerase-associated protein TEP1 (Kickhoefer et al., 1999), and several small untranslated RNAs of about 100 nt in length. (Kedersha and Rome, 1986; Kickhoefer et al., 1993; Van Zon et al., 2001). Vaults are uniform in size and morphology when imaged by electron microscopy, presenting a barrel-like structure with an invaginated waist and two protruding caps (Kong et al., 1999). The major vault protein (MVP) is the architect in charge of the construction of this particle since it encodes all the information necessary for the assembly of the vault shell (Kickhoefer et al., 1996; Mikyas et al., 2004). The notion was initially supported by the fact that vault-like particles (VLPs), similar to purified endogenous vaults, were observed when rat MVP was expressed in insect cells, indicating that MVP was capable of generating the minimal vault structure and the entire outer shell of the vault particle (Poderycki et al., 2006; Stephen et al., 2001). This was further confirmed by comparing the X-ray structures of intact rat vaults (Tanaka et al., 2009; Querol-Audí et al., 2009; Casañas et al., 2013), and the structures of recombinant rat derived VLPs, solved by cryo-electron microscopy (cryo-EM) (Ding et al., 2018; Guerra et al., 2022). All these structures have shown that the vault shell is organized into two identical halves, each consisting of 39 copies of MVP, which assemble to form a barrel-like cage with a large internal cavity where the minor components are located. The copy numbers may range from 2-4 copies for TEP1 to 4–16 copies of vPARP (Kong et al., 2000).

Vaults have been identified from a wide range of species including, in addition to diverse mammals, evolutionary widely separated entities such as protozoa (for example *Dictyostelium discoideum* amoeba), molluscs and echinoderms (the sea urchin *Strongylocentrotus purpuratus*), but also from amphibians (*Rana catesbeiana*, *Xenopus laevis*), avian (*Gallus gallus*) and fish (electric ray *Torpedo marmorata*). Surprisingly, vaults are absent in several other species popular in molecular research such as *Saccharomyces cerevisiae*, *Caenorhabditis elegans* and *Drosophila melanogaster* as well as in plants (Berger et al., 2009). The high evolutionary conservation of vaults suggests a fundamental function associated with its barrel-like structure. Figure 2 depicts a comparison of MVP sequences from different organisms, with the conservation zones highlighted in red.

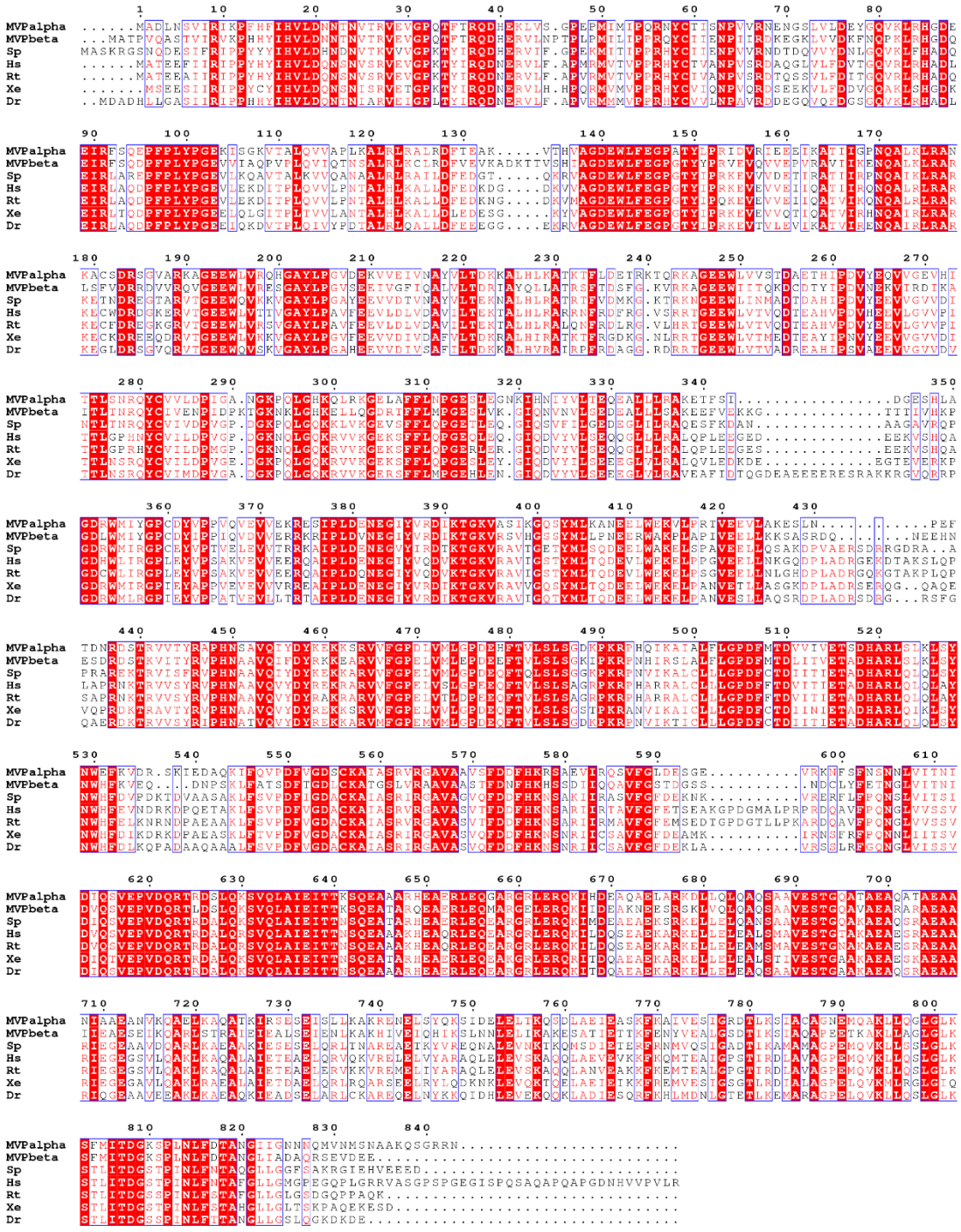

Figure 2. Sequence comparison of the MVP between protozoa (*Dictyostelium discoideum*: MVPα and MVPβ), echinoderm (*Strongylocentrotus purpuratus* [Sp]), Human (*Homo sapiens* [Hs]), Rat (*Rattus norvegicus* [Rt]), frog (*Xenopus laevis* [Xe]) and Zebrafish (*Danio rerio* [Dr]) obtained with ESPript software (Robert, X. and Gouet, P., 2014).

2. Vault Minor Components

2.1 vPARP

In 1999, Kickhoefer and colleagues identified the 193 kDa vault component as a poly-(ADP)-ribose polymerase (vPARP) (Kickhoefer et al., 1999). Known collectively as the PARP family, these related enzymes are capable of catalysing the covalent transfer of ADP-riboses to acidic residues of certain proteins (poly-ADP-ribosylation) (Amé et al., 2004). In addition, PARP family has a critical role in DNA repair and in other genome stability processes such transcription, replication and chromatin structure regulation (Meyer-Ficca et al., 2005).

PARP family is formed by at least 18 members that are encoded by different genes, which shared the conserved catalytic domain (Morales et al., 2014). In particular, the vPARP dubbed as PARP-4 is predicted to contain a BRCA1 C-terminal (BRCT) domain at the N-terminus (Figure 3A), followed by the catalytic domain, a vault inter-alpha-trypsin domain (VIT), a von Willebrand type a (vWa) domain, a nuclear localization sequence (NLS) and a MVP-interacting (INT) domain at the C-terminus (Figure 3-A) that binds MVP close to the midsection of the particle (Yu et al., 2017). The number of vPARP molecules per vault remains unclear (4-16 copies), however it is known that *in vitro* vPARP is able to poly-(ADP)-ribosylate itself and the MVP (Kickhoefer et al., 1999).

2.2 TEP1

As a homolog of *Tetrahymena* p80 protein, one of the protein components of *Tetrahymena* telomerase complex, the telomerase associated protein-1 (TEP1) was identified in 1997 (Harrington et al., 1997). The catalytic subunit of the telomerase complex is the reverse transcriptase (hTERT), TEP1 is not a core component (Weinrich et al., 1997). Data from a TEP1 deficient mouse model demonstrated that TEP1 is not essential for telomerase activity or telomerase length maintenance *in vivo* (Liu et al., 2000) (Liu et al., 2004). Less density was seen in the cap region of vaults from TEP1-deficient mice, suggesting that TEP1 was located there (Kickhoefer et al., 2001a). Additionally, TEP1 interacts with several human vault RNAs (vtRNAs) (Kickhoefer et al., 1999) (Poderycki et al., 2005), playing a significant role in localizing and maintaining the vtRNA associated with vault particles (Kickhoefer et al., 2001).

The structure of the complete 240 kDa TEP1 protein is not yet known. It is predicted to have a N-terminal domain, consisting of four 30-residue repeats (Figure 3B), followed by the *Tetrahymena* p80 homology region domain which contains a TROVE (Telomerase, Ro and Vault) domain and a vWa domain (Figure 3B). RNA binding is carried out by the evolutionarily conserved TROVE domain, which is also found in the telomerase and Ro proteins (Bateman and Kickhoefer, 2003). Downstream the vWa domain there are a NTPase domain (Koonin and Aravind, 2000) and a 16-fold WD40 repeat region, located at the C-terminus (Harrington et al., 1997) (Mikyas et al., 2004).

2.3 vtRNA

The vault particle is described as a ribonucleoprotein particle (RNP) due to its RNA component. Vault RNAs (vtRNA) are small non-coding RNAs transcribed by RNA polymerase III (Kickhoefer et al., 1993). Human express four vtRNA genes with 88-100 nt long (vtRNA1-1, vtRNA1-2, vtRNA1-3, vtRNA2-1) (Stadler et al., 2009). Despite vtRNAs were the first vault component discovered, only a fraction is associated with vault particles. Outside the vault particle, vtRNAs are involved in different cellular processes: proliferation, cellular differentiation, mRNA regulation, cell-cell communication and cell death (apoptosis, autophagy) (Hahne et al., 2021). With the recent discovery that vaults arrive early in the autophagy process (Carter et al., 2020), and the fact that vtRNA is a regulator of selective autophagy (Horos et al., 2019), the question about vault complex-vtRNA role is open.

Although vtRNA exact tertiary fold has not yet been established, prediction approaches assign both paired and nonpaired regions in terms of their structures (Stadler et al., 2009).

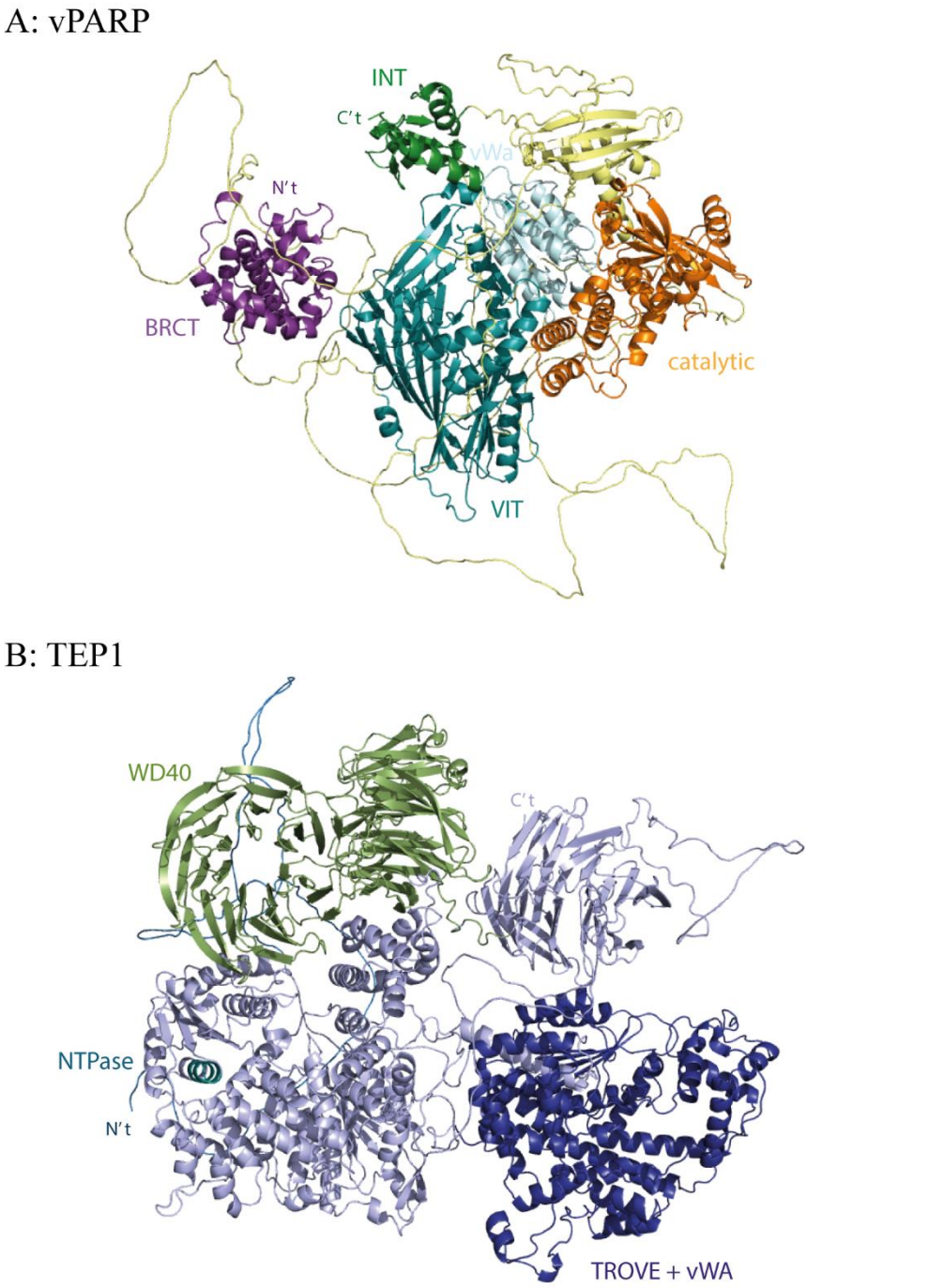

Figure 3. Alphafold prediction models for the Vault minor protein components. (**A**) vPARP (UniProt: Q9UKK3) with the different domains coloured: BRCT domain: magenta, catalytic domain: orange, VIT domain: dark blue, vWa domain: light blue and the INT domain: green. (**B**) TEP1 (UniProt: Q99973) with the different domains coloured: four 30-residues N-terminal repeats: dark blue, TROVE domain and vWa domain: dark purple, NTPase domain: dark blue and WD40 domain: green.

3. Vault localization

The intracellular distribution of vaults has been studied in various cell types and organisms. In mammalian cells vaults are predominantly (>90%) localized in the cytoplasm (Berger et al., 2009). However, a small fraction of vaults is consistently found associated with the nucleus, in particular to the nuclear pore complex (NPC) and the nuclear membrane (Van Zon et al., 2006). One of the first publications about vault localization at the nuclear pore complex, also remarked that mass, diameter and symmetry of the vault particle make it conducive to physically interact in a complementary manner with the NPCs (Chugani et al., 1993). FRET (Fluorescence Resonance Energy Transfer) measurements between labelled vaults and NPC resulted in a significant energy transfer, suggesting that vaults and NPCs are closely associated to the nuclear envelope (Dickenson et al., 2007). An immunolocalization study demonstrated vault/NPC association on cortical neurons (Paspalas et al., 2009). Other investigation could only detect localization to the nuclear envelope, and they observed an accumulation of vaults at the nuclear envelope upon treatment of cells with the protein synthesis inhibitor: cycloheximide (Van Zon et al., 2006). These data suggest that at least occasionally vaults play a role interacting with the NPC.

The rapid movement of vaults at velocities of about 10 µm/s (Slesina et al., 2006) implies the involvement of molecular motors. Indeed, a small fraction of vaults were found associated with intact microtubules, which allowed fast and directional migration (Van Zon et al., 2006; Slesina et al., 2006). A direct association of a subgroup of vaults with microtubules, predominantly bound through their caps, was demonstrated with 5 to 6 vaults bound to each microfilament (Eichenmüller et al., 2003).

The vault complex was also found in different locations: in the neuritic tips of neuronlike PC12 cells (derived from a rat adrenal pheochromocytoma cell line) where colocalized with actin filaments (Herrmann et al., 1999), in lipid rafts, in macrophages, in association either with SR-A (class A scavenger receptor) (Ben et al., 2013), or in human lung epithelial cells infected with *Pseudomonas aeruginosa*, where it appears to play a role in bacterial clearance (Kowalski et al., 2007).

Interestingly, vaults were shown to undergo reversible polymerization at room temperature, giving rise to the so-called "vault tubes" (Figure 4A: d,e and f), in a process that might be promoted by the simultaneous microtubule destabilization (Van Zon et al., 2003). In response to metal-containing oxyanions, such tellurite, vaults aggregate into "vaultosomes", which are large cytoplasmatic structures, around 7 µm in diameter (Figure 4B-B) (Suprenant et al., 2007). Vaultosomes are different to vault-tubes as they are irregularly shaped and not generally elongated, predominantly localise to the cell margins. Co-immunoprecipitation experiments indicated that vaultosomes are different from known forms of aggregosomes and stress granules.

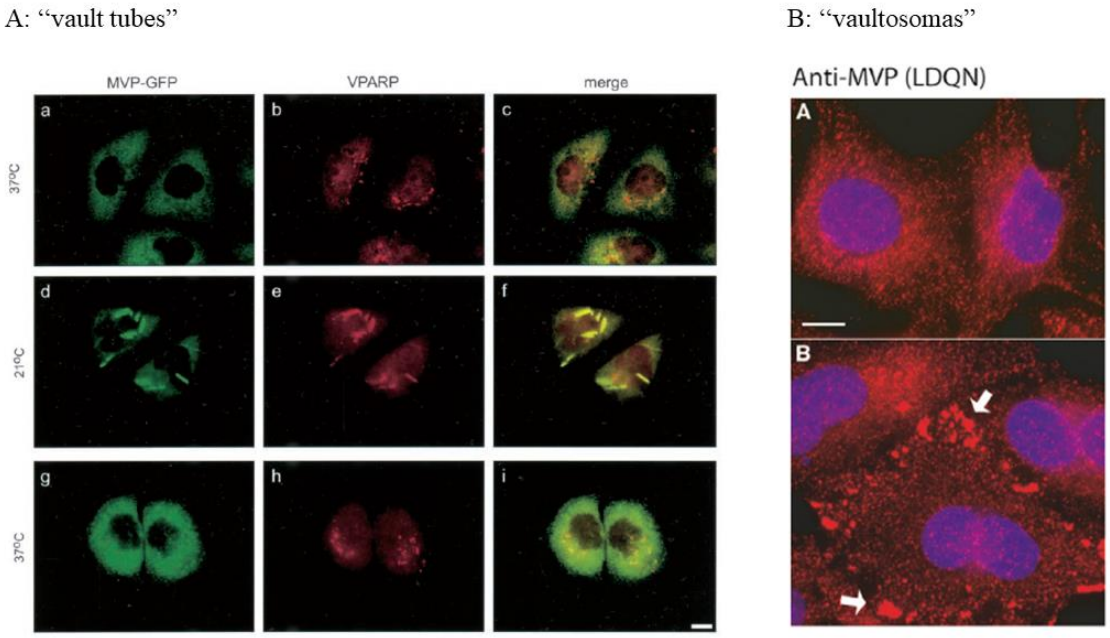

Figure 4. Vault peculiar formations. (**A**) "Vault tubes" were visible at 21ºC in panels d, e and f. Figure from (Van Zon et al., 2003). (**B**) "Vaultosomes" were visible in response to tellurite in panel B. Figure from (Suprenant et al., 2007).

4. Vault Function

Vaults show an ample phylogenetic presence across eukaryotes, hinting at an essential biological role, which, however, remains poorly understood. Although the precise function of vaults remains unclear, its distinct localization within cells, its hollow structure and the rapid movement of the vault complex led to the hypothesis that vaults function is related with cellular transport (Figure 5). In addition, it is known that vaults levels are often upregulated in multidrug resistant cancer cells, suggesting that vaults are involved in drug sequestration or transporting drugs away from their cellular targets, such as the nucleus.

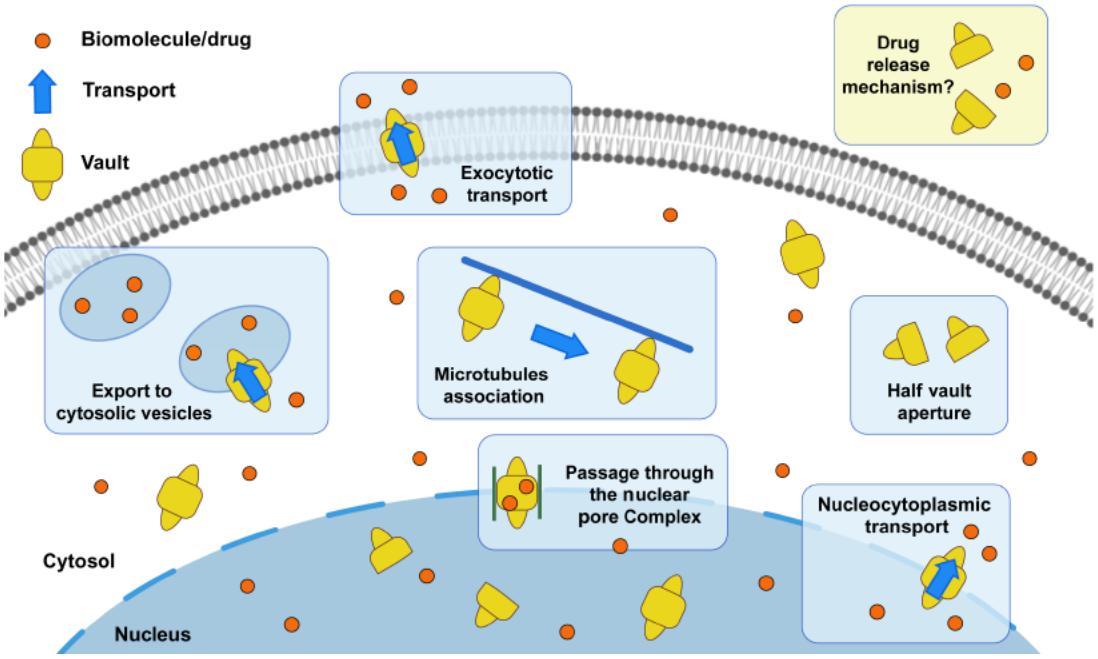

Figure 5. Scheme representing the proposed vault functions, related to transport of variable cargoes in the cell (adapted from Guerra et al., 2022).

4.1 The relationship between vaults and drug resistance

Starting from the very first studies on the vault nanoparticle, and the fact that the murine MVP was found to be orthologous to the human lung resistance protein (LRP), it was proposed that MVP/LRP upregulation correlated with resistance to chemotherapeutic agents in different cancers —e.g., ovarian carcinoma (Izquierdo et al., 1995), acute myeloid leukemia (AML) (List et al., 1996), or oral squamous cell carcinoma (Henríquez-Hernández et al., 2012). These early findings were subsequently confirmed by a wealth

of data, reporting MVP upregulation and drug resistance evoked by drug exposure in several cancer cell types and tissues (summarized in Table 1 Annex- from (Frascotti et al., 2021)). However, MVP upregulation may be observed in cancer even prior to drug treatment (Lötsch et al., 2013; Izquierdo et al., 1996), and a recent report also suggests that forced MVP expression may be sufficient per se to induce cancer development (Yu et al., 2020).

Taken together, these findings raise the question of what precise mechanisms vault uses to inhibiting the cytotoxic effect of drugs. Two different mechanisms have been described in a large number of reports: the first is based on DNA-damaging agent sequestration and/or export from the nucleus and the second is based on the uncoupling of the epidermal growth factor receptor (EGFR) stimulation from downstream AKT (protein kinase B) activation, with resulting uncontrolled cell proliferation. Based on the available data, the latter effect appears only associated to treatments with gefitinib, a well-known EGFR inhibitor (Loser et al., 2012; Lou et al., 2020). In contrast, different mechanisms participate in DNA-damaging drug sequestration/export. For instance, vault mediates doxorubicin efflux from the nucleus and accumulation in cytoplasmic vesicles, which are then released into the extracellular medium (Lehuédé et al., 2019) or sequestered in lysosomes (Herlevsen et al., 2007). A similar vesicle mediated efflux mechanism has been proposed for bleomycin, although possible drug handover from vault to drug efflux pumps has also been suggested (Tang et al., 2013; Mossink et al., 2003). Vaults have also been implicated in similar mechanisms of cisplatin efflux, suggesting that vtRNA(s) may also be involved (Fukushima et al., 2014).

However, no MVP upregulation was detected in autopsy samples of lung cancer cells exposed ante-mortem to platinum (Oguri et al., 1998); conversely, embryonic stem cells and bone marrow cells of MVP $^{-/-}$ mouse models did not display hypersensitivity to various cytostatics (Mossink et al., 2002); likewise, MVP knockdown in non-SCLC (non-small cell lung cancer) cell lines did not affect survival of doxorobucin-treated cells (Huffman and Corey, 2005). A recent paper even reports positive correlation between high bone marrow LRP/MVP expression and a favorable therapeutic outcome (Kulsoom et al., 2019).

The list of potential links between vaults and drug resistance is very long and, at times, obviously contradictory. Consequently, we can conclude that despite the large amount of accumulated data, the precise molecular mechanisms implicating vaults in drug resistance remain to be elucidated.

4.2 Vault and signal transduction pathways

Several proteins have been identified as being bound and transported by MVP; however, whether they are encapsulated in the interior of vaults needs to be determined.

- **PTEN**

The first hint that MVP might regulate intracellular signals come from Zhenbao and colleagues who suggested that MVP bound to the C2 domain of the tumor-suppressor phosphatase PTEN, via the putative EF hands in a Ca^{2+}- dependent manner (Zhenbao et al., 2002). However, the structure of MVP has not shown any EF hand domain (Tanaka et al., 2009; Casañas et al., 2013), nor have Ca^{2+} binding sites been identified.

PTEN acts as a tumor suppressor gene and plays a critical role in cell cycle progression, angiogenesis, migration, invasion and stem cell regulation. The PTEN protein has at least two biochemical functions: it has both lipid phosphatase and protein phosphatase activity. The lipid phosphatase activity of PTEN decreases intracellular PtdIns(3,4,5)P(3) level and downstream AKT activity (Csolle et al., 2020). The protein phosphatase activity of PTEN is apparently involved in the inhibition of focal adhesion formation, cell spreading and migration, as well as the inhibition of growth factor-stimulated MAPK (mitogen-activated protein kinase) signaling (Wu et al., 2003). These data led to the hypothesis that MVP regulates PTEN function probably by changing its intracellular localization. Indeed, in a series of papers the group of Dr. Charis Eng indicated that MVP can mediate nuclear import of PTEN (Chung and Eng, 2005; Chung et al., 2005; Minaguchi et al., 2006). This process was dependent on the presence of Ca^{2+}, antagonized by high levels of Mg^{2+}, and independent of MVP tyrosine phosphorylation. These data implicate MVP in facilitating the nuclear tumor-suppressing function of PTEN. In addition, an essential role of nuclear PTEN in maintenance of chromosomal stability has been indicated (Shen et al., 2007). This would imply that MVP counteracts drug-induced DNA damage by delivering nuclear import of PTEN and thus indirectly contributing to drug resistance. However, these hypotheses must be carefully investigated in a normal and a tumor background.

- **SHP-2/ERK**

The indication that MVP might regulate the epidermal growth factor EGF induced MAPK pathway was reported by Kolli and colleagues, showing that the tyrosyl-phosphorylated MVP bound to several effectors of these cascades, namely at least the activated extracellular-regulated kinases (ERKs) and the tyrosine phosphatase SHP-2 (Kolli et al., 2004). MAPK pathways cooperate in transmitting various extracellular signals and thus control a large number of distinct and even opposing cellular processes such as proliferation, differentiation, survival, development, stress response, and apoptosis. These data suggest that the binding of SHP-2 to phosphorylated MVP promotes the supporting activity of SHP-2 in MAPK activation, thus resembling other so called "scaffolding proteins" like IRS, Gab and FRS families (McKay and Morrison, 2007). These proteins foster SHP-2-mediated pathway activation by both direct activation via the H2 domain and by mediating co-localization with other pathway mediators. The fact that activated ERK was also found bound to MVP suggested that vaults might serve a more general signal scaffolding function for the MAPK pathway (Kolli et al., 2004). Interestingly, both ERK and PTEN when activated translocate from the cytosol to the nucleus raising the possibility that vaults represent a versatile cellular transporter.

- **COP1/c-Jun**

Constitutive Photomorphogenic 1 (COP1) is an E3 ubiquitin ligase originally described to be essential for plant development. However, COP1 is highly conserved in evolution and homologues have been detected up to humans (Yi and Deng, 2005). Also, in these organisms, COP1 functions as ubiquitin ligase and is involved in the degradation of important cancer-related proteins such as tumor suppressor p53 (Dornan et al., 2004). p53 monitors DNA damage and when it detects elevated levels of damage either arrests progression through the cell cycle to allow for DNA repair, or triggers apoptosis in cells with lesions that are not or cannot be repaired (Levine, 1997). As p53 is the most frequently mutated protein in human cancers, any protein that binds this "guardian of the genome" is immediately the focus of intense research. As in plants, mammalian COP1 can shuttle between the cytoplasm and the nucleus and forms large cellular protein complexes. Yi used an affinity purification approach to define novel COP1 binding partners (Yi et al., 2006). These experiments have uncovered that MVP binds cytoplasmic COP1 although the implications of this interaction have still to be studied.

- **Estrogen receptor**

One of the earliest findings demonstrated that both MVP and vRNA co-immunoprecipitated with the estrogen receptor from cytosolic and nuclear extracts of the human breast cancer cell line MCF7 (Abbondanza et al., 1998). Accordingly, a small amount of the estrogen receptor migrated with intact vaults in sucrose gradients. These data suggest that vaults may serve an important role in estrogen receptor nuclear import and/or activation. Once again, vaults are related to proteins that when activated, translocate from the cytosol to the nucleus.

4.3 vtRNA functions

In recent years, key regulatory roles for vtRNAs have emerged. Further reports have identified the involvement of vtRNAs in novel interactions and regulatory roles, implicating them in the control of transcription, development, autophagy, and apoptotic functions (Hahne et al., 2021b) (Gallo et al., 2022).

- **vtRNA1-1**

As far as macro-autophagy is concerned, the vtRNA1-1 isoform was identified as a regulator of the process, as supported by its capability of binding sequestome-1/p62 (Büscher et al., 2020; Horos et al., 2019), a selective autophagy receptor. The latter interacts via its UBA (ubiquitin-associated) domain with ubiquitin chains attached to the autophagic cargo and via its LC3 (light chain)-interacting region (LIR) motif, with ATG8 autophagy related family proteins covalently attached to the inner membrane surface of the growing phagophore (Lamark et al., 2017). By using the RIP-qPCR technology, selective vtRNA1-1 binding to p62 was demonstrated in several human and murine cell lines, which resulted in autophagy inhibition. Based on these observations, it was proposed that high levels of vtRNA1-1 prevent autophagy by binding to p62, thus inhibiting its multimerization and the subsequent autophagosome assembly. It has still to be established whether the anti-autophagic role vtRNA1-1 plays in the process may in some way involve other vault components (Horos et al., 2019). It is worthwhile mentioning that, in this context, MVP also plays an anti-autophagic role via the mammalian target of rapamycin (mTOR). This is an intracellular kinase that inhibits autophagy via phosphorylation of downstream effectors (Jung et al., 2010) and, in turn, is activated by AKT. Thus, MVP itself prevents autophagy when involved in the

activation of the PI3K/AKT/mTOR pathway (Lötsch et al., 2013), although no direct interaction MVP/mTOR seems to take place.

vtRNA1-1 was also shown to protect Burkitt lymphoma BL2 cells from Epstein–Barr virus (EBV)-induced apoptosis (Amort et al., 2015). This led the authors to speculate that vtRNA/vaults could be involved in anti-viral defense by nucleo-cytoplasmatic transport mechanisms. In addition, ectopic expression of vtRNA1- 1 results in an improved viral establishment and reduced apoptosis, a function located in the central domain of vtRNA1-1. Knockdown of MVP has no effect on these phenotypes revealing that vtRNA1-1 and not the vault complex contributes to general cell death resistance (Bracher et al., 2020).

- **vtRNA1-2**

vtRNA1-2, and its paralog, vtRNA1-1, can bind to and sequester chemotherapeutics compounds: mitoxantrone, doxorobucin and etoposide (Mashima et al., 2008) (Gopinath et al., 2005) (Gopinath et al., 2010). Possible playing a role in chemotherapy resistance. Elevated level of promoter methylation causes the decrease expression levels of vtRNA1-2 in tumors (Fort & Duhagon, 2021). This pattern of gene silencing in neoplastic tissue is typical of tumor suppressor genes. On the contrary, vtRNA1-2 levels were high in liver-derived metastasis (Gallo et al., 2022). Future research is required to resolve these contradictory findings.

- **vtRNA1-3**

The expression of vtRNA1-3 was increased in multi-drug resistant cells and vaults extracted from these cells contained a higher amount of vtRNA1-3 associated. (Van Zon et al., 2001).

- **vtRNA2-1**

DNA methylation in tumors, also interferes decreasing vtRNA2-1 expression levels (Treppendahl et al., 2012). In other study, they discovered that in several cancer cells, vtRNA2-1 binds and inhibits PKR (protein kinase R) activity, suppressing then tumorigenesis (Lee et al., 2011). Furthermore, vtRNA2-1 is a crucial factor in the adenovirus infection cycle by facilitating viral particle nuclear entrance. As a result, the possible use of an anti-tumor therapy known as “oncolytic virotherapy”, which uses viruses to target and destroy proliferation tumor cells. vtRNA2-1 appears to have a tumor surveillance role (Lin et al., 2023).

5. Towards understanding the structure and dynamics of vault particles

Since the discovery of the vault complex in the middle of the 1980s, numerous studies have been performed, aimed to understand the structure of this enigmatic particle. The first structure of vaults was obtained by cryo-EM, single particle analysis (SPA) and 3D reconstruction (Kong et al. 1999). Despite its low resolution, below 30 Å, the barrel-shaped vault morphology with two protruding caps and an invaginated waist was clearly visible (Kong et al. 1999).

Three independent groups were able to crystallized the complete vault particle. The initial crystals were obtained in our lab in 2005, where vaults appeared as contaminants in a human astrovirus preparation (Querol-Audi et al., 2005). Two years later, Anderson and colleagues managed to obtain crystals of recombinant vaults that diffracted near 9Å resolution (Anderson et al., 2007).

The first high resolution (3.5 Å) X-ray structure of intact rat vaults was solved by Tanaka and colleagues in 2009, showing that the vault shell structure was organized as a dimer of half-vaults, with each half-vault comprising 39 quasi-identical MVP copies (Figure 6B) (Tanaka et al., 2009). Each MVP monomer was organized in twelve domains: nine structural repeat domains at the N-terminus, followed by a shoulder domain, a cap-helix domain, and a cap ring domain at the C-terminus (Figure 6A). The nine MVP repeats share a similar fold, each consisting of five antiparallel β-strands connected by loops of different size and conformation. The shoulder domain folds into a single α/β domain with a four-stranded antiparallel β-sheet on one side and four α-helices on the other. The large cap helix domain is formed by a 42-turn-long α-helix that is followed by a U-shaped structure that constitutes the cap ring domain at the MVP C-terminus. The strongest MVP–MVP contacts are found between cap-helix domains (Figure 7A) (Tanaka et al., 2009), where the hydrophobic residues are located on the interface between two adjacent helices and polar residues are exposed to inner or outer surfaces of the particle. The detailed analysis of the lateral inter-subunits interactions evidenced the presence of several MVP-MVP electrostatic interactions (Figure 7) (Llauró et al., 2016).

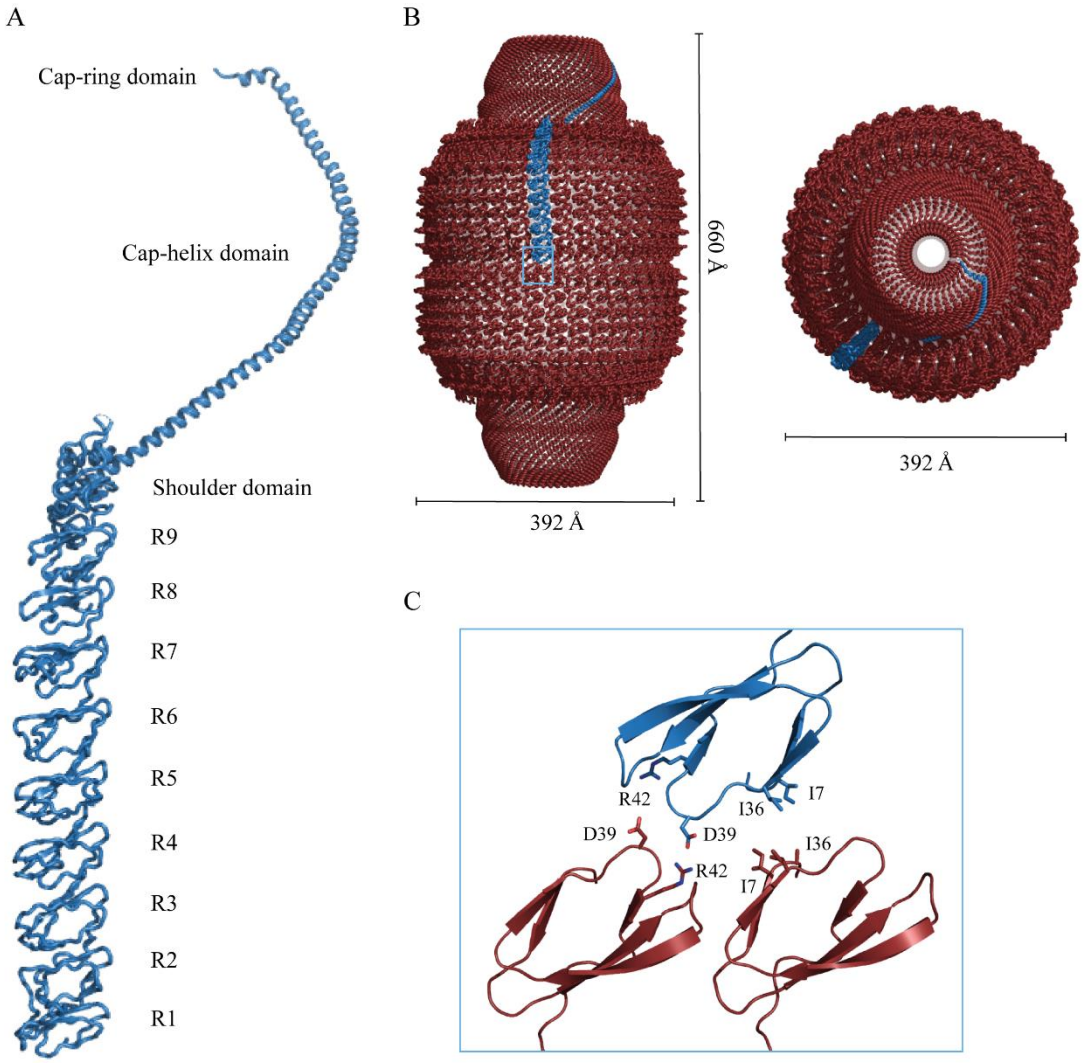

Figure 6. Overall X-ray structure of the vault complex. (**A**) Schematic representation of one MVP subunit with all the domains labelled. (**B**) Left panel: Structure of the vault shell with one MVP monomer coloured in blue. Right panel: top view of the vault structure (PDB ID: 4HL8). (**C**) Zoom representation of the blue square pointed out in (B). Blue square: detail view of R1-R2 contacts at the half vault interface.

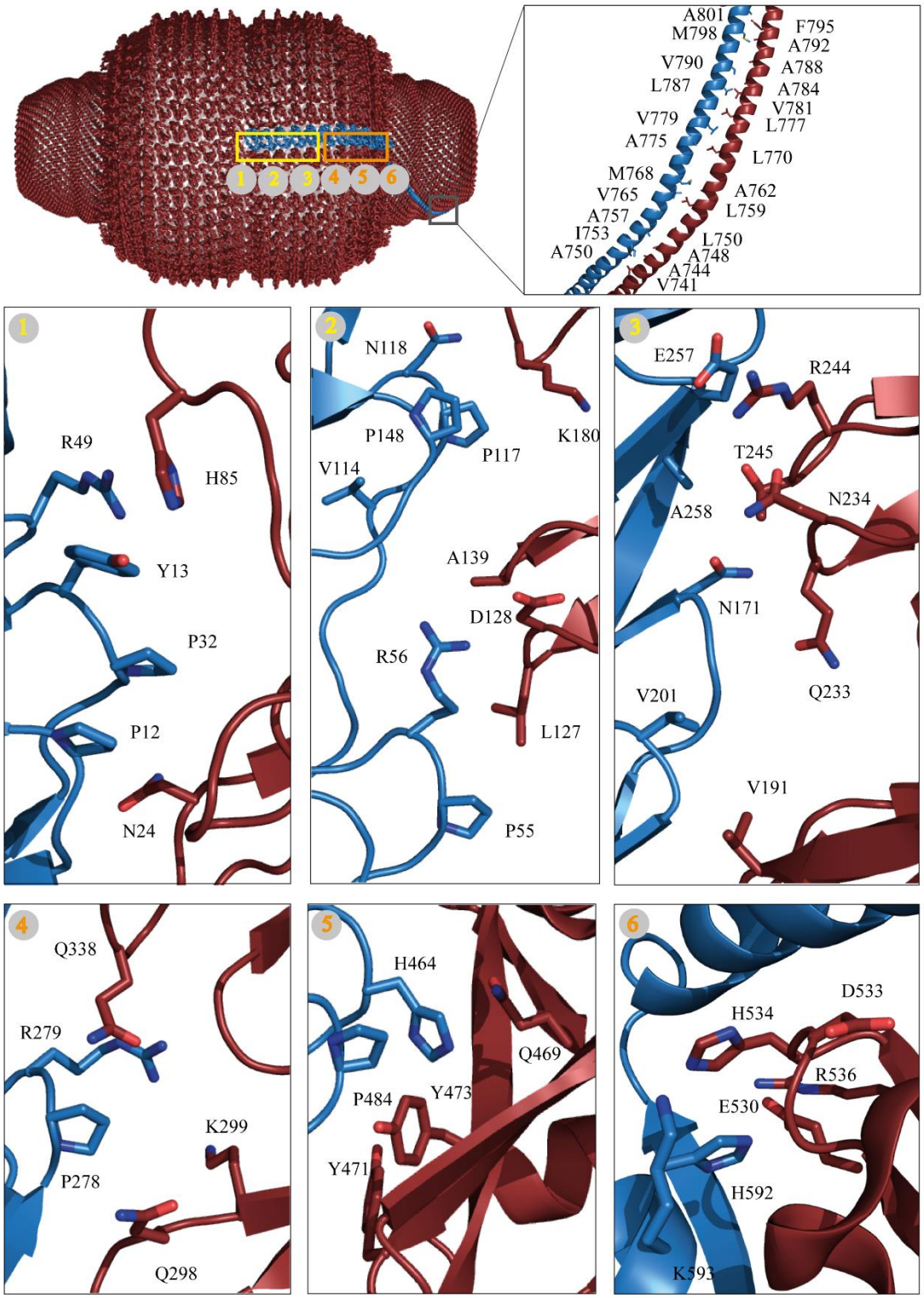

Figure 7. MVP-MVP lateral interactions stabilizing the vault particle. The top left panel shows a cartoon representation of an entire vault (maroon cartoon), with a reference MVP monomer shown in blue. The different panels show representative close up views of the MVP-MVP interactions in the cap-helix (top right panel), in the vault barrel domains (panels 1 to5) and in the α/β shoulder (panel 6).

Also, in 2009, our lab solved the X-ray structure of the seven N-terminal repeat domains (R1–R7) that conform the vault waist at 2.1 Å (Querol-Audi et al., 2009). The structure of the entire vault particle was the refined by incorporating the high-resolution information available for the R1–R7 yielded a new model (PDB ID:4HL8) and applying the strict D39 non-crystallographic symmetry (Casañas et al., 2013). This refinement predicted the breakage of the 39-fold symmetry in the cap-region, which was likely to be formed by only 36 strands defining the narrowest radius (~25 Å) respect to the central vault axis (Figure 8) (Casañas et al., 2013). The precise examination of the refined vaults also indicated that MVP could experience significant movements at its N-terminus during the sealing of the two vault halves. This fact opened the question how is the vault behaviour in solution, non-crystalline environment, and whether it undergoes conformational changes.

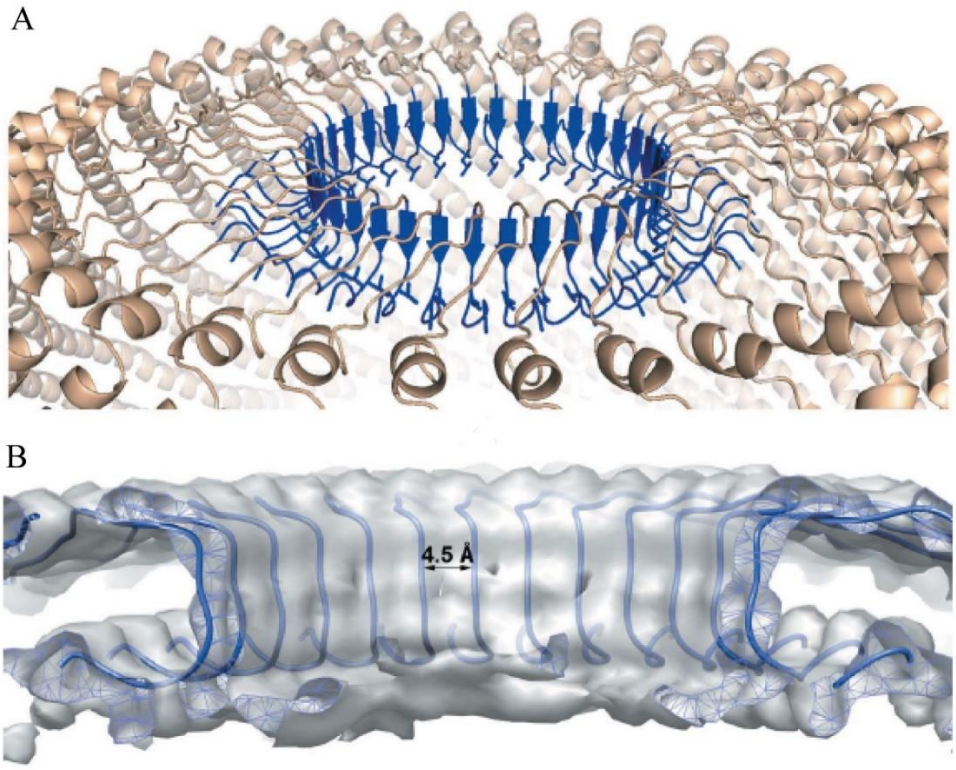

Figure 8. Structure of the vault cap-ring domain (Casañas et al., 2013). (**A**) Representation of a possible arrangement of the cap-region with 36-stranded β-sheet inner ring (radius of ~25 Å) shown in blue and the 39 subunits in the outer part shown in beige. (**B**) View of the continuous electron density that forms the vault cap-ring. The tracing of only 13 chains is shown for clarity, with the distance within strands.

Cryo-EM techniques are able to characterize proteins and macromolecular complexes in a near-native state by flash frozen a purified sample, preventing the formation of crystalline ice. Once frozen, the biological macromolecule is directly visualized using transmission electron microscopy (TEM), which generates 2D images corresponding to projections of the macromolecular structure. Images corresponding to different projections of the sample can be combined to create a 3D map of biological macromolecule (Nogales and Scheres, 2015).

The "Resolution revolution" describes the transition in cryo-EM from low resolution maps to atomic resolution. The main evolution factor was the combination of the development and commercialization of new generation of direct electron detectors (McMullan et al., 2016) with the advances in new maximum likelihood image processing algorithms (Scheres, 2012).

This process was also reflected in the structure determination of the vault complex. For instance, the first cryo-EM structure was solved at 31 Å (Kong et al. 1999), the second one at 38 Å (Kickhoefer at al., 2009) but very recently, the cryo-EM structures determined reached resolutions equivalent to those obtained by X-ray diffraction techniques: ~ 4.8 Å (Ding et al., 2018) and 3.7 Å (Guerra et al., 2022). Ding and colleagues were the first to obtain structures of recombinant rat vault at near-atomic resolution using SPA (single particle analysis) cryo-EM techniques. These authors described two different conformations of vaults: conformation 1 solved at 4.9 Å (PDB ID: 6BP8), and conformation 2 solved at 4.7 Å (PDB ID: 6BP7), both structures were determined by imposing D39 symmetry.

While conformation 1 was identical to the crystal structure (PDB ID: 4HL8) (Casañas et al., 2013), the shoulder in conformation 2 appeared longitudinally translocated up to 10 Å, resulting in an outward-projected cap and consequently in a vault 14 Å longer than conformation 1 along the D39-symmetry axis (Ding et al., 2018).

With the aim to better understand the structural dynamics of the vault particle and to delineate the molecular principles governing the vault opening/closing cycle our lab was also immersed in solving different structure of recombinant rat vaults, using cryo-EM techniques. These studies provided new evidences of the multiple vault populations existing in solution. In particular, we identified and determined the structures of three

different vault states: a half vault state, a fully closed vault, and an additional whole vault state at the beginning of the opening cycle (Figure 10-11) (Guerra et al., 2022).

The structure of the fully closed vault was solved at 3.7 Å by applying D39 symmetry (PDB ID: 7PKR). Structural comparisons with the crystal structure of native rat vaults (PDB ID: 4HL8) (Casañas et al., 2013), showed a number of differences in the shape and size of the particle but maintaining the overall vault architecture shown in Figure 9. The observed differences involved an expansion in the diameter of the barrel region that in our cryo-EM reconstruction was 400 Å while this diameter in the crystallized particles was 392 Å (Figure 9A). Detailed structural comparisons of the MVP monomers showed that the overall conformation is maintained, but the orientation of domains R1 to R5 relative to the C-terminal helix is changed, indicating a built-in structural variability in the whole vault particle affecting the volume of the internal cavity (Figure 9B).

In summary, when the cryo-EM structure of the fully closed vaults (PDB ID: 7PKR) is compared with the X-ray structure of native rat vaults vaults (PDB ID: 4HL8) and with recombinant vaults in conformation-1 (Ding et al., 2018; PDB ID: 6BP8) we observed that the fully closed vaults exhibits a wider, expanded cavity, with a relaxed conformation of the barrel domain (Figure 9B).

Maximum likelihood classification methods, without imposing symmetry, allowed the identification of a second class of full particles but deviating from the symmetry of the “closed” vault state which was named “primed” vault state (Guerra et al., 2022). This deviation was evident in only one region of the vault waist, with R1 domains forming the top and bottom half vaults engaged on one side and disengaged at the other side (Figure 10B). This structure was hypothesized to represent an initial state of the opening cycle of the particle (Guerra et al., 2022).

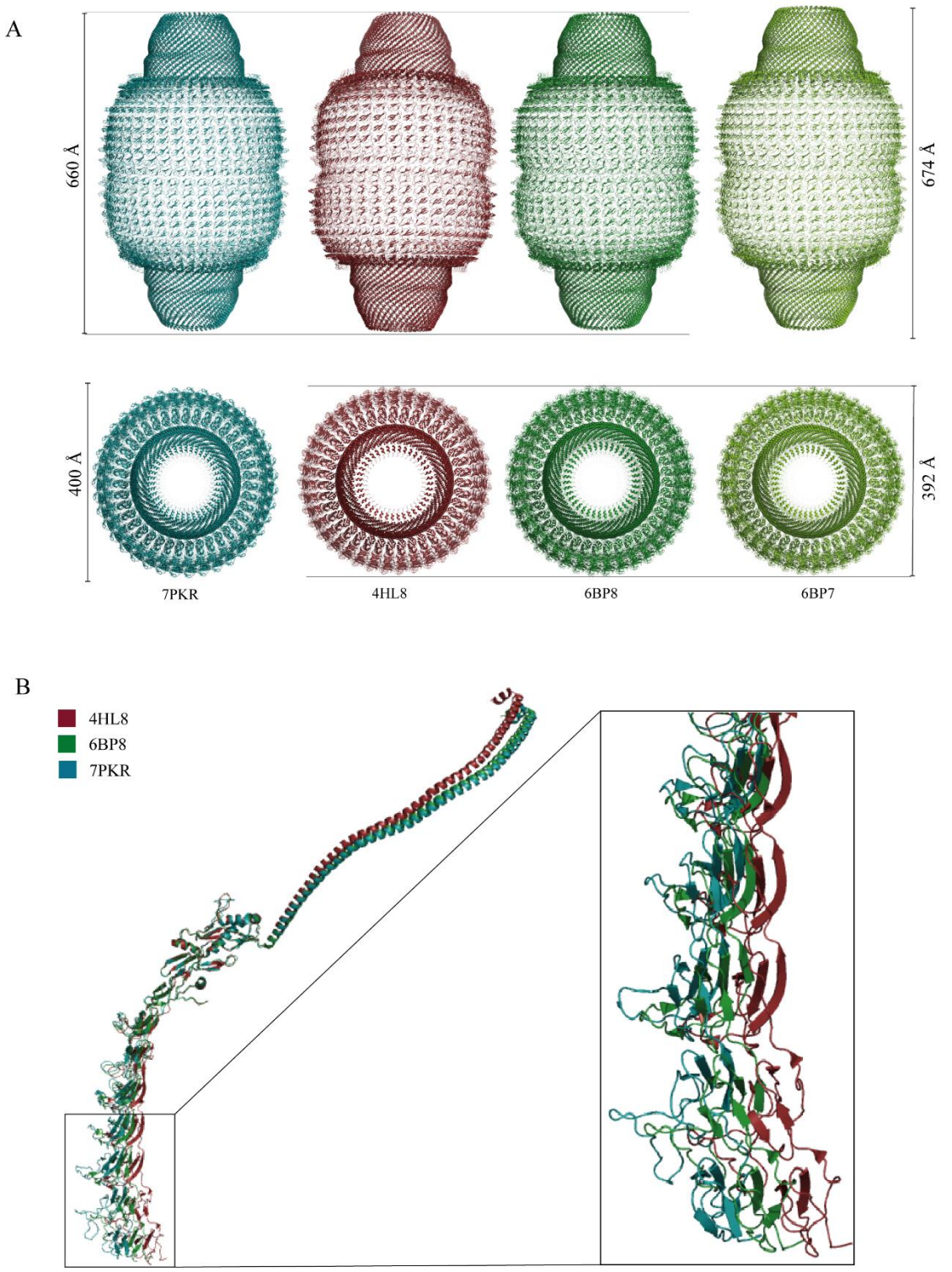

Figure 9. Vault structure comparison. (**A**) Vault structure comparison in size and dimension of all the vault structures solved by X-ray crystallography (PDB ID: 4HL8) and cryo-EM (PDB ID: 7PKR, 6BP8, 6BP7). Showing that conformation 6BP7 is the longest and conformation 7PKR is the widest. (**B**) 4HL8, 6BP8, 7PKR alignment with zoom area showing a change on the degree of curvature of the vault barrel and a distinctive orientation of the cap helices.

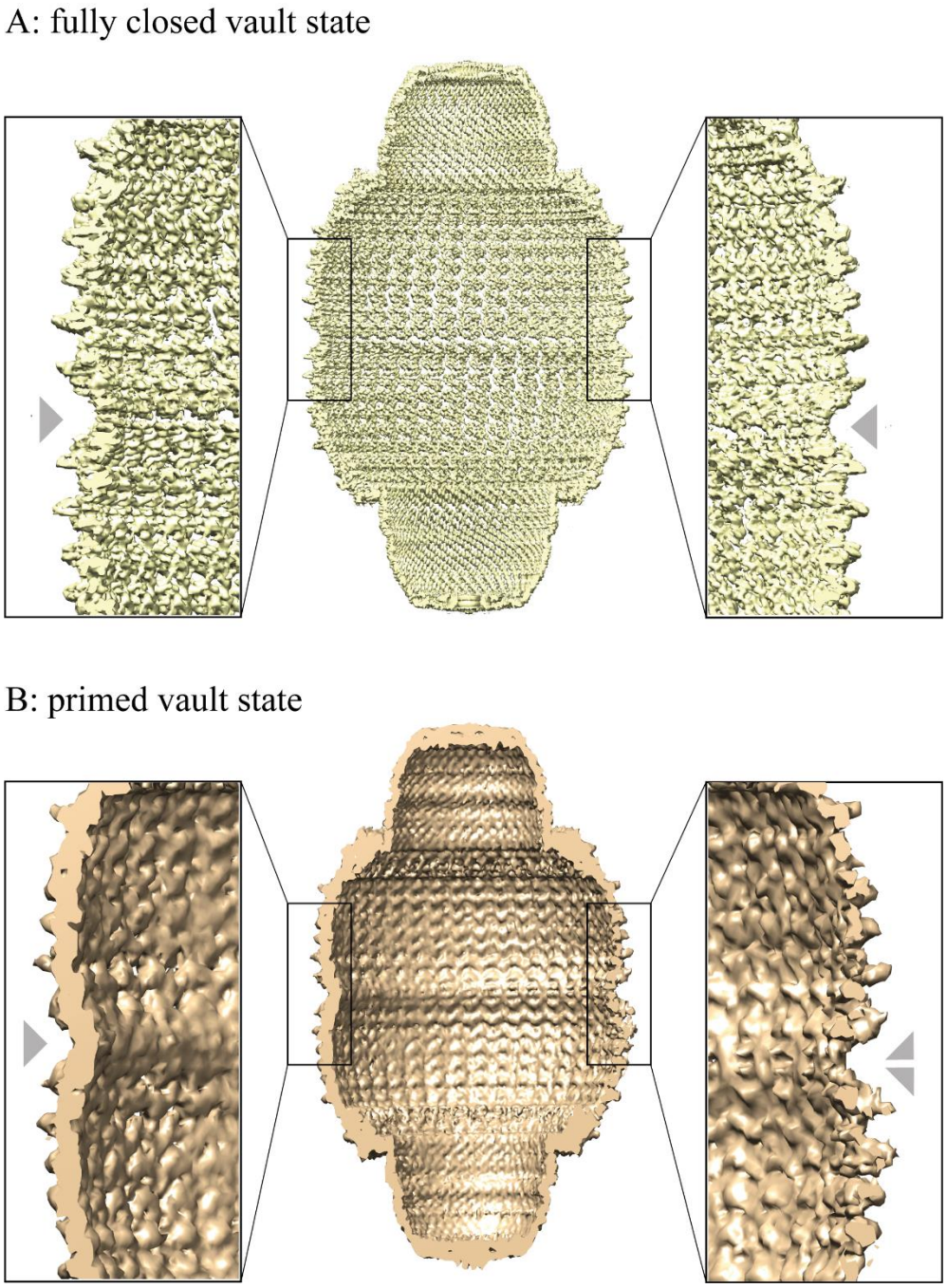

Figure 10. Cryo-EM structures of two vault conformations. (**A**) Cryo-EM density map for the high-resolution vault reconstruction with D39 symmetry (EMD-13478 map, corresponding to PDB ID: 7PKR). Representation of the whole vault in zoom the midsections of the half-vault interface. (**B**) Asymmetrical conformation of another vault class (EMD-13483). Representation of the whole vault in zoom the midsections of the vault interface with R1-R1 domains engaged on left side and disengaged on right side.

The third state of vaults analysed corresponded to opened half vaults (Guerra et al., 2022). These particles showed a distortion of the circular shape of the vault waist, suggesting an oval contour configuration rather than the circular one, present in the closed whole vault state (Figure 11). The reconstructed map (around 9 Å resolution) revealed the structural changes responsible for the oval waist contour, affecting not only the waist but also the central region of the vault barrel. The main structural variation found was a reorganization of the MVP monomers in three clusters of 13 monomers each, while the half vault overall configuration was maintained. The individual MVP N-terminal domains from R3 to R9 of the barrel, the shoulder, and the cap helix and cap ring at the top of the structure matched those of the whole vault state. However, domains R1 and R2 showed great flexibility (Figure 11B). This flexibility would be restricted in the assembled particle, where R1 domains from top and bottom half vaults engage in reciprocal interactions (Guerra et al., 2022).

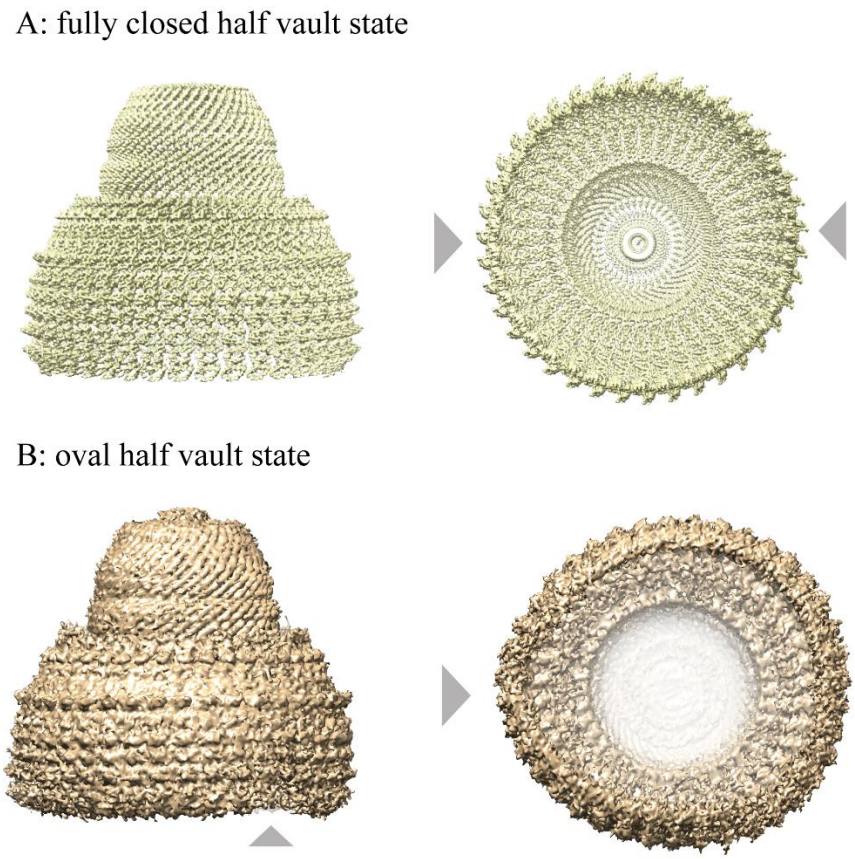

Figure 11. Half vault states. (**A**) Density map of the half vault with a circular contour. (**B**) A third reconstruction of free half vaults (EMD-13482), exhibiting a different architectural feature with an oval contour.

6. The vault aperture process

Along with vault history, and because of its curious architecture, several dynamic scenarios have been studied to understand the vault's role in cargo encapsulation and delivery.

Early experiments showed a particle dissociation in two vault-halves in a putative pH-dependent manner. When pH was less than 4.0, closed intact vaults dissociated quickly into half-vaults (Goldsmith et al., 2007). A reversible mechanism of half vault dissociation induced by a pH change was proposed in light of the observed interactions between the R1-R1 domains at the vault midsection (Querol-Audi et al., 2009). A salt bridge established between the universally conserved residues Asp39 and Arg42 (Figure 2; Figure 6C) appeared to be a critical contact. In addition, the negatively charged amino acids Glu4, Glu5 and Arg37 and a cluster of hydrophobic residues (Ala6, Ile7 and Ile36), interacting through the two-fold axis of the particle, also contributed to the contact surface (Figure 6C). The strong electrostatic character of the interactions observed, with 234 acidic residues at the in the R1-R1 interface, prompted to hypothesize that at low pH these acidic residues would become neutral, leaving a highly electropositive charge and inducing the disassembly of the vault particle by charge repulsion (Querol-Audi et al., 2009). However, this hypothesis was challenged in later studies on the mechanical properties of vaults by atomic force microscopy (AFM), under physiological conditions (Llauró et al., 2014) and also at different pHs (Llauró et al., 2016). In these studies we demonstrated that under physiological conditions vaults possess an intrinsic fracture/recuperation dynamic in which the particle self-repairs over time. This rupture consists of separating two neighbouring MVPs in the barrel structure (Llauró et al., 2014). Further AFM experiments, performed to monitor the structural changes of individual vault particles while changing the pH in real time, showed that decreasing the pH of the solution destabilized the barrel region, but not the vault midsection, finally leading to particle aggregation. The observed topographical defects suggested that low pH weakened the polar bonds between adjacent proteins at the barrel and shoulder regions (Llauró et al., 2016).

Furthermore, *in vivo* experiments at physiological pH performed by Yang and colleagues also supported a model where vault particles were capable of rapidly separating at the particle waist and reassembling back into whole vaults, supporting a half vault exchange mechanism (Yang et al., 2010).

Finally, our recent studies of vault stabilization by combining site-directed mutagenesis and different biophysical approaches, including AFM, negative staining EM, and differential scanning fluorimetry (DSF), confirmed the importance of both hydrophobic and electrostatic interactions mediated by the MVP N-terminal residues, E4, E5 and I7, in the vault assembly process (Guerra et al., 2022). These data integrated with the cryo-EM structures of the three different vault states suggested a mechanistic model for the vault opening-closing cycle with functional implications for cargo encapsulation, transport, and delivery (Figure 12). Fully assembled vaults exhibit a symmetrical configuration with all MVP R1 domains, from top and bottom half vaults, fully engaged in reciprocal interactions (Figure 12: closed state). These particles are functionally committed to cargo delivery. The tight interactions at the vault midsection restricts the flexibility of MVPs, rigidifying the waist cavity and allowing a stable inner compartment needed for cargo delivery. The opening process will begin with a waist relaxation, caused by local displacement of R1 domains of specific MVPs, yielding a localized distortion that increases the angle between the R1 domains involved to around 80° (Figure 12: relaxed state). Local distortions of R1 domain interactions are progressively increased, priming the vault towards opening (Figure 12: primed state). When the angle between these R1 domains exceeds 97° (Figure 12: committed state), the localized distortion can be easily transmitted beyond the area where it started, generating a break between R1 domains that will eventually trigger full separation of the two half vaults (Figure 12: opened state). All these conformational states could coexist in solution as demonstrated in the cryo-EM analyses (Guerra et al., 2022).

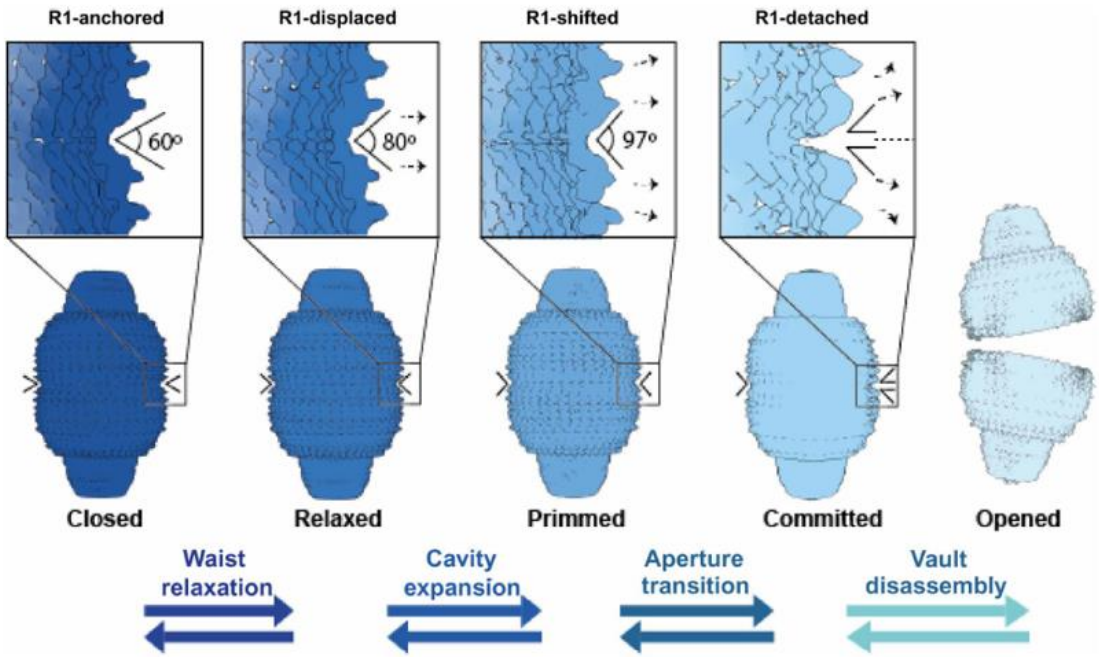

Figure 12. Hypothetical model for the stepwise process of vault aperture (Guerra et al., 2022). Transitioning form a closed to an open state is a critical process in the functional cycle o vault particles.

To further characterize the vault opening/close cycle at the edge of the half vault (MVP R1 domain), several specific residues of the R1 domain were mutated and characterized. The results verified the critical role of the hydrophobic and electrostatic interactions mediated by the MVP N-terminal residues E4, E5 and I7 in the vault assembly and stabilization process (Guerra et al., 2022). The crucial role of residues present in the vault midsection was also supported by previous studies by Rome and Mrazek, where several MVP N-terminal mutants were studied and when these residues were substituted by histidines at the same time (sequence positions 3-7), the result was the generation of unstable vault particles prone to disassembly (Mrazek et al., 2014). They also addressed the dynamic question of how this macromolecular complex is assembled. They presented a model of vault assembly whereby the polyribosomes act like a 3D nanoprinter to direct the ordered translation and assembly of the multi-subunit vault homopolymer. Translated chains on a polyribosome contact with their N-termini to form a dimer. Dimers make side-side contacts and reside in the polyribosome until the 39 dimers associate and the new vault is released (Mrazek et al., 2014). This publication is the first one that gives a clue in vault assembly process.

7. Direct visualization of vaults in cells

Cryo-electron tomography (Cryo-ET) is an emerging technology that allows thin samples, such as macromolecular complexes and small bacterial cells, to be imaged in 3D in a nearly native state and at high-resolution. Cryo-ET can provide insight into the positions and structures of cytoskeleton filaments, cell wall components, motility machines, chemoreceptor arrays, internal compartments and other cellular structures (Murphy and Jensen, 2007). In this way, structural information about organelles and individual proteins can be linked with their exact three-dimensional arrangement within the cell. This unique capability holds enormous potential for cell biology, making cryo-ET a highly promising technology to structurally characterizes the vault complex in their natural microenvironment and characterize its molecular sociology.

For cryo-electron tomography, a biological sample, a cell, tissue or even entire organism is flash frozen, thinned to an appropriate thickness, and then imaged using an electron microscope (Doerr, 2016). The fast-freezing process preserves the sample in a hydrated, close-to-native state. Multiple images are captured as the sample is tilted along an axis. The images are then aligned and merged to reconstruct a three-dimensional image: the tomogram (Beck and Baumeister, 2016).

There are currently two publications where the vault complex was localized in cells, by cryo-ET experiments. The first one provided a direct visualization of vaults within intact cells, revealing that these particles were located in the extreme periphery of the cytoplasm (Figure 14A), predominantly associated with granule-like structures and actin (Figure 14B) (Woodward et al., 2015).

Vaults imaged within cells showed almost identical sizes and shapes to purified and recombinant vaults (Figure 13A; Figure 14A). Subtomogram averaging of intracellular vaults produced an averaged structure showing densities within the vault lumen randomly distributed and high density at the vault's cap (Woodward et al., 2015), consistent with the previous vtRNA localization at the vault caps (Kong et al., 2000) (Kickhoefer et al., 2001b). Analysing the vault structure inside the cells, Jensen and colleagues realized that the vault structure was not entirely rigid, but was able to adopt a range of conformations without significantly altering its overall dimensions (Woodward et al., 2015). These authors observed vaults with a very pronounced indentation at the particle waist and also a few vaults opening up at their waist to interact with closely associated granules. The

intrinsic plasticity of the vault shell seen in particles directly imaged in intact cells (Figure 13), correlated well with the structural changes observed in the cryo-EM structures determined (Figure 10B; Guerra et al., 2022)

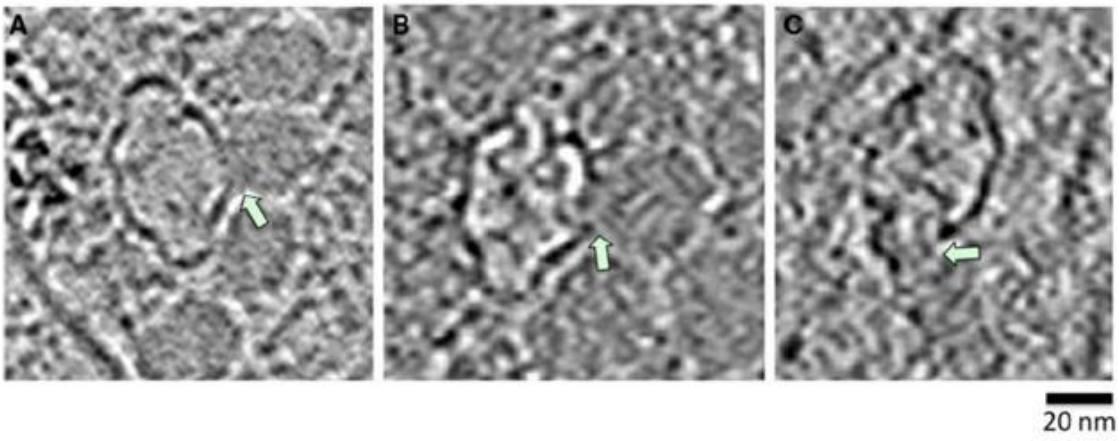

Figure 13. Variable vault morphologies (Woodward et al., 2015). Examples of vaults opening up to the granules at the waist regions (A, B) and the cap (C).

In the second publication, Carter and colleagues observed vaults while studying how exogenous TRIM5 was forming autophagy aggregates *in vivo*. Their cryo-tomograms provided three-dimensional (3D) images of various structures assembled during macroautophagy in their native state, indicating that vaults arrive early in the process before visible aggregate formation (Carter et al., 2020) (Figure 14C). Their findings revealed a chronology in the autophagic pathway: colocalization of substrate, arrival of vault, formation of dense substrate aggregates (sequestosomes), creation of phagophores, phagophore closure around substrate to produce autophagosomes, and finally autophagosome fusion with either endosomes or lysosomes to produce an autophagic vacuole. Because vaults arrived early, they were seen in all autophagic steps: with sequestosomes, phagophores and autophagosomes, as well as within autophagic vacuoles.

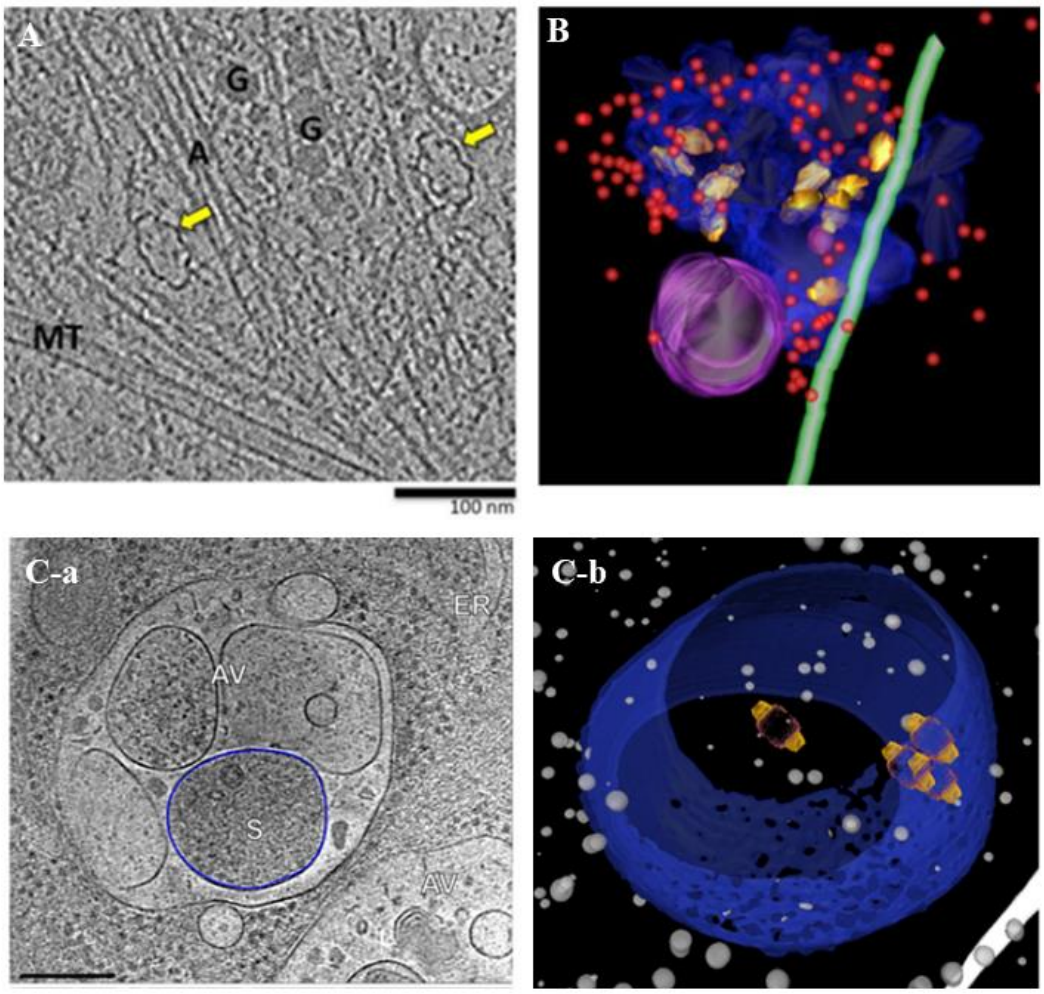

Figure 14. Vault localization in cells by cryo-ET. **(A)** Tomographic slice where vaults are shown in the cytoplasm (Woodward et al., 2015). **(B)** Tomographic segmentation where vaults are predominately associated with granule-like structures (blue), near to a microtubule (green), ribosomes (red) and a round structure (purple) (Woodward et al., 2015)**. (C)** Vaults seen in an autophagic vacuole (Carter et al., 2020) **(a)** Cryo-tomographic slice of and autophagic vacuole with the sequestosome highlighted **(b)** 3D segmentation of the sequestosome where the vaults are localized.

Objectives

OBJECTIVES

The main objective of this thesis is to provide new insights into the structure and dynamics of the vault particle. It is divided in five specific aims:

1- **Structural characterization of endogenous *Dictyostelium discoideum* vaults.**
   - *Dictyostelium* cell culture.
   - Purification of endogenous vaults.
   - Biochemical characterization of ovoid structures using biochemical techniques and the Molisch test.
   - Sample analysis by negative staining.
   - Preliminary characterization by cryo-EM.

2- **Structural characterization of recombinant *Dictyostelium discoideum* vaults**
   - Cloning, expression and purification of *Dictyostelium* vaults.
   - Structure determination of recombinant *Dictyostelium* vaults using cryo-EM and 3D image reconstruction.

3- **Individual characterization of each MVP isoform: MVPα and MVPβ**
   - Expression and purification.
   - Characterization of MVPα polymerization using biochemical techniques.

4- **Structural characterization of mutant recombinant vaults of *Dictyostelium discoideum*, in complex with a α-myc nanobody.**
   - Generation of MVPα and MVPβ mutants.
   - Purification of recombinant *Dictyostelium* vaults.
   - Structure determination of mutant recombinant *Dictyostelium* vaults in complex with a nanobody using cryo-EM and 3D image reconstruction.

5- **Structural characterization of human vaults *in situ***
   - Production and generation of EGFP-vault and EGFP cell line.
   - Light microscopy analysis and effect of different drugs.
   - Visualization of *human* vaults in native environment by cryo-ET.

Results & Discussion

RESULTS and DISCUSSION

1. Structural characterization of *Dictyostelium discoideum* vaults

The main objective of this section is the structural study of *Dictyostelium discoideum* vaults. Although vaults have been found in a wide variety of eukaryotic cells, their abundance varies substantially between different tissues and cell types. The most common vault sources have been *Dictyostelium* and macrophages (Kedersha et al., 1990).

In addition, the amoeboid protozoan *Dictyostelium* is a powerful model system for genetic and functional analysis of gene function. The 34 Mb genome contains many genes that are homologous to those in higher eukaryotes and are missing in *Saccharomyces cerevisiae*, like the major vault protein (MVP). The high percentage of adenine (A) and thymine (T) is one of its genome's characteristics. Another feature of this model organism is that it enables for a wide range of molecular genetics techniques, including as gene knock-out, gene knock-in, restriction enzyme-mediated mutagenesis, RNAi, and inducible gene expression (Kreppel et al., 2004) (Chisholm et al., 2006).

Our interest in solving the structure of the vaults was twofold. On one hand, *Dictyostelium* is the only organism presenting two MVP isoforms (MVPα and MVPβ) in vaults (Kedersha et al., 1990), and the resolution of this singular structure could contribute to understanding the evolutionary relationships linking this particle from an ancient microorganism to higher eukaryotes. On the other hand, endogenous vaults from *Dictyostelium* contain all the vault minor components. Therefore, solving the structure of endogenous vaults, opened the possibility of characterize the minor components as well.

The discovery of vaults in *Dictyostelium* offered the opportunity to conduct molecular genetic investigations into vault structure and function by providing a cell type that allows gene disruption by homologous recombination. The first study, reported the mutation of MVPα gene by homologous recombination to generate a MVPα-negative cell line (Vasu et al., 1993). Functional studies revealed that even in the absence of MVPα, the cell line exhibited a normal growth and development. In addition, authors reported that the MVPα-negative cell line was able to express a "particle", which was supposed to contain the MVPβ protein. This heterogeneous particle exhibited an ovoid morphology which the authors called "ovoid structure" (Figure 15B) (Vasu et al., 1993).

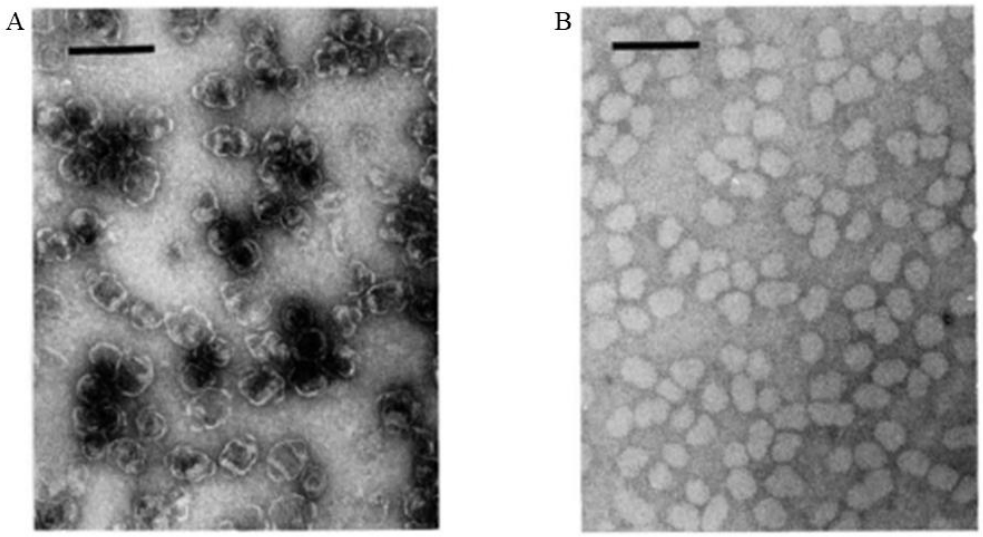

Figure 15. Imaging of *Dictyostelium* vaults by electron microscopy (**A**) Electron micrograph of wild-type vaults, isolated from wild-type cells by standard procedures and negatively stained with uranyl acetate (Vasu et al., 1993). (**B**) Electron micrograph of ovoid structures from MVPα-negative cells, obtained using vault purification procedures and negatively stained with uranyl acetate. *Bar*, 100nm (Vasu et al., 1993).

In a later work, the same authors described the disruption of the MVPβ encoding gene in both wild-type (resulting in MVPβ-negative cell line) and MVPα-negative cell line (resulting in MVP negative cell line: MVPα$^-$ and MVPβ$^-$). Both mutated cell lines displayed normal growth and development, and also contained the "ovoid structures" with no correlation with vault morphology. Authors concluded that MVPα and MVPβ are essential for proper vault formation, and speculated on the possible existence of a new protein to explain the presence of the "ovoid structures" in the MVP negative cell line (MVPα$^-$ and MVPβ$^-$) (Vasu and Rome, 1995).

These findings highlighted the need for further research on *Dictyostelium* vaults and their components. In the first instance, to determine whether both proteins (MVPα and MVPβ) are required for the correct assembly of the particle, and to determine how they are organized in the structure, considering the odd number of MVPs that make up the complete vault (with 39 MVP subunits in each half-vault moiety). Furthermore, the characterization of ovoid structures could contribute to understanding the assembly of this peculiar particle in *Dictyostelium*.

1.2. *In vitro* characterization of endogenous *Dictyostelium discoideum* vaults

Purification of endogenous vaults

Several endogenous *Dictyostelium* vaults high-quality samples were obtained (Figure 16 and Figure 17) following the purification protocol explained in materials and methods.

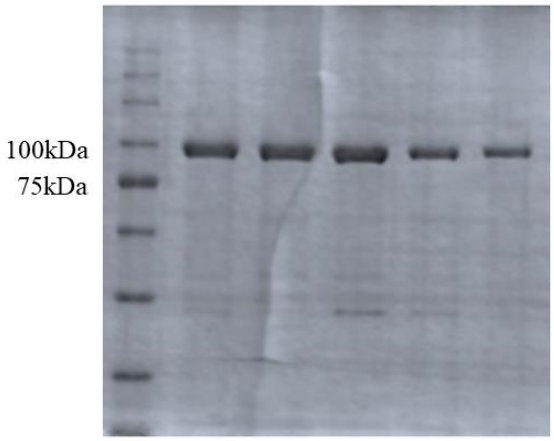

Figure 16. SDS-PAGE fraction analysis of six purifications of endogenous vaults.

Fractions with a 100 kDa band, corresponding to the MVP molecular weight, were combined and subjected to an extra purification step: the CsCl cushion described in materials and methods. Negative staining EM was used to examine the vault fractions before and after the CsCl cushion. During the centrifugation of the CsCl cushion, a viscous precipitate was generated, which was diluted in water and also analysed by negative staining (Figure 17).

As shown in Figure 17, vaults co-purified with ovoid structures as contaminants prior to the CsCl cushion (Figure 17A). Our ovoid structures are similar in shape and morphology to those previously described by Vasu and colleagues (Figure 15) (Vasu et al., 1993). With the CsCl cushion we were able to separate vaults from ovoid structures (Figure 17B-2). However, during the process vaults suffered structural alterations, showing a distorted morphology (Figure 17B-1 in comparison with Figure 17A).

A) Before CsCl cushion

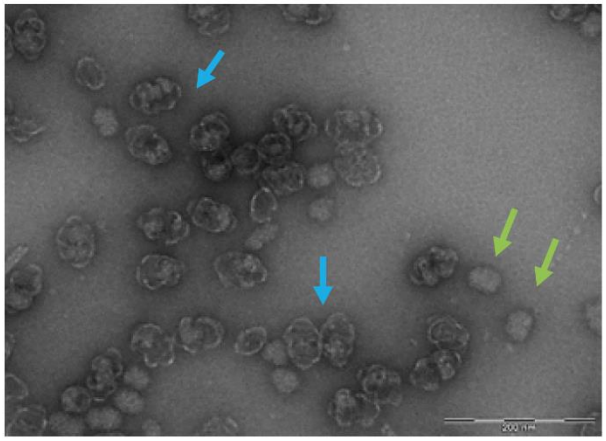

: ovoid structures

: vault protein

B1) After CsCl cushion

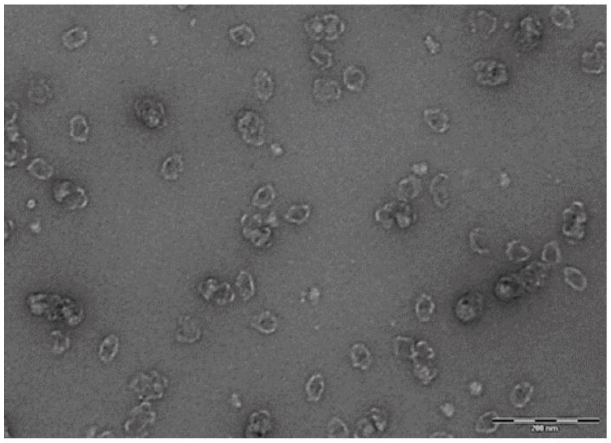

B2) After CsCl cushion: viscuos precipitate

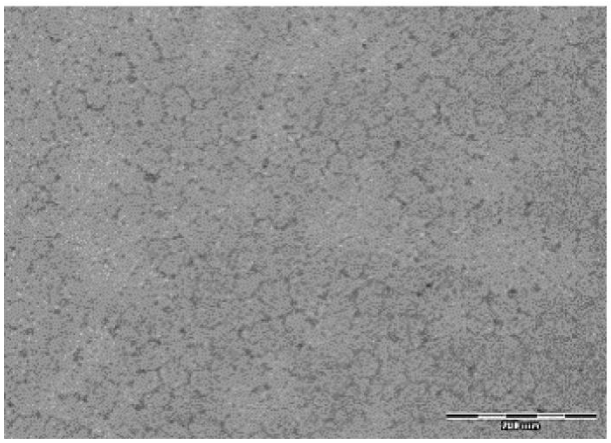

Figure 17. Negative staining analysis of CsCl cushion samples. (**A**) Representative micrograph showing a vault preparation before the CsCl cushion. Selected entire vault particles are indicated by the blue arrows and the contaminant ovoid structures are indicated by the green arrows. (**B1**) Representative micrograph of a vault sample after the CsCl cushion. Many of the particles show a distorted structure. (**B2**) Viscous precipitate after CsCl cushion plenty of ovoid structures.

In order to preserve the vault morphology, the CsCl cushion was replaced by an alternative purification step: a size-exclusion chromatography, using a Superose 6 10/300 GL column. Negative staining EM was used to examine vault morphology and sample purity of the peak-1 containing vaults (Figure 18A). As shown in Figure 18B, this purification step preserved the vault morphology but it was not possible to separate the ovoid structures contamination.

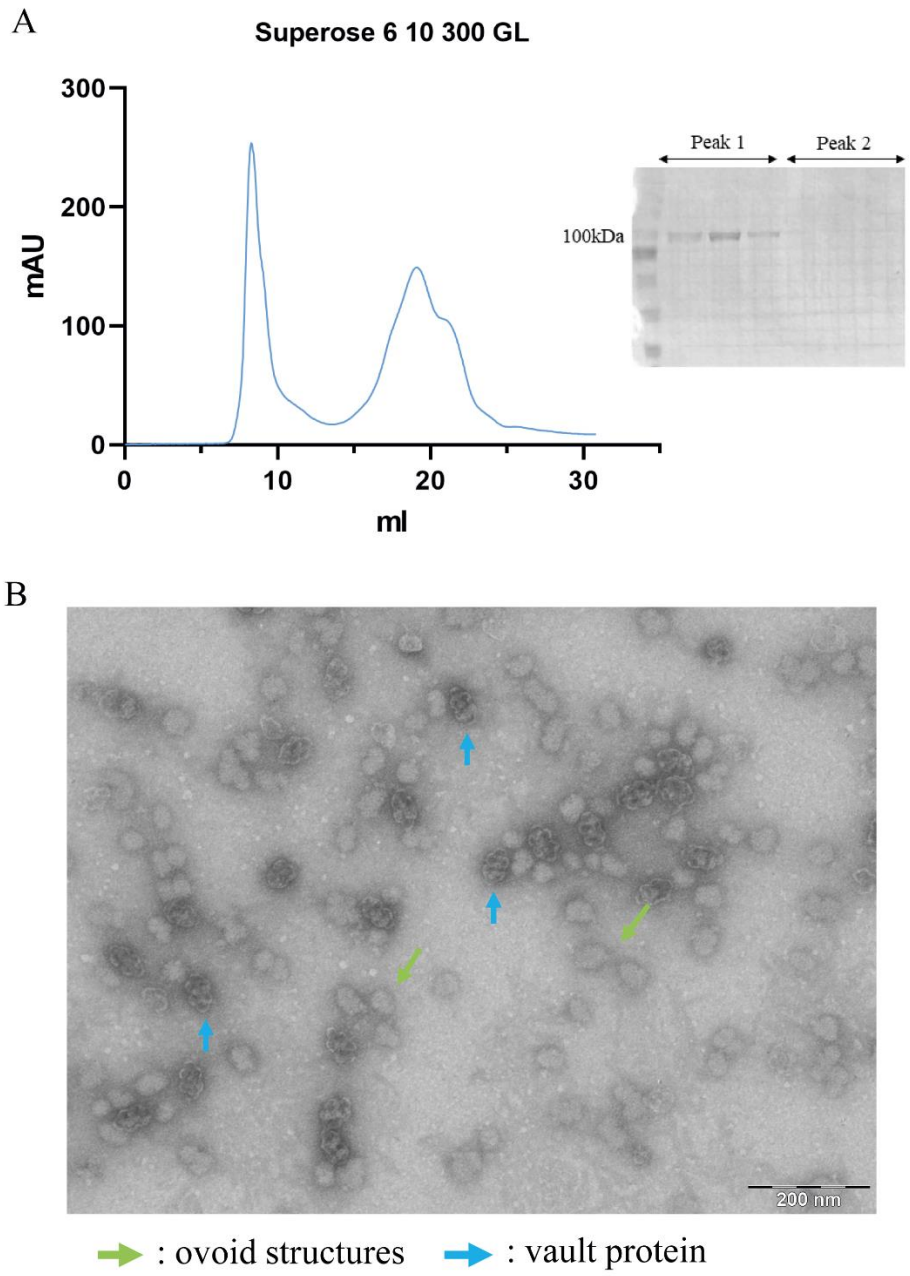

Figure 18. (**A**) Size exclusion chromatogram. Fraction peaks were analysed by SDS-PAGE. (**B**) Negative staining EM analysis after size-exclusion chromatography shows vaults with good morphology and the presence of the contaminant ovoid structures.

Further experiments demonstrated that the presence of ovoid structures in the sample was dependent on *Dictyostelium* culture times, where shorter times resulted in less ovoid structures. The best optimized samples are shown in Figure 19: Figure 19A, where the sample concentration is 1/10, reveals large amounts of endogenous vaults and in Figure 19B, where the concentration is 1/40, vaults present good morphology. The sample concentration and vault morphology were suitable for high-resolution techniques but the sample still contained few ovoid structures.

A

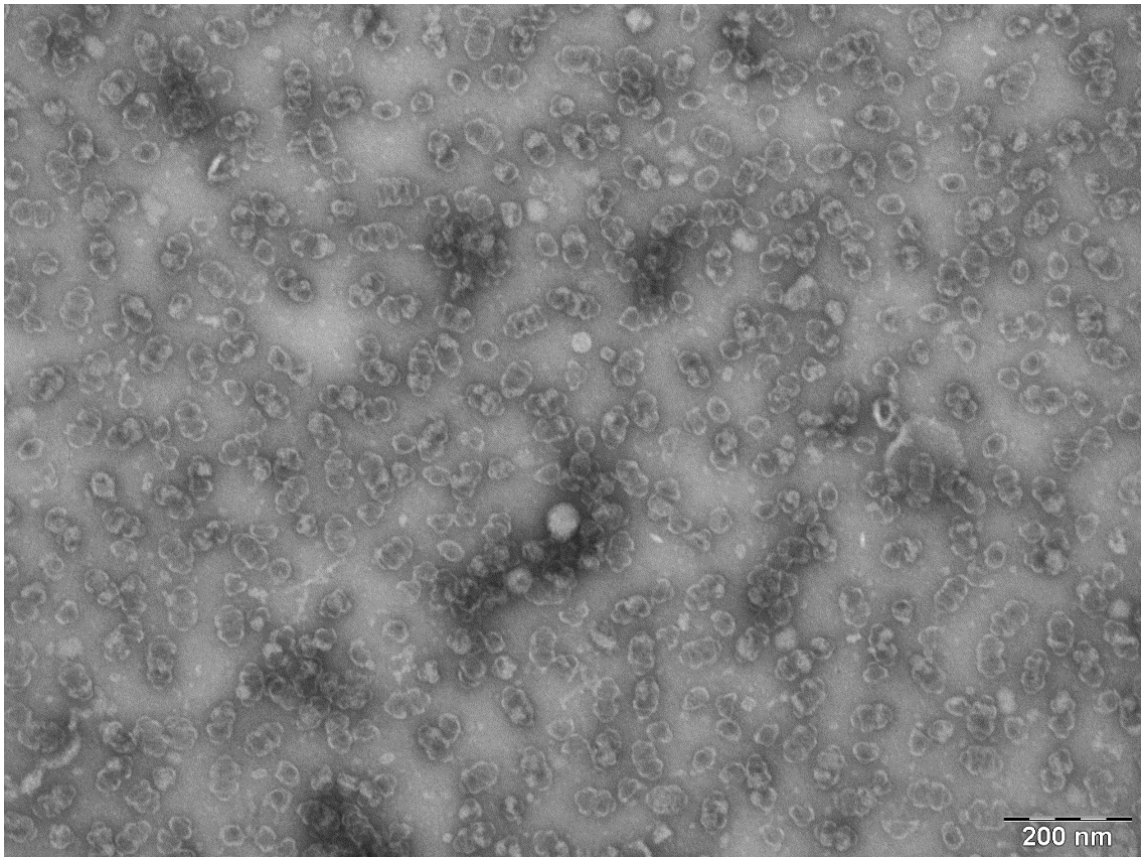

B

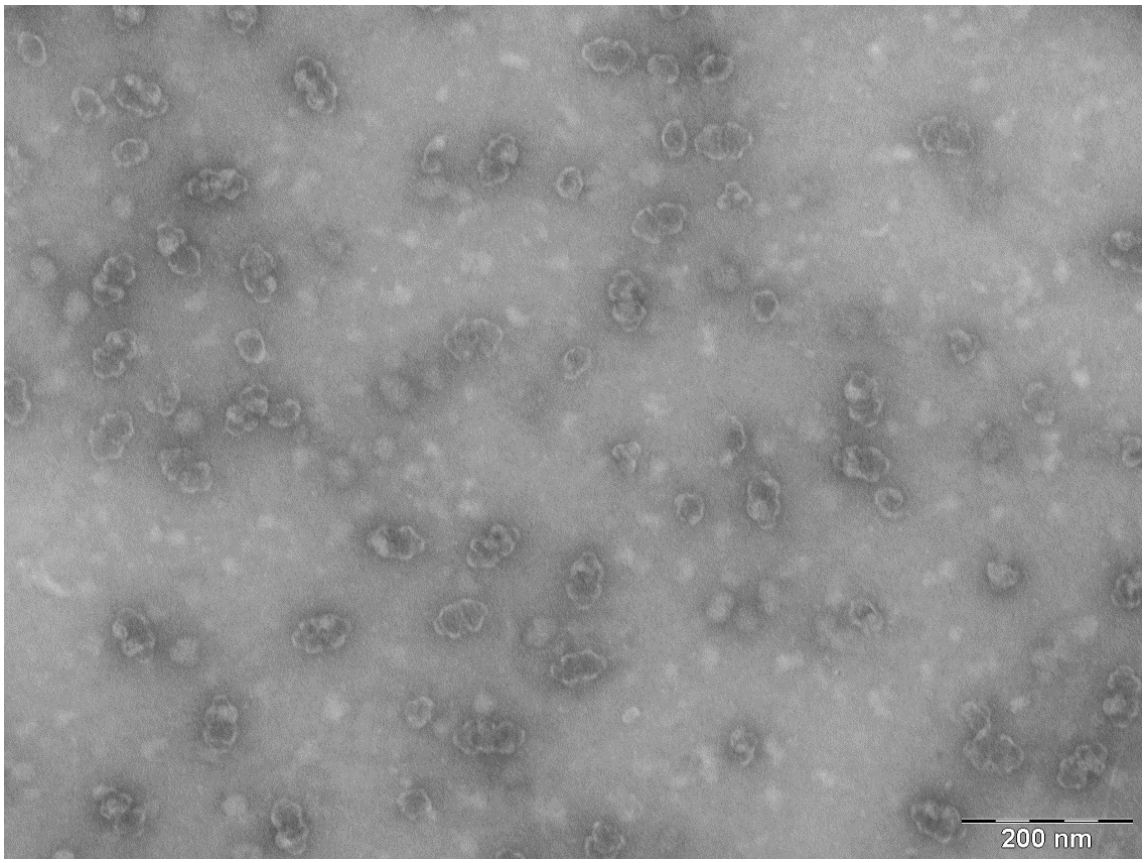

Figure 19. (**A**) Negative staining micrograph after size-exclusion chromatography, sample concentration 1/10: correct vault endogenous concentration. (**B**) Negative staining micrograph, sample concentration 1/40: vaults with good morphology.

1.3 Biochemical characterization of ovoid structures

We were also curious in biochemically characterize the ovoid structures. If we knew their native composition, it would be simple to isolate them from the vault protein. The viscous precipitate with the ovoid structures after CsCl cushion was diluted in water and analysed. Because some scientists thought that the ovoid structures creation was attributable to any MVP subunits or a novel protein, it was initially analysed by SDS-PAGE (Figure 20A). Because protein was absent in the sample, then the sample was run through an agarose gel (Figure 20B) without obtaining any band.

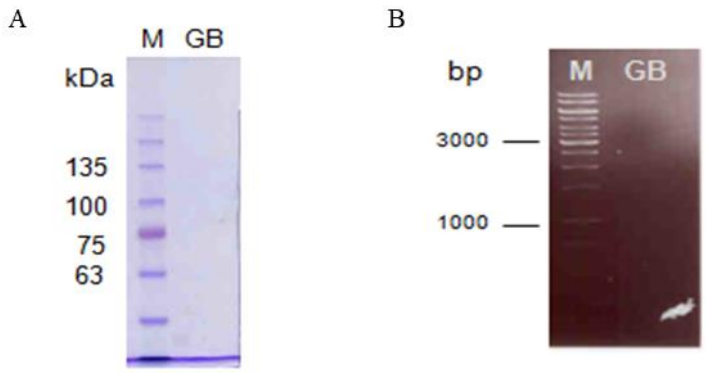

Figure 20. Biochemical assays. M: marker, GB: ovoid structures (**A**) SDS-PAGE analysis of ovoid structures. (**B**) Agarose gel of ovoid structures.

With these results, we could discard proteins and nucleic acids as components of the ovoid structures. The viscosity of the ovoid structures and the fact that the sample could be diluted by water provided us the hint that they could be polysaccharides. We tested this possibility, using the Molisch test (Figure 21).

The Molisch test is a chemical test used to check the presence of carbohydrates (larger than tetroses) in a given sample. The test involves the addition of the Molisch reagent (a solution of α-naphthol in ethanol) to the sample and the subsequent addition of a few drops of concentrated H_2SO_4 (sulphuric acid) to the mixture. The formation of a purple product confirms the presence of carbohydrates in the sample (Foulger, 1931).

The test is on the basis that pentoses and hexoses are dehydrated by concentrated sulphuric acid to form furfural or hydroxymethyl furfural, respectively. These products condense with α-naphthol to form purple condensation product (Figure 21).

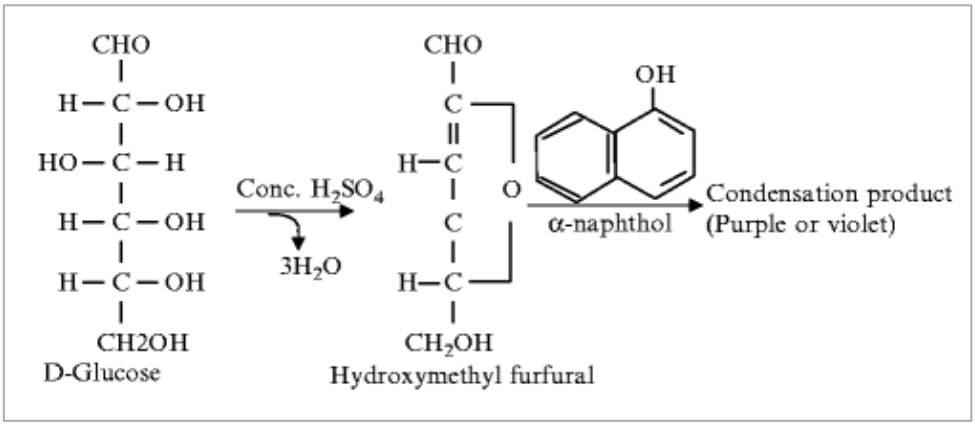

Figure 21. The Molisch test reaction.

We prepared four samples for the Molisch test as specified in methods and materials: a negative control (vaults buffer) (Figure 22A), a positive control (vaults buffer with sucrose) (Figure 22B), the vault fraction separated by CsCl cushion (Figure 22C) and ovoid structures sample (Figure 22D). Visible purple product in our sample that contained ovoid structures (Figure 22D) similar to the positive control (Figure 22B) confirmed that ovoid structures were polysaccharides (Figure 22).

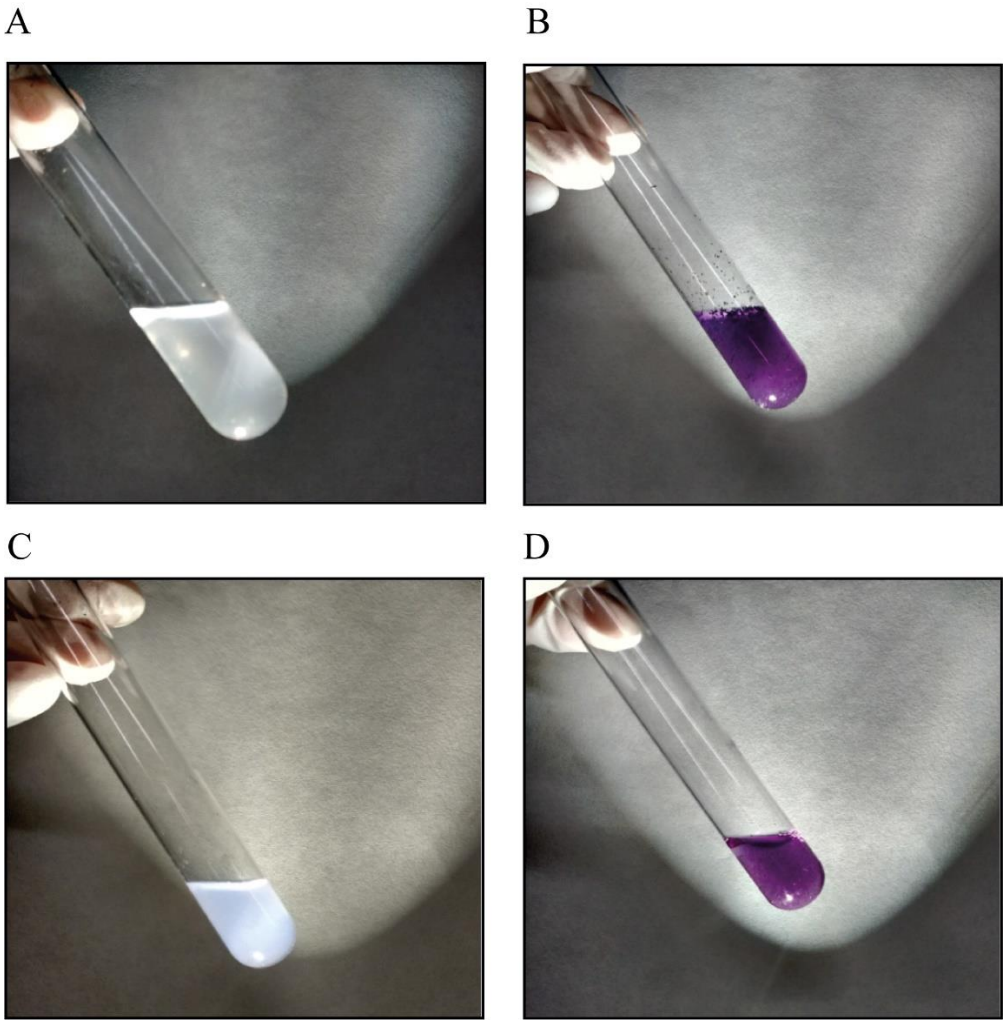

Figure 22. Ovoid structures were polysaccharides by the Molisch test. (**A**) Negative control: 3 ml buffer. (**B**) Positive control: 3 ml 0.5% sucrose solution. (**C**) Sample 1: 3 ml of vault protein diluted in buffer. (**D**) Sample 2: 3 ml of ovoid structures diluted in buffer.

1.4 The final step of purification of endogenous vaults

Once we determined that the ovoid structures were polysaccharides, which generally have negative charge, we decided to change the size-exclusion chromatography by anion exchange chromatography using a Mono Q column, elution fractions where analysed by SDS-PAGE (Figure 23) and negative staining EM (Figure 24). As shown in Figure 24, high quality of purified vaults was obtained after the Mono Q ion exchange chromatography and finally, the ovoid structures were removed.

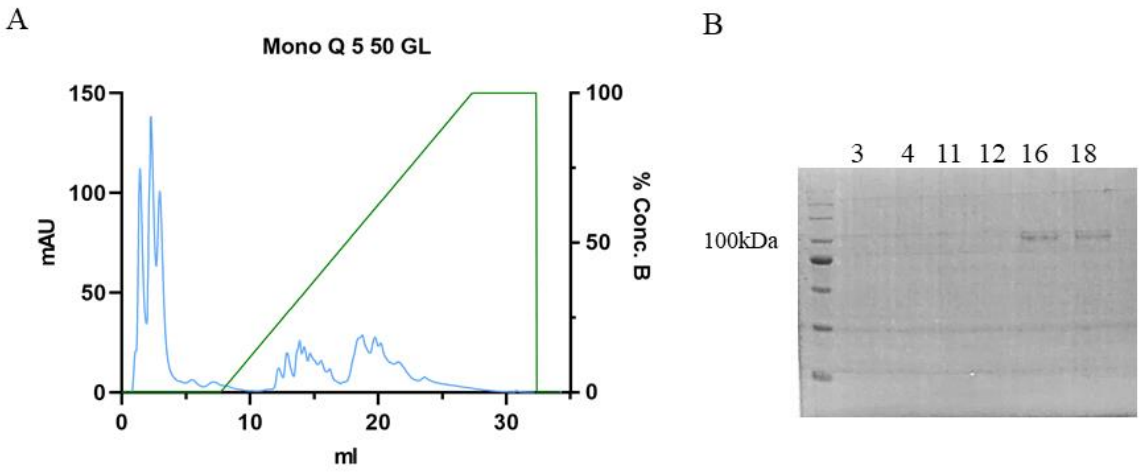

Figure 23. (**A**) Representation of a Mono Q 5 50 GL chromatogram. (**B**) Fractions from the different peaks were analysed by SDS-PAGE. Vaults were present in the last peak.

A

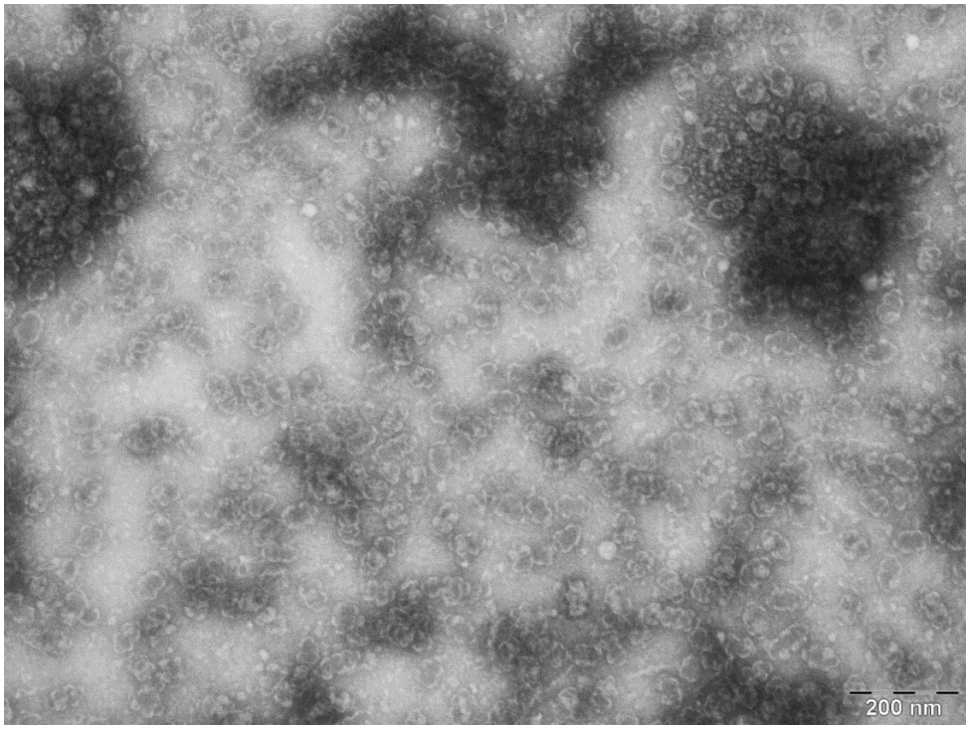

B

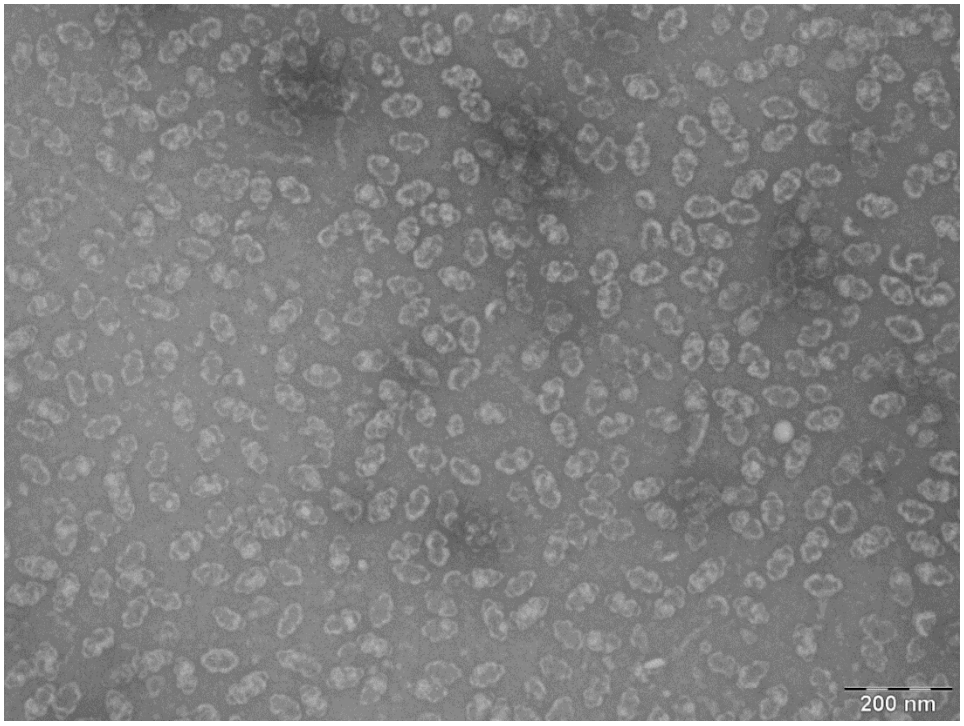

Figure 24. (**A**) Negative staining micrograph after anion exchange chromatography, sample concentration 1/10: correct vault endogenous concentration. (**B**) Negative staining micrograph, sample concentration 1/40: vaults with good morphology. *Dictyostelium* vault internal heterogeneity is noticeable.

1.5 Cryo-electron microscopy

Cryo-EM was chosen as the technique for solving the structure of these particles for two reasons: the first one was the inability to obtain crystals. In addition, as demonstrated by our recent data, single particle cryo-EM has proven to be the best technique to address the structural dynamics of vault particles at high resolution (Guerra et al., 2022). Therefore, we had established the workflow for solving vault structures by cryo-EM.

We prepared cryo-EM grids, optimized the vitrification conditions and we checked them in a 200kV Talos Artica electron microscope (Thermo Scientific), at the CNB in Madrid. Next, high resolution data were collected in a 300kV Titan Krios electron microscope (Thermo Scientific) at the European Synchrotron Radiation Facility (ESRF, Grenoble, France).

Although we collected some cryo-EM data, we were unable to obtain a clear 3D reconstruction of the particle during data processing. We were also unable to characterize the minor vault components due to the high heterogeneity present at the particle's interior. Figure 24B shows the heterogeneity that the vault particle exhibits in its internal volume (white areas in particles interior). Whereas one vault may be empty, another may have only one area on one side, another may have one area on the opposite side, and another may have two or more areas. It is also possible that these volumes correspond not only to the vault its minor components but also to other component related to its role in cellular transport.

In light of all the inconveniences suffered in the production and purification of endogenous *Dictyostelium* vaults we decided to produce recombinant vaults by the over-expression of MVPα and MVPβ, using the baculovirus expression system in insect cells.

2. Structural characterization of recombinant *Dictyostelium discoideum* vaults

2.1 Cloning

To obtain the recombinant vaults from *Dictyostelium,* the two genes (coding for MVPα and MVPβ) were individually cloned. MVPα and MVPβ genomic DNAs are 2531 kb and 2540 kb long respectively and both have one intron (see Figure 71 in materials and methods). Consecutive polymerase chain reactions (PCR) from the genomic DNAs were employed as the cloning strategy to remove the intron. Also, the PCR conditions required to be optimized for two reasons:

1- The high percentage of adenine (A) and thymine (T) in *Dictyostelium* genes results in a low content of guanine (G) and cytosine (C), making it difficult to reach the primer melting temperature (Tm) around 55 °C. The solution was to increase the primers length to get the Tm in an accurate range (55-65 °C).
2- The temperature for the optimal primer extension by the Phusion polymerase (Invitrogen) is 72 °C. However, due to the large amount of AT nucleotides in the genome, the contact between the genomic DNA and the polymerase may disengage at this temperature. We solved this problem by lowering the extension temperature to 65 °C. As a result, the speed was reduced, so the extension times were extended, being longer than specified in the polymerase manual.

2.2 The baculovirus expression system

Each fragment was cloned in the baculovirus transfer vector resulting in the pFastBacHta_MVPα and the pFastBacHta_MVPβ, described in the materials and methods section. Both constructs contained a His-tag at the N-terminus. These vectors were used to produce the MVPα and MVPβ recombinant baculoviruses, using the Bac-to-Bac system (materials and methods). At first instance, it was important to confirm that the recombinant baculoviruses expressed the proteins. To do that, the protein expression by the primary recombinant baculoviruses were analyzed by SDS-PAGE and Western-Blot, using an antibody anti-His (PentHIS; QIAGEN). As shown in Figure 25, both rBV-MVPα and rBV-MVPβ expressed the proteins: MVPα and MVPβ.

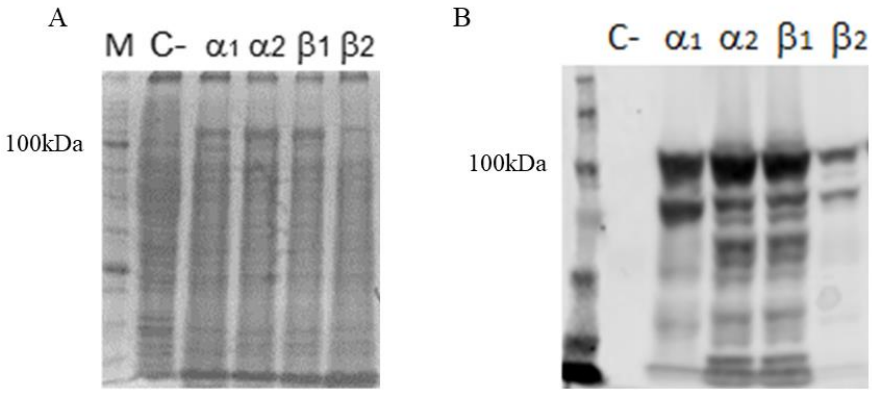

Figure 25. Protein expression: MVP (100 kDa) (**A**) SDS-PAGE analysis (**B**) Western-Blot analysis by an α-His. M: marker, C-: negative control, α1: rBV_MVPα protein expression, α2: α1 duplicate, β1: rBV_MVPβ protein expression, β2: β1 duplicate.

Virus titration

To establish the optimal protein concentration produced by the secondary rBV, it was necessary to titrate the virus, as described in the materials and methods section. Fractions were analysed by SDS-PAGE. As shown in Figure 26, no major differences in protein expression were observed in the different rBV infection quantities (100 kDa band in each wheel). We choose the infection with 25 µl (in M6: plates of 3 ml) as the more efficient.

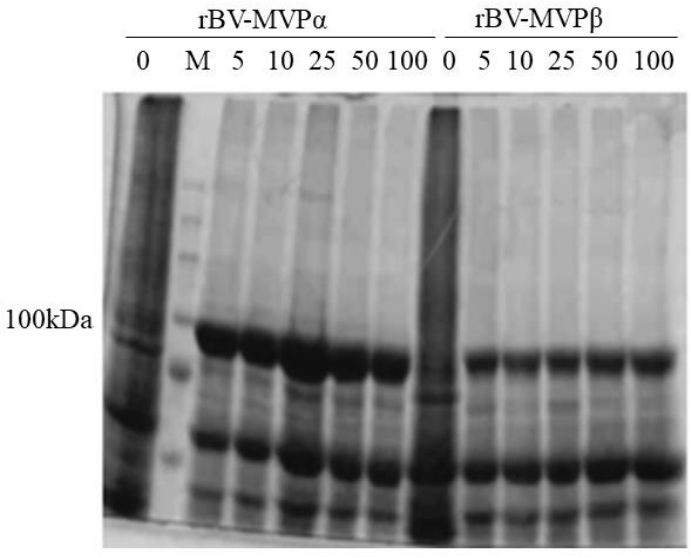

Figure 26. SDS-PAGE analysis of virus titration. The different wheels shown the protein expression level when cells were infected with different rBV infection quantities during 72 h (0, 5, 10, 25, 50 and 100 µl). M: marker. rBV-MVPα: recombinant virus which produced MVPα and rBV-MVPβ: recombinant virus which produced MVPβ.

2.3 Production and purification of recombinant vaults

HighFive insect cells (Invitrogen) were co-infected at the same time with rBV-MVPα and rBV-MVPβ. After 72h harvested, vaults were purified, using a similar protocol to that described in endogenous vaults purification, but adding several changes, mentioned in the materials and methods section. In this protocol, the CsCl cushion was re-introduced as an extra purification step to further clean the sample. The four fractions obtained after the cushion where analysed by SDS-PAGE and Western-Blot (Figure 27).

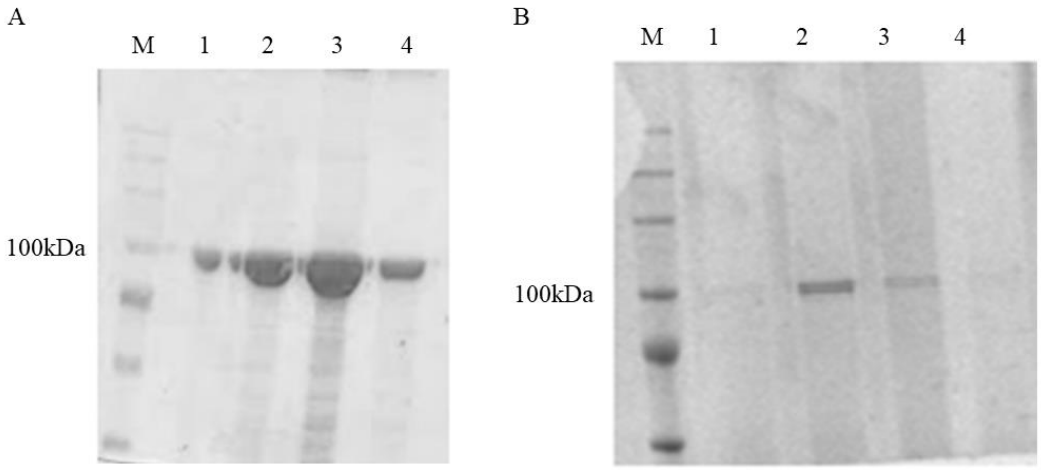

Figure 27. The CsCl cushion fractions where analysed by (**A**) SDS-PAGE and (**B**) Western-Blot by by an α-His antibody.

To confirmed the presence of recombinant vaults, fraction 2 in Figure 27, was analyzed by negative staining EM. As shown in Figure 28 recombinant vaults exhibit good morphology, indicating that these recombinant particles structure is not distorted during ultracentrifugation in the CsCl gradient. Recombinant vaults were stiffer than the endogenous ones, maybe due to the presence of the His-tag in the N-terminal of the MVP. In addition, these particles showed an extra density in its waist due to the presence of the 78 His-tag sequences at the N-terminal ends of the MVPs, indicating that His-tags were localized localized inside the vault particle, without blocking vault assembly, as previously described in other recombinant vaults.

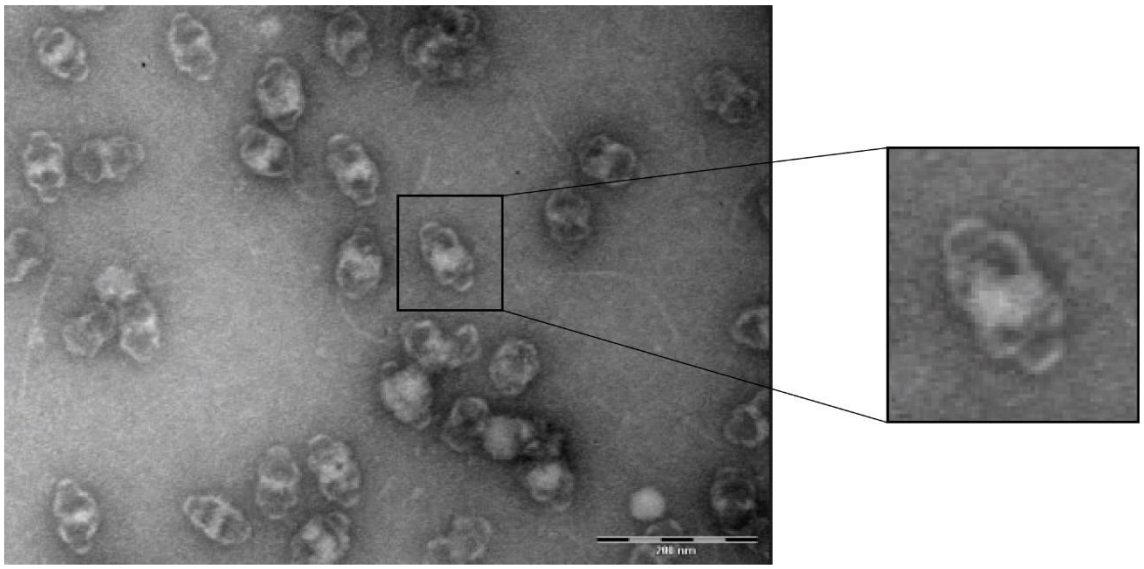

Figure 28. Negative staining micrograph of recombinant *Dictyostelium* vaults. Close up view of an individual vault, showing the extra density in the particle waist.

Once having established the best purification conditions, large scale production of these recombinant vaults was performed for high resolution structural studies. As in the previous studies with endogenous *Dictyostelium* vaults, negative staining EM was used to assess the sample quality before proceeding to high-resolution techniques (Figure 29). Figures 29A and 29B show the ideal conditions for moving to cryo-electron microscopy: good vault concentration (Figure 29A) and good vault morphology (Figure 29B).

A

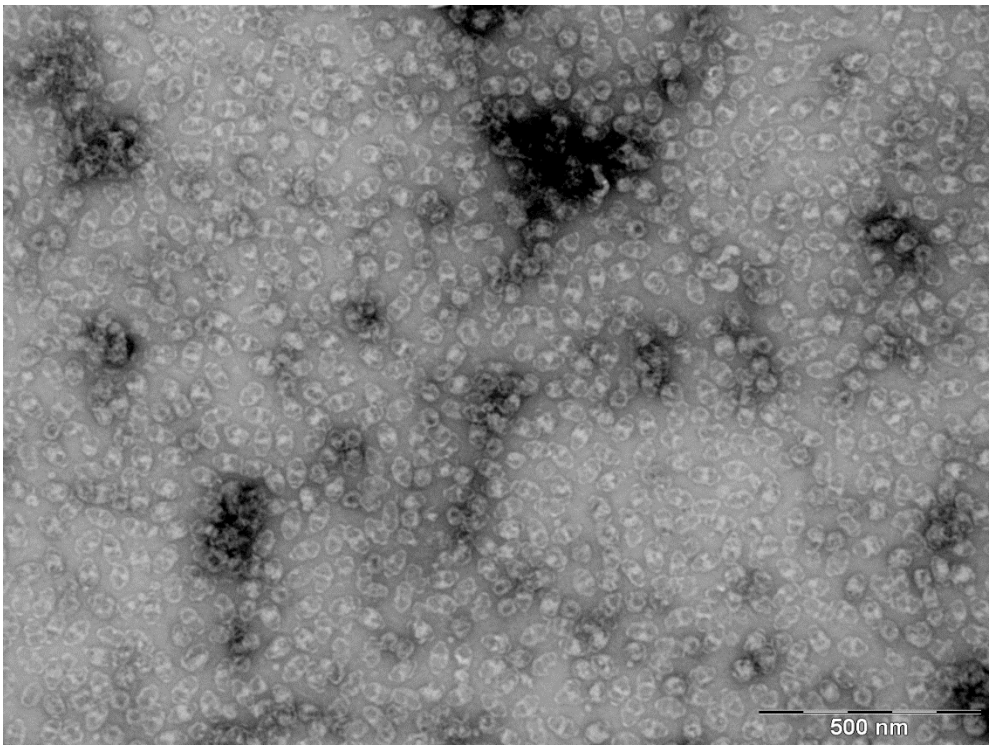

B

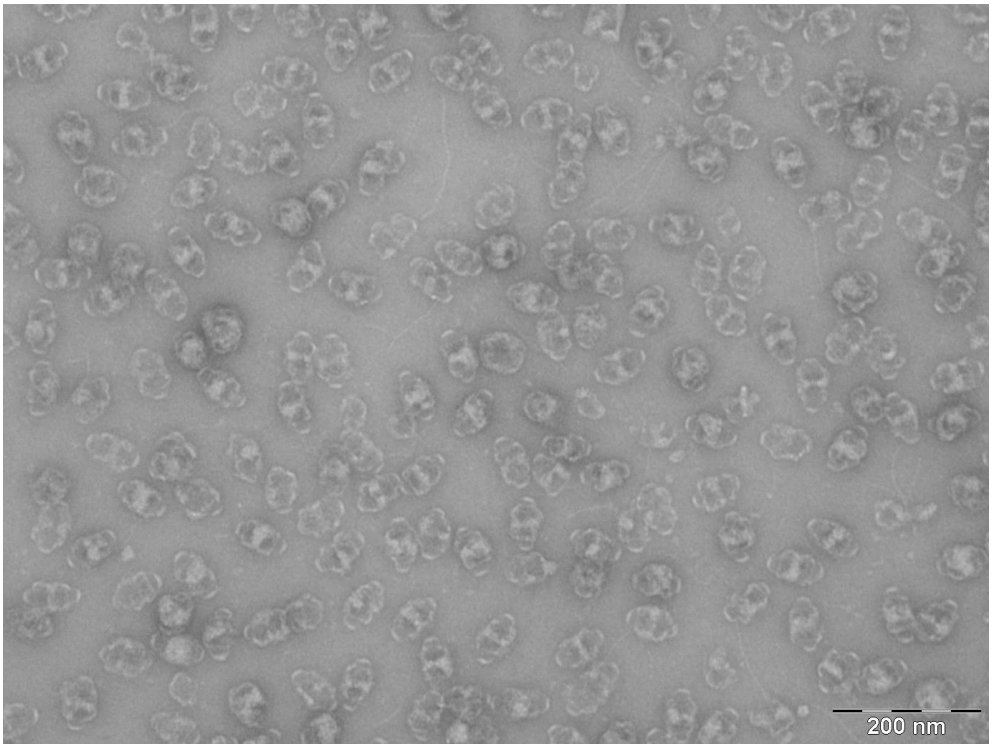

Figure 29. Negative staining of recombinant *Dictyostelium* vaults (**A**) Sample concentration 1/10. (**B**) Sample concentration 1/40.

2.4 Cryo-electron microscopy of recombinant *Dictyostelium* vaults

As mentioned before, during the optimization of the vitrification conditions we realized that the gold grids were better than the carbon ones (Guerra et al., 2022). This was due to two main reasons: first, the mobility of the vitrified specimens was reduced during data acquisition, and second, because the grid composition is made of an inert material, avoiding the protein attachment to the grid support. Grids prepared in different vitrification conditions were checked in the 200 kV Talos Arctica electron microscope, equipped with a Falcon 3 direct electron detector (CNB-CSIC, Madrid). Finally, the best vitrified grids with the optimal thickness for good vault stability, plenty of vault particles, and arranged them in different orientations (Figure 30), were used for high-resolution data collection.

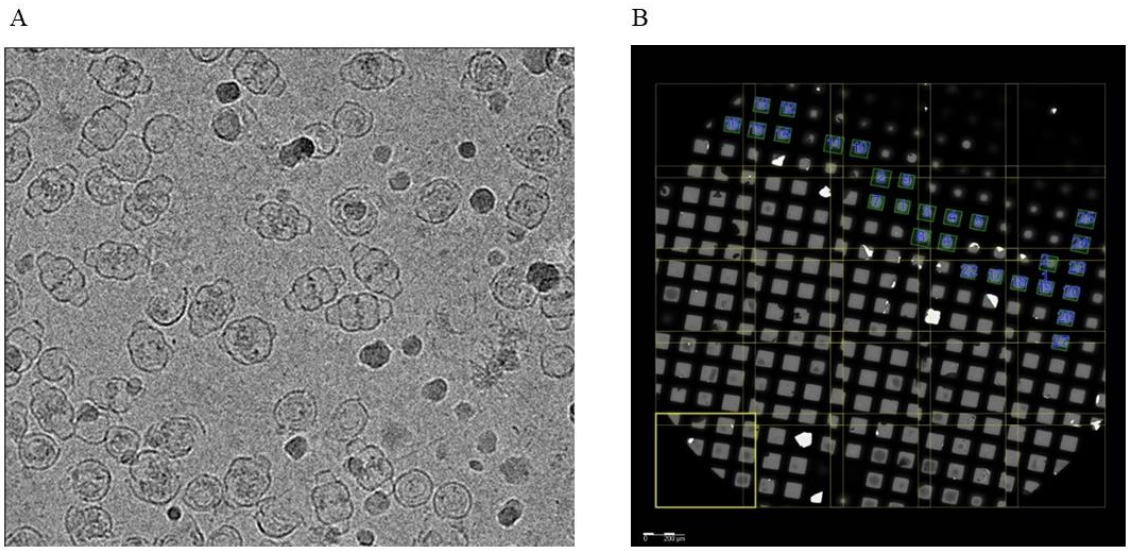

Figure 30. Selection of the best grids for data collection in the 200 kV Talos Artica microscope (**A**) Cryo-micrograph showing the recombinant *Dictyostelium* vaults. (**B**) Selected squares (blue) in the EM grid, chosen to data collection.

This grid and its duplicate were selected for high resolution data collection in a 300 kV Titan Krios electron microscope (Thermo, Scientic), equipped with a Gatan K2 direct detection camera, at the ESRF (Grenoble, France). EM data was collected in counting mode, with EPU software to a magnification of x110000, corresponding to a pixel size of 1.07 Å/pixel. The whole dataset contained 3643 movies.

Aligned micrographs (Figure 31A) were used for the estimation of the contrast transfer (CTF), using Gctf (Zhang, K. 2016), with defocus values ranging from −1.5 to −3.5 µm. A total of 68105 particles were automatically picked using RELION 3.0 (Egelman et al., 2018) with a box of 400 × 400 pixels in size. All picked particles were classified using RELION in a 2D classification process (Class2D) (Figure 31B).

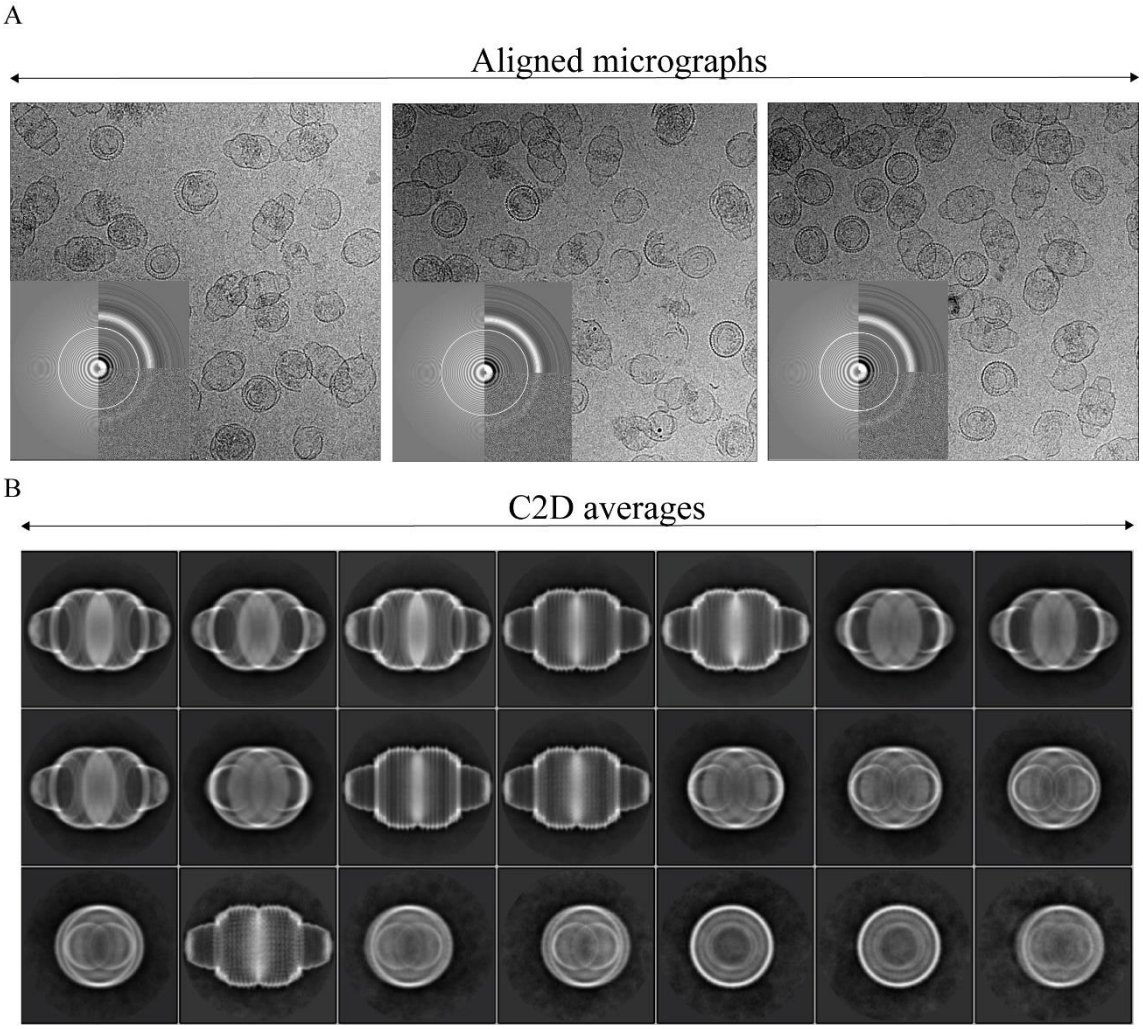

Figure 31. Cryo-EM data of recombinant *Dictyostelium* vaults. (**A**) Three representative aligned micrographs obtained in the Titan Krios microscope. The CTF associated to each image is shown at the bottom left side of the images. (**B**) Representative reference-free two-dimensional class averages after classifying 25414 particles.

Classes with no interpretable features were discarded. A total of 25414 particles were selected for 3D classifications (Class3D) and the calculation of the 3D reconstructed map. The initial model for Class3D was generated from a previous atomic model (PDB: 4HL8) of rat vault, low-filtered to 60 Å resolution to eliminate the risk of model bias. During the 3D reconstruction process, particles were subjected to consecutive 3D classification and refinement processes (Class3D and Refine3D jobs) and additionally, to CTF refinement and particle polishing (Figure 32). We tried different symmetries: C1, C3, C39 and D39. The best class was applying C3 symmetry and was refined separately with RELION. To enhance the signal, a mask was generated around the whole vault, obtaining a map after RELION postprocessing of 3.85 Å (Figure 34). The resolution was determined based on a "gold standard" FSC coefficient of 0.143 (Figure 33A). Selected cryo-EM densities at high resolution are represented in Figure 35.

Although we get a high-resolution map, were the side chains of the residues were visible in several regions (Figure 35), the map did not allow us to identify the subtle sequence differences between MVPα and MVPβ (Figure 36), and consequently we could not discern how the two monomers were distributed in the particle. In addition, both monomers shared a 61.2% of homology (Figure 36, and homology tested by Uniprot-BLAST) fact that make more difficult the detection of differences in the reconstructed map. RELION was unable to discern between the two isoforms during the first alignment reconstructions steps (2D and 3D classifications), losing the characteristic signals of each monomer. As a consequence, in the map obtained all monomers appeared equal.

In light of the results obtained, we devised two strategies to address the problem: on one side, we would try to understand the polymerization capacity of the individual MVPα and MVPβ proteins and on the other side, we planned to create a vault-nanobody complex in which the nanobody exclusively recognized one of the MVP monomers.

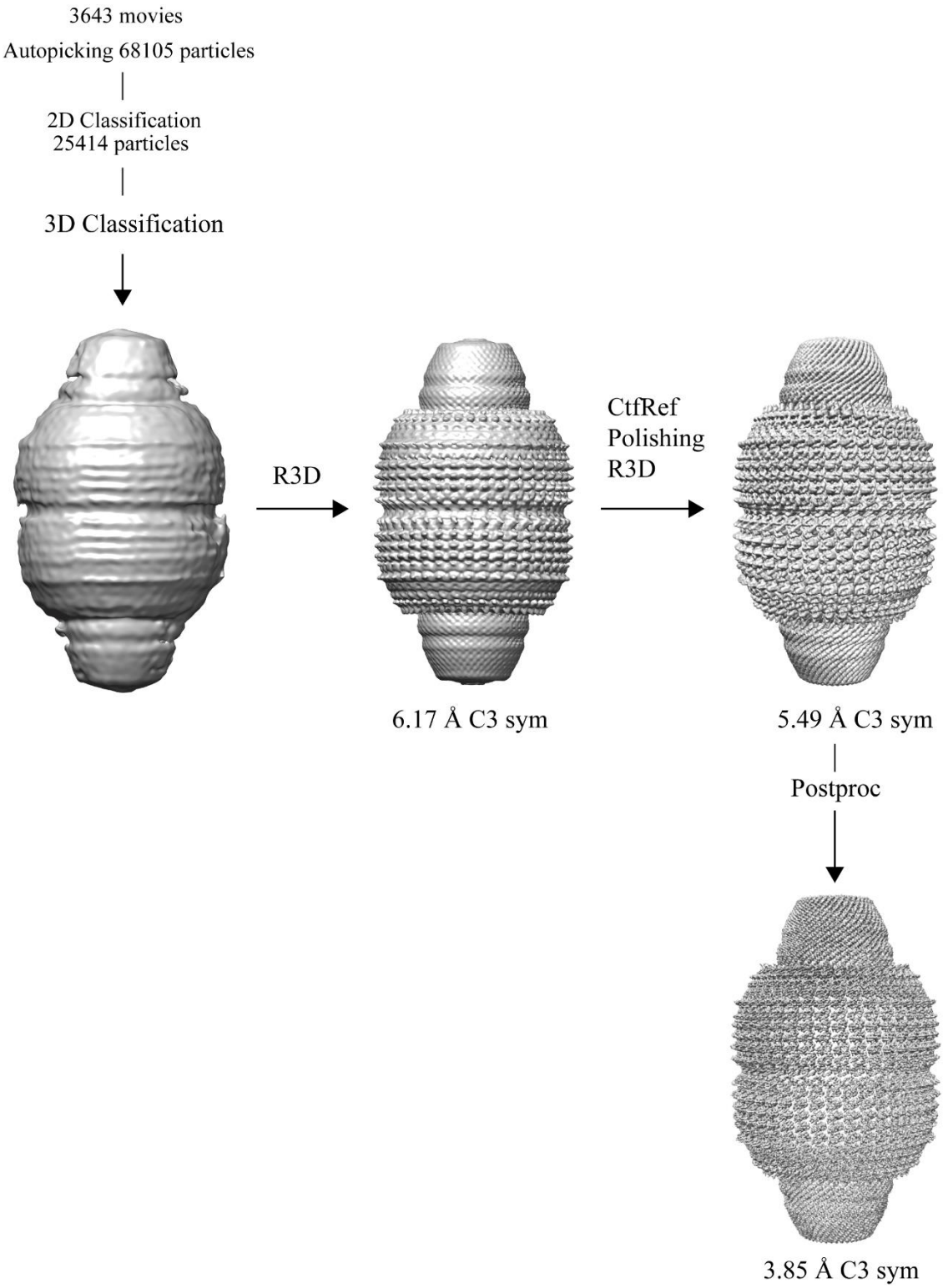

Figure 32. Image processing workflow. After 3D classification, 3D refinements (R3D) and CTF refinement and particle polishing recombinant vault reconstructions using RELION are shown. The best reconstruction was a 3.85Å map with C3 symmetry.

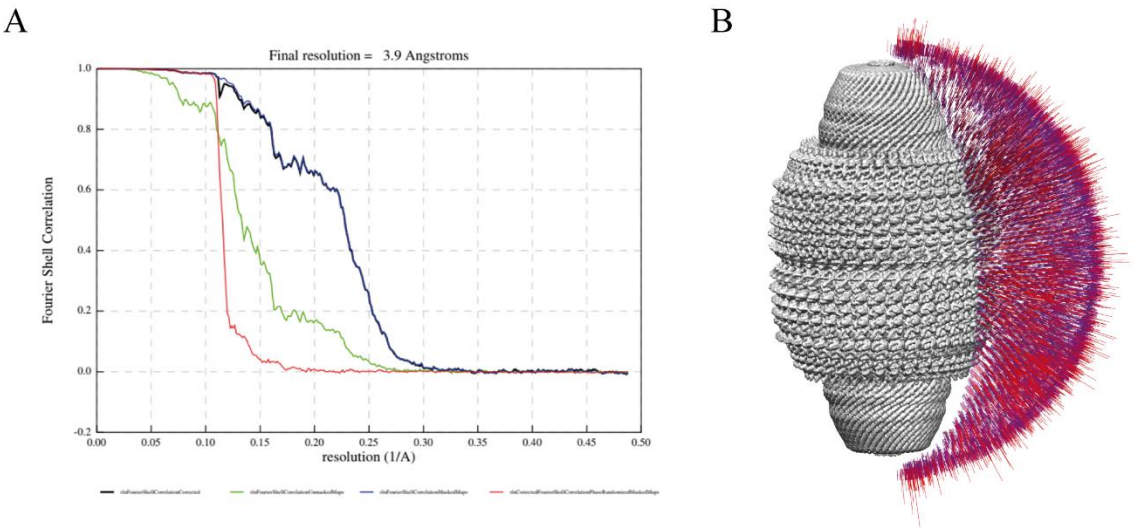

Figure 33. (**A**) Gold-standard Fourier Shell Correlation (FSC) curves between half-maps, refined independently using RELION 4.0. Global resolution by the 0.143 cutoff criterium was estimated to be 3.85 Å. (**B**) Angular distribution of vault particles that contributed to the final map.

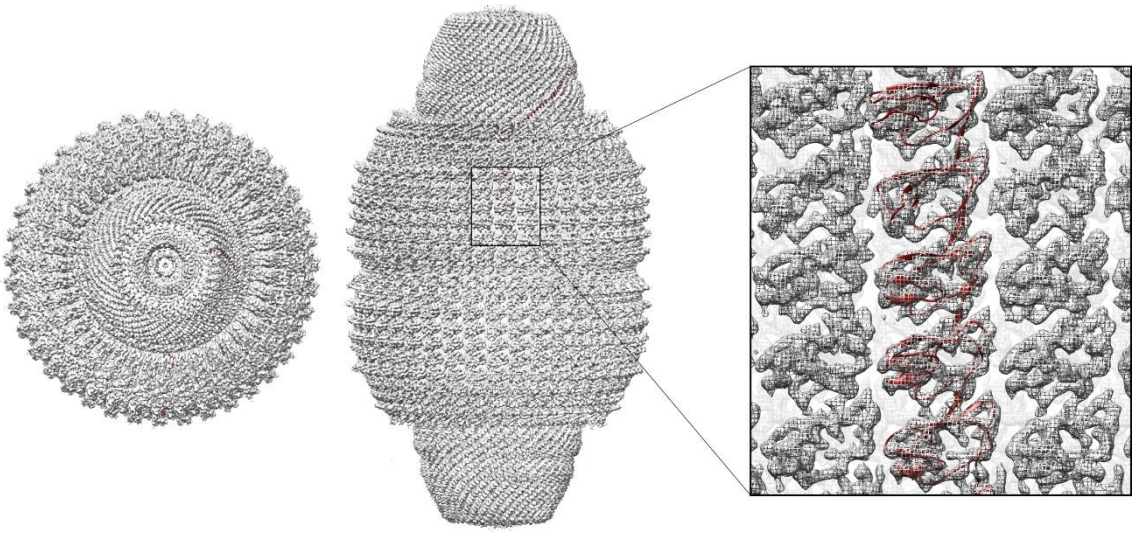

Figure 34. Structure of the recombinant *Dictyostelium* vaults (3.85 Å resolution). The reconstructed map was calculated by imposing the C3 symmetry. The left and middle panels show the top and lateral views of the *Dictyostelium* vaults, respectively. The right panel shows a close up of the map at the vault barrel region (repeats from R3 to R7), with the coordinates of the rat MVP (PDB:4HL8) fitted inside.

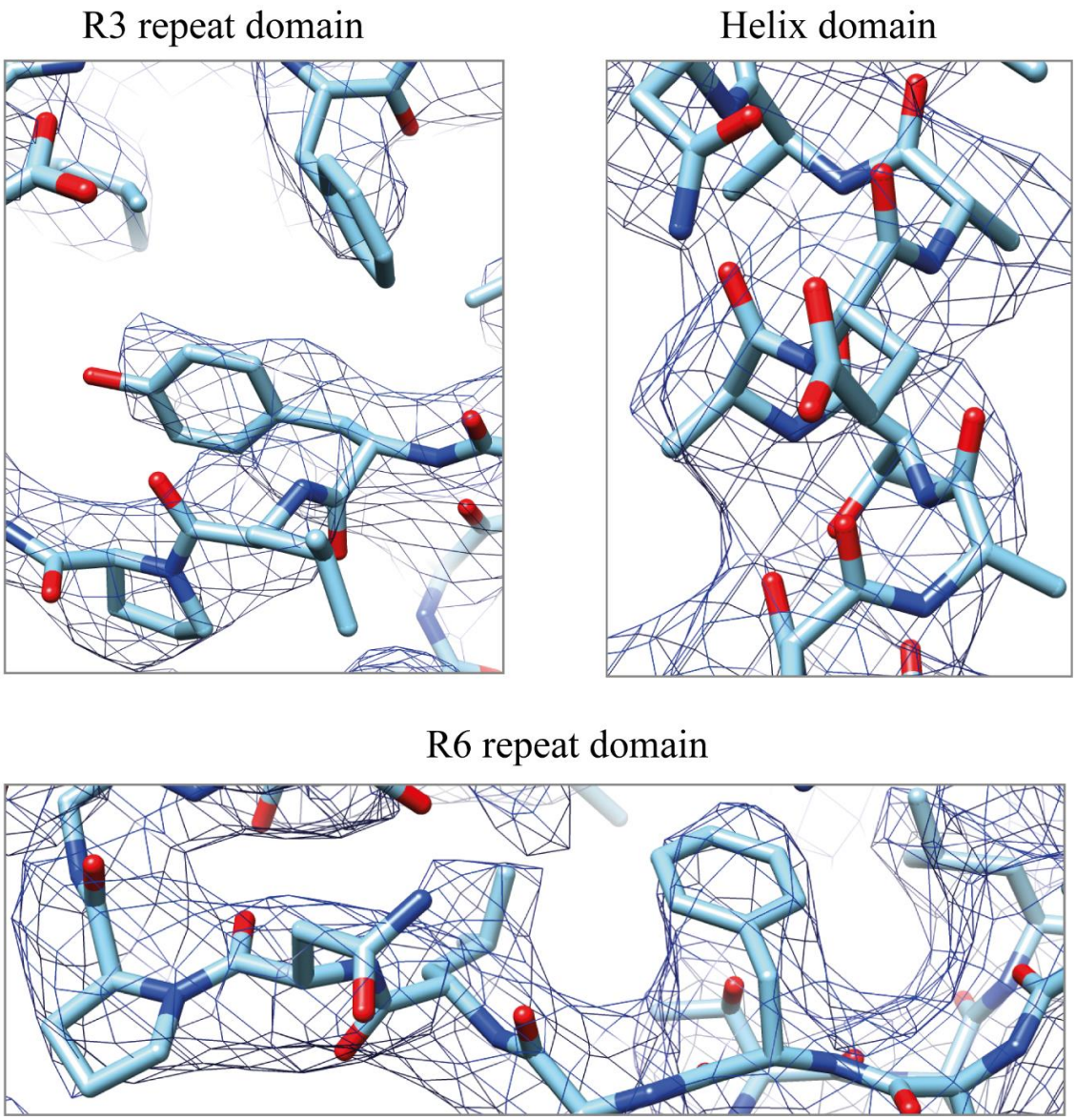

Figure 35. Experimental cryo-EM density for selected regions of the vault reconstruction at 3.85Å with C3 symmetry. Cryo-EM density observed in cap helix domain, in the R3 repeat domain and R6 repeat domain.

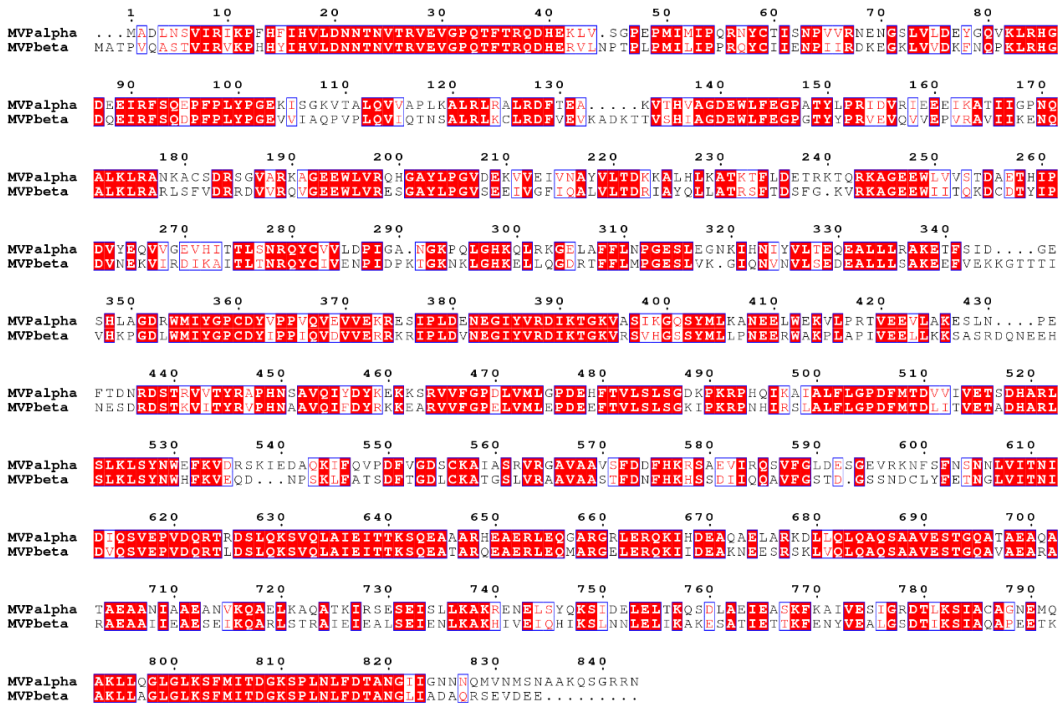

Figure 36. Sequence alignment of MVPα and MVPβ with a 61.2% of homology.

3. Individual characterization of each MVP isoform: MVPα and MVPβ

Even though we had a reconstructed 3D map of recombinant *Dictyostelium* vaults at a reasonable resolution, the inability to clearly identify the distribution of individual MVPα and MVPβ monomers raised the question of whether both subunits were essential for vault assembly or which one would be the guide. The first trial was to infect HighFive cells separately with rVB-MVPα or rVB-MVPβ, in two different attempts to obtain vaults containing only one MVP isoform, α or β, following the standard protocol for vault purification. Fractions obtained in each purification step were analyzed by SDS-PAGE and Western-Blot (Figure 37). The sucrose cushion was the initial purification step, where the membrane drifts were precipitated at the bottom of the centrifuge tube. Two samples were examined: the pellet and the soluble part, where MVP should be found (Figure 37A). The rVB-MVPα infection, resulted in the over-expression of a band at 100 kDa, visible in the soluble fraction that would correspond to MVPα. In contrast, the expression of MVPβ only resulted in an aggregate, only found in the pellet fraction (Figure 37A). Only the MVPα fractions where analyzed after a second purification step in a sucrose gradient (Figure 37B), showing the 100 kDa band, corresponding to MVPα that was further confirmed by a Western-Blot (Figure 37B). This result suggested the possibility that MVPα was able to form an ordered assembly.

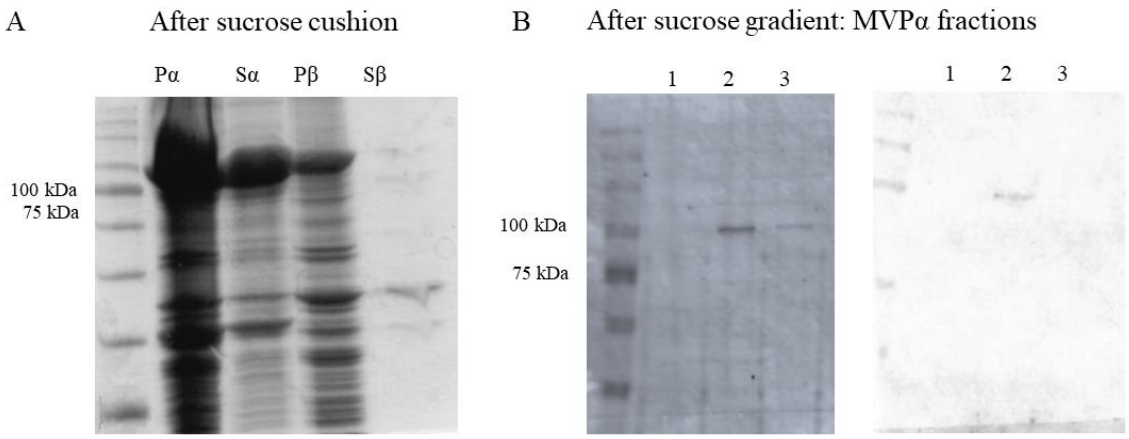

Figure 37. Analysis of MVPα and MVPβ fractions during purification. (**A**) SDS-PAGE analysis of fractions after sucrose cushion. (P: pellet fraction) (S: soluble fraction). (**B**) MVPα fraction analysis after sucrose gradient. Left side, SDS-PAGE analysis. Right side, Western-Blot.

We used negative-staining EM to prove the existence of this macromolecular complex and to check its morphology. When visualized in the electron microscope the MVPα complex showed a morphology, closely resembling to a vault structure but apically smashed (Figure 38).

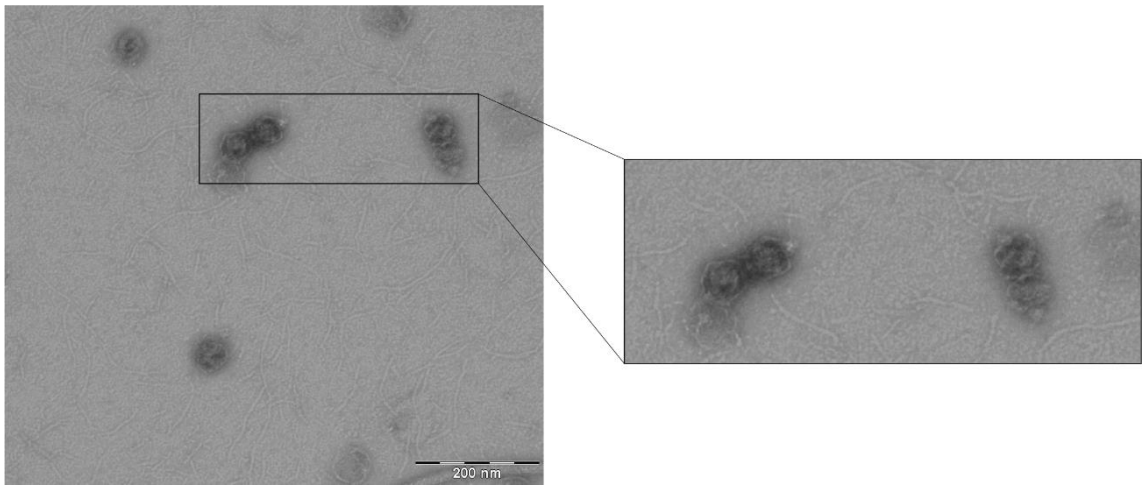

Figure 38. Negative-staining micrograph of MVPα complex. The zoom inset shows two pairs of particles, resembling two fused vaults. However, the barrel-like structure was not properly recognized. Paying attention to one particle, it may resemble the vault structure but as if it was apically smashed.

To better understand the behavior of this protein and its ability to polymerize, purified MVPα was also analyzed by size exclusion chromatography (SEC) coupled with multi-angle light scattering analysis (MALS). On this occasion, MVPα purification was carried out by immobilized metal affinity chromatography (IMAC), using a Ni-affinity column, taking advantage of the fact that the MVPα construct had a His-tag linked to its N-terminus and because MVPα was soluble. The protein obtained after elution (Figure 39B) was concentrated and applied to an analytic SEC column (Superdex 200 5 150 FC) (Figure 40) before MALS analysis. SEC experiments in a temperature-controlled chamber (25 ºC), and coupled to a MALS detector, showed that the purified MVPα construct behaved mainly as a monomer in the protein stabilization buffer. A predominant peak (95 ± 2% sample mass), corresponding to 95 ± 2 kDa matched the calculated molecular weight of this protein. The protein eluted much earlier than globular proteins with similar molecular mass (Figure 41). This altered behaviour could be explained due to the extended conformation of the MVPα monomer.

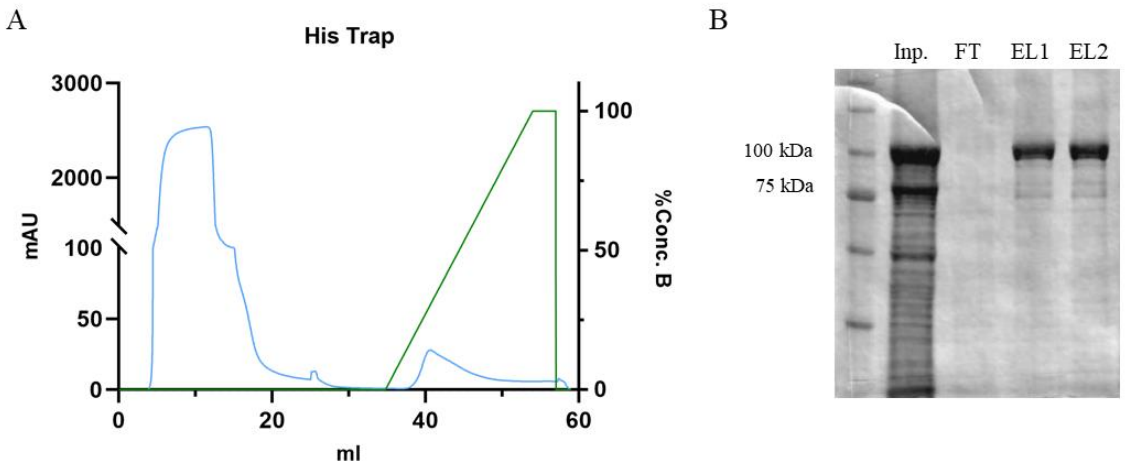

Figure 39. Purification of MVPα by IMAC. (**A**) IMAC chromatogram obtained after purification. (**B**) SDS-PAGE analysis of the different fractions: Inp.: input (sample obtained after cell lysis and loaded to the column), FT (flow through), EL1, EL2: elution fractions, containing the MVPα protein.

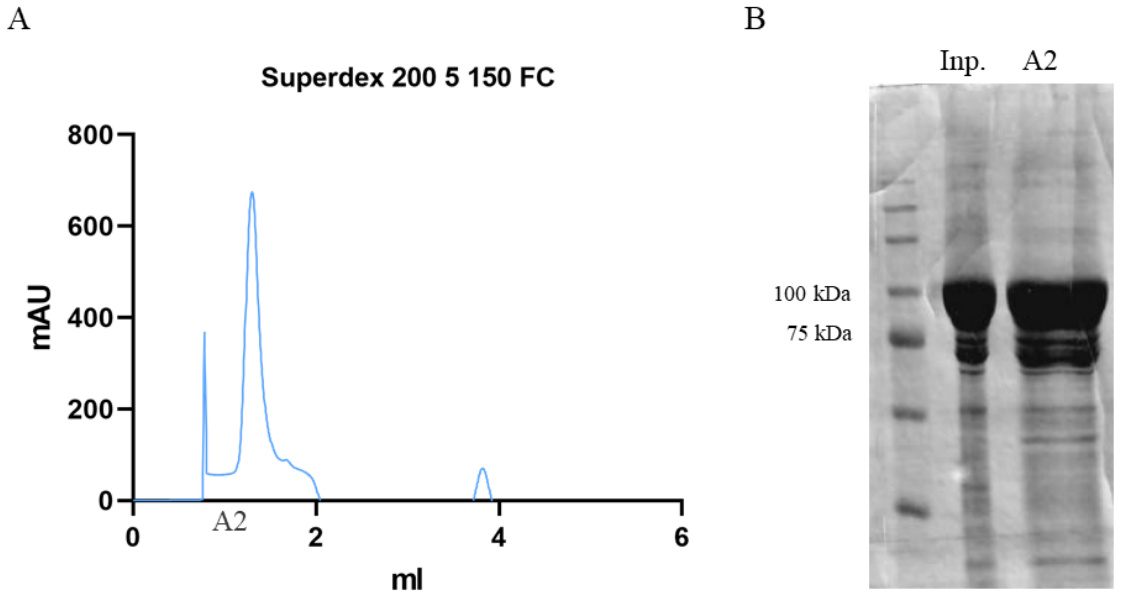

Figure 40. MVPα purification by SEC. (**A**) Chromatogram obtained after Superdex 200 5 150 FC analytic column. (**B**) SDS-PAGE analysis of the different fractions: Inp.: input (sample before loading into the column). A2: fraction obtained during the chromatography where MVPα was present.

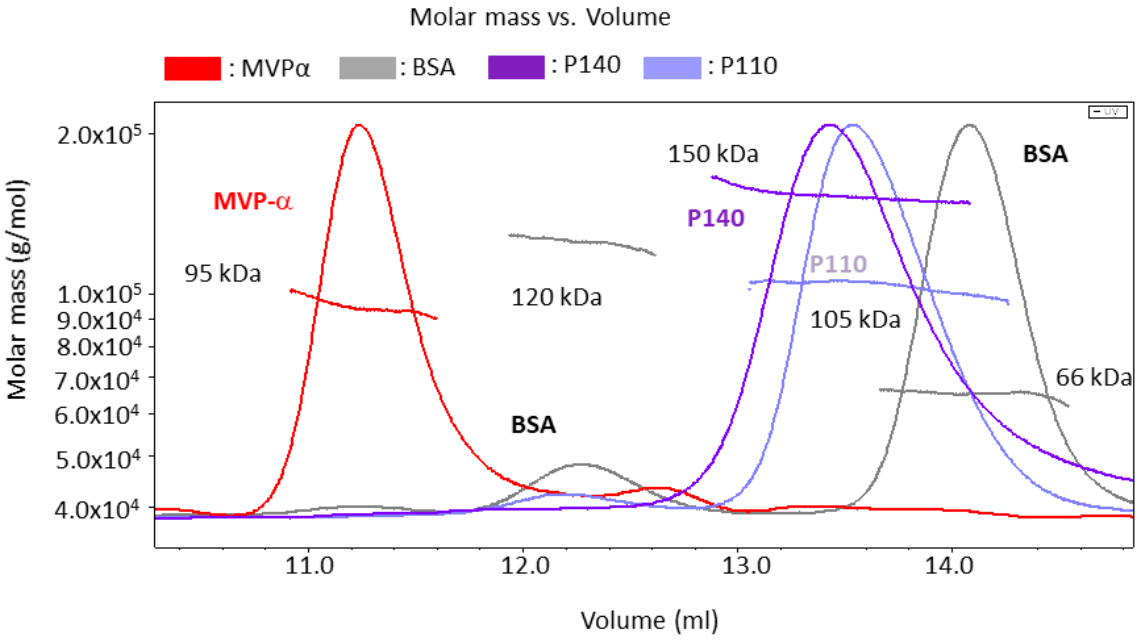

Figure 41. MALS profiles for MVPα (red) and comparison to other samples eluting in Superdex200: P140 (purple), P110 (violet) and BSA (grey).

Although the high homology present in both MVP subunits (Figure 36), MVPα and MVPβ behave different. These results demonstrated that MVPβ aggregated when was individually expressed (Figure 37A). However, when was expressed in parallel with MVPα, the vault assembly occurred (Figures 28 and 29). In contrast, the expression of MVPα alone resulted in a soluble protein that remained as a monomer in solution, at least in buffer A [50mM Tris (pH 7.5), 75mM NaCl, 0.75mM $MgCl_2$], as confirmed by MALS experiment (Figure 41). Furthermore, MVPα was able to assembly in macromolecular complexes that appear homogenous and resemble the vault structure but with a rounded shape (Figure 38). In a hypothetical *Dictyostelium* vault assembly process, MVPα appears to be the assembly guide whereas MVPβ appears essential for obtaining the correct shape of the vault particle.

4. Structural characterization of mutant recombinant vaults from *Dictyostelium discoideum* in complex with an α-myc nanobody

Although we get a high resolution cryo-EM map of recombinant *Dictyostelium* vaults, (Figures 34 and 35), we were not able to figure out how do the MVPα and MVPβ monomers assemble to form the vault complex. In addition, the individual characterization of MVPα and MVPβ subunits did not provided any information on how they could associate.

To address this issue, we decided to obtain a complex of a recombinant vault particle with a nanobody, recognizing only one of the two MVP isoforms. Due to the absence of commercial nanobodies against MVP, we introduced a nanobody recognition tag in just one isoform (MVPα or MVPβ), and among the existing commercial nanobodies, we chose α-myc.

To identify the best position for the MVP/α-myc nanobody complex formation, without altering the structure of the vault particle, we created a set of different myc-MVP constructs where the myc-tag was introduced in different positions within the MVP repeats (in MVPα or in MVPβ). Afterwards, we produced the recombinant baculoviruses for each of the constructs for the co-expression, purification and analysis of vaults containing the myc-tag insertions in one or another MVP isoform. The last step was the incubation of vaults containing the myc-tag insertion with the α-myc nanobody to structurally characterize the complex by cryo-EM. In this way, the nanobody would only bind the MVP monomer, containing the myc-sequence, thus allowing us to identify how the two isoforms would be organized in the assembly of the vault particle.

4.1 Generation of MVPα and MVPβ mutants

The Alphafold predictions of *Dictyostelium* MVPα and MVPβ subunits were compared to the known MVP structure from rat vaults (PDB: 4HL8). The most exposed areas were the loops in the repeat R4, R5, and R6 domains that are visible in Figure 42. The cloning strategy was to clone the myc epitope sequence in these locations (Figure 42: orange arrows) to allow the binding of the nanobody without alteration of the vault structure. We created MVPα and MVPβ mutants as explained in materials and methods. Because of the fewer expression issues, mutations were first produced in the MVPα construct.

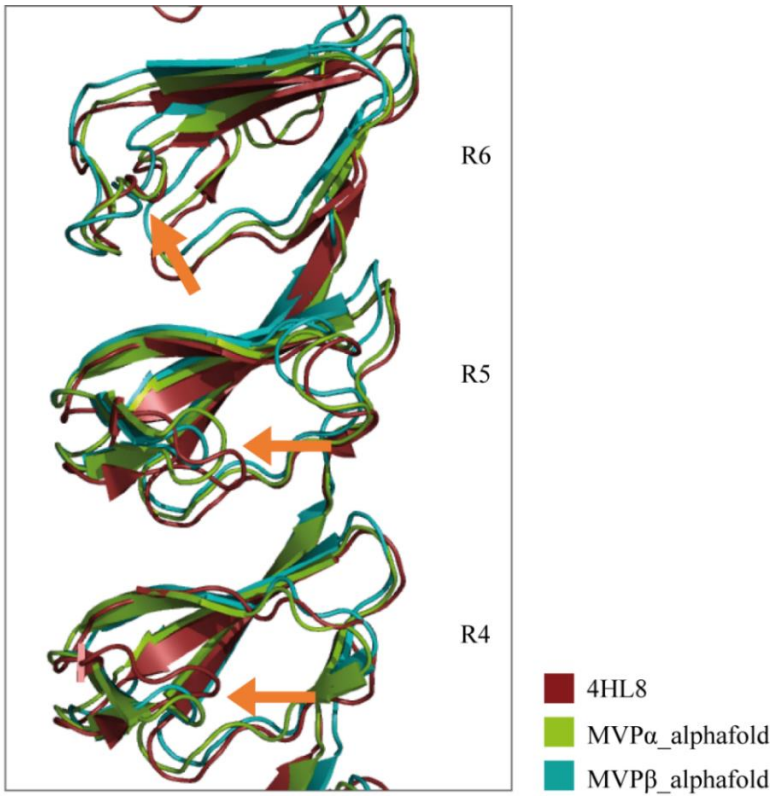

Figure 42. Alignment of the MVPα and MVPβ prediction models with the 4HL8 structure to identify the most exposed loops in the central barrel domains R4, R5 and R6. Orange arrows indicate the location of the selected myc-insertion sites in each domain.

4.2 Generation and analysis of MVPα and MVPβ mutants, containing the myc sequence

We generated a total of 10 different mutants of the MVPα and MVPβ inserted in different loops within the repeat domains:

1. MVPα R4i (S185-R184): we cloned myc sequence by insertion between the R184 and S185 residues in the R4α repeat domain.
2. MVPα R4s (K179-K190): we cloned myc sequence by residues substitution from K179 to K190 in the R4α repeat domain.
3. MVPα R5s (F234-R243): we cloned myc sequence by residues substitution from F234 to R243 in the R5α repeat domain.
4. MVPα R6s (P287-P294): we cloned myc sequence by residues substitution from P287 to P294 in the R6α repeat domain.
5. MVPα R6i (A290-N291): we cloned myc sequence by insertion between the A290 and N291 residues in the R6α repeat domain.

6. MVPβ R4i (R193-R194): we cloned myc sequence by insertion between the R193 and R194 residues in the R4β repeat domain.
7. MVPβ R4s (L188-Q199): we cloned myc sequence by residues substitution from L188 to Q190 in the R4β repeat domain.
8. MVPβ R5s (R241-K252): we cloned myc sequence by residues substitution from R241 to K252 in the R5β repeat domain.
9. MVPβ R6i (D297-K299): we cloned myc sequence by insertion between the D297 and K299 residues in the R6β repeat domain.
10. MVPβ R6s (P295-P298): we cloned myc sequence by residues substitution from P295 to P298 in the R6β repeat domain.

Recombinant baculoviruses were generated for each construct, following the Bac-to-Bac-system (see methods). After the virus titration, Hi5 cells were co-infected with (rBV-MVPα-mutant and rBV-MVPβ) or with (rBV-MVPα and rBV- MVPβ-mutant). After 72h post-infection, purification was performed following the purification protocol for recombinant vaults. Workflow for each construct is included in Table 1. Results for each construct are summarized in the annexes mentioned in the table.

Name	Myc-localization	rBV production	VAULTS	IP α-myc	Annex
R4α-ins-184-185	MVPα R4 ins (R184-S185)	√	X	X	Figure 1. A-A'
R4α-sus-179-190	MVPα R4 sus (K179-K190)	√	X	X	Figure 1. B
R5α-sus-234-243	MVPα R5 sus (F234-R243)	√	X	X	Figure 1. C
R6α-ins-290-291	MVPα R6 ins (A290-N291)	√	X	X	Figure 1. D
R6α-sus-287-294	MVPα R6 sus (P287-P294)	√	X	X	Figure 1. E
R4β-ins-193-194	MVPβ R4 ins (R193-R194)	√	√	√	Figure 2. A-A'
R4β-sus-188-199	MVPβ R4 sus (L188-Q199)	√	√	√	Figure 2. B-B'
R5β-sus-241-252	MVPβ R5 sus (R241-K252)	√	√	√	Figure 2. C-C'
R6β-ins-297-299	MVPβ R6 ins (D297-K299)	√	√	√	Figure 2. D-D'
R6β-sus-295-298	MVPβ R6 sus (P295-P298)	√	√	√	Figure 2. E-E'

Table 1. Summary of results for the different MVP mutants generated. Columns inform about the name of the construct, location of the myc insertion, success in recombinant baculoviruses production, success in vaults purification and immunoprecipitation with α-myc nanobody.

We were only able to purify intact vaults when the myc-tags were introduced in the MVPβ constructs. To choose the best candidates, we compared the morphology of the different vaults obtained, using negative staining EM. The best vault morphology was obtained by the insertion of the myc peptide in domain R6 (Table 1: R6β-sus-295-298) (Figure 2 Annex. E- E'). We chose this construct to produce large-scale vaults for structural studies. We produced 3 purifications of 20 plates each. However, we found several problems in the final purification step, losing many particles in the CsCl gradient (Figure 43A). We obtained similar results by replacing the CsCl gradient with an ion exchange chromatography (Mono Q) (Figure 43B) and finally we carried out the last purification step by size-exclusion chromatography (Figure 44A). Negative staining EM of the purified particles showed the vaults with good morphology (Figure 44B).

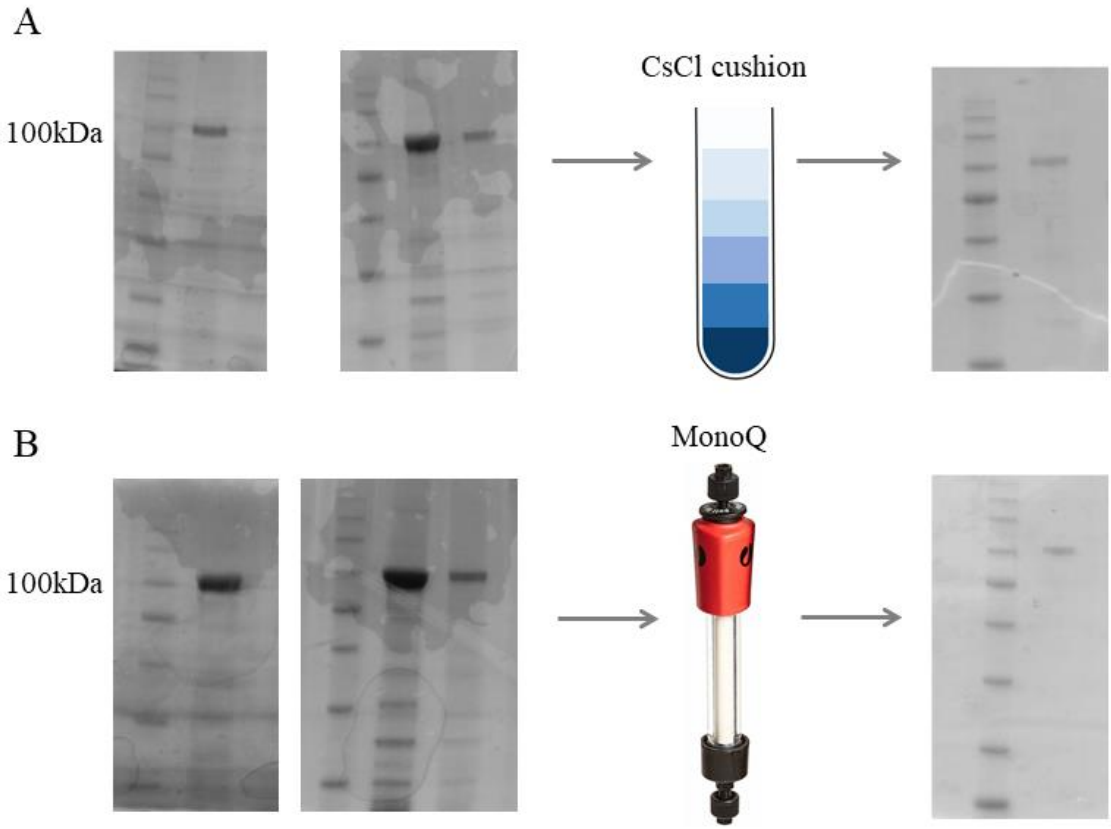

Figure 43. Loosing vaults after extra purification step (**A**) SDS-PAGE before and after CsCl cushion. (**B**) SDS-PAGE before and after MonoQ purification.

A

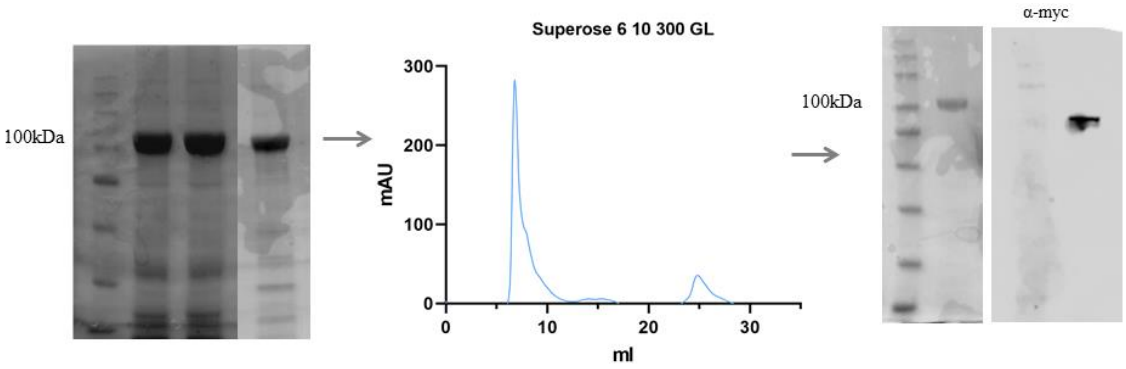

B

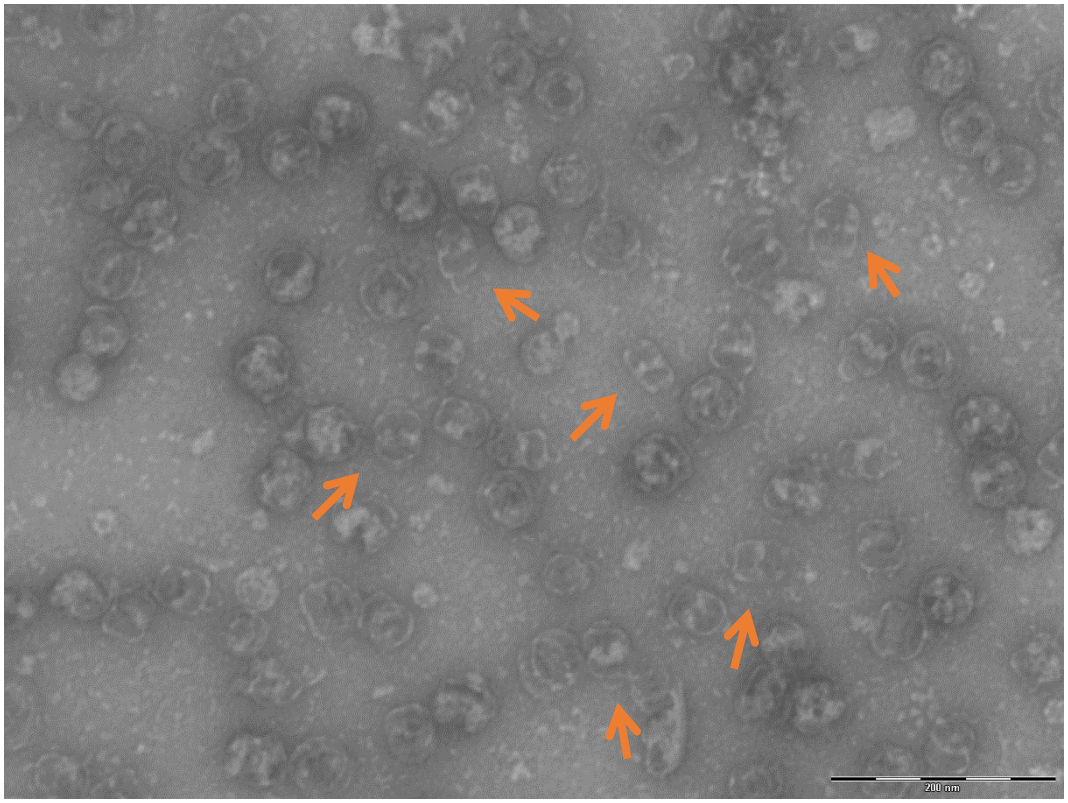

Figure 44. Mutated recombinant vaults after the extra purification step by size exclusion chromatography. (**A**) SDS-PAGE before and after the Superose 6 10/300 (**B**) Negative staining of the sample. Vaults marked with orange arrows.

4.3 Generation of MVPβ R6s-myc link mutants

In order to avoid the problems encountered during the purification of the R6β-sus-295-298 construct, we designed new constructs, cloning the myc sequence at the same location of R6β-sus-295-298 construct but flanked by a Gly-Ser linkers at the N- and C-terminal

ends. These linkers would provide the loop greater flexibility, exposing the myc sequence to the exterior. We obtained two constructs with different link lengths: long (GSGSG_myc_GSGSG) and short (GSG_myc_GSG), and generated the recombinant baculoviruses. Then, we co-infected cells with rBV-MVPα and rBV-R6β-sus-295-298-link (short or long). Recombinant vaults were purified following the standard vault purification protocol, but due to the previous results, the size-exclusion chromatography was chosen for the extra purification step after the gradient. SDS-PAGE and Western-Blot assays were used for checking the purity of the MVPs obtained with the different GS links (Figure 45). Recombinant vaults produced with R6β-sus-295-298-link had better morphology than the ones produced by R6β-sus-295-298 construct without link. We were able to purify them in large scale in order to obtain enough protein to further cryo-EM characterization. Vault protein concentration and morphology were verified by negative staining (Figures 46 and 47).

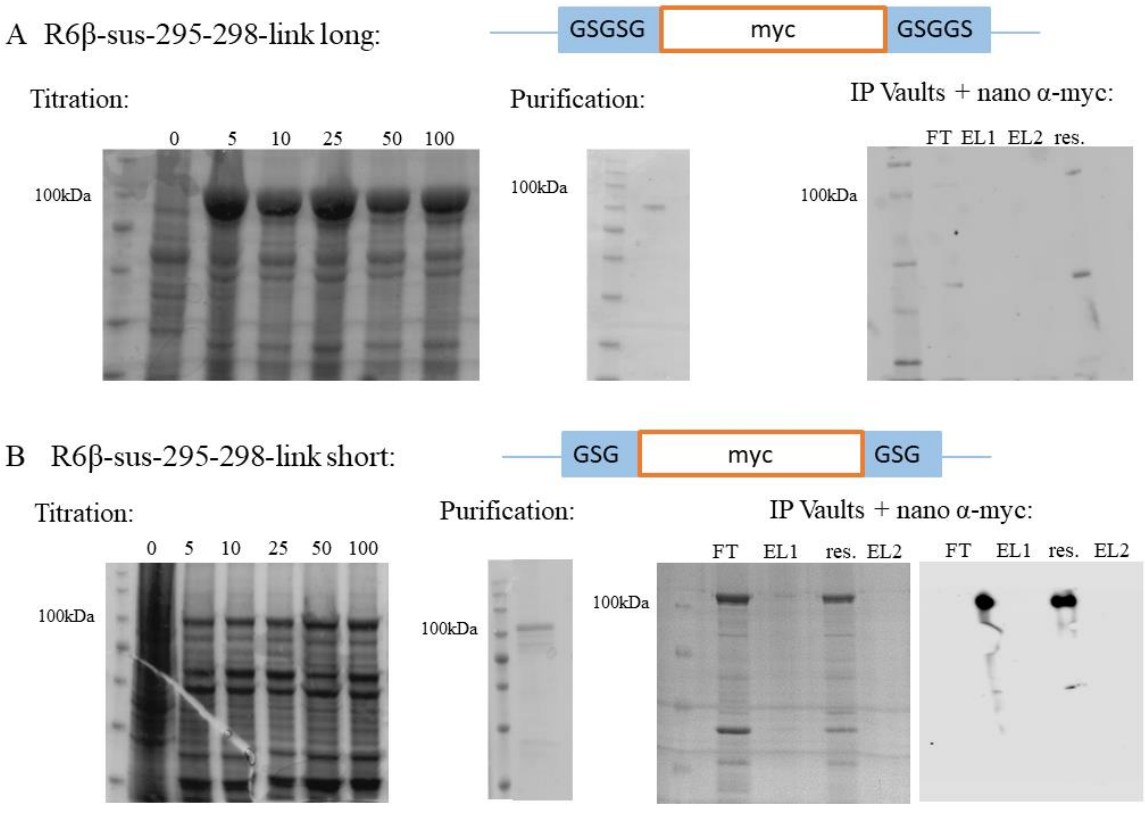

Figure 45. MVPβ-myc link mutant constructs analysis: virus titration, purification of vaults by co-infection each construct with rBV-MVPα and immunoprecipitation with the α-myc nanobody. (**A**) R6β-sus-295-298-link long. (**B**) R6β-sus-295-298-link short.

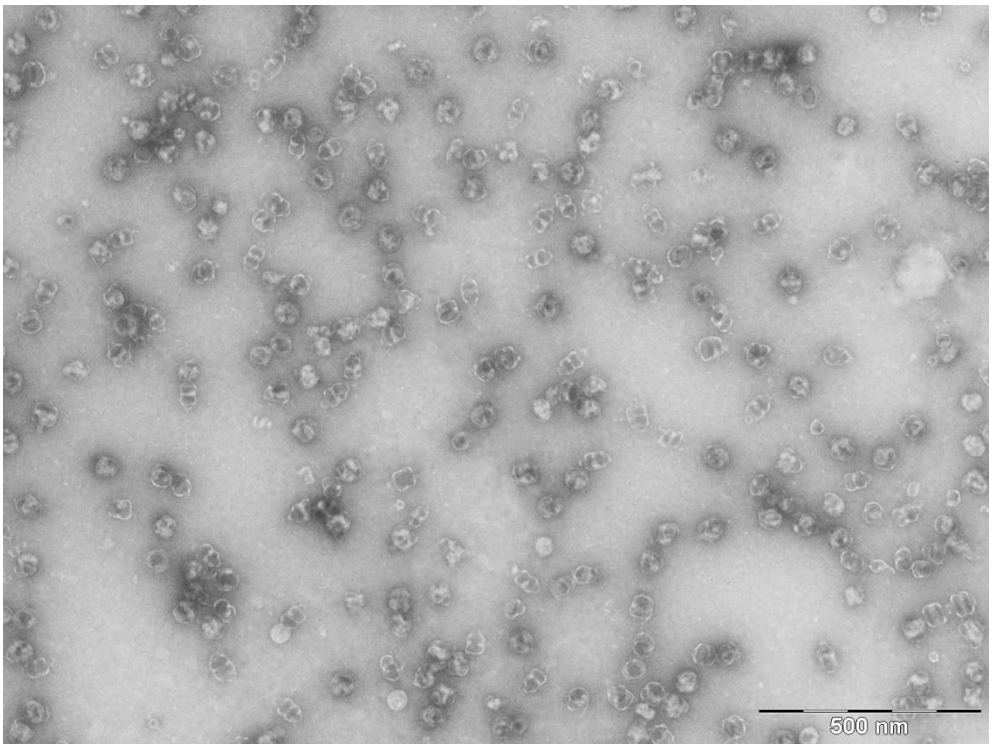

Figure 46. Vaults produced by R6β-sus-295-298-link long construct. (**A**) Negative staining micrograph after size-exclusion chromatography, sample concentration 1/40: vaults with good morphology and correct concentration.

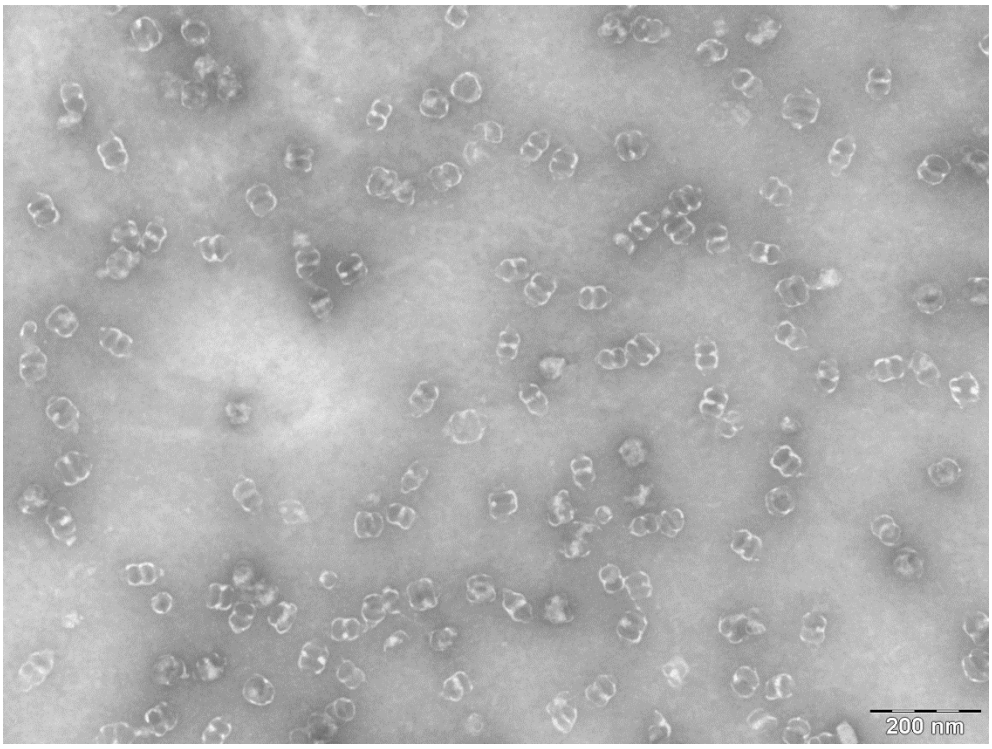

Figure 47. Vaults produced by R6β-sus-295-298-link short construct. (**A**) Negative staining micrograph after size-exclusion chromatography, sample concentration 1/40: vaults with good morphology and correct concentration.

4.4 Cryo-electron microscopy of recombinant *Dictyostelium discoideum* vaults in complex with a nanobody

The incubation of recombinant vaults with the α-myc nanodoy to form the vault-nanobody complex was made immediately before the vitrification of the cryo-EM grids. The stoichiometry vault:nanobody used was 1:80 (calculated assuming 80 copies of MVP). We checked different incubation times: 1 h, 15 min, 1-2 min. The best results were obtained with 1-2 min incubation, because as long as the incubation time was as many as open vaults appeared in the micrographs.

The process of grid preparation, vitrification and initial data collection was performed at the cryo-EM facility of the CNB-CSIC. In this initial session of sample quality checking, we collected two small data sets: a total of 1075 movies from vaults obtained with the long-link construct and the second with 1808 movies from vaults obtained with the short-link.

Initial data processing indicated that the vault-nanobody particles showed preferential orientations and the two data sets were initially joined with the aim of increasing the number of orientations to obtain a preliminary reconstruction. A total of 2883 movies were processed using RELION 4.0. (Kimanius et al., 2021). A total of 162314 particles were auto-picked and after 2D classification a total of 25035 particles were selected. Despite selecting the best particles, the requirement for more orientations was evident in subsequent runs such as the refinements: the inability to reconstruct the particle in some areas was signal of the need for more orientations (Figure 48B-circle areas). The good point was the presence of extra densities in the 2D classification, attributed to the nanobody surrounding the R6 repeat (Figure 48A-green circle). These extra densities were also appreciable in the reconstructed map (Figure 48B-blue arrows).

A

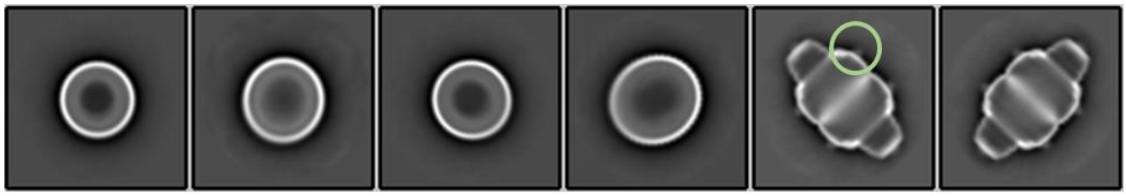

B

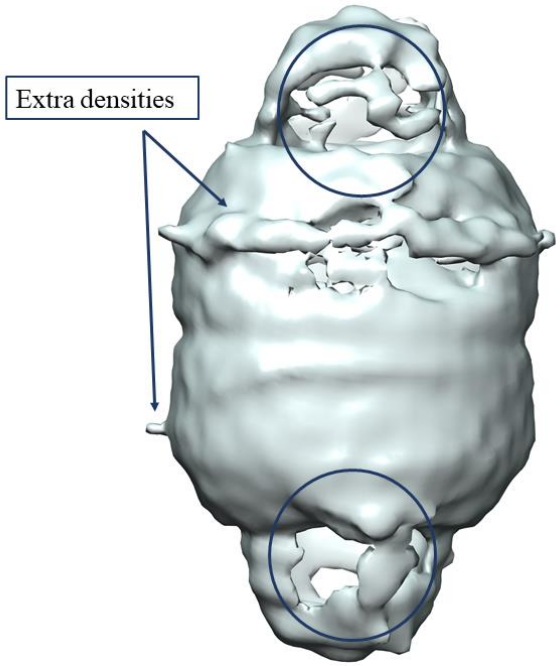

Figure 48. Data processing of the first vault-nanobody data. (**A**) 2D classification of the complex vault-nanobody. Green circle: one of the four extra density circle attributed to the nanobody. (**B**) 3D refinement of the vault-nanobody complex, where circles represent areas without signal and arrows represent extra densities.

For the following data collections, we decided to focus only in MVPβ-myc long link vaults because the quality of the grids was better. To solve the orientation problem, the new grids were prepared in presence of detergent. The detergent chosen for the treatment was N-Dodecyl-β-D-maltoside (DDM) at two different concentrations. Three new small data sets were collected: 1) without DDM, 2) at low DDM concentration (0.002 mg/ml - 0.03 times CMC detergent) and 3) at high DDM concentration (0.003mg/ml - 0.04 times CMC detergent). The 2D classes of each data set were compared, calculating the percentage of different orientations to determine the detergent effect and the optimal detergent concentration. 2D classification of low DDM concentration showed the highest percentage of useful particles (Table 2).

Data collection	Nº particles	% useful	% lateral views	% tilt views	% top views
Without DDM	162314	7368 p -> 4,5	2.1	0.3	2.4
Low DDM concentration	32225	7697 p -> 24%	2.8	6,85	15.46
High DDM concentration	25699	3310 p -> 13%	7.5	1	4.5

Table 2. Percentage of useful particles and orientations in each data collection.

The grids prepared under the best conditions were used for high resolution data collection in the 300 kV Titan Krios microscope (Thermo Scientific) equipped with a K3 direct electron detector (Gatan) at the ESRF (Grenoble, France). We acquired movies in R1.2/1.3 UltraAuFoil gold grids using the counting mode with EPU at x81000 (pixel size of 1.06 Å/pixel). We used an electron dose of 20 electrons/pixel/second and each movie contains 40 frames recorded in 2.2 seconds. The whole dataset had 15152 movies.

RELION 4.0 was used to process the data of the nanobody-vault complex. Aligned micrographs were used to estimate the contrast transfer function (CTF), with the CTFFINF4 software (Rohou and Grigorieff, 2015) (Figure 49A). A total of 460956 particles were automatically picked with a box of 400 × 400 pixels of size. Iterative 2D classifications allowed to select our best particles (Figure 49B). The 2D classification showed, as expected, the extra density, attributable to the presence of the nanobody (Figure 49B green circle: extra densities). A total of 50771 particles were used for 3D classification.

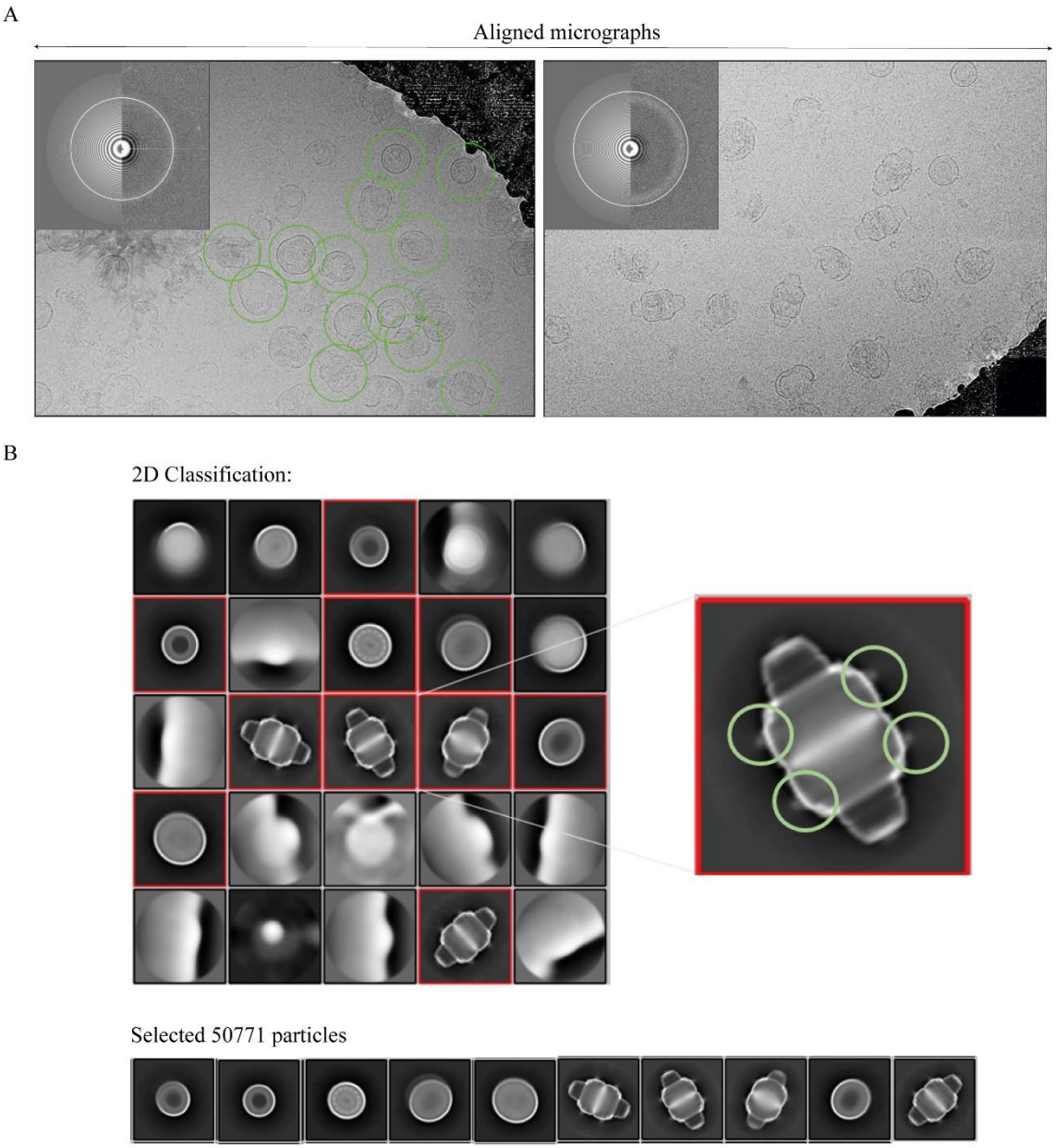

Figure 49. Vault-nanobody complex data processing. (**A**) Two representative aligned micrographs obtained with the Titan Krios electron microscope (ESRF, Grenoble) (**B**) 2D classification with the best particles picked in red and represented at the bottom (a total of 50771 particles). Zoom of one class with the extra densities in green circles.

After the first 3D classification, 16386 particles were selected for further 3D classification and refinements. With the aim of establishing how MVPα and MVPβ were distributed to constitute the vault particle, we tested different symmetries C3, D39, C39 or totally relax symmetry C1. Results obtained for each imposed symmetry were shown in Figure 50 being the 3.7 Å resolution map with C39 symmetry the best map.

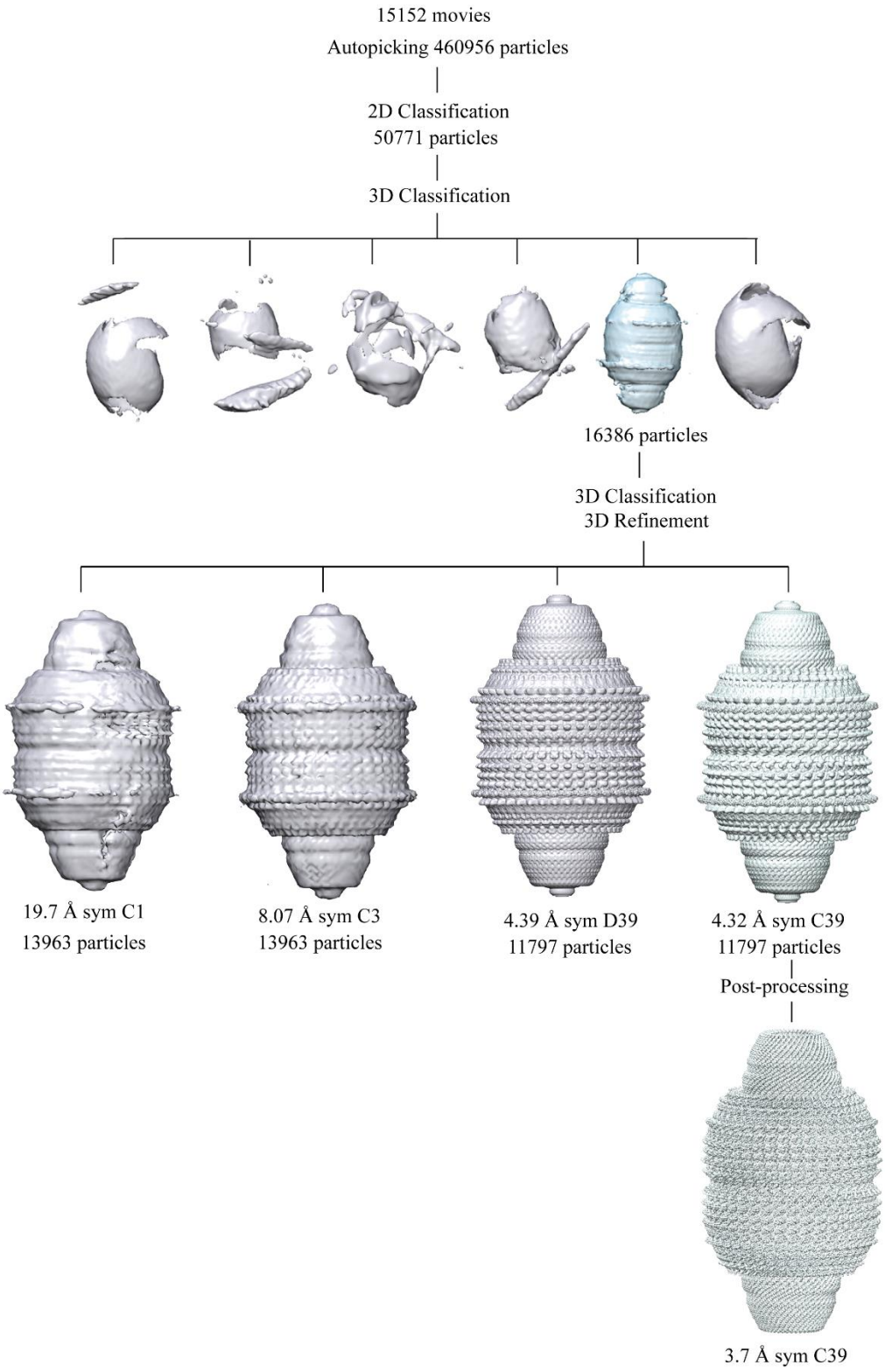

Figure 50. Vault-nanobody complex data processing. After 3D classification, six different classes were produced. The best one (light blue) was submitted to further 3D classification and 3D refinements. Different reconstruction with C1, C3, D39 and C39 symmetries were shown being the best one the reconstruction with C39 symmetry (light blue) and its subsequent post-process obtaining a 3.7 Å resolution map.

While processing, the first thought was to process the hole data set with the relaxed symmetry C1 in order to perfectly differentiate the extra densities and not lose them during averaging. Comparing the reconstruction obtained with relaxed symmetry, C1, with the others obtained by imposing C3, C39 and D39 symmetries we could distinguish that in the C1 reconstruction, the nanobody extra density occupied only some areas but poorly defined (Figure 50). In contrast, when the C3, C39 and D39 symmetries were applied, the nanobody density appeared as an extra ring around the vault due to the imposed symmetry (Figure 50).

However, the process performed without imposing symmetry (C1), resulted in a 3D reconstruction at very low resolution, a 19.7 Å map, and it was not possible to increase the resolution. For this reason, and to push up the resolution of the vault-nanobody complex we tried the imposition of different rotational symmetries. We started with C3, because it was the minimal symmetry that we could applied. By imposing the C3 symmetry the best map obtained reached 8.07 Å resolution. In addition, to corroborate that we had good quality data, we applied D39 symmetry to increase resolution until 4.39 Å. Finally, with C39 symmetry we obtained a 3.7Å resolution map. The resolution was determined based on a "gold standard" FSC coefficient of 0.143 (Figure 51).

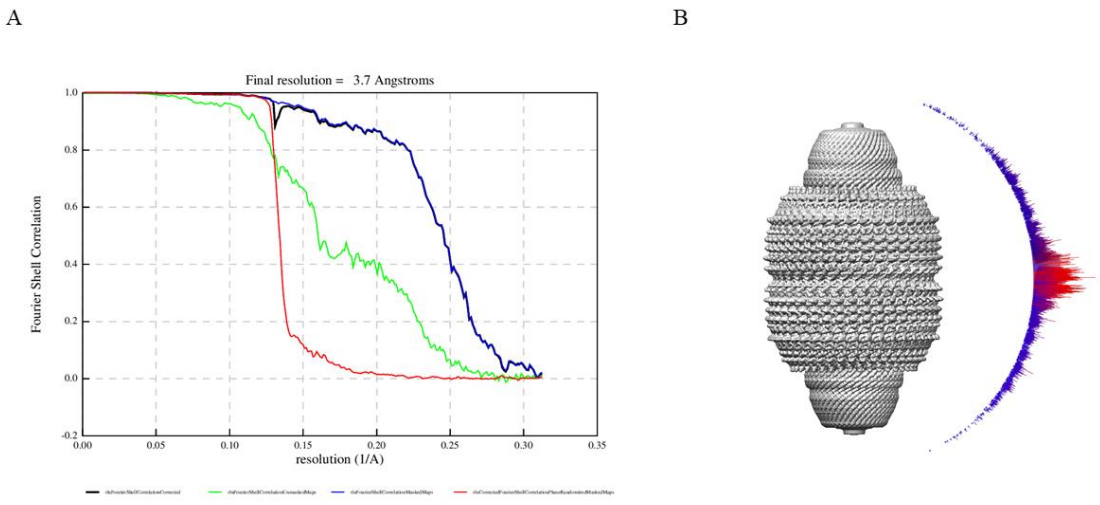

Figure 51. (**A**) Gold-standard Fourier Shell Correlation (FSC) curves between half-maps refined independently using RELION 4.0. Global resolution by the 0.143 cutoff criterium was estimated to be 3.7 Å. (**C**) Angular distribution of vault particles that contributed to the final map.

Even though we were able to obtain a high-resolution map of the vault-nanobody complex, to determine with accuracy the extra densities and establish the MVP distribution, we tried different masks, 3D classifications without alignment and expand symmetry. Besides, with the best particles, we moved to CryoSPARC (Punjani et al., 2017) to explore different solutions: expand symmetry, heterogeneous refinement and 3D variability. However, so far, we were not able to discriminate the nanobody density in the complex nor the MVP isoforms distribution. At this point, we needed high performance image computing to help us figure out the distribution of the MVP isoforms forming the *Dictyostelium* vault shell.

Through the Instruct platform (a pan-European research infrastructure in structural biology, making high-end technologies and methods available to all European researchers) we had access to a high-performance cryo-EM image computing center located at the CNB, in Madrid. They processed the data with Scipion (de la Rosa-Trevín et al., 2016) (a software that integrates several software packages as RELION, cryoSPARC, Xmipp (de la Rosa-Trevín et al., 2013) and others). Aligned micrographs were processed and after iterative 2D and 3D classifications using cryoSPARC and Xmipp, a total of 11327 particles were selected. During refinements, different symmetry tests were applied. At first instance, applying C1 symmetry, the result was a 12 Å map (Figure 52A). After imposing C39 symmetry, the result was a 3.2 Å map, that was used for different strategies such as: expand symmetry and symmetry breaking tool. The best result was a refinement a 5.1 Å resolution map with C1 symmetry obtained after breaking the symmetry (Figure 52B). Both C1 symmetry maps were compared to discard possible artefacts in the 5.1 Å final map due to the breaking symmetry tool (Figure 52). The first thing clear with both maps was that the MVP vault shell distribution was formed by MVPα clusters followed by MVPβ clusters. In other terms, there was not monomers alternation: MVPα and then MVPβ. In addition, it seemed that in one half vault there were more MVPα than MVPβ (around two thirds of MVPα), while the opposite in the other half vault (two thirds of MVPβ).

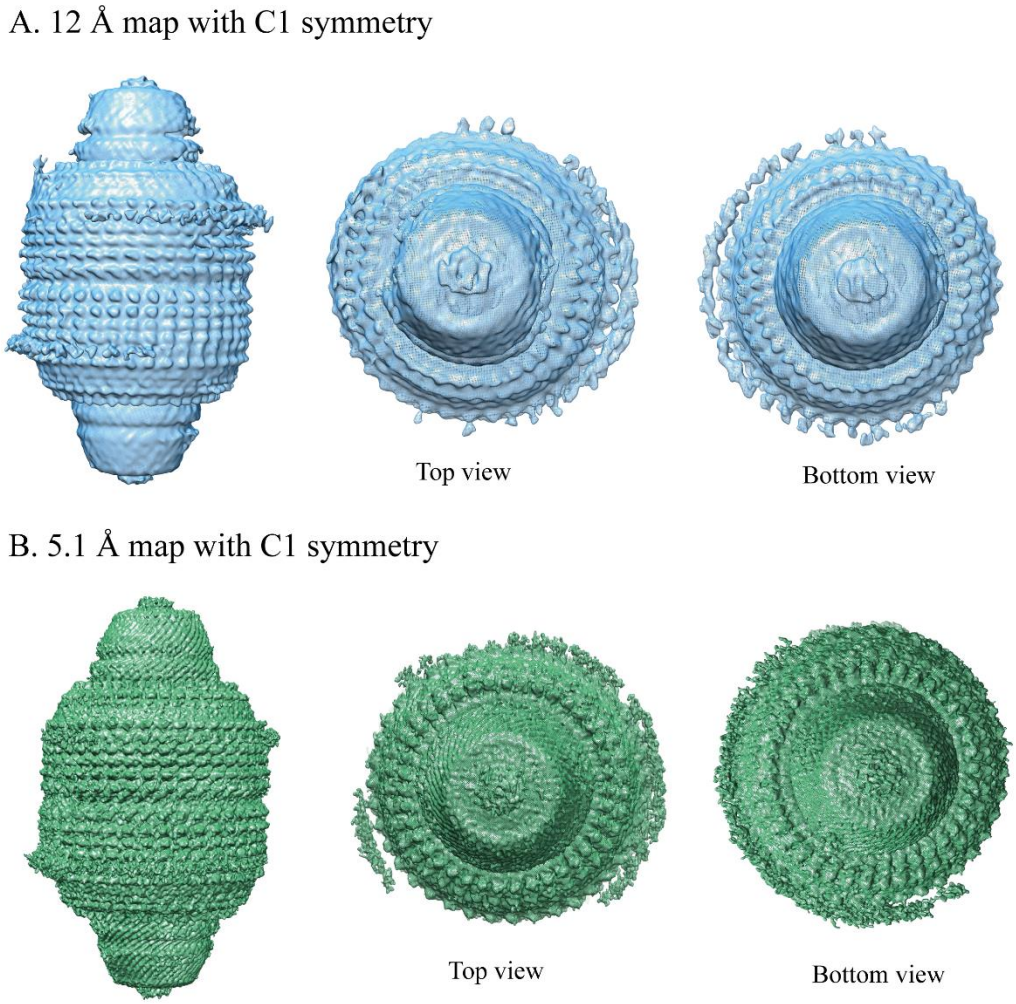

Figure 52. Instruct *Dictyostelium* vault maps. (**A**) 12 Å map with C1 symmetry. (**B**) 5.1 Å map with C1 symmetry after breaking the symmetry.

4.5 Vault-nanobody complex map segmentation

With the 5.1 Å map with C1 symmetry was possible to distinguish, at least, several MVPα from MVPβ because some MVPβ monomers contained clear extra densities localized in the R6 repeat domain due to the nanobody. For that reason, the first idea was to locally average the MVP that we found as identical ones in order to strengthen its density. Chimera (Pettersen et al., 2004) software has a segmentation tool for extracting map zones. The strategy was to extract clear densities that correspond to MVPα and averaged them in Coot (Emsley and Cowtan, 2004). And the same process for MVPβ densities with the nanobody extra density. Once we had the local averages and the particular features of each MVP subunit were strengthened, the MVPα and MVPβ averages were superimposed and compared (Figure 53-A green: MVPα averaged map, blue: MVPβ averaged maps). We verified that the 5.1 Å map contained MVPα and MVPβ subunits, as we expected, because MVPα expression alone nor MVPβ could not assembly into vaults. We observed that MVPβ contained, a part from the extra nanobody density, certain loops extension in several repeat domains, but the most significant was the extension in the R7 domain, visualized in Figure 53A, represented in Cα tracing in Figure 53B red arrow.

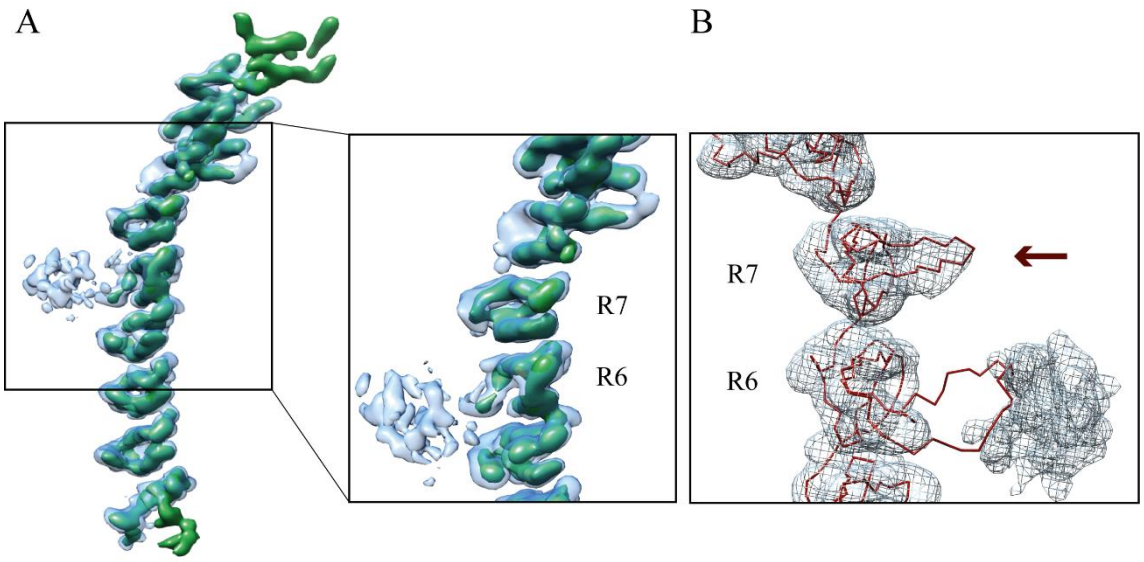

Figure 53. Local averaging of MVPα and MVPβ densities. (**A**) MVP averaged maps superimposed (green: MVPα; blue: MVPβ) with the extra nanobody density present in MVPβ and an extension in the R7 domain. (**B**) The MVPβ model fitted in the averaged density (image rotated 90º from A), clearly showing the nanobody extra density bound to the loop extension of R6 (red chain: MVPβ).

4.6 Model Fitting

Although the 5.1 Å final map was not a high-resolution map, we had been able to fit the protein backbone, moving the different protein domains as rigid bodies. The Alphafold2 structural predictions for MVPα and MVPβ were used as model guides with some changes. The MVPα prediction model was directly available in the Alphafold2 database. However, as the monomer MVPβ contained the myc sequence flanked by the link, we run an Alphafold prediction to obtain the modified MVPβ model. When we compared the two predicted models with the MVP structure of rat vaults (PDB: 7PKR), the most noticeable difference was that in the Alphafold models the cap helix was downward, in a position not compatible with the formation of the protruding cap. Remodelling of the cap helix was performed with the Coot software, using coordinates of the MVP cap helices from the cryo-EM structure of recombinant rat vaults (PDB ID: 7PKR) and subsequently replacing the side chains of this region by the correct sequence.

As mentioned above, the extra densities accounting for the anti-myc nanobody were localized such a way that prompted to speculate that one half-vault could be formed by approximately by two thirds of MVPα and one third of MVPβ and the second half would be complementary, formed by one third of MVPα and two thirds of MVPβ (Figure 52). We also suspected that some additional extra densities, appearing in the 5.1 Å map could be artefacts due to the breaking symmetry tool, because these densities did not appear in the 12 Å map (Figure 52). In accordance with the hypothesis, we built a putative model with 13 MVPα copies in the top half and with 13 MVPβ copies in the bottom half (Figure 54A). The geometry of the fitted model was optimized using Phenix software (Adams et al., 2010). Figure 54 shows the fitting of the model in different areas: in the cap helix (Figure 54B), where the MVPα copies are localized (Figure 54C), and where the MVPβ copies are situated (Figure 55D).

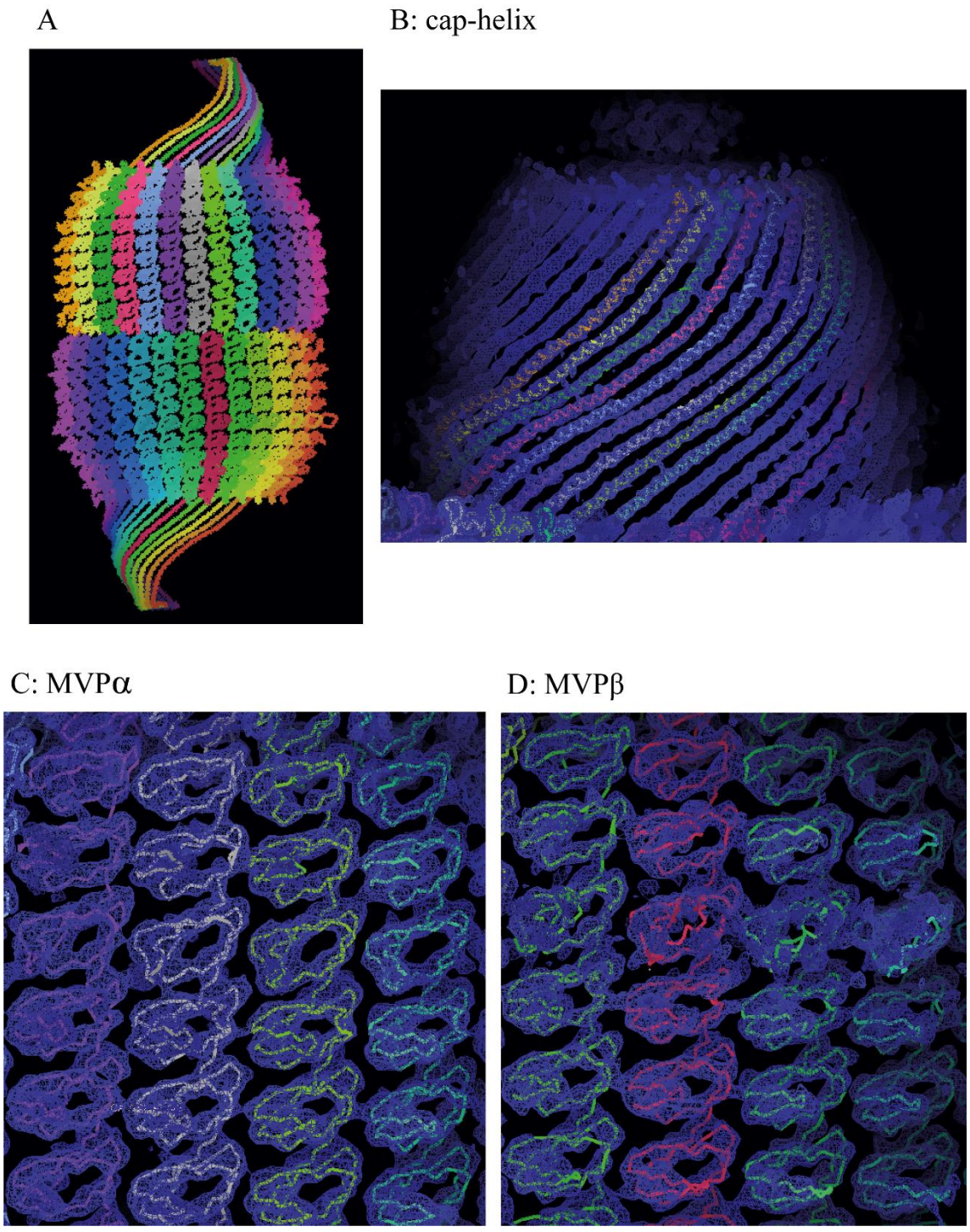

Figure 54. Model fitting. (**A**) Prediction model with 13 MVPα copies in the top half and with 13 MVPβ copies in the bottom half. (**B**) Fitting the model in the cap helix. (**C**) Fitting the model in MVPα density. (**D**) Fitting the model in MVPβ density.

4.7 MVPα and MVPβ-myc interface comparison

Once we had the *Dictyostelium* vault model, we were curious about how the MVP-MVP interaction worked. How the MVPα and MVPβ lateral contacts were in order to assembly the vault structure. Each possible contact: MVPα-MVPα, MVPβ-MVPβ, MVPα-MVPβ and MVPβ-MVPα was analyzed with PISA software (PDBePISA). Figure 55 shows a representation of the contact interfaces MVPα-MVPα, MVPβ-MVPβ, MVPα-MVPβ, and MVPβ-MVPα in the cap helix that are predominantly hydrophobic.

Cap-helix interfaces:

A. MVPα-MVPα

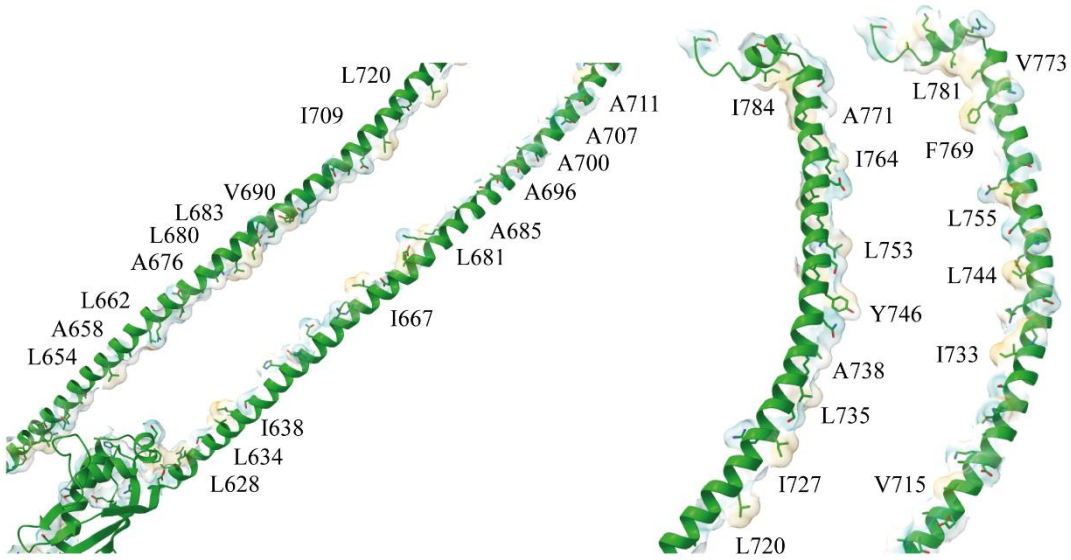

B. MVPβ-MVPβ

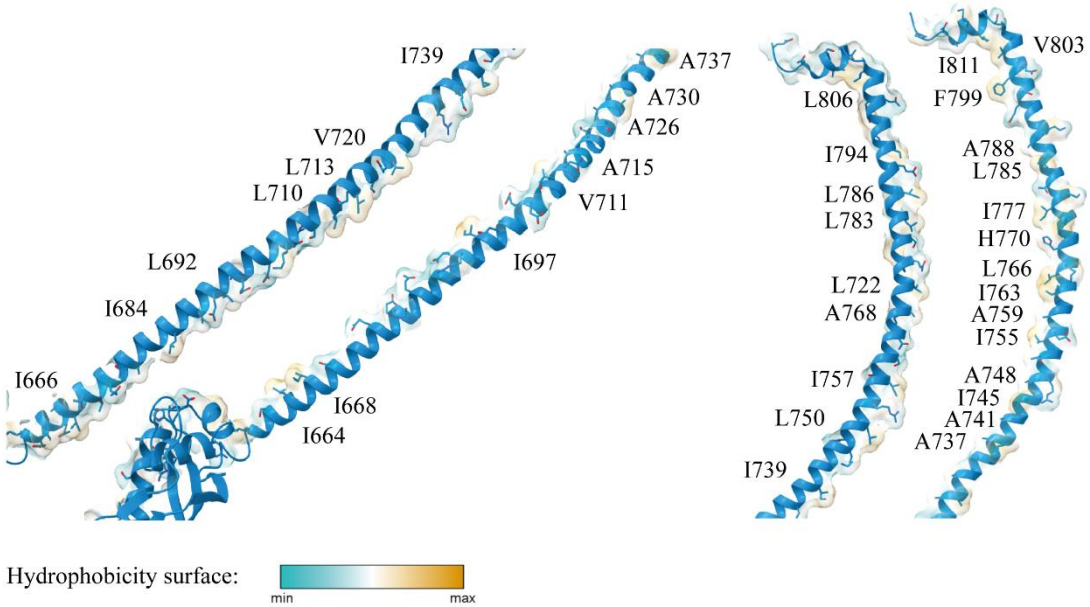

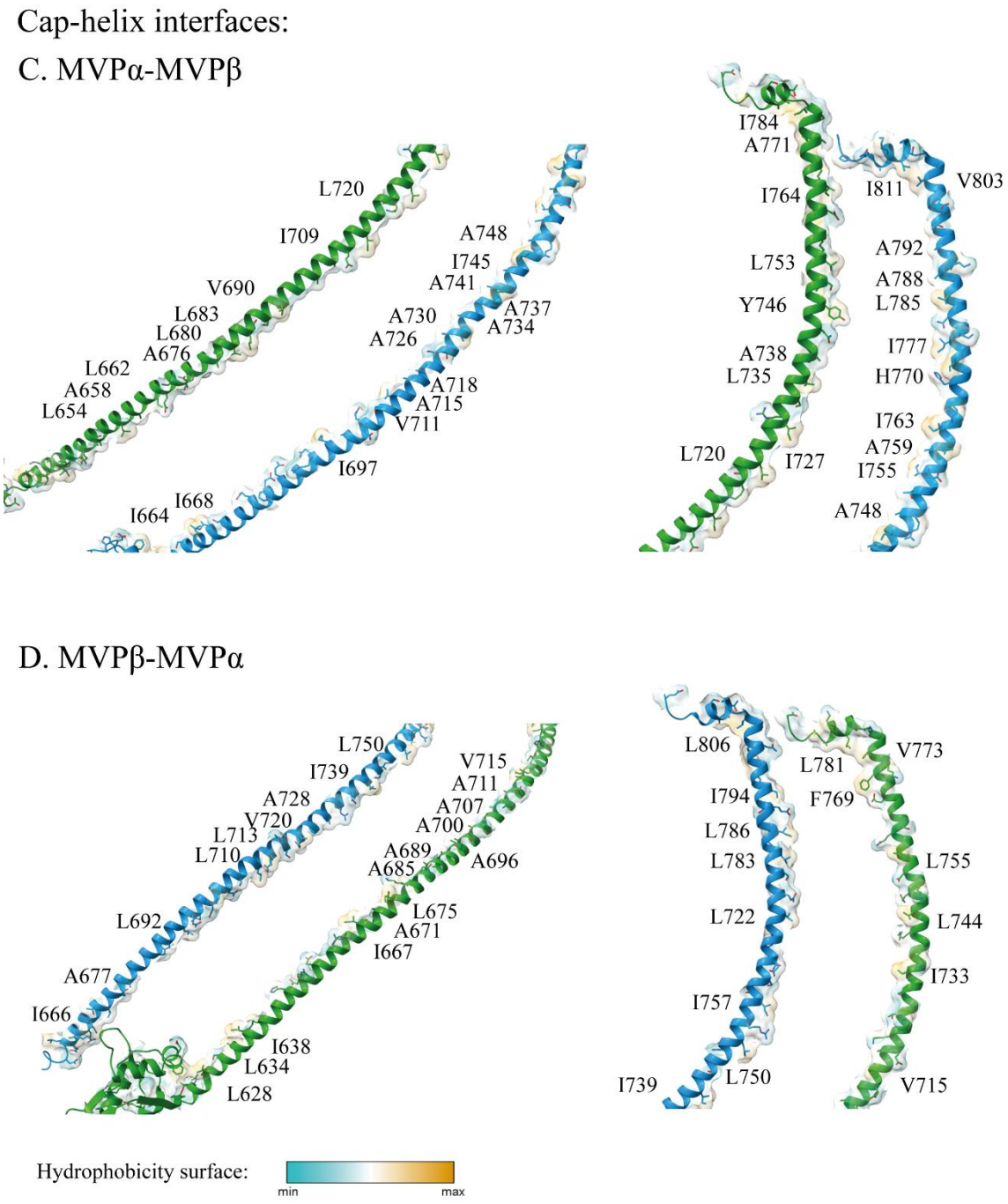

Figure 55. Representation in detail of the interface contacts in the cap helix, where the hydrophobic residues prevail in all combinations. (**A**) MVPα-MVPα contacts. (**B**) MVPβ-MVPβ contacts. (**C**) MVPα-MVPβ contacts. (**D**) MVPβ-MVPα contacts.

Figure 56 shows a representation of the main R1-R9 domain contacts in detail between all possible combinations in the model: MVPα-MVPα (Figure 56A), MVPβ-MVPβ (Figure 56B), MVPα-MVPβ (Figure 56C) and MVPβ-MVPα (Figure 56D). The colored squares explain the main interactions altered or maintained in the different interfaces. The yellow squares, show the hydrophobic contacts involving the R1-R2 domains in MVPα-MVPα. These contacts are maintained in all the MVP combinations (MVPβ-MVPβ, MVPα-MVPβ and MVPβ-MVPα), despite the few substitutions in the amino acid sequence (yellow squares in Figure 56A-D, sequence alignment in Figure 3 Annex). The red panels show the interactions involving the R3-R4-R5 domains that combine both hydrophobic and polar contacts in MVPα-MVPα, MVPα-MVPβ and MVPβ-MVPα interfaces (red squares in Figure 56A-C-D), while the MVPβ-MVPβ interface is mainly polar (red squares in Figure 56B). The brown squares show a double salt bridge, involving R7 residues αE329, αK391 and βK379 in MVPβ-MVPβ and MVPα-MVPβ. As βK379 is not present in MVPα. The MVPα-MVPα and MVPβ-MVPα interfaces are formed by only a salt bridge (brown squares in Figures 56A-D). The blue panel shows the main interactions involving the R8-R9 domains. These contacts are mainly hydrophobic in all interfaces, but the contact surfaces MVPα-MVPβ and MVPβ-MVPα are larger (blue squares in Figures 56A-D).

A. MVPα-MVPα interface interactions:

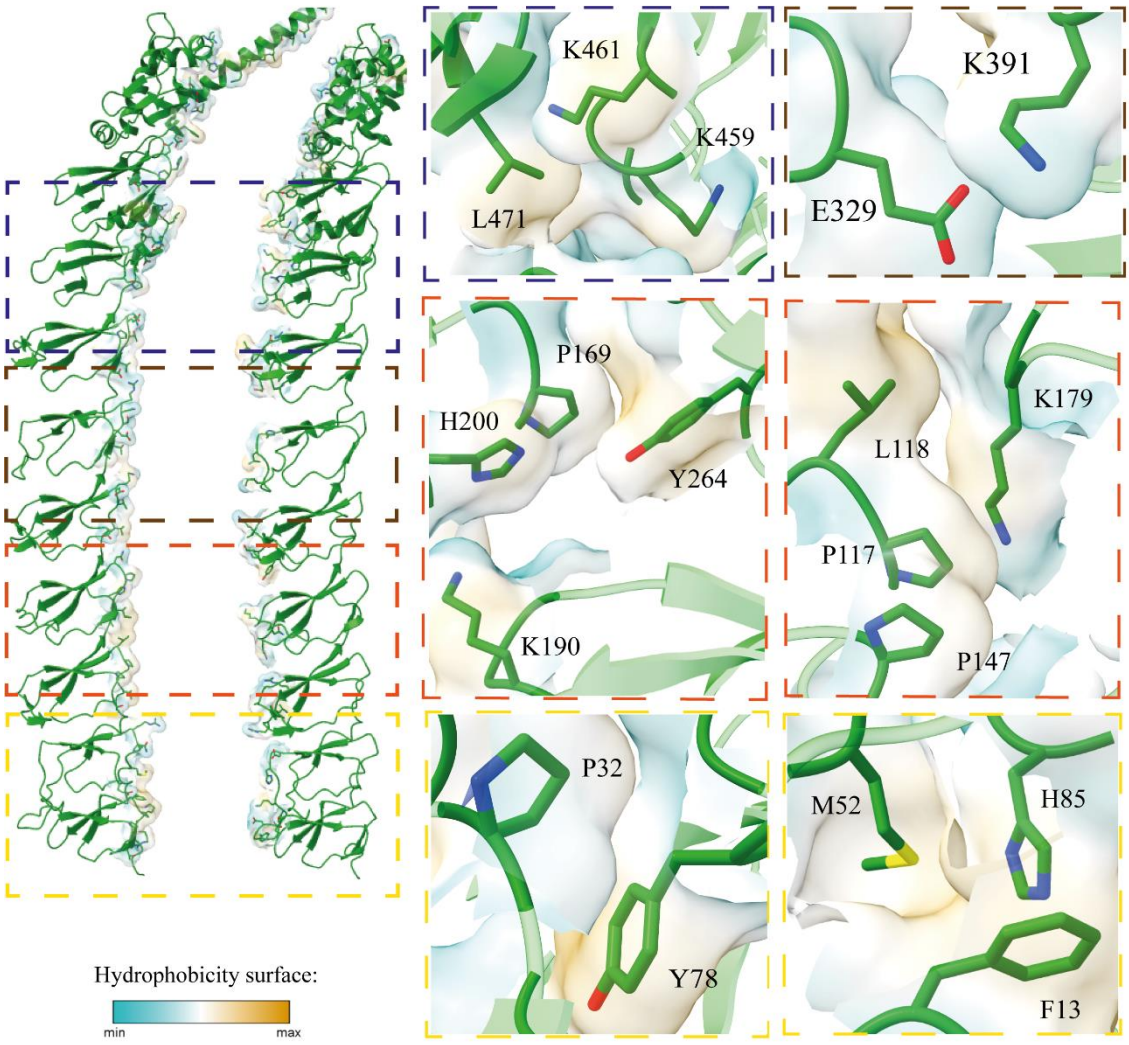

B. MVPβ-MVPβ interface interactions:

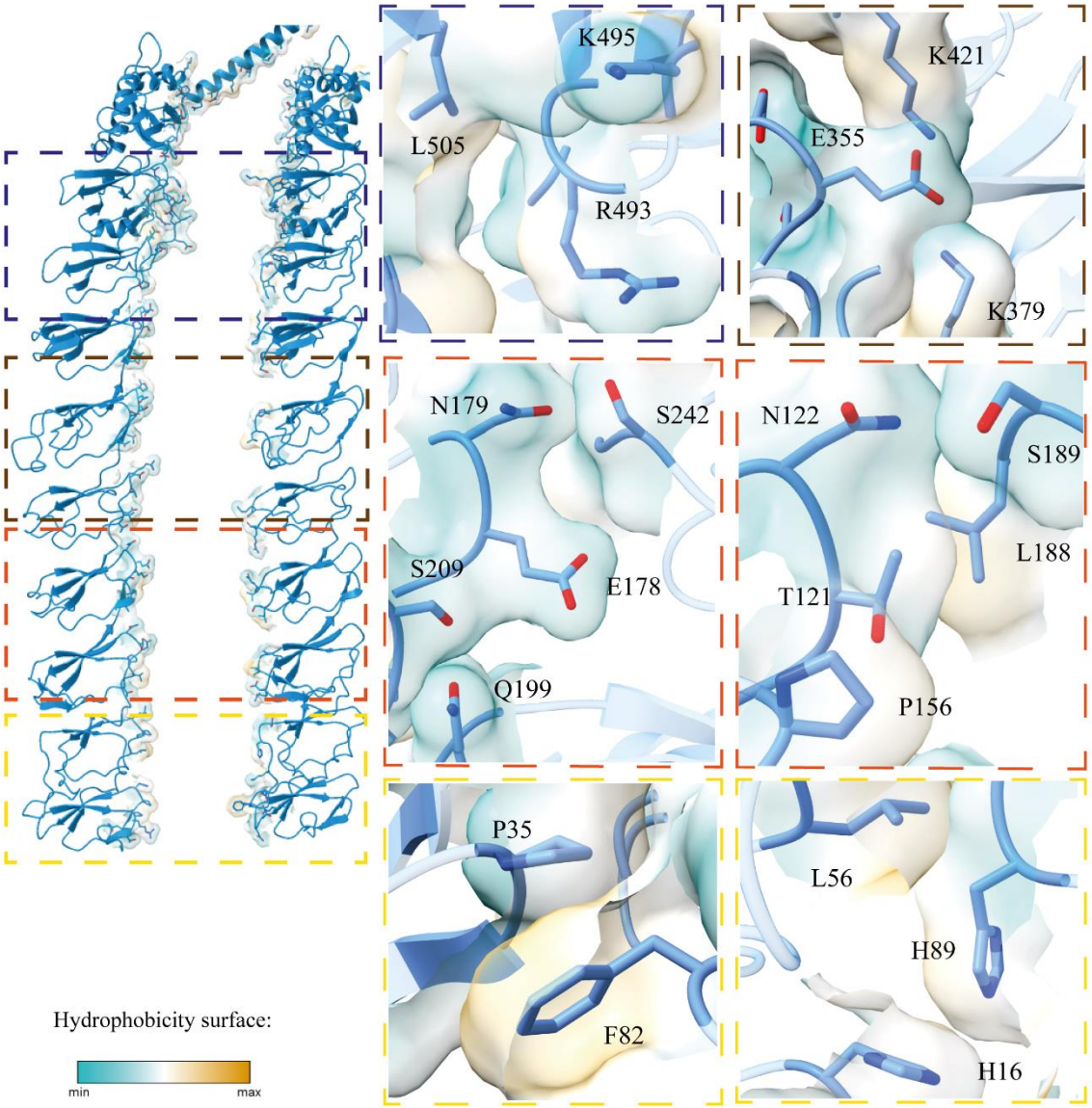

C. MVPα-MVPβ interface interactions:

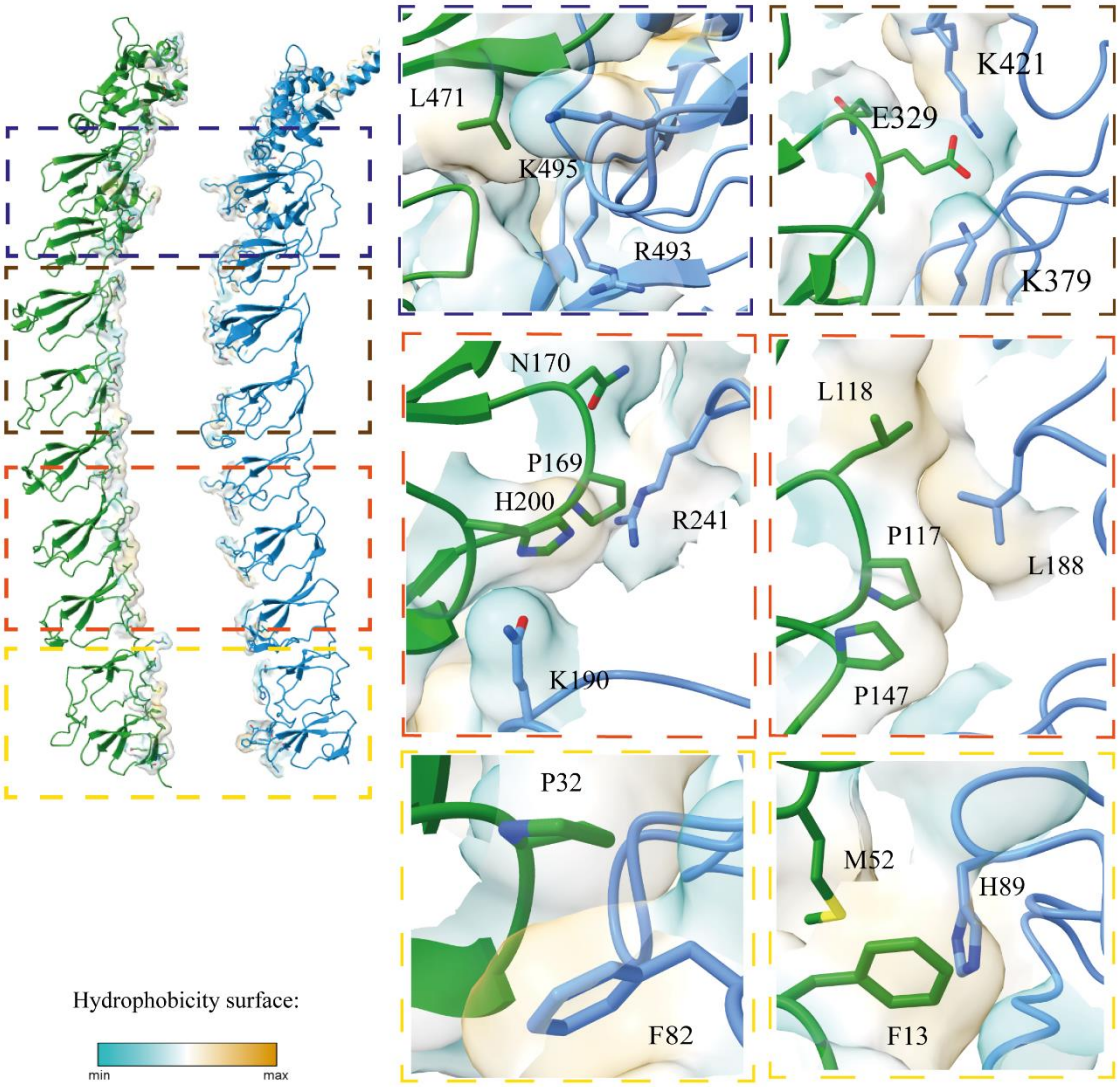

D. MVPβ-MVPα interface interactions:

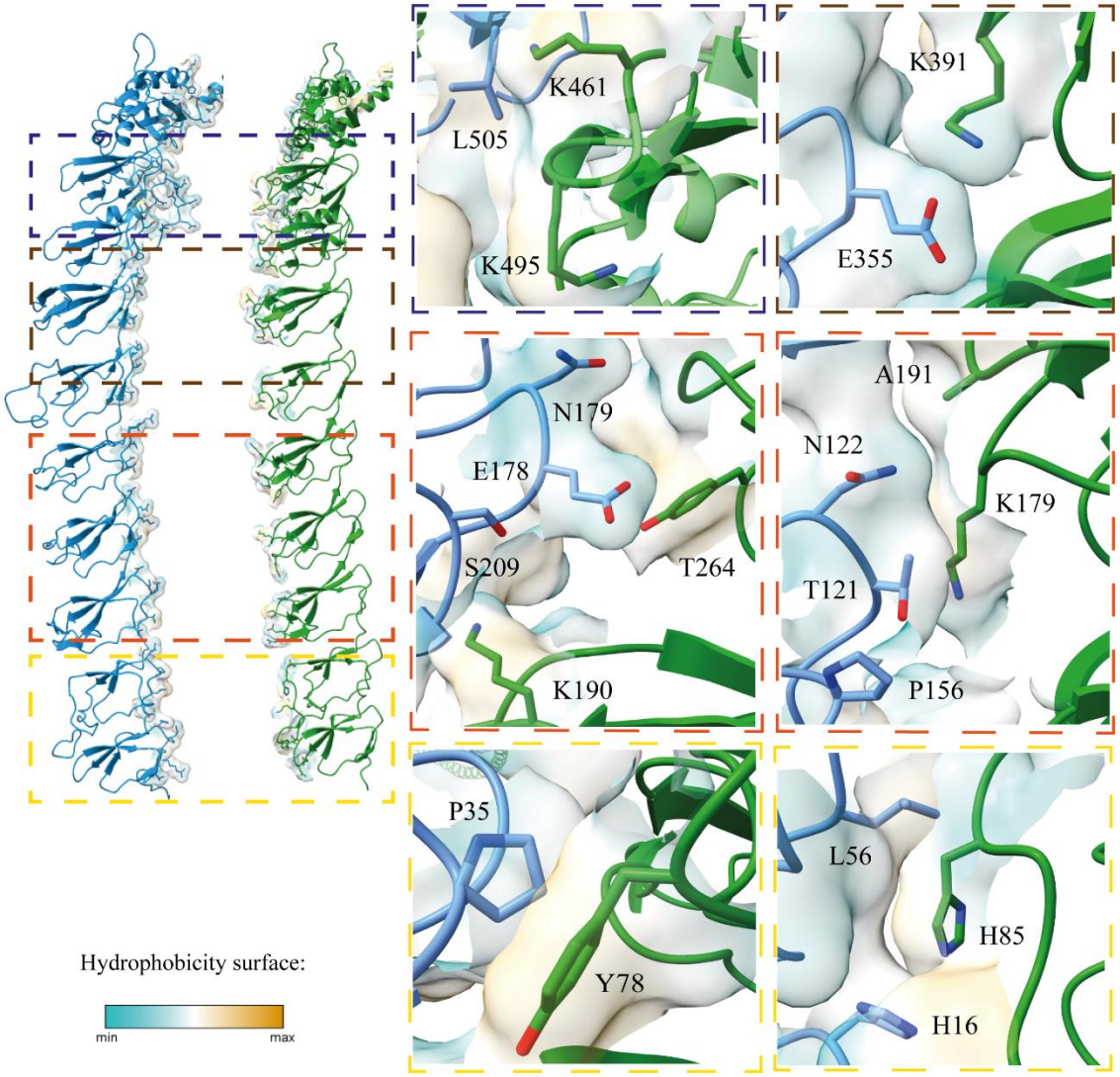

Figure 56. Representation of the hydrophobic and hydrophilic contacts between all possible interfaces. Detail interactions in colored panels. (**A**) MVPα-MVPα interface interactions. (**B**) MVPβ-MVPβ interface interactions. (**C**) MVPα-MVPβ interface interactions. (**D**) MVPβ-MVPα interface interactions.

4.8 MVPα and MVPβ model comparison

We compared the overall domain arrangement of the MVPα and the MVPβ in recombinant *Dictyostelium* vaults with the MVPs of other vault structures previously solved. In particular, with the recombinant rat vault solved by cryo-EM (PDB ID: 7PKR) and with the X-ray structure of natural rat vaults (PDB ID: 4HL8). As mentioned in the introduction, the cryo-EM structure of recombinant rat vaults showed the barrel region a little wider than the crystal structure of native rat vault. Comparisons show that *Dictyostelium* vaults are in between. Pairwise comparison between MVPβ and MVPα shows that MVPβ is a bit more opened than MVPα.

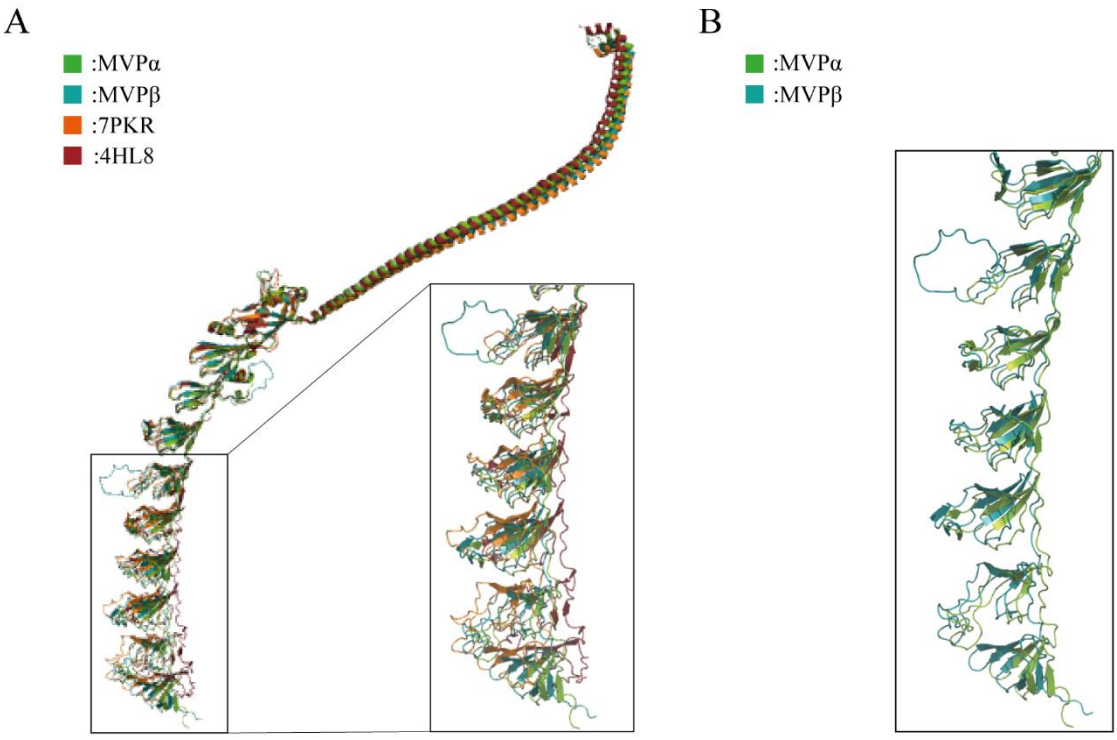

Figure 57. Comparison MVP models. (**A**) Comparison four MVP models: MVPα, MVPβ. 7PKR and 4HL8 (**B**) Comparison MVPα and MVPβ models.

5. Structural characterization of *human* vaults *in situ*

5.1 Towards deciphering the structural details of vault particles in *human* cells by cryo-ET

As mentioned in the introduction section, the intracellular distribution of vaults has been studied in various cell types and organisms. In mammalian cells, vaults predominantly localize to the cytoplasm. However, a small fraction (~ 5%) of them is consistently found associated with the nucleus. In particular, located in the nuclear envelope (NE) and in the nuclear pore complex (NPC) (Chungani et al., 1993), and it was hypothesized that vaults were involved in nucleocytoplasmic transport. In addition, the vaults expression levels often appeared upregulated in multidrug resistant cancer cells (Frascotti et al., 2021), suggesting the involvement of these particles in drug sequestration or transport of drugs away from their cellular targets, such as the nucleus (Van Zon et al., 2006).

With the aim of shedding new light on the role of vault particles in nucleo-cytoplasmatic transport, we decided to start the study of the structure and interactions of vaults in its native environment, inside the cell and in the presence of chemotherapeutic compounds. The study was performed by using *in situ* cryo-electron tomography (cryo-ET) techniques.

5.2 Production and generation of EGFP-vault and EGFP cell line

5.2.1 Cloning

We first established a stable HeLa cell line expressing the human MVP, tagged with EGFP, to be able to follow the vault particles inside the cell. EGFP was cloned in the MVP N-terminus because it was previously described that the N-terminal EGFP-tag did not interfere with the vault function (Van Zon et al. 2003).

The resulting construct EGFP-MVPh was cloned into the lentiviral pINDUCER20 vector (destination vector) by the Gateway Recombination Cloning Technology (see the materials and methods section). Lentiviral pINDUCER20 vector is an inducible Lenti-vector system, which carried both rtTA-advanced and neomycin-resistance genes under the UBC promotor as well as a cDNA of interest under the control of a tetracycline-responsive promoter (Meerbrey et al., 2011).

In the Tet-on system, rtTA-advanced protein binds to the tetracycline-responsive element and stimulates transcription only in the presence of tetracycline or doxycycline (Dox: tetracycline derivate) (Figure 58).

A

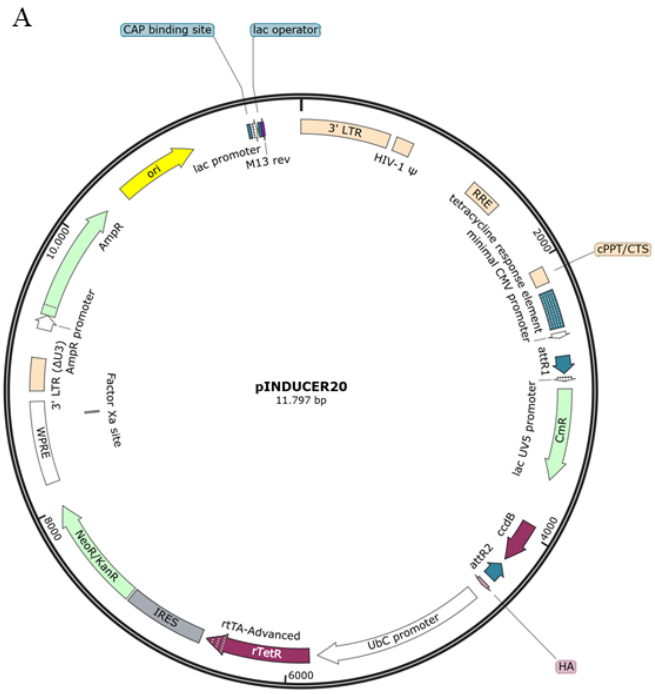

B

Tet on sytem:

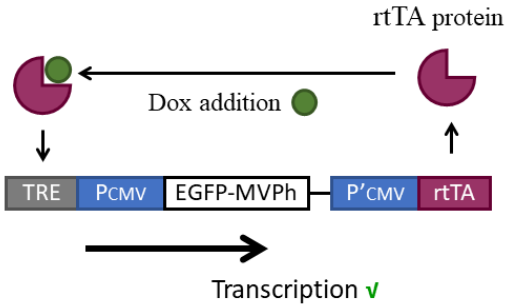

rtTA: is trancribed and translate and binds to TRE but only activates transcription of EGFP-MVPh in presence of Doxycycline.
TRE: tetracyclin response element

Figure 58. (**A**) Destination vector: pINDUCER20 with the different features described. (**B**) Tet-on inducible expression system by doxycycline.

To determine the functionality of our pINDUCER20, HeLa cells were transfected with the vector and cultured with or without doxycycline. As seen in Figure 59, transfected cells, cultured with doxycycline, presented fluorescence due to the expression of the target genes: MVPh-EGFP and the EGFP control (Figure 59), meaning that the vector was functional.

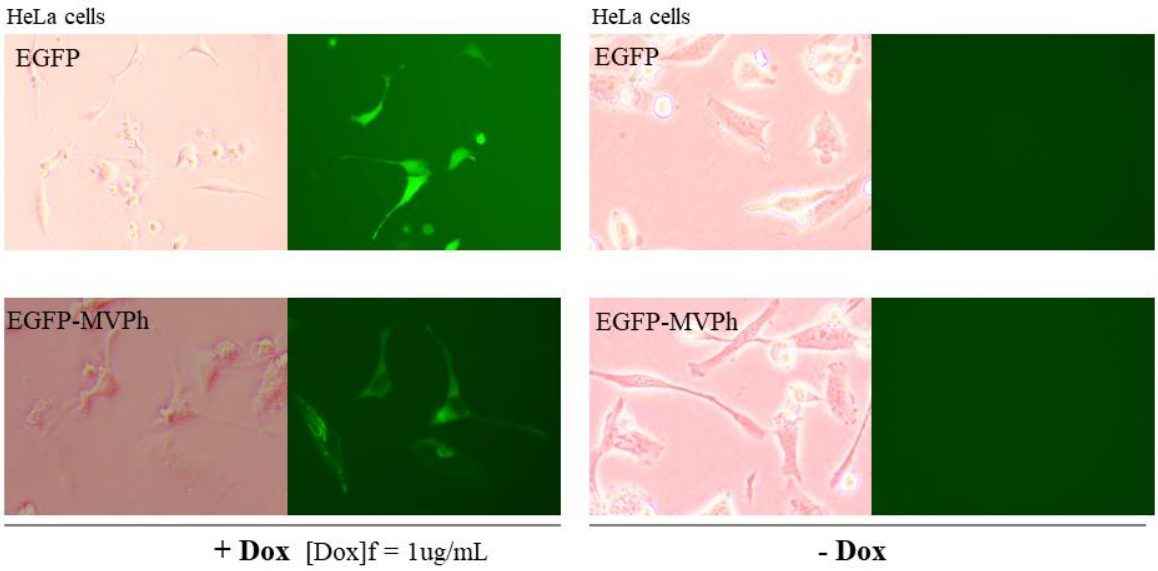

Figure 59. pINDUCER20 vector functionality. HeLa cells transfected with pINDUCER-EGFP or pINDUCER-MVPh-EGFP cultured with or without doxycycline.

Having the functional vector, the next step was the production of the recombinant lentiviruses and the lentivirus infections in HeLa cells to generate the stable cell lines for protein expression. Protocols are described in materials and methods.

After antibiotic cell selection, we produced two stable cell lines with fluorescence induced by doxycycline. The induction lasted 48 h in order to obtain higher number of fluorescence cells (Figure 60A). Cells were lysed and the soluble part was analyzed by Wester-Blot α-GFP. The first cell line expressed the recombinant MVPh-EGFP protein (MVP (100 kDa) fused with EGFP (35 kDa) resulting in a 135 kDa band) and the second one expressed the EGFP protein control, resulting in a 27 kDa band (Figure 60B). Cells were sorted by Fluorescence-Activated Cell Sorting (FACS) in different fluorescence stages.

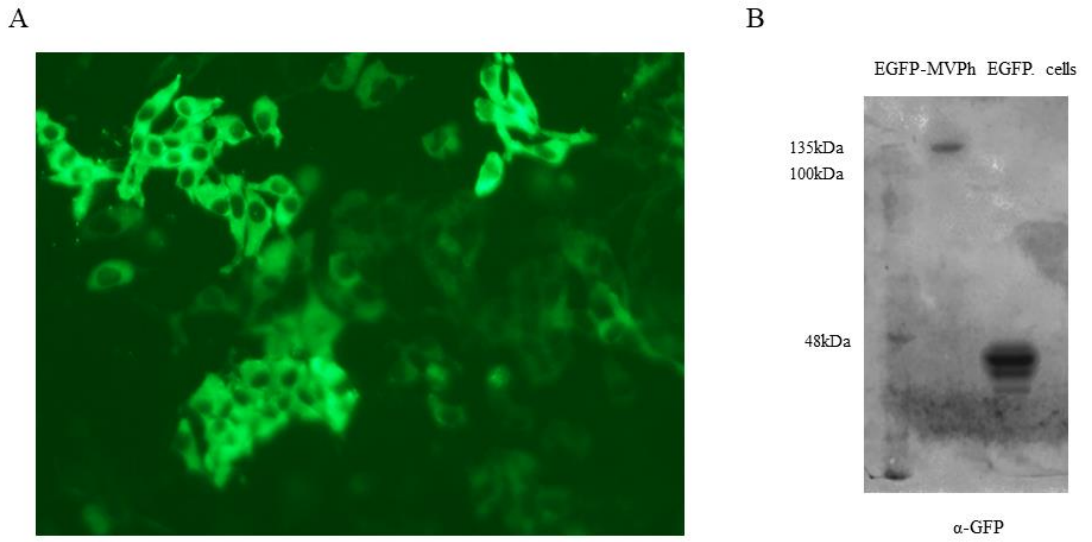

Figure 60. Production of stable cell line, expressing MVP (**A**) Stable line cultures with Dox resulting in fluorescent cells. (**B**) Western-Blot showing the correct protein expression by each cell line.

5.2.2 The new cell line produced functional vaults

As a proof of concept, we reproduced a previously published experiment, that described the changes in MVP localization in cells under stress conditions. Cells suffered an environmental change by transferring them from an incubator at 37 ºC and 5% CO_2 to room temperature on the bench (Van Zon et al., 2003). This change resulted in the formation of aggregosomes, generated by MVP (Figure 61). Because of the morphologies of these formations, these vaults aggregates have previously been described in the literature as "vaultosomes" or "vault tubes". Figure 61 shows that the vaults expressed by the new cell line present the same behavior against stress as that previously described (Van Zon et al., 2003), indicating that our stable cell line was functional and that the formation of "vault tubes" and "vaultosomes" occurred (Figure 61 B1-B2). We also discovered that this process was reversible, cells recovered their typical vault distribution after returning the plates to the incubator (Figure 61C).

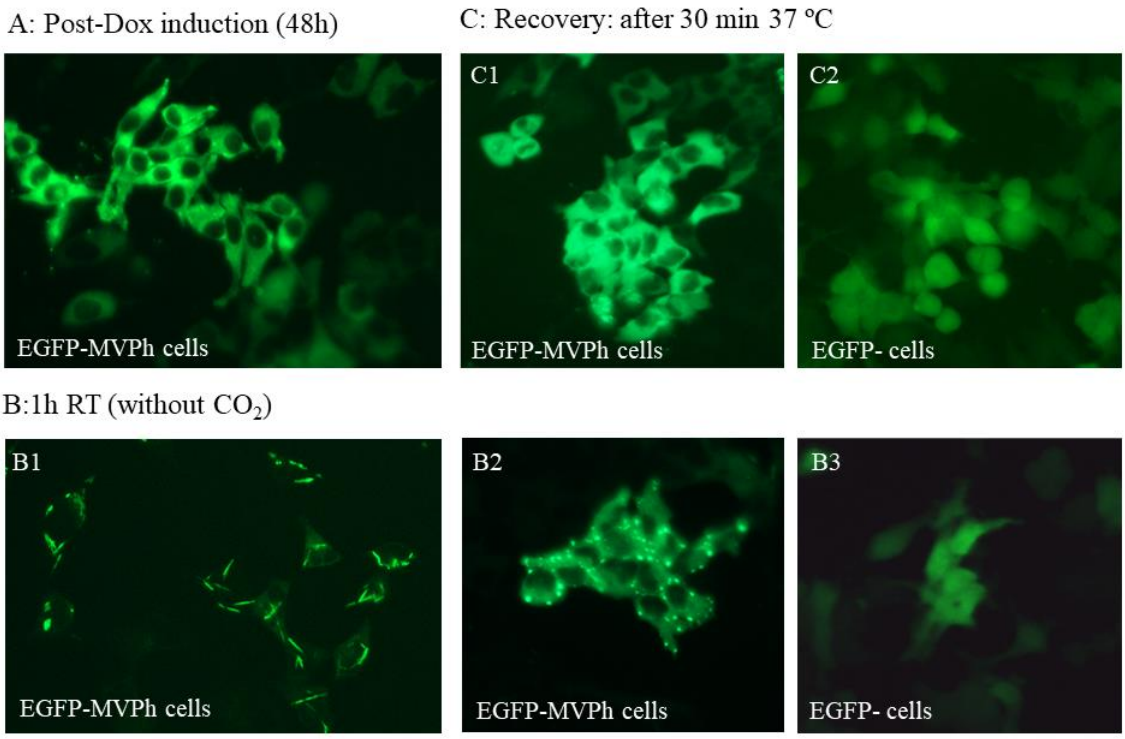

Figure 61. Cell line biologically functional. (**A**) Cell line after Dox post-induction (**B**) Results after 1 h at RT (**B1**) formation of vault-tubes (**B2**) formation of vaultosomes (**B3**) EGFP control cell line (**C**) Cells recovery: after 30 min in the incubator (**C1**) EGFP-MVPh cells (**C2**) EGFP control cell line.

5.3 The effect of different drugs in vault intracellular location, visualized by light microscopy

Confocal microscopy experiments were performed by immune-labeling to localize the vaults around the nucleus. As a proof of concept, we reproduced a previous published experiment, describing an accumulation of vault particles at the cytoplasmic side of the nuclear membrane when cells were treated with cycloheximide (CHX) (Van Zon et al., 2006). Cycloheximide is an inhibitor of translation elongation in eukaryotic cells that plays an essential role in studies of protein synthesis. Under these conditions, the functional pore size of the NPC (~250Å) increases by approximately 60Å (Feldherr, Akin, and Cohen 2001).

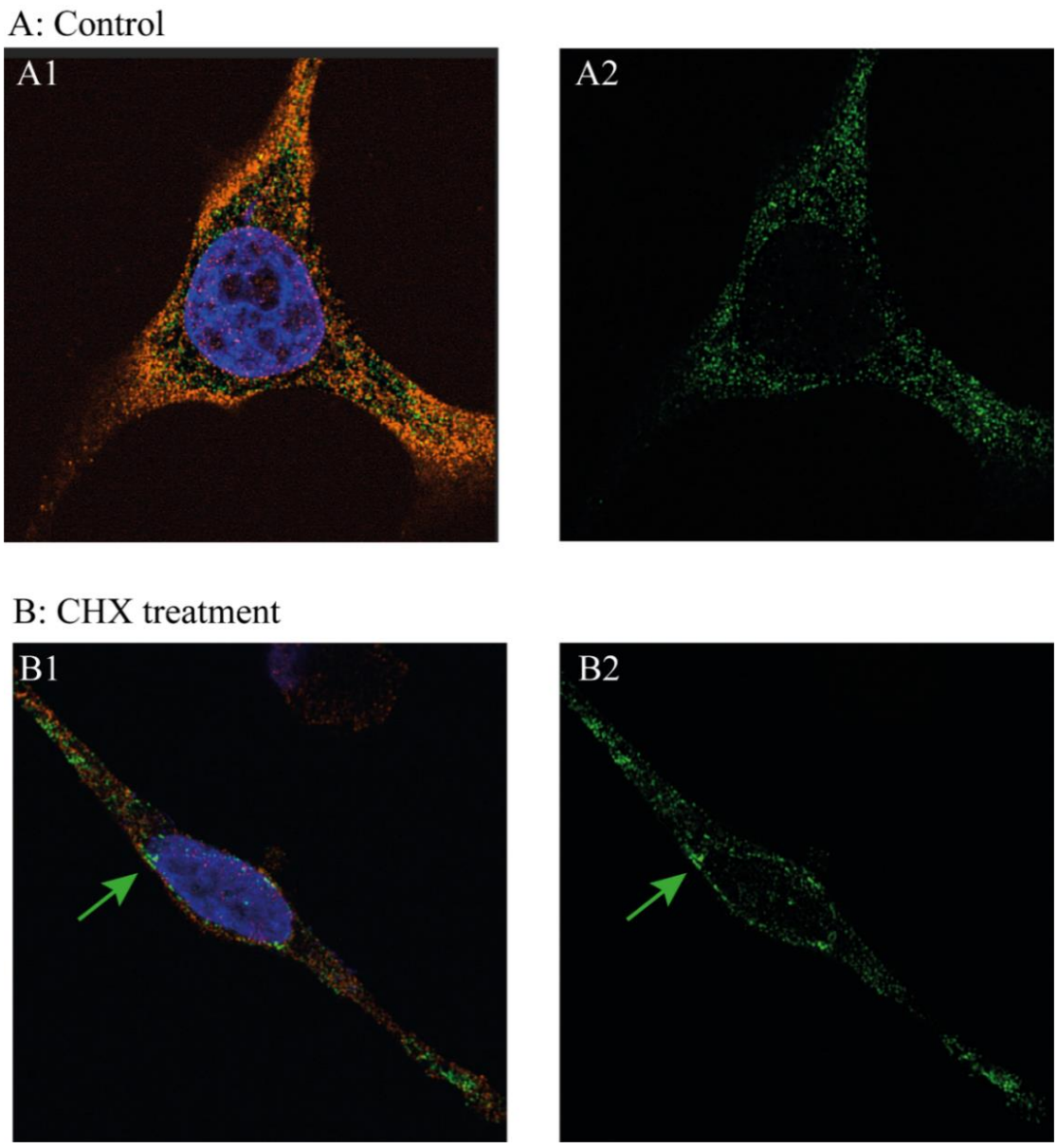

Figure 62. Vault particles localize at the nuclear membrane. Confocal images showing a selected cell with the nucleus depicted in blue: DAPI; the nucleoporin-p62 in red: Ab α-nucleoporin p62, Ab Alexa-568; vaults/MVP in green: MVP-EGFP (**A**) Control: HeLa cells expressing MVP-EGFP without cycloheximide. (**A1**) Merged image (**A2**) MVP-EGFP pattern, where vaults appeared homogenously distributed along the cytoplasm. (**B**) Treatment: HeLa cells expressing MVP-EGFP under 10 µM cycloheximide for 48 h. (**B1**) merged image (**B2**) MVP-EGFP pattern shows a change in the particle distribution, resulting in an accumulation of vaults around the nucleus (indicated by a green arrow).

Cells expressing MVP-EGFP were treated with 10 µM of cycloheximide for 48 h and immuno-stained with an antibody that recognizes nucleoporin p62, a member of the NPC (610497). The comparison between control and treated cells showed a different pattern distribution of vault particles. In the case of the control cells, vaults appeared homogenously distributed along the cytoplasm, otherwise, in the treated cells particles were more concentrated around the nuclear region (Figure 62B- green arrows).

Due to the low specificity of the p62 antibody, we decided to use another antibody against the NPC, the nucleoporin 107 antibody (ab3488). Nucleoporin 107 is localized to the nuclear rim and is an essential component of the NPC. We carried out several immuno-labelling experiments with the new antibody, tuning the antibody concentrations, mounting medium… but in all the cases, the antibody appeared non-specifically located around the cell. This fact made impossible the study of the colocalization of the vault with the NPC.

Due to this issue, we were forced to change the approach to study the formation of this complex. Lamin A (LA) is an intermediate filament protein that forms a network lining the inner nuclear membrane (Goldberg et al. 2008). The interesting thing is that the unique holes, located in the lamin A network, are occupied by the NPC (Figure 63). The antibody against this filament protein is specific to nuclear envelope, avoiding signals in the rest of the cytoplasm (Figure 65 B1).

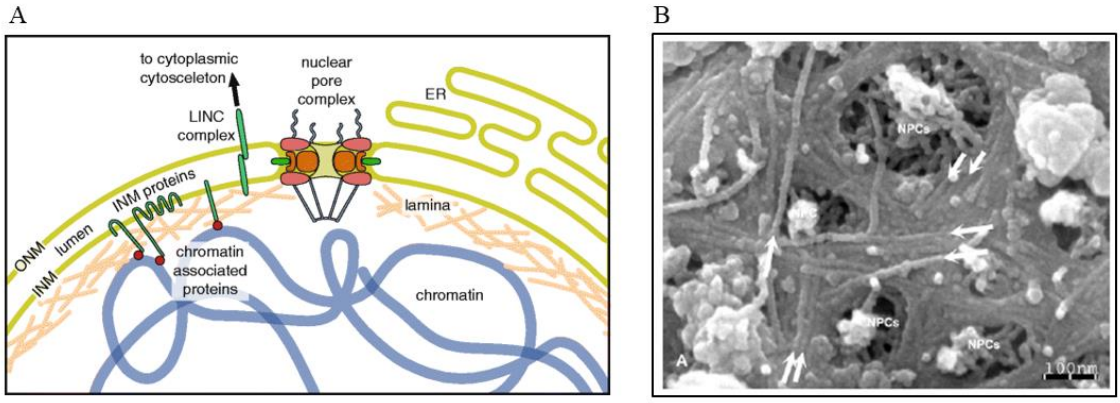

Figure 63. Lamin A and the NPC. (**A**) Picture to localized the nuclear pore complex in lamine A holes (Schooley et al., 2012). (**B**) NPC position in the lamin A holes (Goldberg et al. 2008).

Knowing the effect of some drugs, forcing the location of vaults in the nuclear envelope, we decided to study the effect of rapamycin in vault cellular distribution. Rapamycin (Rapa) is a drug used in cancer treatment, acting as inhibitor of mTOR (Lamming, 2016). The mTOR signalling pathway is a master regulator of cell growth and metabolism. The addition of rapamycin to cells produces the same effect that cycloheximide, but enhanced the population of vaults around the nuclear envelope. As shown in Figure 65, the pores, located between the lamin A signal are occupied by vault signal. These experiments were repeated several times giving the same results summarized in this graphic.

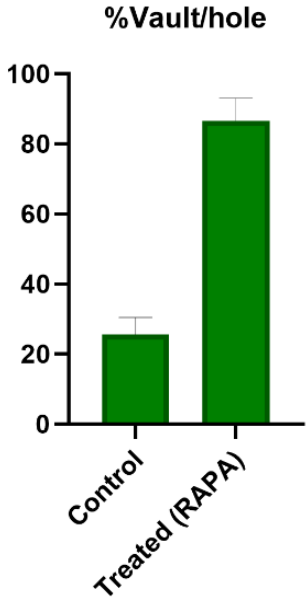

Figure 64. Percentage of vault signal per hole in control vs treated cells.

At this point, we found good conditions to localize a high number of vaults in contact with the nuclear pore complex at the LA-level and we were in a position to start new structural studies at higher resolution. Cryo-ET allowed us to obtain high-resolution data from the NPC-vault complex to learn about their native organization and function.

A: Rapa treatment

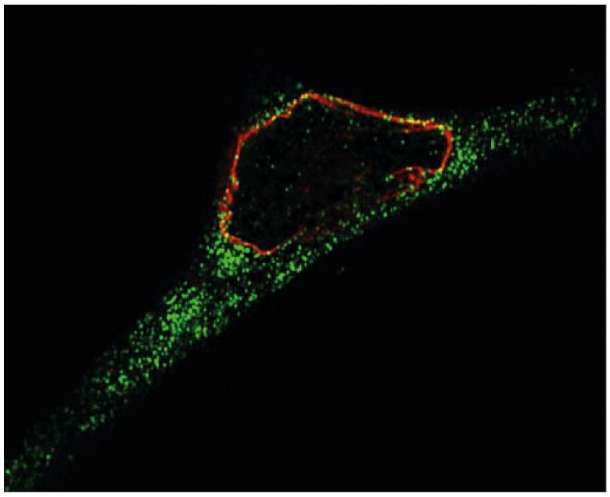

C: Control

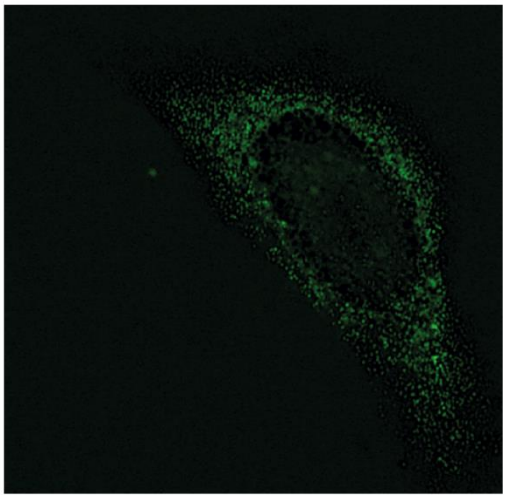

B: Rapa treatment pores zone

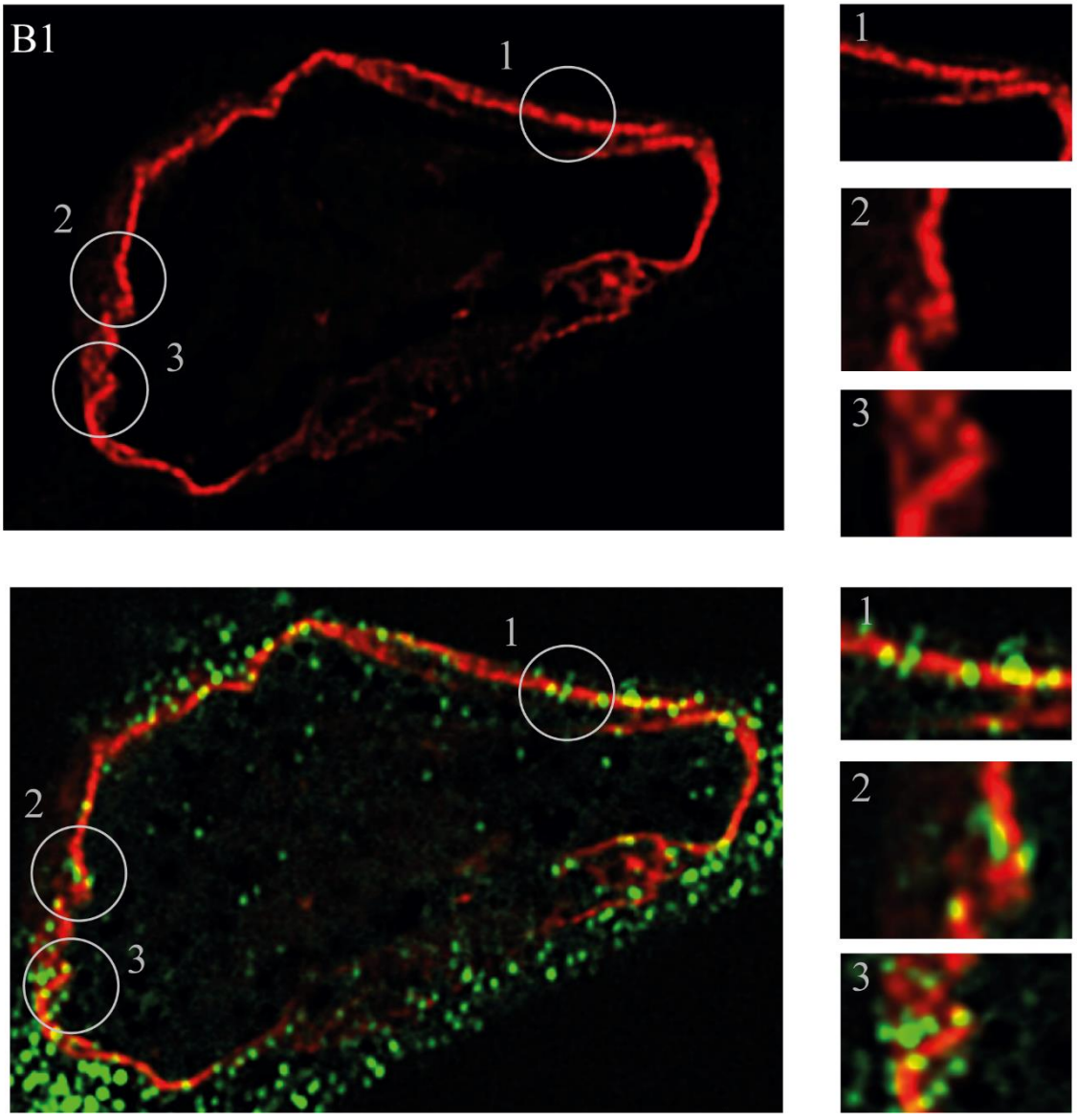

Figure 65. Vault particles localized at the pores of the lamin A, suggesting a vault-NPC connection. Lamin A in red: Ab α-lamin A, Ab Alexa-568; MVP/vaults in green: MVP-EGFP (**A**) Treatment: HeLa cells expressing MVP-EGFP under 10 μM rapamycin for 48 h. MVP-EGFP and Lamin A pattern. (**B**) Pores treatment zones: (**B1**) Lamin A pattern (**B2**) MVP-EGFP and Lamin A pattern. (**1,2,3**) circles mark the zoom pores, where there are lamin A pores we found vault signal. (**C**) Control: HeLa cells expressing MVP-EGFP without rapamycin.

5.4 *In situ* cryo-electron tomography of *human* vaults

As mentioned in the introduction, I had the opportunity to do a stage in the laboratory of Dr. Philipp S. Erdmann at the Human Technopole (Milan, Italy) to learn essential notions about the cryo-ET methodologies and carry out some experiments. The main objective was to characterize the structure and interactions of the vault particle within cells and, if possible, provide new information on the role these particles in nucleo-cytoplasmatic transport.

The complete cryo-ET workflow was carried out at the Human Technopole as described in materials and methods.

5.4.1 Cell Culture, Sample Preparation and Vitrification

Cells were grown in different type of grids, until we get the best results with the UltraAu R2/2 ones. Once, the stable cell line was induced and treated, the fluorescence was checked before vitrification with an EVOS™ FL Auto 2 Imaging System (Figure 66). After vitrification, grids were mounted and clipped in AutoGrids with cut-out for FIB milling (described in materials and methods).

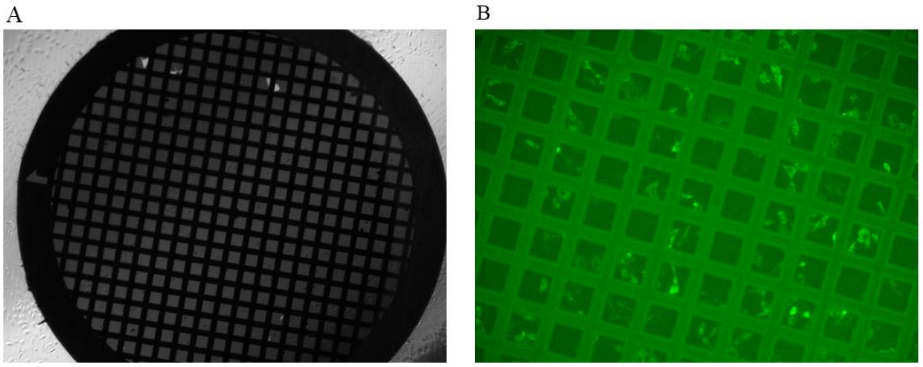

Figure 66. (**A**) Grid overview without fluorescence. (**B**) Fluorescent cells in the grid.

5.4.2 Cryo-Fluorescence Light Microscopy

For each grid, we acquired and overview in fluorescence (GFP) and reflected mode in order to choose the areas of interest containing positive cells. The grid should contain few cells and the cells should be localized in the middle of the grid's squares. Figure 67 shown eight selected squares where the cells were in a properly position.

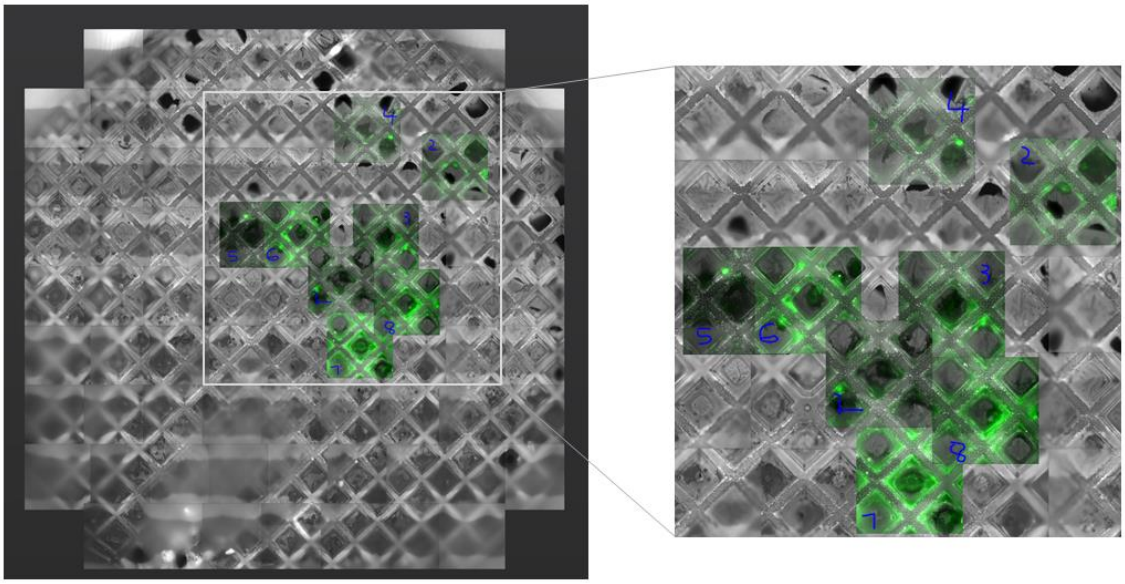

Figure 67. Selected squares in a grid with some cell located in the middle of the square.

5.4.3 FIB-Milling

Lamellas were prepared on a dual beam focused ion beam microscope (Thermo Scientific Aquilos 2). Figure 68 represent results obtained with the dual beam focused ion beam microscope: grid overview with one cell in the middle of the square (Figure 68A), a finished lamella at 150nm (Figure 68B) and several lamellas in one grid (Figure 68C).

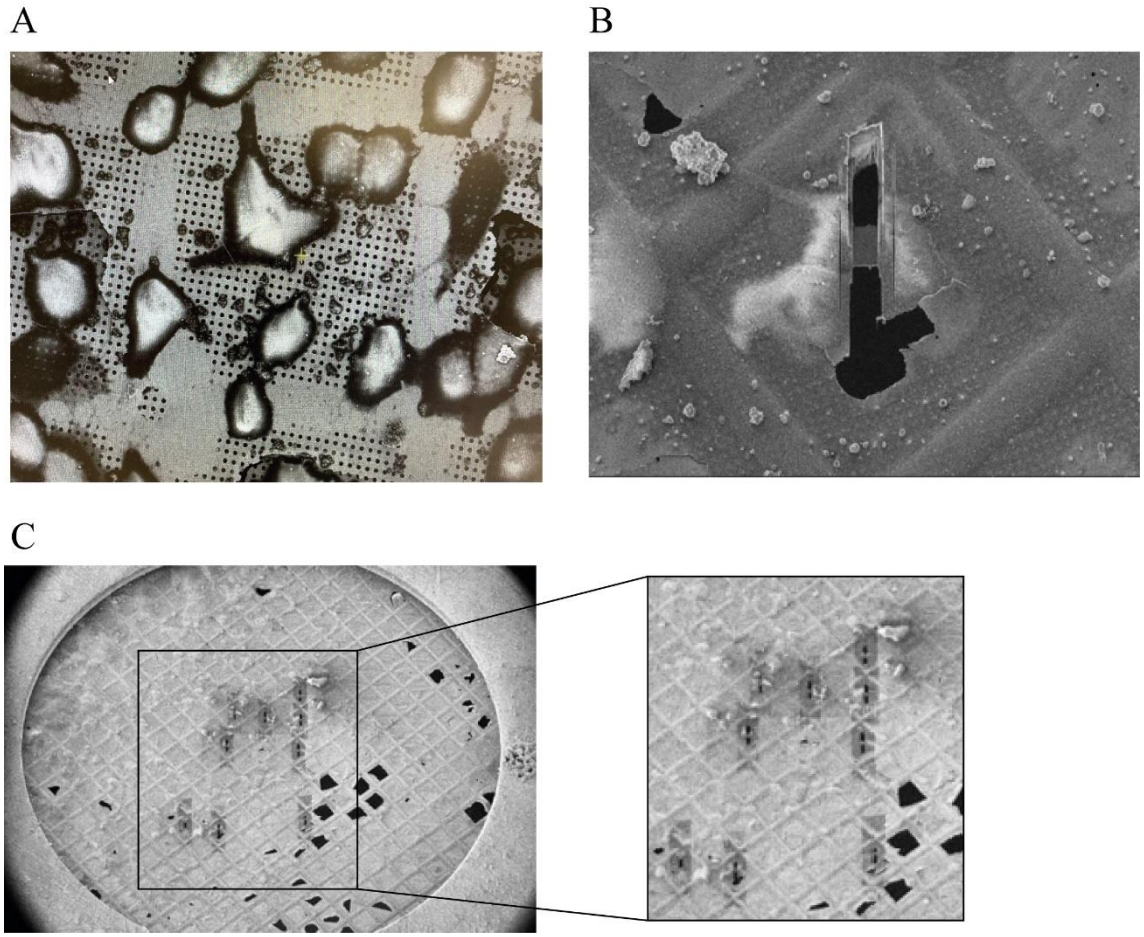

Figure 68. Screening for suitable grids and lamella milling. (**A**) After plunge freezing, grids are inspected in the SEM: 1 cell/square with some fluorescence beads and good ice gradient. (**B**) Lamella milled with a thickness of 150 nm. (**C**) Grid representation with 9 lamellas.

5.4.4 Cryo-Electron Tomography and data processing

Cryo-tomograms were acquired on a transmission electron microscope (Titan Krios G4i 300kV TEM). In total, we collected 30 tomograms at a magnification of 64kx (calibrated pixel size 1.96 Å) and 20 tomograms at a magnification of 42kx (calibrated pixel size 3.057Å) from the control cells and 10 tomograms a 42kx magnification (calibrated pixel size 3.057Å) and 20 tomograms at a 64kx magnification of the treated cells.

Tomogram reconstruction and processing was handled by the wrapper scripts in TOMOMAN (Khavnekar et al., 2023). Individual frames were aligned using MotionCor2 (Zheng et al., 2017) and the contrast transfer function (CTF) was estimated using CTFFIND4 (Rohou and Grigorieff, 2015). Motion-corrected images were aligned and tomogram reconstruction was performed in IMOD (Danita et al., 2022) after automatic

alignment with AreTomo (Zheng et al., 2022). In several tomograms, individual vaults were visible after denoising with cryoCARE (Buchholz et al., 2019) (Figure 69 and 70).

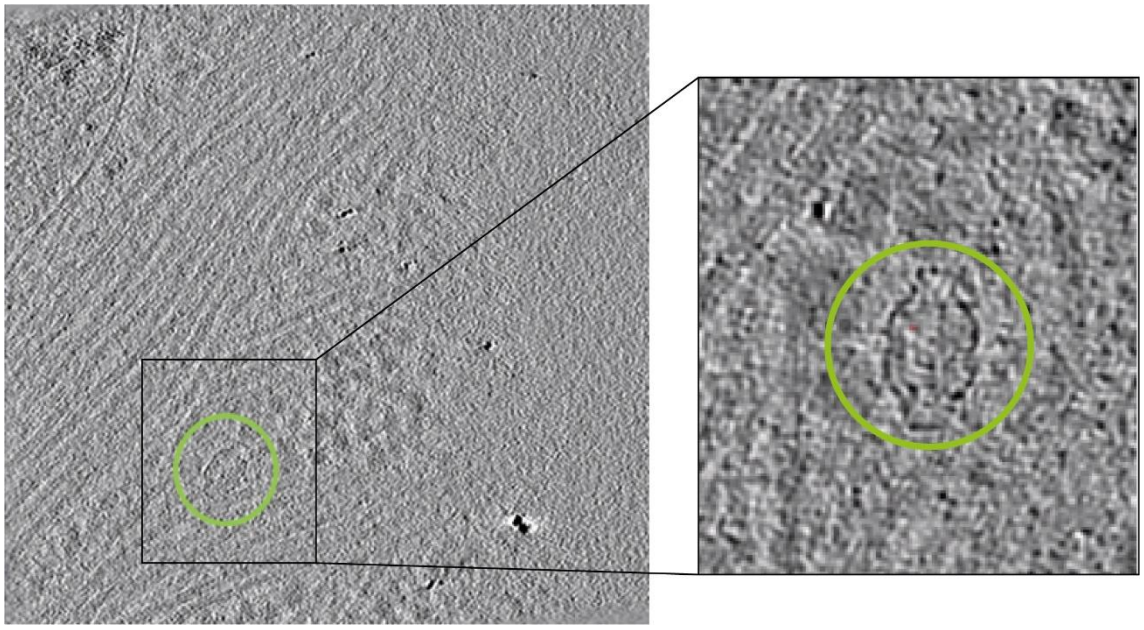

Figure 69. Tomogram reconstruction: representative tomogram with a clearly visible vault structure. Zoom and rotation of the area where the vault protein is located (green circle around the vault particle).

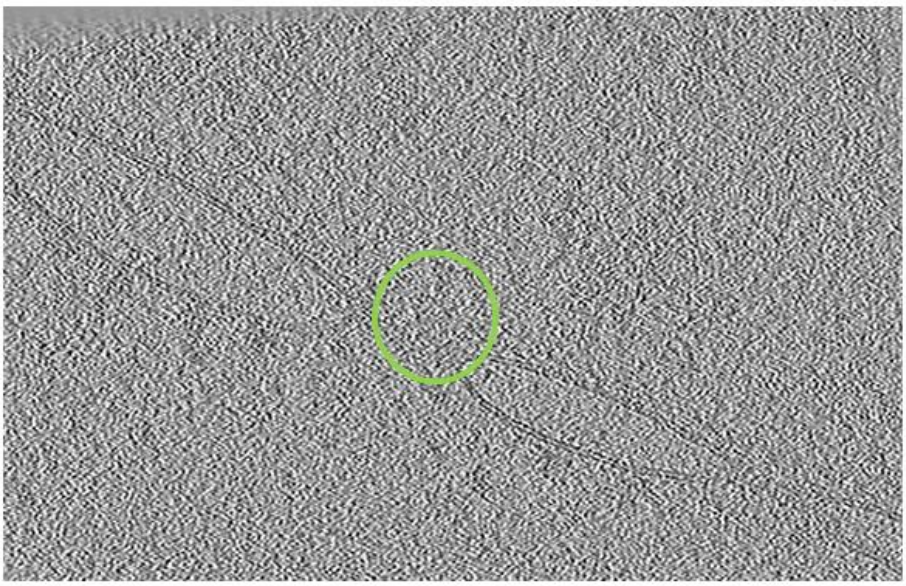

Figure 70. Tomogram reconstruction: representative tomogram with a visible vault structure (green circle around the vault particle).

The issue at the time of writing this thesis is the small number of vaults found in the tomograms. The subsequent steps in data processing to obtain high resolution averages, such as the application of template matching and subtomogram averaging (STA) with RELION or STOPGAP (Wan et al., 2020), are still in progress. In particular, we will have to divide the large amounts of information contained in the tomograms in small subsets, containing the structures of interest, in particular vault proteins and NPCs. Then, the identified positions by template matching will be averaged using STA with RELION or STOPGAP, to obtain high resolution averages. With both structures and positions solved, the relative positioning and orientation of the individual vault structures could provide new information about their role in the nucleocytoplasmic transport.

Despite the fact that we only detected one vault per tomogram, the data confirmed that *human* vaults are similar in general size and shape to purified recombinant vaults from rat and *Dictyostelium*, confirming that vault structure is conserved among species, from an ancient organism to mammalian species, always presenting the barrel like structure with two protruding caps and an invaginated waist such as the ones described previously (Woodward et al., 2015).

Finally, aside from the results obtained in this thesis chapter, the challenge of the project was the experience of being abroad learning an emerging powerful technique such as cryo-electron tomography.

Conclusions

CONCLUSIONS

Structural characterization of endogenous vaults of *Dictyostelium discoideum*

1. Negative staining EM shows that endogenous vaults of *Dictyostelium discoideum* have the same shape and morphology as the mammalian vaults.

2. The ovoid structures present in the vault preparations as contaminants are polysaccharides. It is corroborated using the Molisch test reaction.

Structural characterization of recombinant *Dictyostelium discoideum* vaults

3. Purification of recombinant *Dictyostelium discoideum* vaults is possible when MVPα and MVPβ are co-expressed at the same time.

4. Recombinant *Dictyostelium discoideum* vaults conserve the same structure as the endogenous particles.

5. Recombinant *Dictyostelium discoideum* vaults are stiffer than the endogenous particles, facilitating the high resolution cryo-EM analysis.

6. Data processing, imposing the rotational C3 symmetry, shows a high-resolution (3.85 Å) reconstructed 3D map of recombinant *Dictyostelium discoideum* vaults, allowing to visualize many of the amino acid side chains.

Individual characterization of each MVP isoform: MVPα and MVPβ

7. MVPα and MVPβ behave different when expressed individually. While MVPβ aggregates, MVPα is soluble and remains as a monomer in solution.

8. MVPα is able to assembly in an apparently homogenous macromolecular complex that resembles the vault structure but with a rounded structure.

Structural characterization of mutant recombinant vaults from *Dictyostelium discoideum* in complex with an α-myc nanobody

9. The purification of mutant recombinant vaults from *Dictyostelium discoideum* is only possible when the myc-tag is introduced in the MVPβ subunit.
   The more stable and good shaped vaults are obtained when the myc sequence is flanked by a long link (GSGSG_myc_GSGSG) and cloned by residues substitution from P295 to P298 in the loop of R6β repeat domain.

10. Data processing of mutant *Dictyostelium discoideum* vaults in complex with the α-myc nanobody shows a 3D reconstructed map at 3.7 Å resolution by imposing the rotational C39 symmetry.

11. A 12 Å resolution reconstructed map, obtained with C1 symmetry, allowed discern the localization of the nanobodies bound to the particle and in consequence the approximate distribution of the MVPα and MVPβ subunits.

12. MVP vault shell distribution was formed by MVPα clusters followed by MVPβ clusters. This distribution appears to be that in one half vault there are more MVPα than MVPβ (around two thirds of MVPα), while the opposite in the other half vault (two thirds of MVPβ).

13. MVPα-MVPα interaction interfaces and MVPβ-MVPβ interaction interfaces share the same hydrophobic pattern at the cap-helix, however, the interaction patterns in the R1-R9 repeats domains are different.

Structural characterization of *human* vaults *in situ*

14. The MVP-EGFP HeLa cell line produces functional vaults.

15. When cells expressing MVP-EGFP are treated with cycloheximide and rapamycin, the vaults signal is enhanced around the nuclear membrane.

16. *Human* vaults visualized in cells are similar in size and shape to the purified vaults from *Dictyostelium discoideum*. Meaning that vault structure is conserved among species.

Materials & Methods

MATERIALS and METHODS

1. Prokaryotic cells:

The cloning was done in *E.coli* DH5α (Raleigh et al., 2002) strain.

The strain *E.coli* DH10Bac (Luckow et al.,1993) was used to generate the recombinant bacmids, used in insect cells transfection. *E.coli* DH10Bac strain contains a baculovirus shuttle vector (bacmid) that can recombine with a donor plasmid, pFastBac (Invitrogen), to create an expression bacmid containing a cloned gene of interest.

2. Biochemical analysis:

2.1. SDS-PAGE

SDS-PAGE electrophoresis is the biochemical technique used to analyse the purity of the sample, to localize the target fractions in the gradients and to estimate the protein concentration (Laemmli, 1970). The sample was mixed with a 5x loading buffer (125 mM Tris-HCl pH 6.8, 50 % v/v glycerol, 7.5 % SDS, 25% β-mercaptoethanol and a spatula tip of blue bromophenol) and heated at 95 ºC for 5 min. Then, the sample was load in 10% acrylamide gels and the electrophoresis took place at 35 mA. The gels were stained with Coomassie staining solution (0.25% w/v Coomassie blue in 10% v/v isopropanol and 10% v/v acetic acid) and after, were immersed in a destaining solution (10% isopropanol v/v and 10% v/v acetic acid).

2.2 Western Blot

Assay performed to detect a specific protein in a sample previously resolved by SDS-PAGE electrophoresis. Proteins were transferred from the gel to a nitrocellulose membrane using a 50 V current that makes them flow from the negative to the positive side of a multi-layered cassette. To set up the electrical reaction, a sponge, filter paper, gel, nitrocellulose membrane, filter paper and another sponge were placed into a cassette, following this order from negative to positive side. Then the cassette was covered with Transfer buffer (25 mM Tris-HCl, 192 mM glycine, 0.05% SDS and 10% methanol). The transference was done at 50 V ON. Next day, the nitrocellulose membrane was blocked 2 h with 5% milk in PBS-Tween20 1%. Then, it was incubated for 2 h with the first antibody, washed and incubated 1 h with the second antibody that it is an HRP-conjugated secondary antibody that contains the horseradish peroxidase. Proteins were detected when

the enzyme substrate (from ECL kit; BIO-RAD) was added and a chemiluminescent was formed and the light signal was captured with a digital imaging system (Odissey XF; LI-COR).

3. Oligos, plasmids and sequence analysis:

SnapGene Viewer software was used for the design of the oligonucleotides for PCR reactions and for the analysis of the constructs. Clustal Ω software (Sievers and Higgins, 2018) for sequence alignment. All the plasmids used and oligos designed during this thesis are listed in these tables (Table 3: plasmids, Table 4-7: oligos per project).

PLASMIDS		
Name	**Resistance**	**Features**
pFastBac HT a	Amp	Invitrogen
pGEM-T	Amp	Commercial and contains MVPhuman
pDONR221	Kan	Gateway system
pINDUCER20	Amp/Kan	Gateway system-Lentiviral vector
pEGFP-C1	Kan	MCS at the C-terminal of EGFP
pVSV-G	Amp	Lentivirus envelop plasmid
pPAX-8	Amp	Lentivirus packaging plasmid

Table 3. Table with the plasmids used during the thesis.

Project: Structural characterization of *Dictyostelium* recombinant vaults		
Name:	**Direction:**	**Sequence:**
MVPα construct		
MVPalfa_146_25	Fwd	TTAAACCATTTCATTTCATTCACGTATTAGATAATAATACAAATGTTACTAGAGTTGAAGTTGG
MVPalfa_1_28NcoI	Fwd	ATCCCATGGCCGATTTAAACTCTGTTATTAGAATTAAACCATTTCATTTCATTCACG
MVPalfa_XhoI	Rev	ATCCTCGAGTCATTAATTTCTTCTACCAGATTGTTTGGCAGC
mvpa_pm_1	Fwd	AACATGGTGCCTACCTCCCAG
mvpa_pm_2	Fwd	TTGCCAAAGAATCACTCAACCCAG
mvpa_pm_3	Fwd	TCAACGTACTCGTGATTCACTCC
mvpa_pm_4	Fwd	ACTGCTGAAGCTGCTAACATTG
MVPβ construct		
MVPbeta_174_20	Fwd	AACCACATCATTATATTCATGTATTAGATAATAATACAAATGTTACAAGAGTTG
MVPbeta_1_25_25	Fwd	AAGCTTCTACTGTAATTCGTGTTAAACCACATCATTATATTCATGTATTAG
MVPbeta_2_16_NcoI	Fwd	ATCCCATGGCTACACCAGTCCAAGCTTCTACTGTAATTCGTGTTAAACCAC
MVPbeta_26_54_XhoI	Rev	ATCCTCGAGTCATTATTCTTCATCGACTTCTGATCTTTGAGC
mvpb_pm_1	Fwd	ACCGTCGTGATGTAGTTCGTC
mvpb_pm_2	Fwd	GTTCGTTCAGTTCATGGTTCATCC
mvpb_pm_3	Fwd	GCCAGCACCTTTGATAACTTCCAC
mvpb_pm_4	Fwd	GTCGAATCAACTGGTCAAGC

Table 4. Table with the oligos used for MVPα and MVPβ constructs.

Project: recombinant *Dictyostelium* vaults (MVPα mutants)		
Name:	**Direction:**	**Sequence:**
MVPα mutation construct		
R4 insertion		
MVPalfa_S185_myc_pcr_5	Fwd	TCAGAAGAGGATCTGTCAGGTGTTGCAAGAAAAGCTGG
MVPalfa_R184_myc_pcr_3	Rev	GATGAGTTTTTGTTCACGATCGGAACATGCTTTGTTGG
R4 substitution		
MVPalfa_myc_sust_K190_5	Fwd	CAGAAGAGGATCTGAAAGCTGGTGAAGAGTGGTTAGTTCG
MVPalfa_myc_sust_K179_3	Rev	AGATGAGTTTTTGTTCTTTGTTGGCACGTAATTTGAGTGC
R5 substitution		
MVPalfa_myc_sust_R243_5	Fwd	TCAGAAGAGGATCTGAAAGCTGGTGAGGAATGGTTAG
MVPalfa_myc_sust_F234_3	Rev	GATGAGTTTTTGTTCGGTTTTAGTGGCTTTGAGGTG
R6 insertion		
MVPalfa_myc_ins_A290_3	Rev	GATGAGTTTTTGTTCGGCACCAATTGGATCCAAAAC
MVPalfa_myc_ins_N291_5	Fwd	TCAGAAGAGGATCTGAATGGTAAACCACAACTTGGTC
R6 substitution		
MVPalfa_myc_sust_P287_3	Rev	AGATGAGTTTTTGTTCTGGATCCAAAACAACACAGTATTG
MVPalfa_myc_sust_P294_5	Fwd	CAGAAGAGGATCTGCCACAACTTGGTCATAAACAATTAAG

Table 5. Table with the oligos used for the creation of MVPα mutants.

Project: recombinant *Dictyostelium* vaults (MVPβ mutants)		
Name:	**Direction:**	**Sequence:**
MVPβ mutation construct		
R4 insertion		
MVPbeta_R194_myc_pcr_5	Fwd	TCAGAAGAGGATCTGCGTGATGTAGTTCGTCAAGTTGG
MVPbeta_R193_myc_pcr_3	Rev	GATGAGTTTTTGTTCACGGTCAACAAATGAGAGACG
R4 substitution		
MVPbeta_myc_sust_Q199_5	Fwd	CAGAAGAGGATCTGCAAGTTGGTGAAGAATGGTTAGTTCG
MVPbeta_myc_sust_L188_3	Rev	AGATGAGTTTTTGTTCGAGACGAGCACGTAATTTGAGTGC
R5 substitution		
MVPbeta_myc_sust_K252_5	Fwd	CAGAAGAGGATCTGAAAGCTGGTGAAGAATGGATTATCAC
MVPbeta_myc_sust_R241_3	Rev	AGATGAGTTTTTGTTCACGAGTGGCTAATAATTGATAAGCG
R6 insertion		
MVPbeta_myc_ins_D297_3	Rev	GATGAGTTTTTGTTCATCAATTGGATTCTCAACGATACAG
MVPbeta_myc_ins_K299_5	Fwd	TCAGAAGAGGATCTGAAAACCGGTAAAAATAAATTGGGTC
R6 substitution		
MVPbeta_myc_sust_P295_3	Rev	GATGAGTTTTTGTTCTGGATTCTCAACGATACAGTATTG
MVPbeta_myc_sust_P298_5	Fwd	TCAGAAGAGGATCTGCCAAAAACCGGTAAAAATAAATTGG
Link long		
Link_long_R6	Rev	TCCGGATCCACTTCCTGGATTCTCAACGATACAGTATTG
Link_long_R6	Fwd	GGATCCGGAAGTGGACCAAAAACCGGTAAAAATAAATTGG
Link short		
Link_short_R6	Rev	TCCGGATCCTGGATTCTCAACGATACAGTATTG
Link_short_R6	Fwd	GGATCCGGACCAAAAACCGGTAAAAATAAATTGG
Myc-link		
Myc-link	Comp.	TCCGGATCCCAGATCCTCTTCTGAGATGAGTTTTTGTTCTCCGGATCCCAT
Myc-link	Comp.	ATGGGATCCGGAGAACAAAAACTCATCTCAGAAGAGGATCTGGGATCCGGA

Table 6. Table with the oligos used for the creation of MVPβ mutants.

Project: Structural characterization of *human* vaults		
Name:	**Direction:**	**Sequence:**
pGEM-T		
MVPhum_HindIII_5	Forward	ATTAAGCTTCGATGGCAACTGAAGAGTTCATCATCC
MVPhum_SalI_3	Reverse	ATTGTCGACTTAGCGCAGTACAGGCACCAC
Seq. pEGFP-C1 with MVPh		
Sequence CMV promoter		GGGAGGTCTATATAAGCAGAGC
MVPhum_P1		ACCGGATGGCAAGAATCAGC
pEGFP_C1_PM_3		GGACAAACCACAACTAGAATGCAG
MVPhum_atg_3		GGATGATGAACTCTTCAGTTGCCAT
EGFP-MVPh with attB extremos		
MVPhum_attB1_5	Forward	GGGGACAAGTTTGTACAAAAAAGCAGGCTTCACCATGGTGAGCAAGGGCGAGGAGC
MVPhum_attB2_3	Reverse	GGGGACCACTTTGTACAAGAAAGCTGGGTTTTAGCGCAGTACAGGCACCACGTG
Sequence pDONR221 EGFP-MVPh		
attL1_pDONR_5	Forward	TCGCGTTAACGCTAGCATGGATG
attL2_pDONR_3	Reverse	GTAACATCAGAGATTTTGAGACAC

Table 7. Table with the oligos used for the creation of MVPβ mutants.

4. Purification and characterization of endogenous vaults of *Dictyostelium discoideum*

4.1. Cell culture:

Dictyostelium is a free-living unicellular organism, there is no need to control nitrogen or carbon dioxide. *Dictyostelium* Ax2 cell line was grown in HL5 medium (Formedium) supplemented with 0.5% glucose in suspension at 22 °C, 180 rpm. Antibiotics were added to the medium to create an axenic culture, meaning free of bacteria, yeast, and fungi: ampicillin (0.1 mg/ml) and streptomycin (0.25 mg/ml). Normally, 4 litters of culture were prepared (8 Erlenmeyer of 0.5 litters each). Purification started when the desired density, $1x10^7$ cells/ml, was obtained.

4.2. Purification of endogenous *Dictyostelium* vaults:

The purification protocol was carried out in accordance with the one previously used in the laboratory by Dr. P.Guerra (Guerra et al., 2022) to purify the recombinant vaults in insect cells, with a few modifications. At first instance, the cellular culture was pelleted with a 20 min centrifugation at 1000 rpm (9.1000 Beckman rotor). The pellet was resuspended in 35 ml of buffer A [50 mM Tris (pH 7.5), 75 mM NaCl, 0.75 mM $MgCl_2$] with RNase A, DNase I, plus 0.1% Triton X-100 and protease inhibitors (protease inhibitor cocktail tables; Roche, Basel, Switzerland) maintained on ice for 30 min and vortex each 5 min.

The resuspend pellet was centrifuged during 20 min at 18000 rpm (25.50 Beckman rotor) and cellular debris were removed. The supernatant was applied to six cushions of 4 ml of buffer A with 25% sucrose and centrifuged at 37000 rpm (using SW41Ti Beckman rotor) for 2.5 h. The resulting pellet was resuspended in 900 µl of buffer A and centrifuged for 5 min at 13000 rpm (using a F-45-6-30 rotor). The supernatant was applied to a 25% to 50% sucrose gradient in buffer A and centrifuged for 45 min at 37000 rpm (using SW41Ti rotor). The gradient was fractionated and then analysed by SDS-polyacrylamide gel electrophoresis. Last, fractions enriched in *Dictyostelium* vaults were joined and analysed by negative-stain EM.

In order to avoid the presence of ovoid structures in the sample, an extra step was added. The sample was applied to 3 ml cushion of buffer A with 36% CsCl and centrifuged at 43500 rpm during 2 h (using SW55Ti Beckman rotor). The cushion was illuminated and a white ring was seeing where the protein was present. The target fractions were collected and *Dictyostelium* vaults were concentrated to 5 mg/ml using a centrifugal filter device (Centricon YM-100, Merck Millipore, Billerica, MA) and were analysed again by negative-stain EM.

When we checked the vaults by negative-stain EM after the CsCl, vault morphology suffered because of the high speed. In order to avoid the morphological alterations caused by the CsCl cushion, we decided to replace this step by a size exclusion chromatography (SEC). The SEC was performed in a Superose 6 10/300 GL column (GE, Healthcare) (MW range, 5 to 5000 kDa) connected to a high-performance liquid chromatography system (AKTA Pure), equipped with an autosampler. Sample elution was monitored with a UV detector. Peak fractions were collected and concentrated to 5 mg/ml using a centrifugal filter device (Centricon YM-100, Merck Millipore, Billerica, MA) and analysed by negative-staining EM.

As some ovoid structures still persisted after SEC separation, a new chromatographic step was performed by anion exchange chromatography, in a Mono Q column. If the ovoid structures were polysaccharides with negative charge they could be attached to the cationic resin. The column was equilibrated with buffer A, and the protein was eluted with a linear gradient of buffer B (buffer A with 1M NaCl). Fractions were collected, recovered initial conditions (buffer A) and concentrated to 5 mg/ml using a centrifugal filter device (Centricon YM-100, Merck Millipore, Billerica, MA). Sample quality was checked by negative-stain EM (see below).

4.3. Molisch test

We prepared four tubes with different solutions. The negative control with 3 ml of buffer A [50 mM Tris (pH 7.5), 75 mM NaCl, 0.75 mM $MgCl_2$], the positive control with a 0.5% sucrose solution, 3 ml vault protein in buffer A solution and 200 µl ovoid structures until 3 ml with buffer A. Then, we added 3 drops of Molisch reagent (a 6% solution of ∝-naphthol in ethanol 96%) in each tube. Subsequently, we added 1 ml of concentrated sulphuric acid (H_2SO_4) to the mixture. We observed the formation of a purple product in the sample, indicating the presence of carbohydrates.

5. Production and characterization of recombinant *Dictyostelium discoideum* vaults

5.1. Production of recombinant MVPα and MVPβ:

In order to obtain *Dictyostelium* recombinant vaults was necessary to clone individually each isoform: MVPα and MVPβ. MVPα is 2531 kb long and MVPβ is 2540 kb long, both isoforms have one intron in their genomic DNA (as shown in Figure 71).

Consecutive polymerase chain reactions (PCR) from *Dictyostelium discoideum* genomic DNA were employed as the cloning strategy to remove the intron. In this manner, the result of the first reaction serves as the substrate for the second reaction (Figure 71). For MVPα, two consecutives reactions are needed, for MVPβ three reactions because of its length.

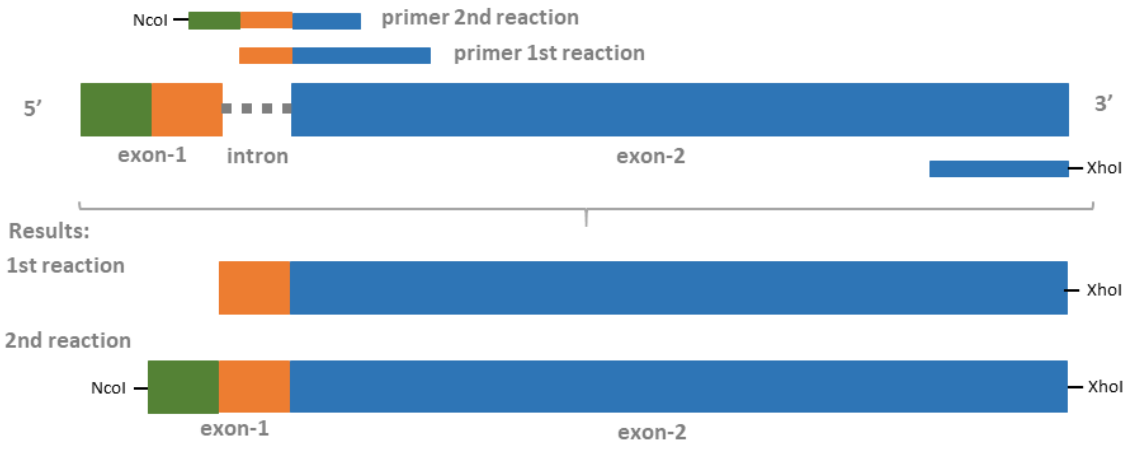

Figure 71. Consecutive PCRs strategy. Gen MVP: exon-1 (green + orange) + intron (grey) + exon-2 (blue). Primers: blue area: hybridization part with exon-2, orange/green areas: nucleotides added in order to amplify exon-1 avoiding the intron.

MVPα and MVPβ fragments, both flanked by Nco I and Xho I, were generated by PCR as explained before. Oligonucleotides described in Table 4. Each fragment was digested with Nco I and Xho I at 37 °C and purified. Each one was inserted into a multiple cloning site of the baculovirus transfer vector pFastBacHta (Invitrogen) by T4 DNA ligase at 16 °C, previously the vector was digested with the same restriction enzymes and purified. The resulting plasmids pFB_MVPα and pFB_MVPβ were subjected to nucleotide sequencing to assess the correctness of the inserted MVP sequence.

5.2. Recombinant baculoviruses production

The resulting plasmids (pFB_MVPα and pFB_MVPβ) were used to produce the corresponding recombinant baculoviruses (rBV) using the Bac-to-Bac system according to the manufacturer's instructions (Invitrogen) (Figure 72). This expression system is based on the transposition of the gen of interest into a bacmid (infective baculovirus genome contain in a vector) which resides in *E.coli* DH10Bac strain (Luckow et al.,1993). Recombinant baculoviruses MVPα and MVPβ were produced.

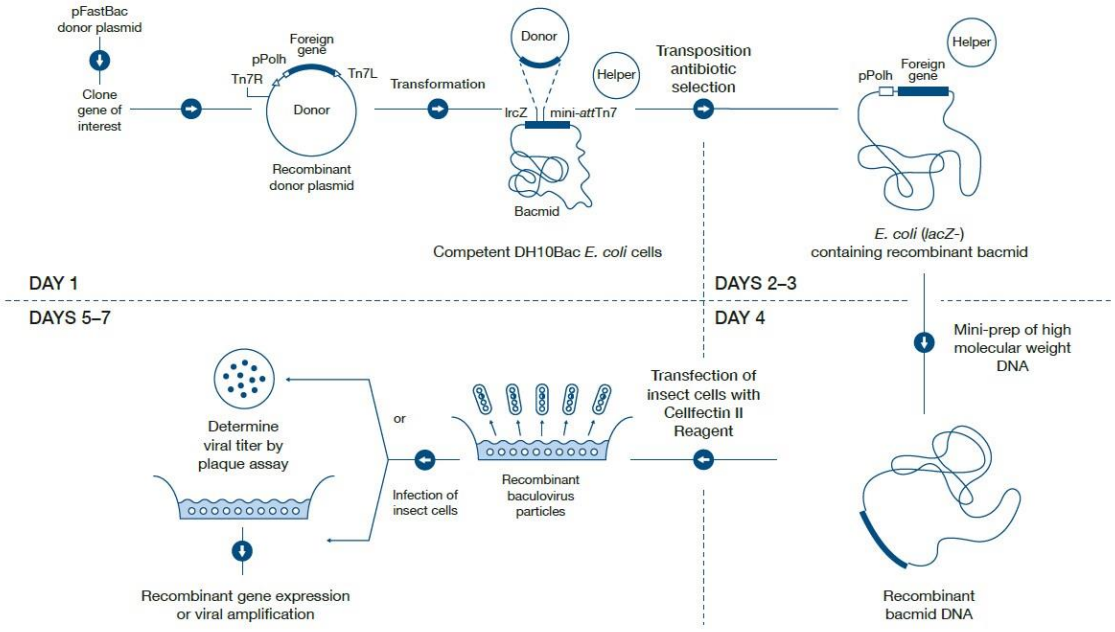

Figure 72. Overview of the Bac-to-Bac Baculovirus protocol.

First, the resulting plasmids (pFB_MVPα and pFB_MVPβ) were transformed in *E.coli* DH10Bac cells. Colonies containing recombinant bacmids were identified by antibiotic selection and blue/white screening, since the transposition results in disruption of the *lacZ*α gene. High molecular weight mini-prep DNA was prepared from selected clones

containing the recombinant bacmid. This DNA was then used to transfect insect H5 cells in order to generate recombinant baculoviruses. The supernant containing the recombinant baculoviruses was collected after 72-96 h and marked as primary recombinant baculovirus. Amplification of baculovirus was performed infecting H5 with the primary recombinant baculovirus obtained before. Supernant was collected after 72-96 h and marked as secondary recombinant baculovirus. The last one is used to large scale infections in order to produce recombinant protein.

5.3. HighFive cells

Fort the generation, amplification and expression of rBV, High Five cells (H5) were used, adapted for the growth in monolayer from the Sf9 strain of *Spodoptera frugiperda* (Vaughn et al., 1977). H5 cultures were grown at 28 ºC in TC-100 medium (ITW Reagents) supplemented with 5% of fetal bovine serum (FBS; Gibco), gentamicin (50 µg/ml; Sigma-Aldrich), penicillin/streptomycin (100 µg/ml; Sigma-Aldrich) and fungizone (2.5 µg/ml; Gibco).

5.4. Virus titration

The secondary rBV were tritiated in order to determine the multiplicity of infection (MOI), a critical parameter to achieve optimal protein concentration yield with baculovirus gene expression. Confluent cell cultures were infected with different rBV quantities (0, 5, 10, 25, 50 and 100 µl) during 72-96 h. The medium and cells were collected and centrifuged at 1500 rpm during 5 min. The pellet was resuspended in 1 ml PBS and centrifuged at 1500 rpm during 5 min. The pellet was resuspended in 100 µl of H_20 and each fraction was analysed by SDS–polyacrylamide gel electrophoresis in order to establish the optimal multiplicity of infection by protein expression.

5.5. Production and purification of recombinant vaults

H5 cells (Invitrogen) were infected with rBV-MVPα and rBV-MVPβ at the same time with a multiplicity of infection of 5 plaque-forming units per cell. Cells were harvested 72 h after infection, washed using phosphate-buffered saline (PBS), and pelleted with a 5 min centrifugation at 1500 rpm (using a A-4-38 rotor). This pellet was resuspended in 10 ml of buffer A [75 mM NaCl, 50 mM tris (pH 7.4), 0.75 mM MgCl2, and 1 mM

dithiothreitol] plus RNase A, DNase I, 1% Igepal and protease inhibitors (protease inhibitor cocktail tablets; Roche, Basel, Switzerland) and maintained on ice for 30 min.

The resuspended pellet was sonicated, and cellular debris was removed by centrifugation at 10000 rpm (using an F-34-6-38 rotor) for 30 min. The supernatant was applied to 4 ml of buffer A with 25% sucrose and centrifuged at 37000 rpm (using a SW41Ti rotor) for 2.5 h. The resulting pellet was resuspended in 600 µl of buffer A and centrifuged for 1 min at 13000 rpm (using an F-45-6-30 rotor). The supernatant was applied to a 25 to 50% sucrose gradient in buffer A and centrifuged for 45 min at 40000 rpm (using a SW41Ti rotor). The gradient was fractionated and then analysed by SDS–polyacrylamide gel electrophoresis and negative-stain EM. Fractions with protein were joined in 600 µl of buffer A and centrifugated at 1000 rpm 5min.

A second purification step by applying a CsCl cushion was added. The sample was applied to 3 ml cushion of buffer A with 36% CsCl and centrifugated at 43500 rpm during 2 h (using SW55Ti Beckman rotor). The cushion was illuminated and a white ring was seeing where the vault complex was present. The vaults fraction was carefully collected and particles were concentrated to 5 mg/ml using a centrifugal filter device (Centricon YM-100, Merck Millipore, Billerica, MA). Sample quality was checked by negative-stain EM (see below).

6. Individual characterization of each protein: MVPα and MVPβ

6.1. MVPα purification

Cells were lysated at specified before. A 5 ml HiTrap SP (General Electric) column was equilibrated with buffer A before applying the protein sample, an extensive wash with the same buffer were performed to remove unbound sample and then, recombinant protein was eluted with a linear gradient of 500 mM imidazole. Fractions that showed an increased absorbance at 280 nm were collected and analyzed by SDS-PAGE to evaluate the purity. Best fractions were pooled together, recovered initial conditions (buffer A) and submitted to an analytic column (Superdex 200 5 150 FC) equilibrated in buffer A. Fractions that corresponded to the MVPα were pooled together and concentrated using a 100 K centrifugal device (Millipore) before MALS analysis. The same protocol was applied for MVPβ subunit, but result as an insoluble protein.

6.2. SEC with multi-angle laser light scattering (MALS)

For analysis of the polymerization in solution of MVP, SEC combined with light scattering analysis was used. The SEC data was measured using a Superdex 200 10/300 GL column (GE Healthcare; MW range: 10–600 kDa), connected to high-performance liquid chromatography system (Shimadzu), equipped with an autosampler. The elution from SEC was monitored by a UV detector, differential refractometer (OPTI-rEx, Wyatt Corp.) and static, multi-angle laser LS detector (DAWN-HELEOS, Wyatt Corp.). The SEC-UV/MALS/RI system was equilibrated in 7.8 mM sodium phosphate pH=7.3, NaCl 150 mM at the flow rate of 0.5 ml/min. The ASTRA 7 software (Wyatt Corp.) was used for data collection and analysis.

7. Production and characterization of mutant recombinant *Dictyostelium discoideum* vaults in complex with a nanobody

7.1. Production of MVPα and MVPβ variants, containing an inserted Myc epitope

A Myc epitotope sequence: EQKLISEED, was introduced in one exposed loop of different MVP repeat domains (R4, R5 or R6) to generate the best MVP variant able to produce stable high-quality vaults for structural studies. Three different strategies were applied: i) the introduction the myc sequence directly between two exposed residues, ii) by replacing several residues forming the loop with the myc sequence and iii) the introduction of the Myc sequence, flanked in both ends by a short (GSG_myc_GSG) or by a long link (GSGSG_myc_GSGSG). Mutations in pFB_MVPα and in pFB_MVPβ were generated by PCR. Oligonucleotide sequences used to mutagenize the MVP gene (α or β) are in Tables 5 and 6. Baculoviruses production, titration and production of mutant recombinant vaults were performed as previously described.

7.2. Assays of α-myc antibody by Immunoprecipitation

Immunoprecipitation (IP) is the small-scale affinity purification of antigens using a specific antibody that is immobilized to a solid support such as an agarose resin. Incubation steps were performed in a batch-wise manner. First, the vault protein fraction was incubated with the α-myc antibody O/N at 4 ºC. Before adding the solution to the resin, the 60 µl of protein A/G agarose was centrifuged at 11000 rpm for 10 min to discard the commercial buffer, cleaned with 500 µl of H_2O and equilibrated with 500 µl of buffer A. The solution containing vaults and α-myc antibody was then added to a protein A/G

agarose resin and incubated during 2 h. The sample was centrifuged at 7000 rpm for 5 min and the flow through (FT) was collected. For cleaning, two steps of 500 µl of buffer A were added and centrifuged collecting elution fractions (EL1: elution 1; EL2: elution 2). The pellet was directly resuspended in the loading buffer and the samples collected were analysed by SDS-PAGE electrophoresis and by Western-Blot.

8. Transmission Electron Microscopy (TEM)

Due to the dynamic nature of the vault complex, which made it difficult to obtain good diffracting crystals, the main methodology applied in this thesis work has been the electron microscopy (EM).We used three different approaches: negative staining EM, to obtain a preliminary characterization of the particles and check the sample quality; cryo-EM, single particle analyses to obtain high resolution structural information of the purified vault particles and cryo-electron tomography to visualize vaults in their native environment inside the cell and capture the "sociology" of this macromolecular complex.

8.1. The EM history

To establish EM as a general structural determination tool, several methodological and technical challenges had to be overcome:

i) The first practical solution applied by De Rosier and Klug (De Rosier and Klug, 1968) was the use of heavy-atom salts, such as uranyl acetate, as staining reagents to generate a dried ‘cast’ of the molecules before insertion in the scope. Heavy-metal staining reduces the problem of radiation damage, as it is the inorganic cast, not the protein itself, that is imaged. This method also generates a high-contrast image due to the high atomic number of uranium (because the protein scatters less that the surrounding stain, this method is known as ‘negative staining’ (reviewed in Nogales, 2016).

ii) Because electrons are scattered by molecules in the air, electron microscopes must be confined in a high vacuum. This poses a problem when studying biological samples, because they are sensitive to radiation damage. For each electron that contributes to the formation of an image, there will be three electrons that deposit energy in the sample. This energy causes the cleavage of chemical bonds and ultimately destroys the structures of interest. By keeping samples at cryogenic temperatures, cryo-EM enables their preservation against the effects of radiation damage (Taylor and Glaeser, 1974). The practical application of this

approach led to the development of a sample vitrification method, by cryo-plunging of thin solutions into a powerful cryogen, such a liquid ethane or liquid propane) (Dubochet et al., 1982).

iii) Radiation damage by high-energy electron beams limits the total electron dose that can be used to image biological samples. The consequence is that images recorded with such a low electron dose have very poor signal-to-noise ratios (SNRs). Henderson and colleagues overcame this problem by use of a crystallographic approach, averaging images of many identical proteins packed as 2D crystals (Henderson et al., 1990). In parallel, Frank and co-workers proposed an idea to determine structures without crystallization: computationally combining images of many individual protein particles of the same type. The samples contain individual macromolecular complexes, "single particles" that adopt random (or at least multiple) orientations on the EM grid (Frank, 1996). Therefore, the term "single particle cryo-EM" refers to the later combination of this strategy with the plunge freezing sample preparation.

8.2. The recent progress in cryo-EM

One of the most exciting developments of the last decade has been the irruption of the single particle cryo-EM into atomic resolution, previous monopoly of X-ray crystallography. The two fundamental barriers dampening cryo-EM have been overcome: crossing beyond the 2 Å resolution barrier as well as obtaining structures of proteins with sizes under 100 kDa, establishing that cryo-EM could be used generally in the detailed investigation of a broad spectrum of samples, ranging from large multicomponent complexes down to drug-target interactions and heterogeneous dynamic conformational states. This "revolution in resolution" of the cryo-EM (Kühlbrandt, 2014) has been possible due to recent advances in instrumentation and software. New direct electron detector cameras (McMullan et al., 2016), and image-processing methods have been developed (Scheres, 2012), and throughput has increased with the advent of automation in data collection and analysis.

At the beginning of cryo-EM, electron micrographs were recorded on photographic films. But in the early 2000s, digital charge-couple device (CCD) cameras were introduced to record EM micrographs digitally. Photographic film detects only about one-third of the incoming electrons. CCDs were even less efficient, because an extra conversion from

electrons to photons leaded to an overall detection rate of less than one-fifth of the incoming electrons (Potter et al., 1999). Since the number of electrons used for imaging must be very low to limit radiation damage, the resulting images were very noisy, making it difficult to accurately determine particle orientations. In 2012, three companies produced prototypes of a new generation of direct electron detectors. The innovative chips were sufficiently resistant to radiation damage to enable the direct detection of electrons, which improved the efficiency of detection to around half of the incoming electrons (McMullan et al., 2014). Moreover, the modernized electronics that surrounded these detectors facilitated fast image capture. Fast image capture also addressed a problem associated with frozen hydrated samples: energy released by the incoming electrons causes movement inside the ice layer, which blurs the resulting images. Movies recorded during exposure of the sample to electrons could be processed to effectively remove the blurring effects (Brilot et al., 2012; Campbell et al., 2012) which facilitated structure determination to a high resolution (Li et al., 2013; Bai et al.2013).

The resolution of a reconstruction also depends on the conformational homogeneity of the sample and accuracy of image alignment of all particles used to reconstruct the density map. Image classification and alignment are thus the two most critical steps in the computational image processing. Because each particle image has a poor singal-to-noise-ratio, individual particles cannot be classified and assigned to a specific class and orientation with certainty, making a probabilistic approach better suited for image classification and alignment. Early attempts to use a maximum likelihood–based probabilistic approach in cryo-EM image processing were made in the late 1990s (Sigworth, 1998). At the same time that direct electron detectors were becoming widely used, the extension of maximum likelihood methods into an empirical Bayesian approach to cryo-EM reconstruction was described and implemented in the RELION software (Scheres, 2012). RELION is a user-friendly program that soon became very popular in single-particle cryo-EM image processing. This approach is more powerful and robust than traditional deterministic approaches, particularly in classifying a subset of particle images with homogeneous conformations out of a larger and more heterogeneous dataset.

8.3. Negative staining EM

Transmission electron microscopy (TEM) of uranyl acetate–stained vaults was used to check the quality of purified vaults in terms of overall particle morphology and

concentration. Purified vaults were absorbed onto ionized carbon-coated copper EM grids for 1 min at room temperature. Following sample adsorption, the non-adsorbed sample was removed, using a filter paper. Grids were then positioned on top of a 70 µl 2% uranyl acetate drop for 10 s at room temperature, then on another drop of acetate uranyl acetate for another 10 s and dried on filter paper after. The samples were viewed with a JEM-1010 (JEOL) transmission electron microscope equipped with a CCD Megaview at the Parc Cientific de Barcelona. The images were acquired at 100 kV with magnifications between 50000x and 75000x.

8.4. Single-particle cryo-electron microscopy

Cryo-EM SPA allows the structure determination of isolated macromolecular complexes in a near native state. The approach is based on the alignment and averaging of thousands of projections of individual particles that allow its 3D reconstruction (Danev et al., 2019).

Macromolecular structure determination through cryo-EM SPA involves several stages: sample grid preparation, data collection and data processing followed by 3D reconstruction. The workflow of cryo-EM is shown in Figure 73. To prepare the sample, a few microlitres of a biochemically purified protein solution is applied to a metal (usually copper) grid, on top of which lies a thin film of amorphous carbon that contains holes. The excess liquid is blotted away with filter paper. The grid is plunged into liquid ethane (Dubochet et al.,1982), which flash-freezes the sample and embeds the particles in vitreous ice. Ideally, this results in the formation of a thin layer of non-crystalline ice, in which copies of the protein are deposited in a range of orientations. The grid is stored in liquid nitrogen until it is transferred to the transmission electron microscope. Images that are captured through the holes in the carbon film contain two-dimensional (2D) projections of individual protein complexes, which are called particles. Projections of particles in various orientations provide complementary information about the underlying 3D object. Numerous 2D projections can therefore be combined into a single 3D reconstruction of the biological sample (Figure 73).

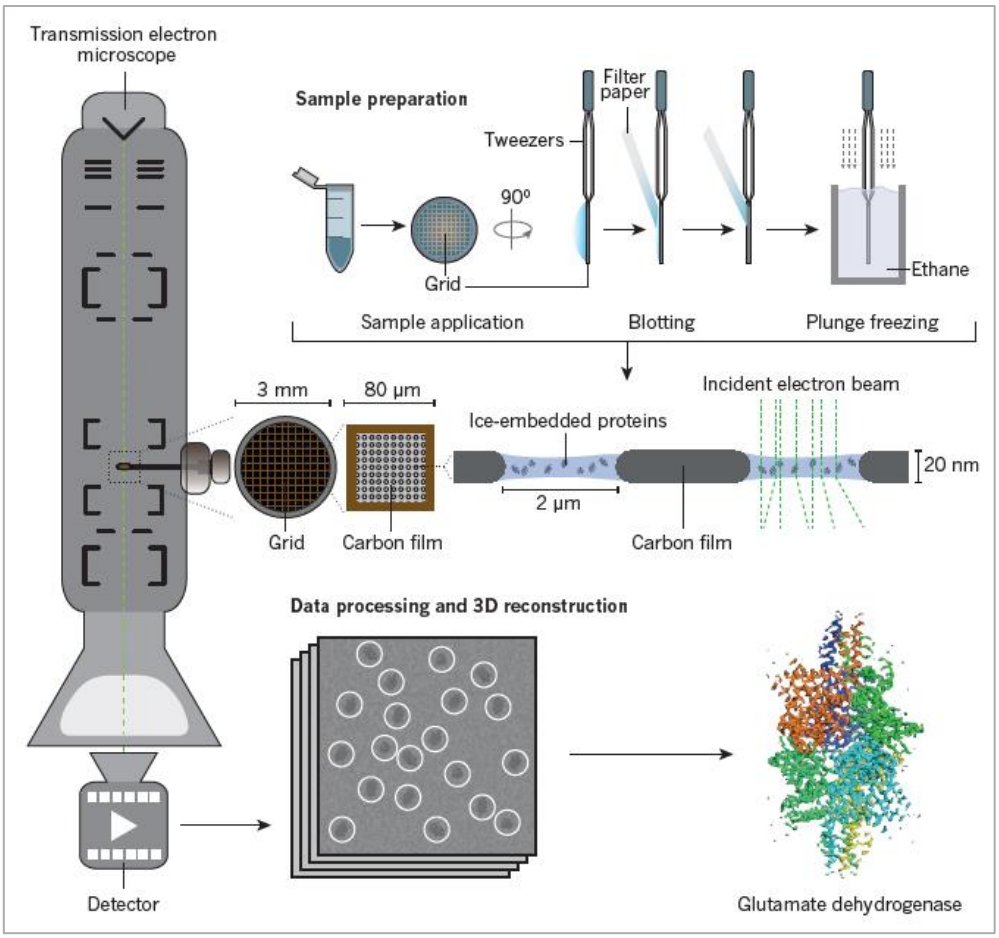

Figure 73. Schematic representation of cryo-EM SPA workflow (Fernandez-Leiro and Scheres, 2016). The approach allows to characterize a macromolecule in a near-native state by flash frozen a purified sample, which prevents the formation of crystalline ice. Once frozen, the biological sample is directly visualized using transmission electron microscopy (TEM), which generates 2D images, corresponding to different projections of the sample. These projections are then combined to create a 3D reconstruction of biological sample.

8.5. Data collection

8.5.1. Data collection endogenous *Dictyostelium* vaults

Purified endogenous *Dictyostelium* vaults were frozen on a Vitrobot Mark IV (FEI, settings: blotforce = 0, blottime = 3 s, temperature = 4 °C, humidity = 95%) using liquid ethane. The grids were checked in a 200 kV Talos Arctica electron microscope equipped with a Falcon 3 (Thermo Fisher) at the Centro Nacional de Biotecnología (CNB-CSIC), in Madrid. The best grids were used for high resolution data collection in in a 300 kV

Titan Krios electron microscope (Thermo Scientific) equipped with a K2 (Gatan) at the European Synchrotron Radiation Facility (ESRF, Grenoble, France).

R 0.6/1 UltraAuFoil gold grids were used to acquired 2525 movies, in counting mode, using the EPU software at magnification x110000 (pixel size of 1.05 Å/pixel). The electron dose used was 7.2 electrons/pixel/second and each movie contained 30 frames recorded in 6 seconds.

8.5.2 Data collection recombinant *Dictyostelium* vaults

Recombinant vaults were frozen on a Vitrobot Mark IV (FEI, settings: blotforce = 0, blottime = 3 s, temperature = 4 °C, humidity = 95%) using liquid ethane too. The grids were also checked at the cryo-EM facility of the CNB-CSIC in Madrid and the best grids were used for high resolution data collection in the 300 kV Titan Krios equipped with a K2 (Gatan) (ESRF, Grenoble, France).

R 2/2 UltraAuFoil gold grids were used to acquire 3643 movies in counting mode with EPU at x110000 magnification (pixel size of 1.07 Å/pixel). The electron dose used was 7.7 electrons/pixel/second and each movie contained 30 frames recorded in 6 seconds.

8.5.3. Data collection recombinant *Dictyostelium* vaults in complex with the α-Myc nanobody

High quality of recombinant vaults obtained with the myc epitope bound to the R6 repeat of MVPβ. The stoichiometry vault:nanobody used was 1:80 (calculated assuming 80 copies of MVP). The complex was frozen on a Vitrobot Mark IV (FEI, settings: blotforce = 0, blottime = 3 s, temperature = 4 °C, humidity = 95%) using liquid ethane. The quality of the vitrified grids was checked the a 200kV Talos Arctica electron microscope equipped with a Falcon 3 (Thermo Fisher) at the cryo-EM facility of the CNB-CSIC. In the first instance, we did a small data collection, acquiring 1808 movies in R1.2/1.3 UltraAuFoil gold grids to confirm the presence of the nanobody in the structure of the complex. During the first data processing steps, we realized that the complex showed preferential orientations and we did not have enough orientations of the particle to perform the 3D reconstruction. Due to this fact, a small amount of n-dodecyl β-D-maltoside (DDM) was added to the complex nanobody-protein just before vitrificaction. The best grids containing DDM were used for high resolution data collection in the 300 kV Titan Krios equipped with a K3 (Gatan) (ESRF, Grenoble, France).

We acquired 15152 movies in R 1.2/1.3 UltraAuFoil gold grids using the counting mode with EPU at x81000 (pixel size of 1.06 Å/pixel). The electron dose used was 20 electrons/pixel/second and each movie contained 40 frames recorded in 2.2 seconds.

8.6. Data processing

The micrographs were aligned using MotionCor2 (Zheng et al., 2017). The transfer contrast function (CTF) was calculated using the software Gctf (Zhang, K. 2016) for the recombinant vaults and with the CTFFIND4 (Rohou and Grigorieff, 2015) for the recombinant mutant vault in complex with the nanobody. These particles were then used in a 2D classification process to generate templates for a template matching auto-picking job.

All the 2D and 3D classifications as well as the refinements were performed using two versions of RELION: RELION 3.0 (Egelman et al., 2018) and RELION 4.0 (Kimanius et al., 2021). For the recombinant mutant vaults in complex with the nanobody, the best particles were analyzed with CryoSPARC (Punjani et al., 2017). As vault map reference for the 3D classifications and refinements, the PDB ID: 4HL8 was used filtered to 60Å.

8.7. Data refinement

Alphafold2 (Jumper et al., 2021) prediction models of the MVP subunits with some manual changes with Coot (Emsley and Cowtan, 2004) as explained in results were used for fitting the model into the 5.1 Å map. The MVP subunits were first fitted into the averaged maps of each subunit (MVPα or MVPβ-myc). For improving the fitting, the repeat domains of each monomer and the helix were rigid body fitted into the density map using Coot. Using Coot and Chimera (Pettersen et al., 2004) a PDB with 13 MVPα subunits in the up half and 13 MVPβ in the bottom half was created. This PDB was fitted in the map density and then, refined with Phenix (Adams et al., 2010).

9. Structural characterization of *human* vaults *in situ*

9.1. Cloning

HeLa cells were used to establish a stable cell line, expressing the human MVP tagged with EGFP at the N-terminus. EGFP was cloned at the N-terminus because it was previously described that the N-terminal EGFP-tag did not interfere within the vault function (Van Zon et al. 2003). MVP human gene was amplified by PCR from the pGEM-T commercial vector and cloned into the pEGFP-C1 vector by HindIII and SalI restriction enzymes. Primer sequences are described in Table 7.

The construct EGFP-MVPh was cloned into the pINDUCER20 vector between the attB1 and attB2 sites through LR/BP recombination reactions, taking advantage of the Gateway Recombination Cloning Technology. The same protocol was applied for the EGFP construct used as control. Primer sequences are described in Table 7. Both EGFP WT and EGFP-MVPh constructs were induced by the addition of doxycycline (1 µg/ml), incubated for 48 h.

The Gateway Technology is a universal cloning method based on the site-specific recombination propertied of bacteriophage lambda (Landy,1989). Lambda recombination is catalyzed by a mixture of enzyme that bind to specific sequences (*att* sites), bring together the target sites, cleave them and covalently attach the DNA. Two recombinant reactions constitute the bases of the Gateway Technology:

- **BP reaction**: facilitates recombination of an attB substrate (attB-PCR product or a linearized attB expression clone) with and attP substrate (pDONOR vector) to create an attL-containing entry clone. This reaction is catalyzed by BP Clonase enzyme mix.

Figure 74. BP reaction to create an attL-containing entry clone (Landy,1989).

- **LR reaction**: facilitates recombination of an attL substrate (entry clone) with and attR substrate (destination vector: pINDUCER20) to create an attB-containing expression clone. This reaction is catalyzed by LR Clonase enzyme mix.

Figure 75. LR reaction to attB-containing expression clone (Landy,1989).

Once, we have cloned our construct in the destination vector: pINDUCER20 vector, we checked its functionality.

9.2. Lentiviral transduction

The stable expression of recombinant EGFP-MVPh protein and EGFP protein was generated in HeLa cells by lentiviral infection. Lentiviruses were produced in HEK2397 cells by co-transfecting p-INDUCER (contains the target gene: EGFP-MVPh or EGFP) with p-VSV-G and p-GAG-POL plasmids which encode the viral capsid and the transcriptional machinery respectively. Media containing the viral particles were filtered and used for HeLa infection plus 2.5 µl/ml polybrene (Sigma) added to increase infection efficiency. For several days, cells were selected with 600 µg/ml gentamicin (G418 Millipore; Merck).

9.3. Fluorescence-Activated Cell Sorting (FACS)

EGFP-MVPh and EGFP cells were sorted by flow cytometry using facs-Aria Fusion flow cytometer.

9.4. Cell culture

HeLa cell lines were grown at 37 °C in Dulbecco's Modified Eagle Medium (DMEM, Gibco) supplemented with 10% FBS (Gibco), gentamicin (50 µg/ml; Sigma-Aldrich), penicillin/streptomycin (100 µg/ml; Sigma-Aldrich), fungizone (2.5 µg/ml; Gibco) and non-essential amino acid solution (100x v/v; Sigma).

9.5. Cell culture treatment

The stable cell line was treated under different drugs: cycloheximide (10 µM) rapamycin (10 µM and 500 nM) for 48 h. Control cells (doxycycline induction) vs treatment cells (doxycycline induction plus the drug).

9.6. Immunofluorescence assay

Cells were fixed in 4% paraformaldehyde (PFA) and 4% sucrose for 20-30 min at 4 °C and after, three times washed for 5 min each with PBS at RT. Cells were permeabilized in methanol for 5 min at 4 °C and washed two times for 5 min each with PBS at RT. Then, coverslips were blocked for 30 min in 5% FBS in PBS. Next, coverslips were incubated with primary antibody diluted in 5% FBS PBS during 2 h at RT or overnight at 4 °C. Washed again three times and incubated with secondary antibody and DAPI diluted in 5% FBS PBS for 30 min at RT. Cells were then washed again with PBS and dried with ethanol before mounting the coverslips on microscope slides with Prolong-Gold. For cells overexpressing EGFP proteins, the intrinsic fluorescence of the molecules was captured without using either primary or secondary antibodies. Confocal images were obtained using a High Speed and Super-Resolution DragonFly 505 (Andor; Molecular Imaging Platform IBMB). Z-stacks were acquired with the optimal step. Image processing and quantification were performed using ImageJ software.

10. *In situ* cryo-electron tomography

Cryo-ET is an emerging technology that allows thin samples, such as macromolecular complexes and small cells, to be directly imaged in 3D in a nearly native state and at high-resolution. Cryo-ET can provide insight into the positions and structures of cytoskeleton filaments, cell wall components, motility machines, chemoreceptor arrays, internal compartments and other cellular structures (Murphy and Jensen, 2007). In this way, structural information about organelles and individual proteins can be linked with their exact three-dimensional arrangement within the cell. This unique capability holds enormous potential for cell biology, making cryo-ET a highly promising technology to achieve the objectives of our project.

For cryo-ET, a biological sample, a cell, tissue or even entire organism is flash frozen, thinned to an appropriate thickness, and then imaged using an electron microscope (Doerr, 2016). As in SPA, the fast-freezing process preserves the sample in a hydrated, close-to-native state. Multiple images are captured as the sample is tilted along an axis. The images are then aligned and merged to reconstruct a three-dimensional image: the tomogram (Beck and Baumeister, 2016).

The process comprises five essential steps: vitrification, cryo-light microscopy, 3D-correlative cryo-FIB milling, cryo-electron tomography, and analysis by subtomogram averaging (STA) and segmentation (Figure 76).

I. VITRIFICATION: Cells are grown on electron microscopy grids and plunge-frozen in a cryogenically cooled fluid, typically liquid ethane (Figure 76B-1). Vitrification occurs within microseconds, preventing the disruption of lipid membranes and changes in solvent concentration within the sample. Artifacts that are usually caused by ice crystal growth. Different combinations of grid types, vitrification conditions (time and blotting force), as well as cell density must be checked before obtaining a grid with optimal properties for cryo-FIB milling. Since vitrification of cells can be challenging, the use of additives that prevent crystalline ice formation is explored.

II. CRYO-FLUORESCENCE LIGHT MICROSCOPY (cryo-FLM): Locating a structure of interest in the vast landscape of the cell can be challenging. However, using cryo-correlative fluorescent light microscopy, the structures of interest can be identified by genetically encoded fluorescent tags such as EGFP. Their exact location in three dimensions can then be captured by acquiring z-stacks at the positions of interest. As reference point, fluorescent beads are used, which are both visible in cryo-FLM, FIB, and TEM (Arnold et al., 2016) (Bieber et al., 2021). This information is necessary to decide which cells and which parts of them will be used during sample preparation and data acquisition.

III. FIB MILLING: Once a suitable position is found and fluorescence Z-stacks have been acquired, cellular lamellas can be produced. Using cryo-FLM overviews, positions of interest are first localized in the FIB-SEM instrument to plan the milling strategy. The ion beam is then used to remove cellular material from above and below the target region of the vitrified cells until a lamella, with the precise dimensions and width as specified by the user, ideally containing the fluorescent puncta, is obtained. Lamella containing the

region of interest and can be milled as thin as 100-200 nm. This is essential for the tomography workflow because of the nature of the interactions between the electron beam in the TEM and the sample. If the sample is too thick, more of the electrons are inelastically scattered and therefore only contribute to noise (Schaffer et al., 2017). Lamella quality will be screened and monitored to obtain suitable samples for to the next step: cryo-electron tomography.

IV. CRYO-ELECTRON TOMOGRAPHY: The thin lamella on the EM grid is transferred to a cryo-electron microscope, equipped with a direct electron detector and an energy filter. Tilt series, i.e. a collection of 2D images from different perspectives of the lamella, are then recorded as the sample is tilted in specific angle increments (generally ±60 º at 3 º intervals). For cellular tomography in particular, the use of a 300 kV microscope and an energy filter is necessary, to reduce the background signal produced by inelastically scattered electrons, thereby allowing the localization of specific cellular structures. In order to acquire enough data for the averaging and obtaining a high-resolution structure of native protein, multiple rounds of data acquisition using different lamellas will be required.

V. PROCESSING, SUBTOMOGRAM AVERAGING AND SEGMENTATION: Once the data acquisition has finished, sample movement during imaging is removed from the individual tilt-frame series using MotionCor2 (Zheng et al., 2017) and the CTF is estimated using CTFFIND4 (Rohou and Grigorieff, 2015). The motion-corrected images are then aligned and tomograms of the lamella reconstructed using IMOD (Mastronarde and Held, 2017). This process has recently been automated by William Wan and Philipp Erdmann in TOMOMAN (Khavnekar et al., 2023), a collection of scripts making use of the aforementioned standard programs. With the reconstructed tomograms in hand, the huge amount of information contained within them needs to be divided in small subsets containing structures of interest in a process called segmentation. Moreover, cellular complexes such as ribosomes and MVPs can be localized by template matching and subsequently averaged by STA using RELION or STOPGAP (Wan and Briggs, 2016) to obtain high-resolution averages of the target protein.

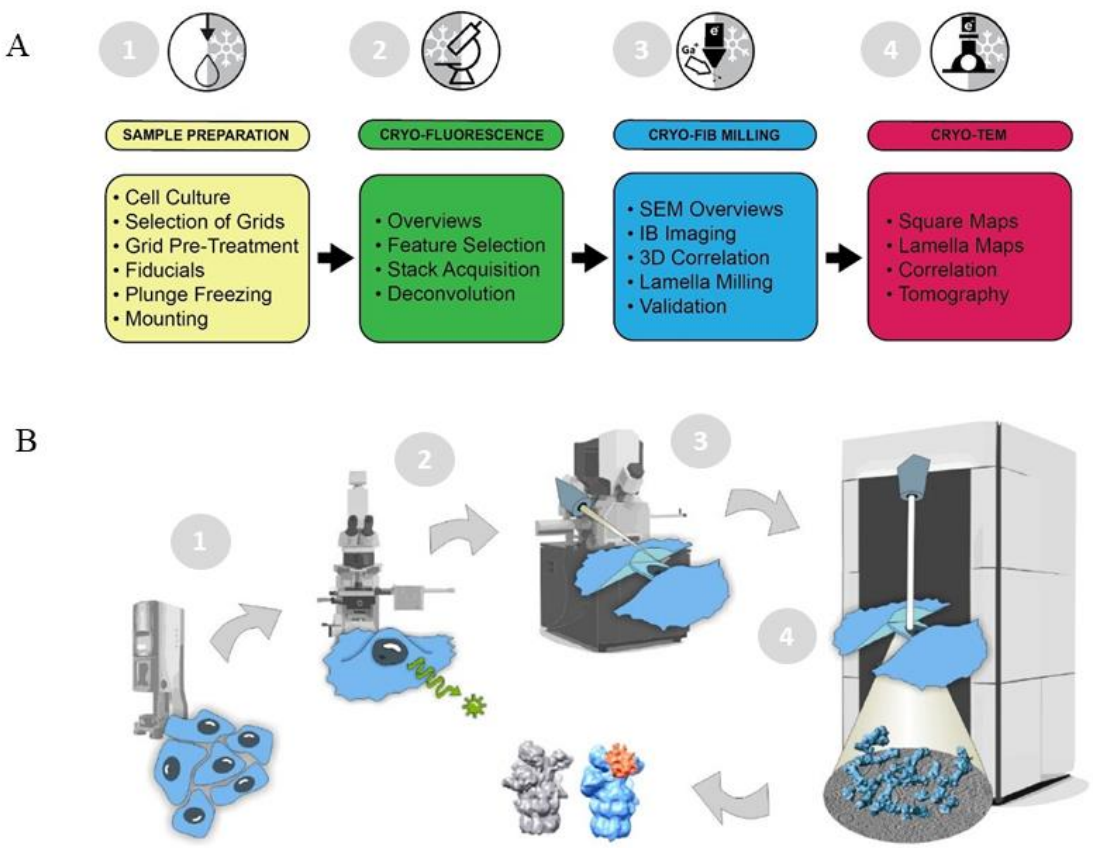

Figure 76. Summary and schematic representation of Cryo-ET workflow (**A**) Description in detail of each critical step of *in situ* cryo-ET (Bieber et al., 2021): (1) Sample preparation, (2) Cryo-fluorescence, (3) Cryo-FIB milling and (4) Cryo-electron tomography. (**B**) Workflow representation of each step in (**A**) (Figure adapted from Thermo).

10.1. Sample preparation, cryo-fluorescence, FIB-milling and cryo-ET data acquisition of EGFP-tagged human vaults in cells

Cell Culture. In this study, the stable HeLa cell line expressing human MVP-EGFP fusion protein when induced by doxycycline was used. The cell line was maintained in DMEM supplemented with 10% fetal bovine serum (FBS). The stable cell line was treated with 500 nM of rapamycin for 48h. Both control cells (doxycycline induction) and treatment cells (doxycycline induction plus rapamycin) were generated.

Sample Preparation. Cells were grown on UltraAu R2/2 TEM grids which were plasma-cleaned, sterilized using UV-radiation, and coated with poly-L-lysine for attachment.

Vitrification and Fiducial Addition. Before vitrification, 10% Glycerol (final conc.) was added to the HeLa medium as cryoprotectant. Cells were incubated for 10 min at 37 ºC before further processing. Just before plunge freezing, 4 ul of fluorescence beads (Dynabeads ByBioOne) diluted (1:20) in cell culture medium (with glycerol) were directly applied to the grid. Cells were frozen on a Vitrobot Mark IV (FEI, settings: blotforce = 10, blottime = 10 s, temperature = 37 °C, humidity = 90%) using liquid ethane.

Clipping Grids. Plunge-frozen grids were mounted and clipped in AutoGrids with cut-out for FIB milling with the cells facing up for subsequent cryo-fluorescence imaging and FIB milling.

Cryo-Fluorescence Light Microscopy. For each grid, we acquired and overview in fluorescence (GFP) and reflected mode in order to choose the areas of interest containing both cells positive for vault expression and a sufficient number of fiducial markers surrounding them. For each of the identified areas, we acquired a fluorescent stack for later deconvolution and potential 3D targeting.

FIB-Milling. Lamellas were prepared on a dual beam focused ion beam microscope (Thermo Scientific Aquilos 2). Lamellas from control and treated cells were cut in the cytoplasm and near the nuclear membrane. Lamellas were cut with to a thickness of 150 nm (final pattern offset).

Cryo-Electron Tomography. Cryo-tomograms were acquired on a transmission electron microscope (Titan Krios G4i 300kV TEM).

Bibliography

BIBLIOGRAPHY

Abbondanza, C., Rossi, V., Roscigno, A., Gallo, L., Belsito, A., Piluso, G., Medici, N., Nigro, V., Molinari, A. M., Moncharmont, B., & Puca, G. A. (1998). Interaction of Vault Particles with Estrogen Receptor in the MCF-7 Breast Cancer Cell. In *The Journal of Cell Biology* (Vol. 141, Issue 6). http://www.jcb.org1301

Adams, P. D., Afonine, P. V., Bunkóczi, G., Chen, V. B., Davis, I. W., Echols, N., Headd, J. J., Hung, L. W., Kapral, G. J., Grosse-Kunstleve, R. W., McCoy, A. J., Moriarty, N. W., Oeffner, R., Read, R. J., Richardson, D. C., Richardson, J. S., Terwilliger, T. C., & Zwart, P. H. (2010). PHENIX: a comprehensive Python-based system for macromolecular structure solution. *Acta crystallographica. Section D, Biological crystallography*, *66*(Pt 2), 213–221. https://doi.org/10.1107/S0907444909052925

Amé J-C, Spenlehauer C, de Murcia G. (2004) The PARP super-family. *BioEssays.* 26(8):882–93. [PubMed: 15273990]

Amort, M., Nachbauer, B., Tuzlak, S., Kieser, A., Schepers, A., Villunger, A., & Polacek, N. (2015). Expression of the vault RNA protects cells from undergoing apoptosis. *Nature Communications*, *6*. https://doi.org/10.1038/ncomms8030

Anderson, D. H., Kickhoefer, V. A., Sievers, S. A., Rome, L. H., & Eisenberg, D. (2007). Draft crystal structure of the vault shell at 9-Å resolution. *PLoS Biology*, *5*(11), 2661–2670. https://doi.org/10.1371/journal.pbio.0050318

Arnold, J., Mahamid, J., Lucic, V., de Marco, A., Fernandez, J. J., Laugks, T., Mayer, T., Hyman, A. A., Baumeister, W., & Plitzko, J. M. (2016). Site-Specific Cryo-focused Ion Beam Sample Preparation Guided by 3D Correlative Microscopy. *Biophysical Journal*, *110*(4), 860–869. https://doi.org/10.1016/j.bpj.2015.10.053

Bai, X. C., Fernandez, I. S., McMullan, G., & Scheres, S. H. W. (2013). Ribosome structures to near-atomic resolution from thirty thousand cryo-EM particles. *ELife*, *2013*(2). https://doi.org/10.7554/eLife.00461

Bateman, A., & Kickhoefer, V. (2003). The TROVE module: A common element in Telomerase, Ro and Vault ribonucleoproteins. *BMC Bioinform.* 4, 49.

Beck, M., & Baumeister, W. (2016). Cryo-Electron Tomography: Can it Reveal the Molecular Sociology of Cells in Atomic Detail? *Trends in Cell Biology*, *26*(11), 825–837. https://doi.org/10.1016/j.tcb.2016.08.006

Bibliography

Ben, J., Zhang, Y., Zhou, R., Zhang, H., Zhu, X., Li, X., Zhang, H., Li, N., Zhou, X., Bai, H., Yang, Q., Li, D., Xu, Y., & Chen, Q. (2013). Major vault protein regulates class a scavenger receptor-mediated tumor necrosis factor-α synthesis and apoptosis in macrophages. *Journal of Biological Chemistry*, *288*(27), 20076–20084. https://doi.org/10.1074/jbc.M112.449538

Berger, W., Steiner, E., Grusch, M., Elbling, L., & Micksche, M. (2009). Vaults and the major vault protein: Novel roles in signal pathway regulation and immunity. *Cellular and Molecular Life Sciences*, 66 (1), 43–61. https://doi.org/10.1007/s00018-008-8364-z

Bieber, A., Capitanio, C., Wilfling, F., Plitzko, J., & Erdmann, P. (2021). Sample Preparation by 3D-Correlative Focused Ion Beam Milling for High-Resolution Cryo-Electron Tomography. *Journal of Visualized Experiments*, *176*, 1–22. https://doi.org/10.3791/62886

Bracher, L., Ferro, I., Pulido-Quetglas, C., Ruepp, M. D., Johnson, R., & Polacek, N. (2020). Human vtRNA1-1 levels modulate signaling pathways and regulate apoptosis in human cancer cells. *Biomolecules*, *10*(4). https://doi.org/10.3390/biom10040614

Brilot, A. F., Chen, J. Z., Cheng, A., Pan, J., Harrison, S. C., Potter, C. S., Carragher, B., Henderson, R., & Grigorieff, N. (2012). Beam-induced motion of vitrified specimen on holey carbon film. *Journal of Structural Biology*, *177*(3), 630–637. https://doi.org/10.1016/j.jsb.2012.02.003

Buchholz, T. O., Krull, A., Shahidi, R., Pigino, G., Jékely, G., & Jug, F. (2019). Content-aware image restoration for electron microscopy. *Methods in cell biology*, *152*, 277–289. https://doi.org/10.1016/bs.mcb.2019.05.001

Büscher, M., Horos, R., & Hentze, M. W. (2020). 'High vault-age': Non-coding RNA control of autophagy. *Open Biology*, *10*(2). https://doi.org/10.1098/rsob.190307

Campbell, M. G., Cheng, A., Brilot, A. F., Moeller, A., Lyumkis, D., Veesler, D., Pan, J., Harrison, S. C., Potter, C. S., Carragher, B., & Grigorieff, N. (2012). Movies of ice-embedded particles enhance resolution in electron cryo-microscopy. *Structure*, *20*(11), 1823–1828. https://doi.org/10.1016/j.str.2012.08.026

Carter, S. D., Mamede, J. I., Hope, T. J., & Jensen, G. J. (2020). Correlated cryogenic fluorescence microscopy and electron cryo-tomography shows that exogenous TRIM5α can form hexagonal lattices or autophagy aggregates in vivo. *Proc. Natl. Acad. Sci.* U.S.A. 117, 29702-29711 https://doi.org/10.1073/pnas.1920323117/-/DCSupplemental

Casañas, A., Querol-Audí, J., Guerra, P., Pous, J., Tanaka, H., Tsukihara, T., Verdaguer, N., & Fita, I. (2013). New features of vault architecture and dynamics revealed by novel refinement using the deformable elastic network approach. *Acta Crystallographica Section D: Biological Crystallography*, *69*(6), 1054–1061. https://doi.org/10.1107/S0907444913004472

Chisholm, R. L., Gaudet, P., Just, E. M., Pilcher, K. E., Fey, P., Merchant, S. N., & Kibbe, W. A. (2006). dictyBase, the model organism database for Dictyostelium discoideum. *Nucleic Acids Research*, *34*(Database issue). https://doi.org/10.1093/nar/gkj090

Chugani, D. C., Rome, L. H., & Kedersha, N. L. (1993). Evidence that vault ribonucleoprotein particles localize to the nuclear pore complex. *Journal of Cell Science*, *106*(1), 23–29.

Chung, J.-H., Ginn-Pease, M. E., & Eng, C. (2005). Phosphatase and tensin homologue deleted on chromosome 10 (PTEN) has nuclear localization signal-like sequences for nuclear import mediated by major vault protein. *Cancer Res.* 65(10): 4108-16. http://aacrjournals.org/cancerres/article-pdf/65/10/4108/2532022/4108-4116.pdf

Chung, J. H., & Eng, C. (2005). Nuclear-cytoplasmic partitioning of phosphatase and tensin homologue deleted on chromosome 10 (PTEN) differentially regulates the cell cycle and apoptosis. *Cancer Research*, *65*(18), 8096–8100. https://doi.org/10.1158/0008-5472.CAN-05-1888

Csolle, M. P., Ooms, L. M., Papa, A., & Mitchell, C. A. (2020). Pten and other ptdins(3,4,5)p3 lipid phosphatases in breast cancer. In *International Journal of Molecular Sciences* (Vol. 21, Issue 23, pp. 1–23). MDPI AG. https://doi.org/10.3390/ijms21239189

Danev, R., Yanagisawa, H., & Kikkawa, M. (2019). Cryo-Electron Microscopy Methodology: Current Aspects and Future Directions. In *Trends in Biochemical Sciences* (Vol. 44, Issue 10, pp. 837–848). Elsevier Ltd. https://doi.org/10.1016/j.tibs.2019.04.008

Danita, C., Chiu, W., & Galaz-Montoya, J. G. (2022). Efficient manual annotation of cryogenic electron tomograms using IMOD. *STAR protocols*, *3*(3), 101658. https://doi.org/10.1016/j.xpro.2022.101658

de la Rosa-Trevín, J. M., Otón, J., Marabini, R., Zaldívar, A., Vargas, J., Carazo, J. M., & Sorzano, C. O. S. (2013). Xmipp 3.0: An improved software suite for image processing in electron microscopy. *Journal of Structural Biology*, *184*(2), 321–328. https://doi.org/10.1016/j.jsb.2013.09.015

de la Rosa-Trevín, J. M., Quintana, A., del Cano, L., Zaldívar, A., Foche, I., Gutiérrez, J., Gómez-Blanco, J., Burguet-Castell, J., Cuenca-Alba, J., Abrishami, V., Vargas, J., Otón, J., Sharov, G., Vilas, J. L., Navas, J., Conesa, P., Kazemi, M., Marabini, R., Sorzano, C. O. S., & Carazo, J. M. (2016). Scipion: A software framework toward integration, reproducibility and validation in 3D electron microscopy. *Journal of Structural Biology*, *195*(1), 93–99. https://doi.org/10.1016/j.jsb.2016.04.010

De Rosier, D. J., & Klug, A. (1968). Reconstruction of Three-Dimensional Structures from Electron Micrographs. *Nature*, *217*(5124), 130–134. https://doi.org/10.1038/217130a0

Dickenson, N. E., Moore, D., Suprenant, K. A., & Dunn, R. C. (2007). Vault ribonucleoprotein particles and the central mass of the nuclear pore complex. *Photochemistry and Photobiology*, *83*(3), 686–691. https://doi.org/10.1111/j.1751-1097.2007.00050.x

Ding, K., Zhang, X., Mrazek, J., Kickhoefer, V. A., Lai, M., Ng, H. L., Yang, O. O., Rome, L. H., & Zhou, Z. H. (2018). Solution Structures of Engineered Vault Particles. *Structure*, *26*(4), 619-626.e3. https://doi.org/10.1016/j.str.2018.02.014

Doerr, A. (2016). Cryo-electron tomography. *Nature Methods*, *14*(1), 34. https://doi.org/10.1038/nmeth.4115

Dornan, D.,Wertz, I., Shimizu, H., Arnott, D., Frantz, G. D., Dowd, P., O_Rourke, K.,Koeppen, H., and Dixit,V. M. (2004) The ubiquitin ligase COP1 is a critical negative regulator of p53. *Nature* 429, 86–92.

Dubochet, J., Lepault, J., Freeman, R., Berriman, J. A., & Homo, J. -C. (1982). Electron microscopy of frozen water and aqueous solutions. *Journal of Microscopy*, *128*(3), 219–237. https://doi.org/10.1111/j.1365-2818.1982.tb04625.x

Egelman, E. H., Zivanov, J., Nakane, T., rn Forsberg, B. O., Kimanius, D., Hagen, W. J., Lindahl, E., & Scheres, S. H. (2018). *New tools for automated high-resolution cryo-EM structure determination in RELION-3*. https://doi.org/10.7554/eLife.42166.001

Eichenmüller, B., Kedersha, N., Solovyeva, E., Everley, P., Lang, J., Himes, R. H., & Suprenant, K. A. (2003). Vaults Bind Directly to Microtubules Via Their Caps and Not Their Barrels. *Cell Motility and the Cytoskeleton*, *56*(4), 225–236. https://doi.org/10.1002/cm.10147

Emsley, P., & Cowtan, K. (2004). Coot: model-building tools for molecular graphics. *Acta crystallographica. Section D, Biological crystallography*, *60*(Pt 12 Pt 1), 2126–2132. https://doi.org/10.1107/S0907444904019158

Fernandez-Leiro, R., & Scheres, S. H. W. (2016). Unravelling biological macromolecules with cryo-electron microscopy. In *Nature* (Vol. 537, Issue 7620, pp. 339–346). Nature Publishing Group. https://doi.org/10.1038/nature19948

Frank, J. (1996) Three-Dimensional Electron Microscopy of Macromolecular Assemblies (Academic Press, San Diego).

Frascotti, G., Galbiati, E., Mazzucchelli, M., Pozzi, M., Salvioni, L., Vertemara, J., & Tortora, P. (2021). cancers The Vault Nanoparticle: A Gigantic Ribonucleoprotein Assembly Involved in Diverse Physiological and Pathological Phenomena and an Ideal Nanovector for Drug Delivery and Therapy. *Cancers*, *13*, 707. https://doi.org/10.3390/cancers

Fort, R. S., & Duhagon, M. A. (2021). Pan-cancer chromatin analysis of the human vtRNA genes uncovers their association with cancer biology. *F1000Research*, *10*, 182. https://doi.org/10.12688/f1000research.28510.1

Foulger, J. H. (1931). *THE USE OF THE MOLISCH (a-NAPHTHOL) REACTIONS IN THE STUDY OF SUGARS IN BIOLOGICAL FLUIDS*.

Fukushima, H., Abe, T., Sakamoto, K., Tsujimoto, H., Mizuarai, S., & Oie, S. (2014). 3'-Ethynylcytidine, an RNA polymerase inhibitor, combined with cisplatin exhibits a potent synergistic growth-inhibitory effect via Vaults dysfunction. *BMC Cancer*, *14*(1). https://doi.org/10.1186/1471-2407-14-562

Gallo, S., Kong, E., Ferro, I., & Polacek, N. (2022). Small but Powerful: The Human Vault RNAs as Multifaceted Modulators of Pro-Survival Characteristics and Tumorigenesis. In *Cancers* (Vol. 14, Issue 11). MDPI. https://doi.org/10.3390/cancers14112787

Goldsmith, L. E., Yu, M., Rome, L. H., & Monbouquette, H. G. (2007). Vault nanocapsule dissociation into halves triggered at low pH. *Biochemistry*, *46*(10), 2865–2875. https://doi.org/10.1021/bi0606243

Gopinath, S. C. B., Matsugami, A., Katahira, M., & Kumar, P. K. R. (2005). Human vault-associated non-coding RNAs bind to mitoxantrone, a chemotherapeutic compound. *Nucleic Acids Research*, *33*(15), 4874–4881. https://doi.org/10.1093/nar/gki809

Gopinath, S. C. B., Wadhwa, R., & Kumar, P. K. R. (2010). Expression of noncoding vault RNA in human malignant cells and its importance in mitoxantrone resistance. *Molecular Cancer Research*, *8*(11), 1536–1546. https://doi.org/10.1158/1541-7786.MCR-10-0242

Guerra, P., González-Alamos, M., Llauró, A., Casañas, A., Querol-Audí, J., de Pablo, P. J., & Verdaguer, N. (2022). Symmetry disruption commits vault particles to disassembly. *Science Advances*, *8*(6). https://doi.org/10.1126/sciadv.abj7795

Hahne, J. C., Lampis, A., & Valeri, N. (2021). Vault RNAs: hidden gems in RNA and protein regulation. In *Cellular and Molecular Life Sciences* (Vol. 78, Issue 4, pp. 1487–1499). Springer Science and Business Media Deutschland GmbH. https://doi.org/10.1007/s00018-020-03675-9

Hamill, D. R., & Suprenant, K. A. (1997). Characterization of the sea urchin major vault protein: A possible role for vault ribonucleoprotein particles in nucleocytoplasmic transport. *Developmental Biology*, *190*(1), 117–128. https://doi.org/10.1006/dbio.1997.8676

Harrington, L.; McPhail, T.; Mar, V.; Zhou, W.; Oulton, R.; Bass, M.B.; Arruda, I.; Robinson, M.O. (1997) A mammalian telomerase associated protein. *Science*. 275, 973–977.
Henderson, R., Baldwin, J. M., Ceskat, T. A., Zemlin, F., Beckmann, E., & Downing, K. H. (1990). Model for the Structure of Bacteriorhodopsin Based on High-resolution Electron Cryo-microscopy. In *J. Mol. Biol* (Vol. 213).

Henríquez-Hernández, L. A., Moreno, M., Rey, A., Lloret, M., & Lara, P. C. (2012). MVP expression in the prediction of clinical outcome of locally advanced oral squamous cell carcinoma patients treated with radiotherapy. *Radiation Oncology*, *7*(1). https://doi.org/10.1186/1748-717X-7-147

Herlevsen, M., Oxford, G., Owens, C. R., Conaway, M., & Theodorescu, D. (2007). Depletion of major vault protein increases doxorubicin sensitivity and nuclear accumulation and disrupts its sequestration in lysosomes. *Molecular Cancer Therapeutics*, *6*(6), 1804–1813. https://doi.org/10.1158/1535-7163.MCT-06-0372

Herrmann, C., Golkaramnay, E., Inman, E., Rome, L., & Volknandt, W. (1999). Recombinant Major Vault Protein Is Targeted to Neuritic Tips of PC12. In *The Journal of Cell Biology* (Vol. 144, Issue 6). http://www.jcb.org

Herrmann, C., Zimmermann, H., & Volknandt, W. (1997). Analysis of a cDNA encoding the major vault protein from the electric ray Discopyge ommata. *Gene*, 188.

Horos, R., Büscher, M., Kleinendorst, R., Alleaume, A. M., Tarafder, A. K., Schwarzl, T., Dziuba, D., Tischer, C., Zielonka, E. M., Adak, A., Castello, A., Huber, W., Sachse, C., & Hentze, M. W. (2019). The Small Non-coding Vault RNA1-1 Acts as a Riboregulator of Autophagy. *Cell*, *176*(5), 1054-1067.e12. https://doi.org/10.1016/j.cell.2019.01.030

Huffman, K. E., & Corey, D. R. (2005). Major vault protein does not play a role in chemoresistance or drug localization in a non-small cell lung cancer cell line. *Biochemistry*, *44*(7), 2253–2261. https://doi.org/10.1021/bi047948g

Izquierdo, M.A.; van der Zee, A.G.; Vermorken, J.B.; van der Valk, P.; Beliën, J.A.; Giaccone, G.; Scheffer, G.L.; Flens, M.J.; Pinedo, H.M.; Kenemans, P.; (1995) Drug resistance-associated marker Lrp for prediction of response to chemotherapy and prognoses in advanced ovarian carcinoma. *J. Natl. Cancer Inst.,* 87, 1230–1237.

Izquierdo, M. A., Scheffer, G. L., Flens, M. J., Giaccone, G., Broxterman, H. J., Meijer, C. J. L. M., van der Valk, P., & Scheper, R. J. (1996). Broad Distribution of the Multidrug Resistance-Related Vault Lung Resistance Protein in Normal Human Tissues and Tumors. In *American Journal of Pathology* (Vol. 148, Issue 3).

Jumper, J., Evans, R., Pritzel, A., Green, T., Figurnov, M., Ronneberger, O., Tunyasuvunakool, K., Bates, R., Žídek, A., Potapenko, A., Bridgland, A., Meyer, C., Kohl, S. A. A., Ballard, A. J., Cowie, A., Romera-Paredes, B., Nikolov, S., Jain, R., Adler, J., … Hassabis, D. (2021). Highly accurate protein structure prediction with AlphaFold. *Nature*, *596*(7873), 583–589. https://doi.org/10.1038/s41586-021-03819-2

Jung, C. H., Ro, S. H., Cao, J., Otto, N. M., & Kim, D. H. (2010). MTOR regulation of autophagy. In *FEBS Letters* (Vol. 584, Issue 7, pp. 1287–1295). Elsevier. https://doi.org/10.1016/j.febslet.2010.01.017

Kedersha, N. L., M. C. Miquel, et al. (1990). Vaults. II. Ribonucleoprotein structures are highly conserved among higher and lower eukaryotes. *Journal of Cell Biology*, 110(4), 895-901.

Kedersha, N. L., Hill, D. E., Kronquist, K. E., & Rome, L. H. (1986). Subpopulations of liver coated vesicles resolved by preparative agarose gel electrophoresis. *Journal of Cell Biology*, 103(1), 287-297. http://rupress.org/jcb/article-pdf/103/1/287/1053272/287.pdf

Kedersha, N. L., & Rome, L. H. (1986). Isolation and characterization of a novel ribonucleoprotein Particle: large structures contain a single species of Small RNA. *Journal of Cell Biology*, 103. http://rupress.org/jcb/article-pdf/103/3/699/1053878/699.pdf

Khavnekar, S., Erdmann, P., & Wan, W. (2023). TOMOMAN: Streamlining Cryo-electron Tomography and Subtomogram Averaging Workflows Using TOMOgram MANager. *Microscopy and microanalysis: the official journal of Microscopy Society of America, Microbeam Analysis Society, Microscopical Society of Canada*, *29*(Supplement_1), 1020. https://doi.org/10.1093/micmic/ozad067.516

Kickhoefer, V. A., Searlesl, R. P., Kedershall, N. L., Garber, M. E., Johnson, D. L., & Rome, L. H. (1993). Vault ribonucleoprotein particles from rat and bullfrog contain a related small RNA that is transcribed by RNA polymerase III. *Journal of Cell Biology* 268(11): 7868-73.

Kickhoefer, V. A., S. K. Vasu, et al. (1996). Vaults are the answer, what is the question? *Trends in Cell Biology* 6(5): 174-8.

Kickhoefer, V. A., A. C. Siva, et al. (1999). The 193-kD vault protein, VPARP, is a novel poly(ADP-ribose) polymerase. *Journal of Cell Biology*, 146(5), 917-28.

Kickhoefer, V. A., A. G. Stephen, et al. (1999). Vaults and telomerase share a common subunit, TEP1. *Journal of Cell Biology*, 274(46), 32712-7. http://www.jbc.org

Kickhoefer, V. A., Liu, Y., Kong, L. B., Snow, B. E., Stewart, P. L., Harrington, L., & Rome, L. H. (2001). The Telomerase/Vault-associated Protein TEP1 Is Required for Vault RNA Stability and Its Association with the Vault Particle. In *The Journal of Cell Biology* (Vol. 152, Issue 1). http://www.jcb.org/cgi/content/full/152/1/157

Kickhoefer, V. A., Han, M., Raval-Fernandes, S., Poderycki, M. J., Moniz, R. J., Vaccari, D., Silvestry, M., Stewart, P. L., Kelly, K. A., & Rome, L. H. (2009). Targeting vault nanoparticles to specific cell surface receptors. *ACS Nano*, *3*(1), 27–36. https://doi.org/10.1021/nn800638x

Kimanius, D., Dong, L., Sharov, G., Nakane, T., & Scheres, S. H. W. (2021). New tools for automated cryo-EM single-particle analysis in RELION-4.0. *Biochemical Journal*, *478*(24), 4169–4185. https://doi.org/10.1042/BCJ20210708

Kolli, S., Zito, C. I., Mossink, M. H., Wiemer, E. A. C., & Bennett, A. M. (2004). The major vault protein is a novel substrate for the tyrosine phosphatase SHP-2 and scaffold protein in epidermal growth factor signalling. *Journal of Biological Chemistry*, *279*(28), 29374–29385. https://doi.org/10.1074/jbc.M313955200

Kong, L. B., Siva, A. C., Rome, L. H., & Stewart, P. L. (1999). Structure of the vault, a ubiquitous cellular component. *Structure* 7(4):371-9. http://biomednet.com/elecref/0969212600700371

Kong, L. B., Siva, A. C., Kickhoefer, V. A., Rome, L. H., & Stewart, P. L. (2000). RNA location and modeling of a WD40 repeat domain within the vault. *RNA*, 6(6), 890-900.

Koonin, E.V. and Aravind, L. (2000) The NACHT family—a new group of predicted NTPases implicated in apoptosis and MHC transcription activation. *Trends Biochem.* Sci. 2000, 25, 223–224.

Kowalski, M. P., Dubouix-Bourandy, A., Bajmoczi, M., Golan, D. E., Zaidi, T., Coutinho-Sledge, Y. S., Gygi, M. P., Gygi, S. P., Wiemer, E. A. C., & Pier, G. B. (2007). Host resistance to lung infection mediated by major vault protein in epithelial cells. *Science*, *317*(5834), 130–132. https://doi.org/10.1126/science.1142311

Kreppel, L., Fey, P., Gaudet, P., Just, E., Kibbe, W. A., Chisholm, R. L., & Kimmel, A. R. (2004). dictyBase: A new Dictyostelium discoideum genome database. *Nucleic Acids Research*, *32*(DATABASE ISS.). https://doi.org/10.1093/nar/gkh138

Kühlbrandt, W. (2014). The resolution revolution. In *Science* (Vol. 343, Issue 6178, pp. 1443–1444). American Association for the Advancement of Science. https://doi.org/10.1126/science.1251652

Kulsoom, B., Shamsi, T. S., & Afsar, N. A. (2019). Lung resistance-related protein (LRP) predicts favorable therapeutic outcome in Acute Myeloid Leukemia. *Scientific Reports*, *9*(1). https://doi.org/10.1038/s41598-018-36780-8

Laemmli U. K. (1970). Cleavage of structural proteins during the assembly of the head of bacteriophage T4. *Nature*, *227*(5259), 680–685. https://doi.org/10.1038/227680a0

Lamark, T.; Svenning, S.; Johansen, T. (2017) Regulation of selective autophagy: The p62/SQSTM1 paradigm. *Essays Biochem*. 61, 609–624

Lamming, D. W. (2016). Inhibition of the mechanistic target of rapamycin (mTOR)–Rapamycin and beyond. *Cold Spring Harbor Perspectives in Medicine*, *6*(5). https://doi.org/10.1101/cshperspect.a025924

Lee, K., Kunkeaw, N., Jeon, S. H., Lee, I., Johnson, B. H., Kang, G. Y., Bang, J. Y., Park, H. S., Leelayuwat, C., & Lee, Y. S. (2011). Precursor miR-886, a novel noncoding RNA repressed in cancer, associates with PKR and modulates its activity. *RNA*, *17*(6), 1076–1089. https://doi.org/10.1261/rna.2701111

Lehuédé, C., Li, X., Dauvillier, S., Vaysse, C., Franchet, C., Clement, E., Esteve, D., Longué, M., Chaltiel, L., le Gonidec, S., Lazar, I., Geneste, A., Dumontet, C., Valet, P., Nieto, L., Fallone, F., & Muller, C. (2019). Adipocytes promote breast cancer resistance to chemotherapy, a process amplified by obesity: Role of the major vault protein (MVP). *Breast Cancer Research*, *21*(1). https://doi.org/10.1186/s13058-018-1088-6

Levine, A. J. (1997). p53, the Cellular Gatekeeper Review for Growth and Division. In *Cell* (Vol. 88).

Li, X., Mooney, P., Zheng, S., Booth, C. R., Braunfeld, M. B., Gubbens, S., Agard, D. A., & Cheng, Y. (2013). Electron counting and beam-induced motion correction enable near-atomic-resolution single-particle cryo-EM. *Nature Methods*, *10*(6), 584–590. https://doi.org/10.1038/nmeth.2472

Bibliography

Lin, D., Shen, Y., & Liang, T. (2023). Oncolytic virotherapy: basic principles, recent advances and future directions. In *Signal Transduction and Targeted Therapy* (Vol. 8, Issue 1). Springer Nature. https://doi.org/10.1038/s41392-023-01407-6

List, A. F., Spier, C. S., Grogan, T. M., Johnson, C., Roe, D. J., Greer, J. P., Wolff, S. N., Broxterman, H. J., Scheffer, G. L., Scheper, R. J., & Dalton, W. S. (1996). Overexpression of the Major Vault Transporter Protein Lung-Resistance Protein Predicts Treatment Outcome in Acute Myeloid Leukemia. Blood, 87, 2464-2469. http://ashpublications.org/blood/article-pdf/87/6/2464/620908/2464.pdf

Liu, Y., Snow, B. E., Prakash Hande, M., Baerlocher, G., Kickhoefer, V. A., Yeung, D., Wakeham, A., Itie, A., Siderovski, D. P., Lansdorp, P. M., Robinson, M. O., & Harrington, L. (2000). Telomerase-Associated Protein TEP1 Is Not Essential for Telomerase Activity or Telomere Length Maintenance In Vivo. In *Molecular and Cellular Biology.* (Vol. 20, Issue 21).

Liu, Y., Snow, B. E., Kickhoefer, V. A., Erdmann, N., Zhou, W., Wakeham, A., Gomez, M., Rome, L. H., & Harrington, L. (2004). Vault Poly (ADP-Ribose) Polymerase Is Associated with Mammalian Telomerase and Is Dispensable for Telomerase Function and Vault Structure In Vivo. *Molecular and Cellular Biology*, *24*(12), 5314–5323. https://doi.org/10.1128/mcb.24.12.5314-5323.2004

Llauró, A., Guerra, P., Irigoyen, N., Rodríguez, J. F., Verdaguer, N., & de Pablo, P. J. (2014). Mechanical stability and reversible fracture of vault particles. *Biophysical Journal*, *106*(3), 687–695. https://doi.org/10.1016/j.bpj.2013.12.035

Llauró, A., Guerra, P., Kant, R., Bothner, B., Verdaguer, N., & de Pablo, P. J. (2016). Decrease in pH destabilizes individual vault nanocages by weakening the inter-protein lateral interaction. *Scientific Reports*, *6*. https://doi.org/10.1038/srep34143

Losert, A., Lötsch, D., Lackner, A., Koppensteiner, H., Peter-Vörösmarty, B., Steiner, E., Holzmann, K., Grunt, T., Schmid, K., Marian, B., Grasl-Kraupp, B., Schulte-Hermann, R., Krupitza, G., Berger, W., & Grusch, M. (2012). The major vault protein mediates resistance to epidermal growth factor receptor inhibition in human hepatoma cells. *Cancer Letters*, *319*(2), 164–172. https://doi.org/10.1016/j.canlet.2012.01.002

Lötsch, D., Steiner, E., Holzmann, K., Spiegl-Kreinecker, S., Pirker, C., Hlavaty, J., Petznek, H., Hegedus, B., Garay, T., Mohr, T., Sommergruber, W., Grusch, M., & Berger, W. (2013). Major vault protein supports glioblastoma survival and migration by upregulating the EGFR/PI3K signalling axis. In *Oncotarget* (Vol. 4). www.impactjournals.com/oncotarget

Lou, L., Wang, J., Lv, F., Wang, G., Li, Y., Xing, L., Shen, H., & Zhang, X. (2020). Y-box binding protein 1 (YB-1) promotes gefitinib resistance in lung adenocarcinoma cells by activating AKT signalling and epithelial-mesenchymal transition through targeting major vault protein (MVP). *Cell. Oncol.* https://doi.org/10.1007/s13402-020-00556-y/Published

Luckow, V. A., Lee, S. C., Barry, G. F., & Olins, P. O. (1993). Efficient generation of infectious recombinant baculoviruses by site-specific transposon-mediated insertion of foreign genes into a baculovirus genome propagated in Escherichia coli. *Journal of virology*, *67*(8), 4566–4579. https://doi.org/10.1128/JVI.67.8.4566-4579.1993

Mashima, T., Kudo, M., Takada, Y., Matsugami, A., Gopinath, S. C. B., Kumar, P. K. R., & Katahira, M. (2008). Interactions between antitumor drugs and vault RNA. *Nucleic Acids Symposium Series (2004)*, *52*, 217–218. https://doi.org/10.1093/nass/nrn110

Mastronarde, D. N., & Held, S. R. (2017). Automated tilt series alignment and tomographic reconstruction in IMOD. *Journal of Structural Biology*, *197*(2), 102–113. https://doi.org/10.1016/j.jsb.2016.07.011

McKay, M. M., & Morrison, D. K. (2007). Integrating signals from RTKs to ERK/MAPK. In *Oncogene* (Vol. 26, Issue 22, pp. 3113–3121). https://doi.org/10.1038/sj.onc.1210394

McMullan, G., Faruqi, A. R., Clare, D., & Henderson, R. (2014). Comparison of optimal performance at 300keV of three direct electron detectors for use in low dose electron microscopy.*Ultramicroscopy*,*147*,156–163. https://doi.org/10.1016/j.ultramic.2014.08.002

McMullan, G. et al. (2016) Chapter one – direct electron detectors. In Methods in Enzymology (Vol. 579) (Crowther, R.A., ed.), pp. 1–17, Academic Press

Meyer-Ficca, M. L., Meyer, R. G., Jacobson, E. L., & Jacobson, M. K. (2005). Poly(ADP-ribose) polymerases: Managing genome stability. In *International Journal of Biochemistry and Cell Biology* (Vol. 37, Issue 5 SPEC. ISS., pp. 920–926).

Mikyas, Y., Makabi, M., Raval-Fernandes, S., Harrington, L., Kickhoefer, V. A., Rome, L. H., & Stewart, P. L. (2004). Cryoelectron microscopy imaging of recombinant and tissue derived vaults: Localization of the MVP N termini and VPARP. *Journal of Molecular Biology*, *344*(1), 91–105. https://doi.org/10.1016/j.jmb.2004.09.021

Minaguchi, T., Waite, K. A., & Eng, C. (2006). Nuclear localization of PTEN is regulated by Ca2+ through a tyrosil phosphorylation-independent conformational modification in major vault protein. *Cancer Research*, *66*(24), 11677–11682. https://doi.org/10.1158/0008-5472.CAN-06-2240

Morales, J. C., Li, L., Fattah, F. J., Dong, Y., Bey, E. A., Patel, M., Gao, J., & Boothman, D. A. (2014). Review of Poly (ADP-ribose) Polymerase (PARP) Mechanisms of Action and Rationale for Targeting in Cancer and Other Diseases. *Crit. Re. Eukaryot. Gene Expr*. 24, 15-28.

Mossink, M.H.; van Zon, A.; Fränzel-Luiten, E.; Schoester, M.; Kickhoefer, V.A.; Scheffer, G.L.; Scheper, R.J.; Sonneveld, P.; Wiemer, E.A. (2002) Disruption of the murine major vault protein (MVP/LRP) gene does not induce hypersensitivity to cytostatics. *Cancer Res*. 62, 7298–7304.

Mossink, M. H., van Zon, A., Scheper, R. J., Sonneveld, P., & Wiemer, E. A. C. (2003). Vaults: A ribonucleoprotein particle involved in drug resistance? In *Oncogene* (Vol. 22, Issue 47 REV. ISS. 6, pp. 7458–7467). https://doi.org/10.1038/sj.onc.1206947

Mrazek, J., Toso, D., Ryazantsev, S., Zhang, X., Zhou, Z. H., Fernandez, B. C., Kickhoefer, V. A., & Rome, L. H. (2014). Polyribosomes are molecular 3D nanoprinters that orchestrate the assembly of vault particles. *ACS Nano*, *8*(11), 11552–11559. https://doi.org/10.1021/nn504778h

Murphy, G. E., & Jensen, G. J. (2007). Electron cryotomography. *BioTechniques*, *43*(4), 413–423. https://doi.org/10.2144/000112568

Nogales, E., & Scheres, S. H. W. (2015). Cryo-EM: A Unique Tool for the Visualization of Macromolecular Complexity. In *Molecular Cell* (Vol. 58, Issue 4, pp. 677–689). Cell Press. https://doi.org/10.1016/j.molcel.2015.02.019

Nogales, E. (2016). SPECIAL FEATURE | HISTORICAL COMMENTARY METHOD OF THE YEAR The development of cryo-EM into a mainstream structural biology technique. In *NATURE METHODS* (Vol. 24, Issue 1). http://emdatabank.org/

Oguri, T.; Fujiwara, Y.; Ochiai, M.; Fujitaka, K.; Miyazaki, M.; Takahashi, T.; Yokozaki, M.; Isobe, T.; Ohune, T.; Tsuya, T.; et al. (1998) Expression of lung-resistance protein gene is not associated with platinum drug exposure in lung cancer. *Anticancer Res*. 18, 4159–4162

Paspalas, C. D., Perley, C. C., Venkitaramani, D. v., Goebel-Goody, S. M., Zhang, Y., Kurup, P., Mattis, J. H., & Lombroso, P. J. (2009). Major vault protein is expressed along the nucleus-neurite axis and associates with mRNAs in cortical neurons. *Cerebral Cortex*, *19*(7), 1666–1677. https://doi.org/10.1093/cercor/bhn203

Pettersen, E. F., Goddard, T. D., Huang, C. C., Couch, G. S., Greenblatt, D. M., Meng, E. C., & Ferrin, T. E. (2004). UCSF Chimera--a visualization system for exploratory research and analysis. *Journal of computational chemistry*, *25*(13), 1605–1612. https://doi.org/10.1002/jcc.20084

Poderycki, M. J., Rome, L. H., Harrington, L., & Kickhoefer, V. A. (2005). The p80 homology region of TEP1 is sufficient for its association with the telomerase and vault RNAs, and the vault particle. *Nucleic Acids Research*, *33*(3), 893–902. https://doi.org/10.1093/nar/gki234

Poderycki, M. J., Kickhoefer, V. A., Kaddis, C. S., Raval-Fernandes, S., Johansson, E., Zink, J. I., Loo, J. A., & Rome, L. H. (2006). The vault exterior shell is a dynamic structure that allows incorporation of vault-associated proteins into its interior. *Biochemistry*, *45*(39), 12184–12193. https://doi.org/10.1021/bi0610552

Potter, C. S., Chu, H., Frey, B., Green, C., Kisseberth, N., Madden, T. J., Miller, K. L., Nahrstedt, K., Pulokas, J., Reilein, A., Tcheng, D., & Weber, D. (1999). Leginon: a system for fully automated acquisition of 1000 electron micrographs a day. In *Ultramicroscopy* (Vol. 77).

Punjani, A., Rubinstein, J. L., Fleet, D. J., & Brubaker, M. A. (2017). cryoSPARC: algorithms for rapid unsupervised cryo-EM structure determination. *Nature methods*, *14*(3), 290–296. https://doi.org/10.1038/nmeth.4169

Querol-Audí, J., Perez-Luque, R., Fita, I., Lopéz-Iglesias, C., Castón, J. R., Carrascosa, J. L., & Verdaguer, N. (2005). Preliminary analysis of two and three dimensional crystals of vault ribonucleoprotein particles. *Journal of Structural Biology*, *151*(1), 111–115. https://doi.org/10.1016/j.jsb.2005.04.002

Querol-Audí, J., Casãas, A., Usón, I., Luque, D., Castón, J. R., Fita, I., & Verdaguer, N. (2009). The mechanism of vault opening from the high-resolution structure of the N-terminal repeats of MVP. *EMBO Journal*, *28*(21), 3450–3457. https://doi.org/10.1038/emboj.2009.274

Raleigh, E.A., Elbing, K. and Brent, R. (2002), Selected Topics from Classical Bacterial Genetics. Current Protocols in Molecular Biology, 59: 1.4.1-1.4.14. https://doi.org/10.1002/0471142727.mb0104s59

Rome, L., N. Kedersha, et al. (1991). Unlocking vaults: organelles in search of a function. *Trends in Cell Biology*, 1(2-3), 47-50.

Robert, X., & Gouet, P. (2014). Deciphering key features in protein structures with the new ENDscript server. *Nucleic Acids Research*, *42*(W1). https://doi.org/10.1093/nar/gku316

Rohou, A., & Grigorieff, N. (2015). CTFFIND4: Fast and accurate defocus estimation from electron micrographs. *Journal of Structural Biology*, *192*(2), 216–221. https://doi.org/10.1016/j.jsb.2015.08.008

Schaffer, M., Mahamid, J., Engel, B. D., Laugks, T., Baumeister, W., & Plitzko, J. M. (2017). Optimized cryo-focused ion beam sample preparation aimed at in situ structural studies of membrane proteins. *Journal of Structural Biology*, *197*(2), 73–82. https://doi.org/10.1016/j.jsb.2016.07.010

Scheres, S. H. W. (2012). RELION: Implementation of a Bayesian approach to cryo-EM structure determination. *Journal of Structural Biology*, *180*(3), 519–530. https://doi.org/10.1016/j.jsb.2012.09.006

Scheres, S. H. W. (2012). A bayesian view on cryo-EM structure determination. *Journal of Molecular Biology*, *415*(2), 406–418. https://doi.org/10.1016/j.jmb.2011.11.010

Schooley, A., Vollmer, B., & Antonin, W. (2012). Building a nuclear envelope at the end of mitosis: Coordinating membrane reorganization, nuclear pore complex assembly, and chromatin de-condensation. In *Chromosoma* (Vol. 121, Issue 6, pp. 539–554). https://doi.org/10.1007/s00412-012-0388-3

Shen, W. H., Balajee, A. S., Wang, J., Wu, H., Eng, C., Pandolfi, P. P., & Yin, Y. (2007). Essential Role for Nuclear PTEN in Maintaining Chromosomal Integrity. *Cell*, *128*(1), 157–170. https://doi.org/10.1016/j.cell.2006.11.042

Sievers, F., & Higgins, D. G. (2018). Clustal Omega for making accurate alignments of many protein sequences. *Protein science: a publication of the Protein Society*, *27*(1), 135–145. https://doi.org/10.1002/pro.3290

Sigworth, F. J. (1998). A Maximum-Likelihood Approach to Single-Particle Image Refinement. *J. Struct. Biol.* 122, 328-339.

Slesina, M., Inman, E. M., Moore, A. E., Goldhaber, J. I., Rome, L. H., & Volknandt, W. (2006). Movement of vault particles visualized by GFP-tagged major vault protein. *Cell and Tissue Research*, *324*(3), 403–410. https://doi.org/10.1007/s00441-006-0158-8

Stadler, P. F., Chen, J. J. L., Hackermüller, J., Hoffmann, S., Horn, F., Khaitovich, P., Kretzschmar, A. K., Mosig, A., Prohaska, S. J., Qi, X., Schutt, K., & Ullmann, K. (2009). Evolution of vault RNAs. *Molecular Biology and Evolution*, *26*(9), 1975–1991. https://doi.org/10.1093/molbev/msp112

Stephen, A. G., Raval-Fernandes, S., Huynh, T., Torres, M., Kickhoefer, V. A., & Rome, L. H. (2001). Assembly of Vault-like Particles in Insect Cells Expressing only the Major Vault Protein. *Journal of Biological Chemistry*, *276*(26), 23217–23220. https://doi.org/10.1074/jbc.C100226200

Suprenant, K. A., Bloom, N., Fang, J., & Lushington, G. (2007). The major vault protein is related to the toxic anion resistance protein (TelA) family. *Journal of Experimental Biology*, *210*(6), 946–955. https://doi.org/10.1242/jeb.001800

Tanaka H, Kato K, Yamashita E, Sumizawa T, Zhou Y, Yao M, Iwasaki K, Yoshimura M, Tsukihara T (2009). The structure of rat liver vault at 3.5 angstrom resolution. *Science,* 323(5912), 384-8.

Tang, S., Bai, C., Yang, P., & Chen, X. (2013). 14-3-3ε boosts bleomycin-induced DNA damage response by inhibiting the drug-resistant activity of MVP. *Journal of Proteome Research*, *12*(6), 2511–2524. https://doi.org/10.1021/pr301085c

Taylor, K.A. and Glaeser, R.M. (1974) Electron diffraction of frozen hydrated protein crystals. *Science* 186 (4168), 1036–1037.

Treppendahl, M. B., Qiu, X., Søgaard, A., Yang, X., Nandrup-Bus, C., Hother, C., Andersen, M. K., Kjeldsen, L., Möllgaard, L., Hellström-Lindberg, E., Jendholm, J., Porse, B. T., Jones, P. A., Liang, G., & Grønbæk, K. (2012). Allelic methylation levels of the noncoding VTRNA2-1 located on chromosome 5q31.1 predict outcome in AML. *Blood*, *119*(1), 206–216. https://doi.org/10.1182/blood-2011-06-362541

Van Zon, A., Mossink, M. H., Schoester, M., Scheffer, G. L., Scheper, R. J., Sonneveld, P., & Wiemer, E. A. C. (2001). Multiple human vault RNAs: Expression and association with the vault complex. *Journal of Biological Chemistry*, *276*(40), 37715–37721. https://doi.org/10.1074/jbc.M106055200

Van Zon, A., Mossink, M. H., Schoester, M., Houtsmuller, A. B., Scheffer, G. L., Scheper, R. J., Sonneveld, P., & Wiemer, E. A. C. (2003). The formation of vault-tubes: A dynamic interaction between vaults and vault PARP. *Journal of Cell Science*, *116*(21), 4391–4400. https://doi.org/10.1242/jcs.00749

Van Zon, A., Mossink, M. H., Houtsmuller, A. B., Schoester, M., Scheffer, G. L., Scheper, R. J., Sonneveld, P., & Wiemer, E. A. C. (2006). Vault mobility depends in part on microtubules and vaults can be recruited to the nuclear envelope. *Experimental Cell Research*, *312*(3), 245–255. https://doi.org/10.1016/j.yexcr.2005.10.016

Vasu, S. K., Kedersha, N. L., & Rome, L. H. (1993). cDNA cloning and disruption of the major vault protein alpha gene (mvpA) in Dictyostelium discoideum. *The Journal of biological chemistry*, *268*(21), 15356–15360.

Vasu, S. K., & Rome, L. H. (1995). Dictyostelium vaults: disruption of the major proteins reveals growth and morphological defects and uncovers a new associated protein. *The Journal of biological chemistry*, *270*(28), 16588–16594. https://doi.org/10.1074/jbc.270.28.16588

Vaughn, J. L., Goodwin, R. H., Tompkins, G. J., & McCawley, P. (1977). The establishment of two cell lines from the insect Spodoptera frugiperda (Lepidoptera; Noctuidae). *In vitro*, *13*(4), 213–217. https://doi.org/10.1007/BF02615077

Wan, W., & Briggs, J. A. G. (2016). Cryo-Electron Tomography and Subtomogram Averaging. In *Methods in Enzymology* (1st ed., Vol. 579). Elsevier Inc. https://doi.org/10.1016/bs.mie.2016.04.014

Wan, W., Khavnekar, S., Wagner, J., Erdmann, P., & Baumeister, W. (2020). STOPGAP: A Software Package for Subtomogram Averaging and Refinement. *Microscopy and Microanalysis*, *26*(S2), 2516–2516. https://doi.org/10.1017/s143192762002187x

Weinrich, S. L., Pruzan, R., Ma, L., Ouellette, M., Tesmer, V. M., Holt, S. E., Bodnar, A. G., Lichtsteiner, S., Kim, N. W., Trager, mes B., Taylor, R. D., Carlos, R., Andrews, W. H., Wright, W. E., Shay, J., Harley, C. B., & Morin, G. B. (1997). Reconstitution of human telomerase with the template RNA component hTR and the catalytic protein subunit hTRT. *Nat Genet*. 17 (4):498-502.

Woodward, C. L., Mendonça, L. M., & Jensen, G. J. (2015). Direct visualization of vaults within intact cells by electron cryo-tomography. *Cellular and Molecular Life Sciences*, *72*(17), 3401–3409. https://doi.org/10.1007/s00018-015-1898-y

Wu, H., Goel, V., & Haluska, F. G. (2003). PTEN signaling pathways in melanoma. In *Oncogene* (Vol. 22, Issue 20, pp. 3113–3122). https://doi.org/10.1038/sj.onc.1206451

Yang, J., Kickhoefer, V. A., Ng, B. C., Gopal, A., Bentolila, L. A., John, S., Tolbert, S. H., & Rome, L. H. (2010). Vaults are dynamically unconstrained cytoplasmic nanoparticles capable of half vault exchange. *ACS Nano*, *4*(12), 7229–7240. https://doi.org/10.1021/nn102051r

Yi, C., & Deng, X. W. (2005). COP1 - From plant photomorphogenesis to mammalian tumorigenesis. In *Trends in Cell Biology* (Vol. 15, Issue 11, pp. 618–625). https://doi.org/10.1016/j.tcb.2005.09.007

Yi, C., Li, S., Wang, J., Wei, N., & Deng, X. W. (2006). Affinity purification reveals the association of WD40 protein constitutive photomorphogenic 1 with the hetero-oligomeric TCP-1 chaperonin complex in mammalian cells. *International Journal of Biochemistry and Cell Biology*, *38*(7), 1076–1083. https://doi.org/10.1016/j.biocel.2005.12.019

Yu, K., Yau, Y. H., Sinha, A., Tan, T., Kickhoefer, V. A., Rome, L. H., Lee, H., Shochat, S. G., & Lim, S. (2017). Modulation of the Vault Protein-Protein Interaction for Tuning of Molecular Release. *Scientific Reports*, *7*(1). https://doi.org/10.1038/s41598-017-12870-x

Yu, H.; Li, M.; He, R.; Fang, P.; Wang, Q.; Yi, Y.; Wang, F.; Zhou, L.; Zhang, Y.; Chen, A.; (2020) Major vault protein promotes hepatocellular carcinoma through targeting interferon regulatory factor 2 and decreasing p53 activity. *Hepatology* 72, 518–534.

Zhang K. (2016). Gctf: Real-time CTF determination and correction. *Journal of structural biology*, *193*(1), 1–12. https://doi.org/10.1016/j.jsb.2015.11.003

Zhenbao, Fotouhi-Ardakani, N., Wu, L., Maoui, M., Wang, S., Banville, D., & Shen, S. H. (2002). PTEN associates with the vault particles in HeLa cells. *Journal of Biological Chemistry*. https://doi.org/10.1074/jbc.M207608200

Zheng, S. Q., Palovcak, E., Armache, J. P., Verba, K. A., Cheng, Y., & Agard, D. A. (2017). MotionCor2: anisotropic correction of beam-induced motion for improved cryo-electron microscopy. *Nature methods*, *14*(4), 331–332. https://doi.org/10.1038/nmeth.4193

Zheng, S., Wolff, G., Greenan, G., Chen, Z., Faas, F. G. A., Bárcena, M., Koster, A. J., Cheng, Y., & Agard, D. A. (2022). AreTomo: An integrated software package for automated marker-free, motion-corrected cryo-electron tomographic alignment and reconstruction. *Journal of Structural Biology: X*, *6*. https://doi.org/10.1016/j.yjsbx.2022.100068

Annex

ANNEX

Tissue/Cell Lines	Drug(s)	Associated MDR Proteins	Vault Component	Mechanism (When Known)
Several lung cancer cell lines	DOX	-	MVP, vtRNA	-
Human colon carcinoma SW620 cells	DOX; vincristine; etoposide; gramicidin D; paclitaxel	-	MVP	-
U-937 human leukaemia cells	DOX; etoposide; mitoxantrone; 5-fluorouracil	-	MVP *	-
SW620 human colon cancer cells	Doxorubicin; etoposide; cisplatin; SN-38s	-	MVP *	-
Ovarian carcinoma	Platinum based; Alkylating	-	MVP	-
Human lung adenocarcinoma	Cisplatin	Bcl-2; survivin	MVP	-
Human lung adenocarcinoma A549	Cisplatin	-	MVP	-
Myeloma cells	Mitoxantrone	-	MVP; vtRNA	-
Leukaemic cells from AML patients	Mitoxantrone	-	MVP *	-
GBM	Several, including temozolomide or bis-chloroethylnitrosourea	-	MVP	-
Breast cancer cell lines cocultured with adipocytes	DOX	-	MVP	Drug efflux from the nucleus
UMUC-3 human urothelial bladder cancer cell line	DOX	-	MVP	Drug export from the nucleus to lysosomes
HCC cell lines	Gefitinib (EGFR inhibitor)	-	MVP	Possible uncoupling of AKT activation from EGFR
Human lung adenocarcinoma	Gefitinib (EGFR inhibitor)	-	MVP	Uncoupling of AKT activation from EGFR
HCC cell lines	Bleomycin	14-3-3ε	MVP	Drug encapsulation and possible extrusion
KB nasopharingeal carcinoma cell lines	Cisplatin	-	MVP; vtRNA(s)	Drug efflux from nucleus
MG63 and U2OS osteosarcoma; U118MG glioblastoma; U-937 lymphoma;	Mitoxantrone	-	vtRNA1-1	Mitoxantrone sequestration by vtRNA1-1

* Detection of increased mRNA levels.

Table 1 Annex. Multidrug resistance associated with vault overexpression an related mechanisms when known.

Annex

A: R4α-ins-184-185 construct

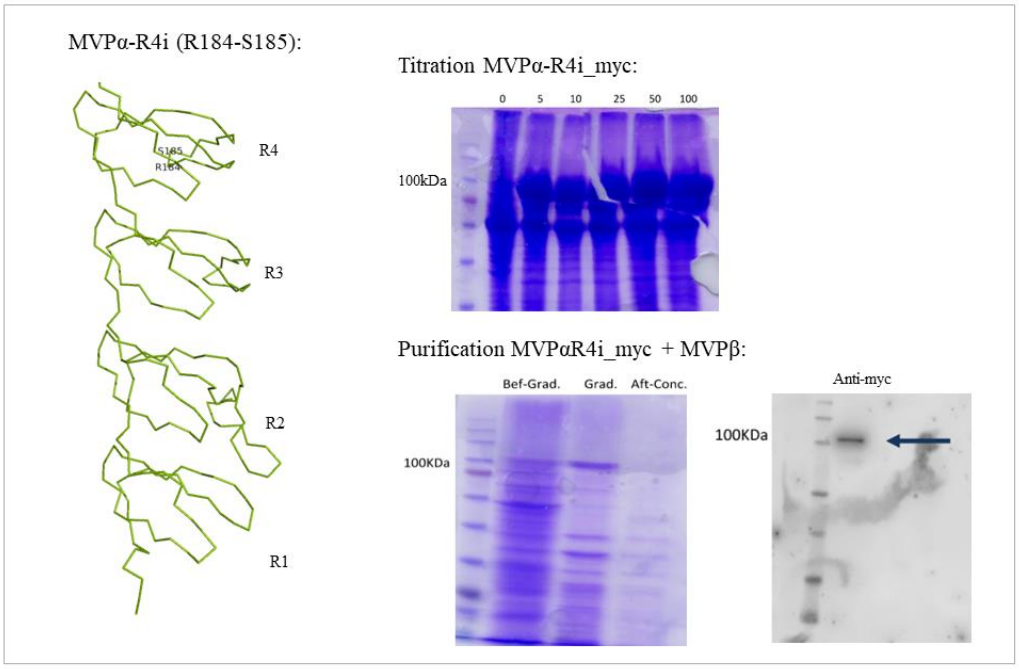

A':

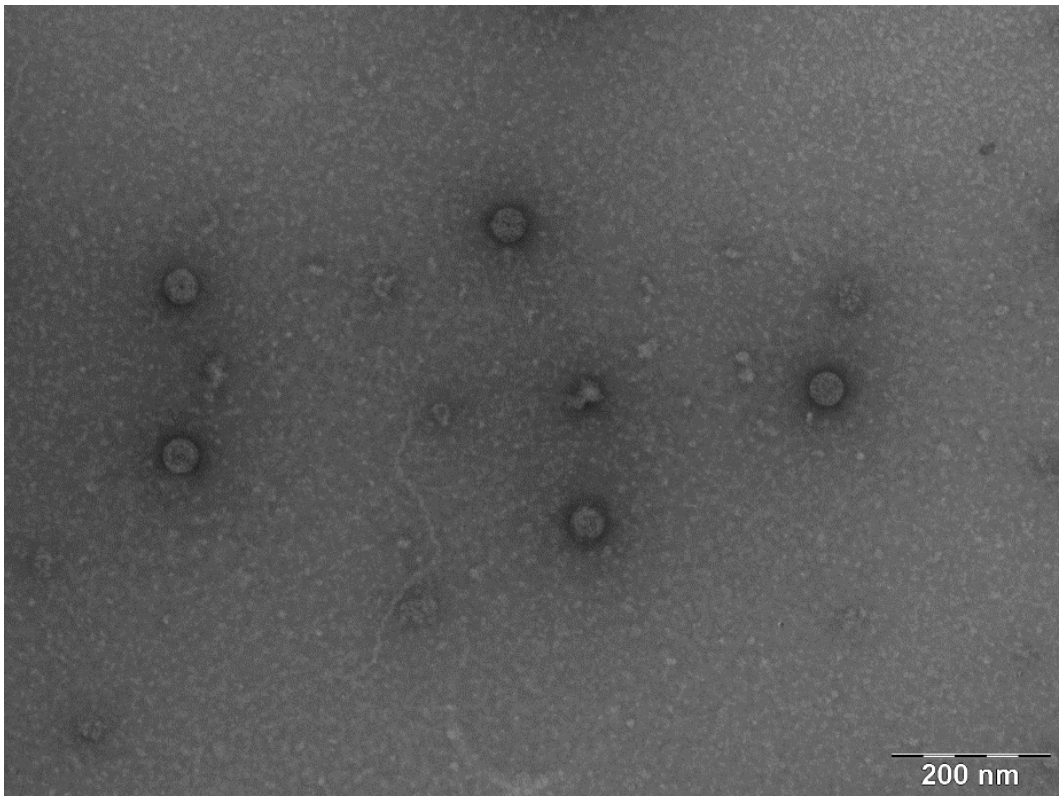

B: R4α-sus-179-190 construct

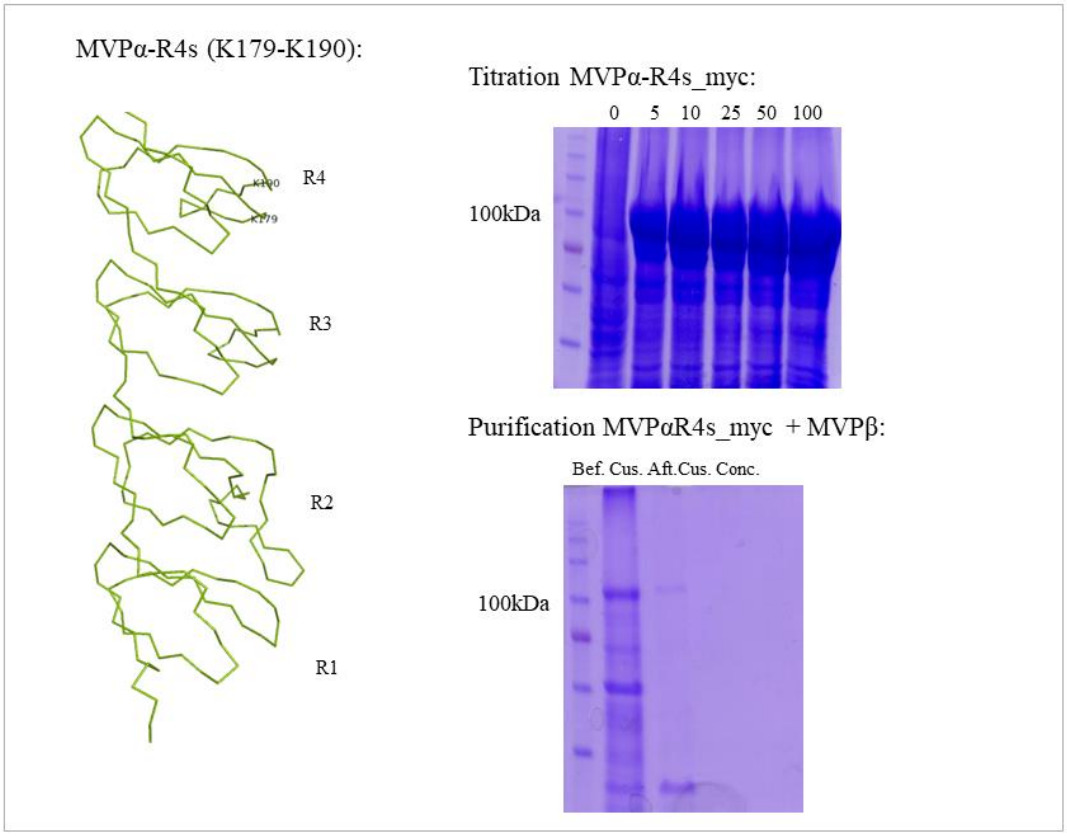

C: R5α-sus-234-243 construct

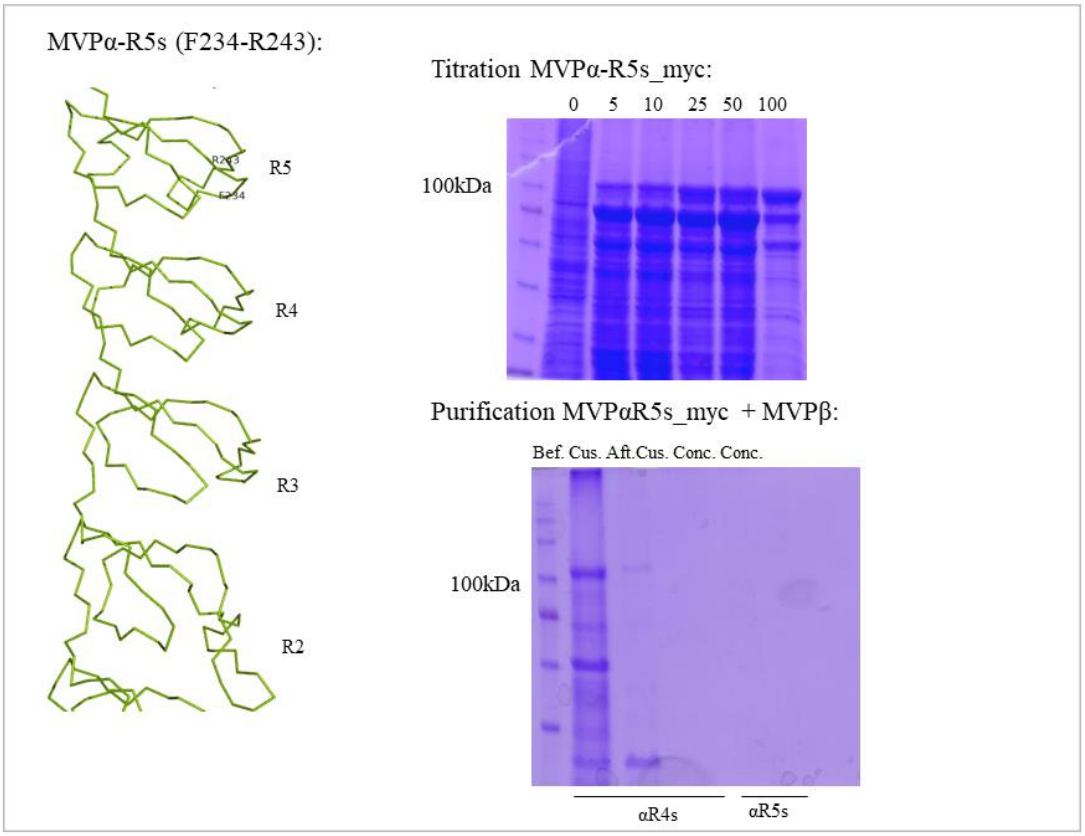

D: R6α-ins-287-294 construct

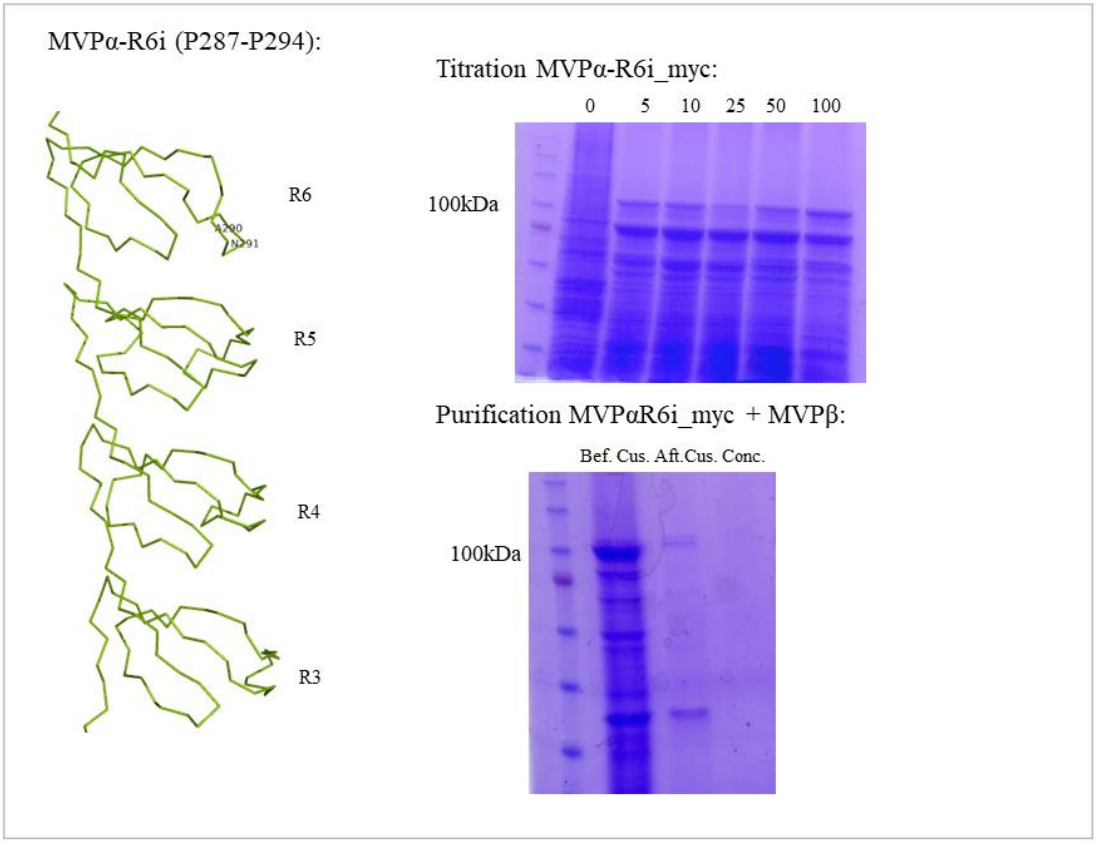

E: R6α-sus-287-294 construct

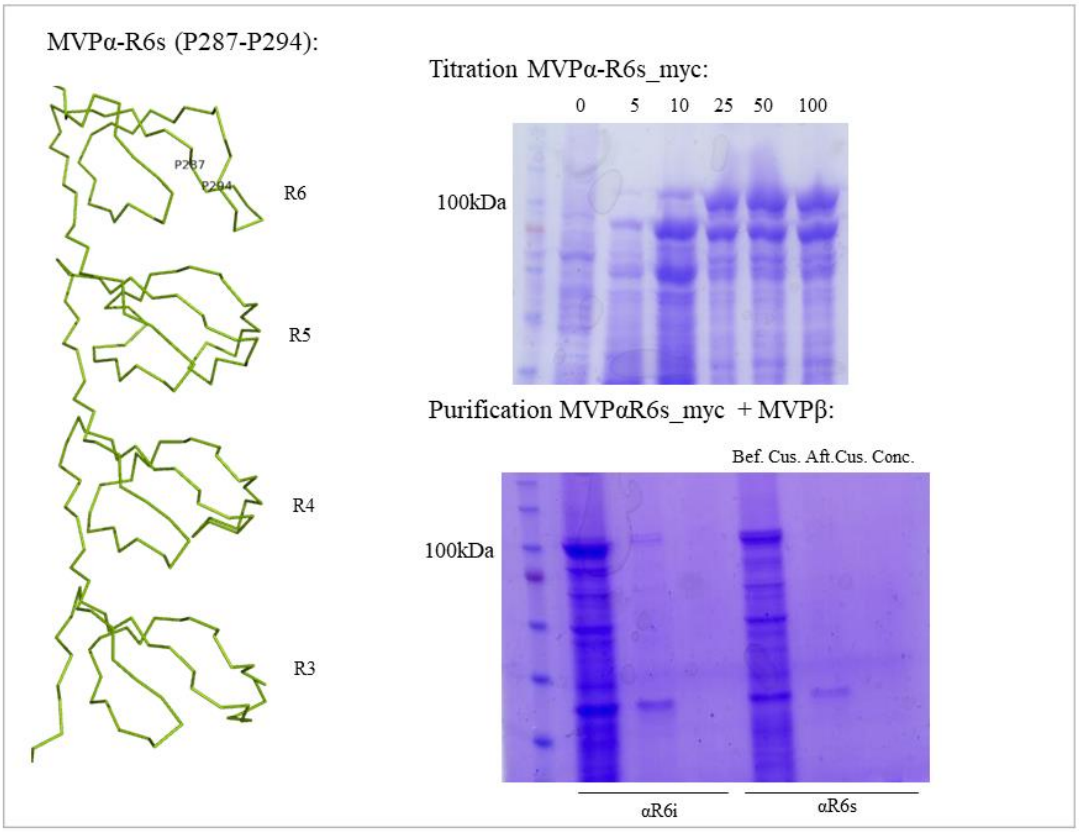

Figure 1 Annex. MVPα-myc mutant construct analysis: virus titration, purification of vaults by co-infection of MVP α-myc mutant with MVPβ. (**A**) R4α-ins-184-185 mutant. (**A'**) Negative staining analysis of the mutant. (**B**) R4α-sus-179-190 mutant. (**C**) R5α-sus-234-243 mutant. (**D**) R6α-ins-287-294 mutant. (**E**) R6α-sus-287-294 mutant.

The results from the first construct (Figure 1 Annex-A) showed a 100kDa band before and after the purification gradient but only the band before the purification still present in the Western-Blot α-myc. When the band was analysed by negative staining (Figure 1 Annex-A') any clear vault was formed.

A: R4β-ins-193-194 construct

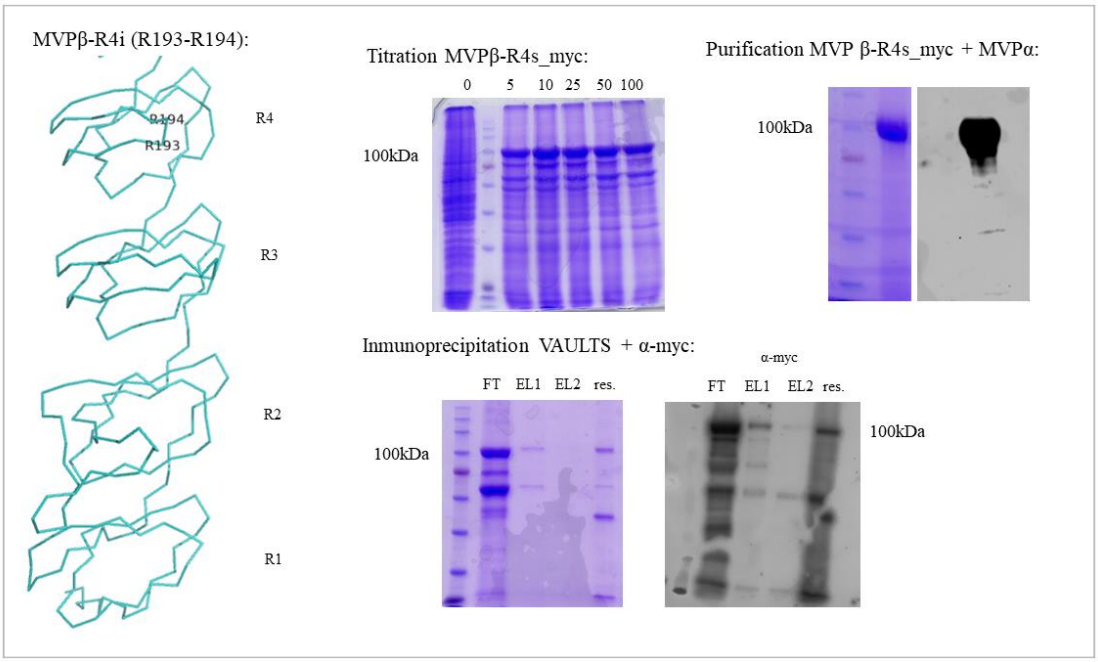

A’

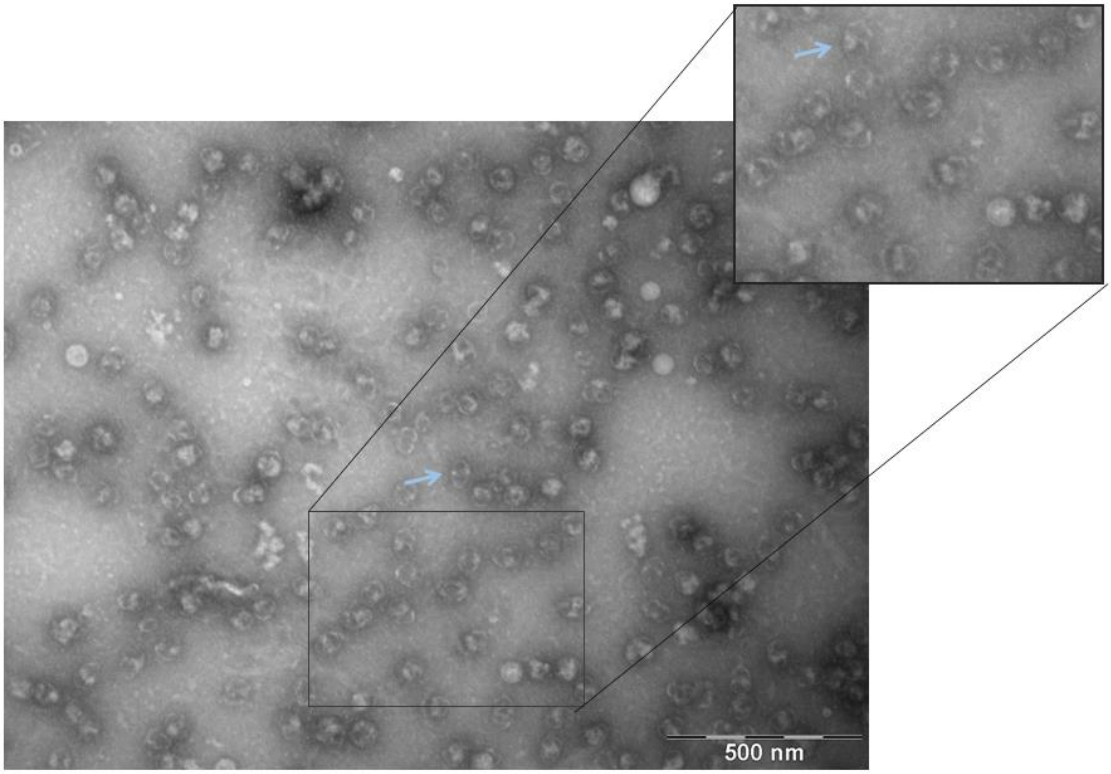

B: R4β-sus-188-199 construct

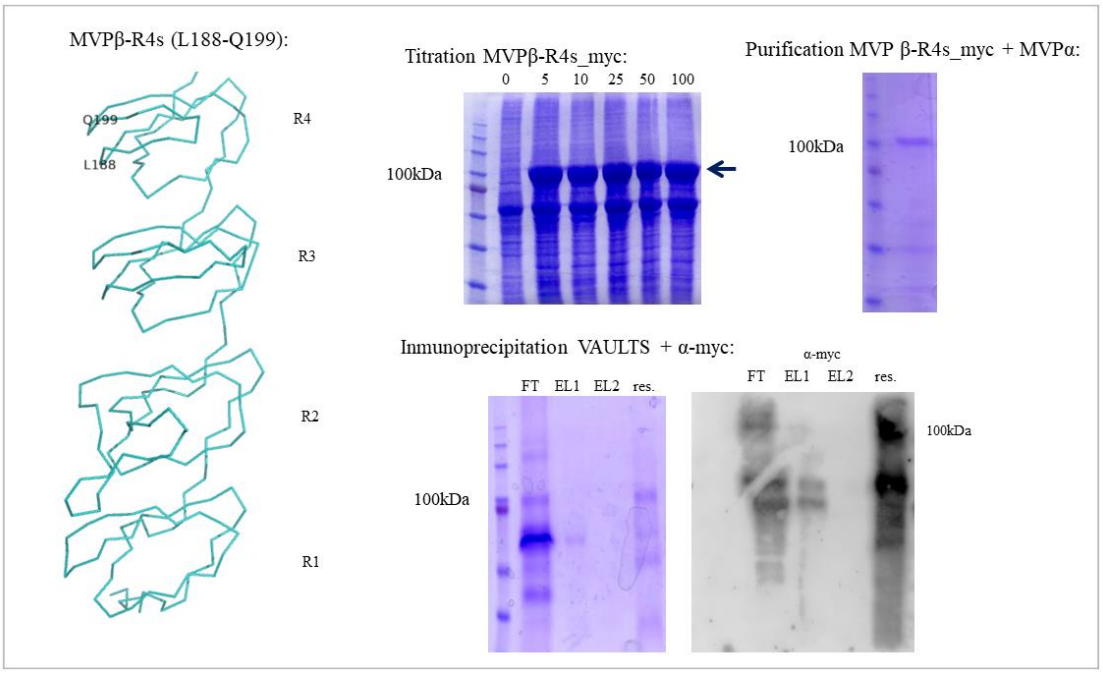

B’

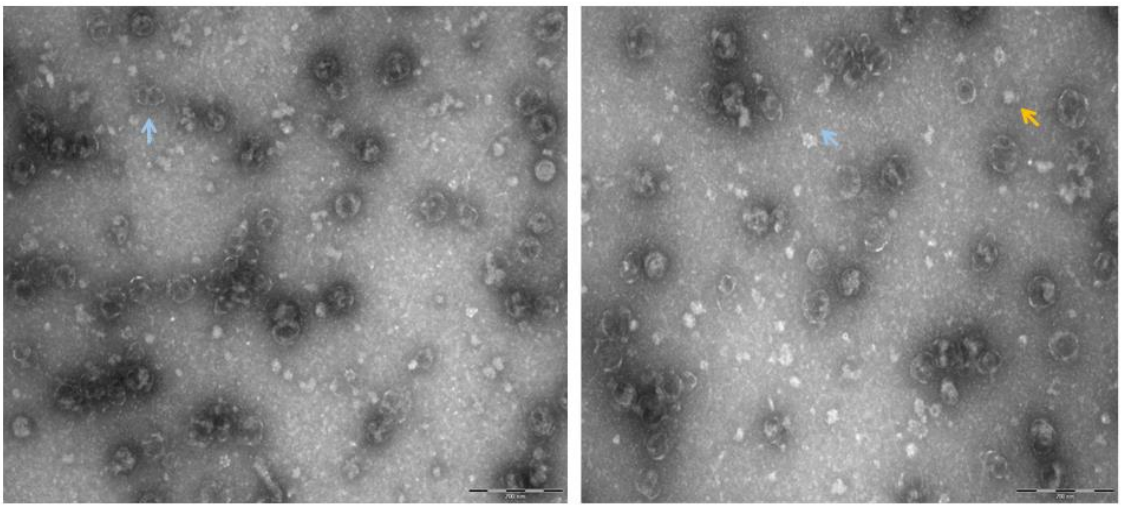

C: R5β-ins-241-252 construct

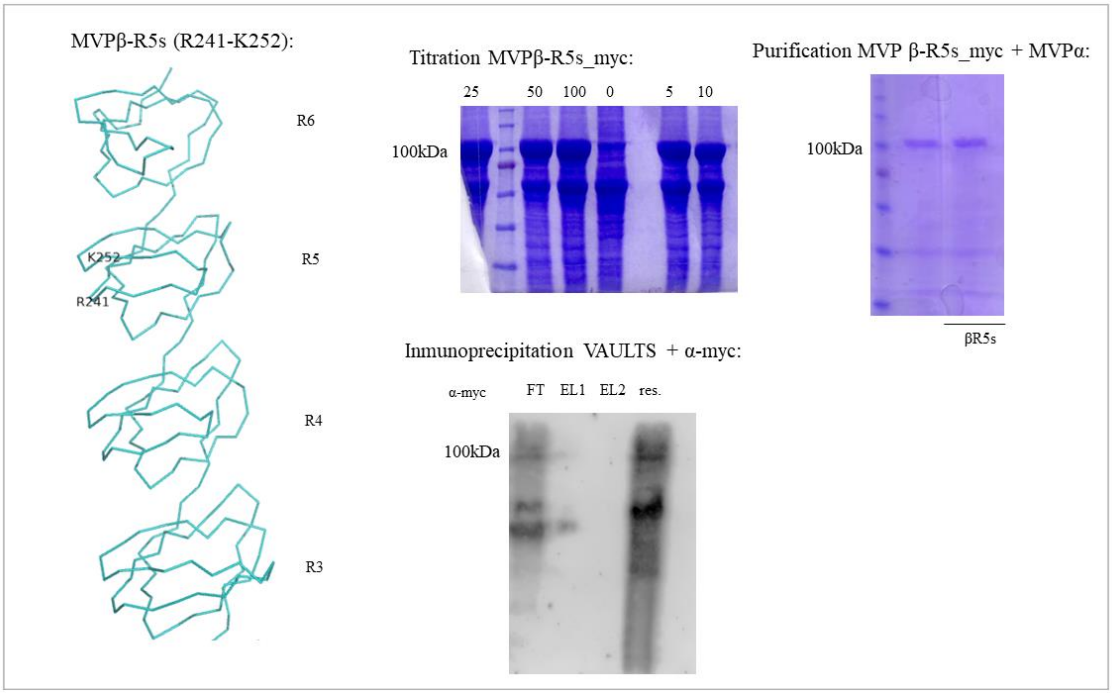

C’

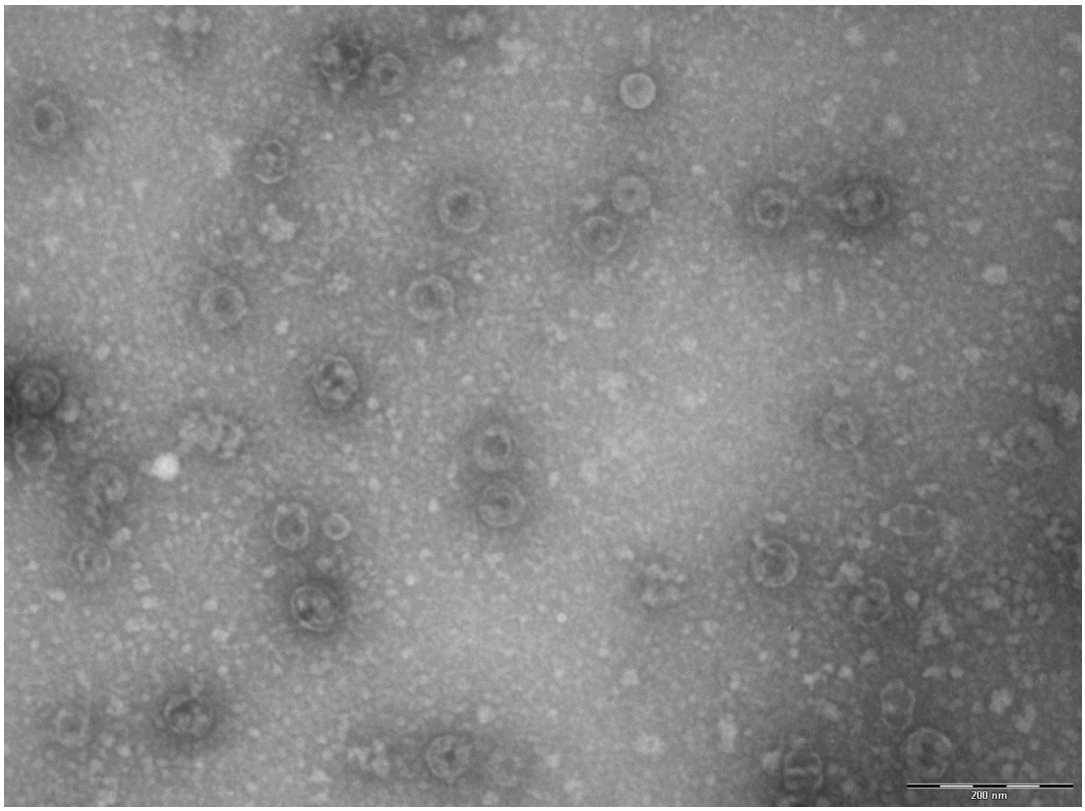

D: R6β-ins-297-299 construct

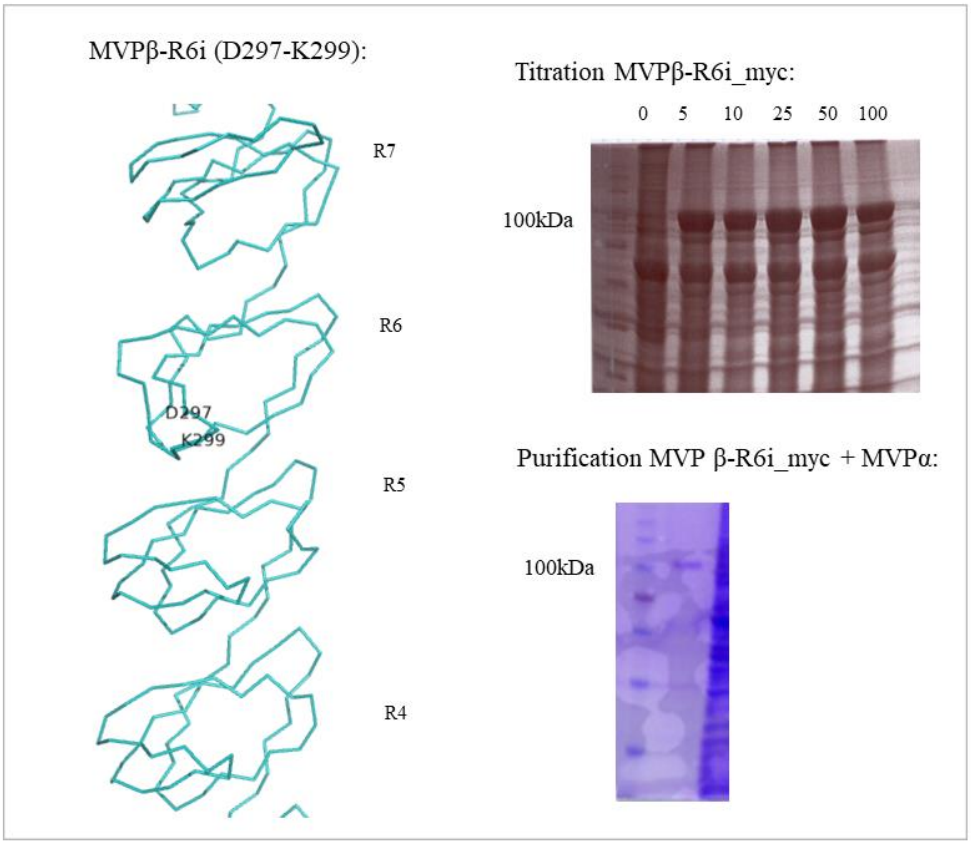

D’

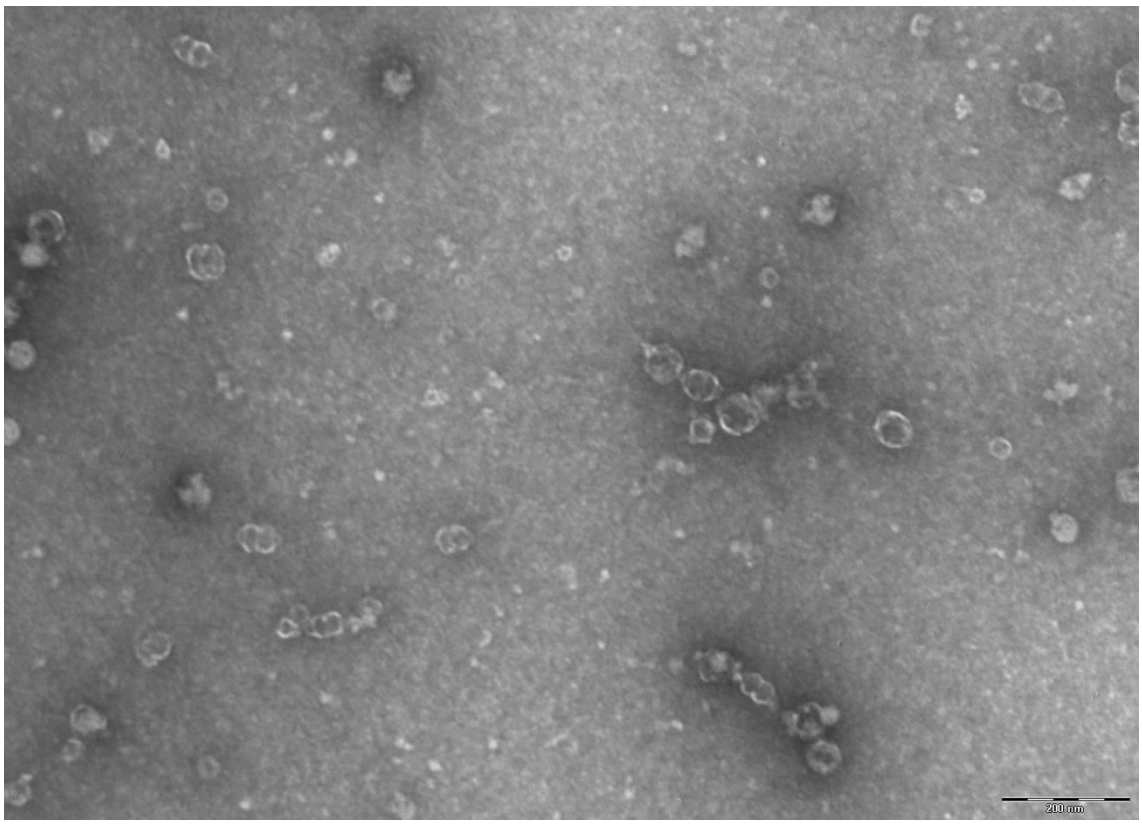

E: R6β-sus-295-298 construct

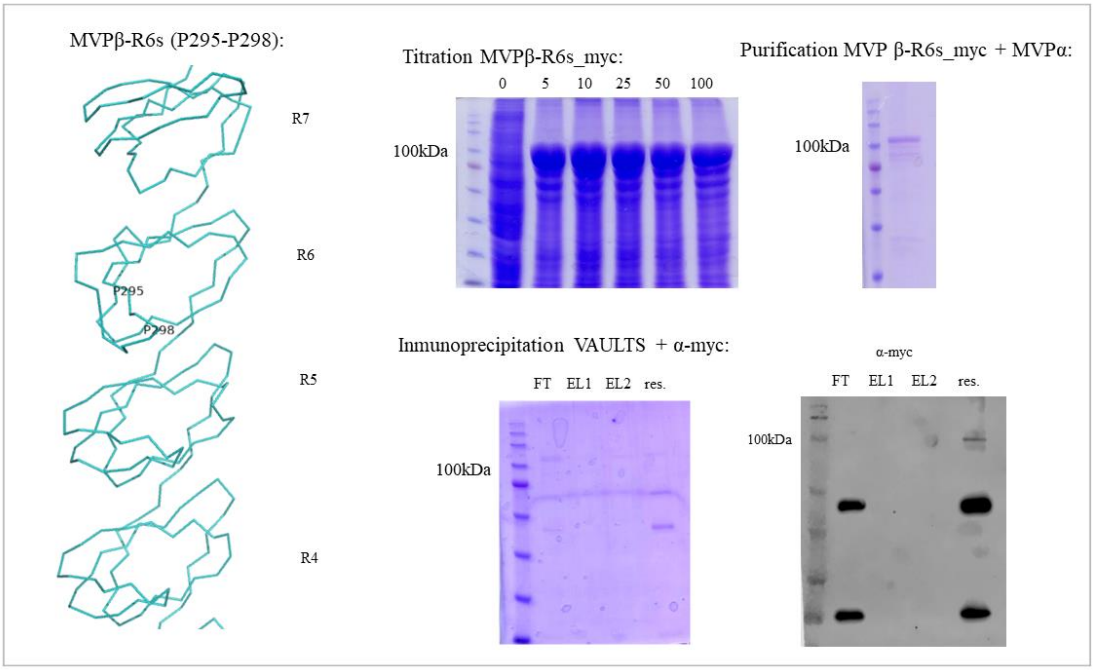

E’

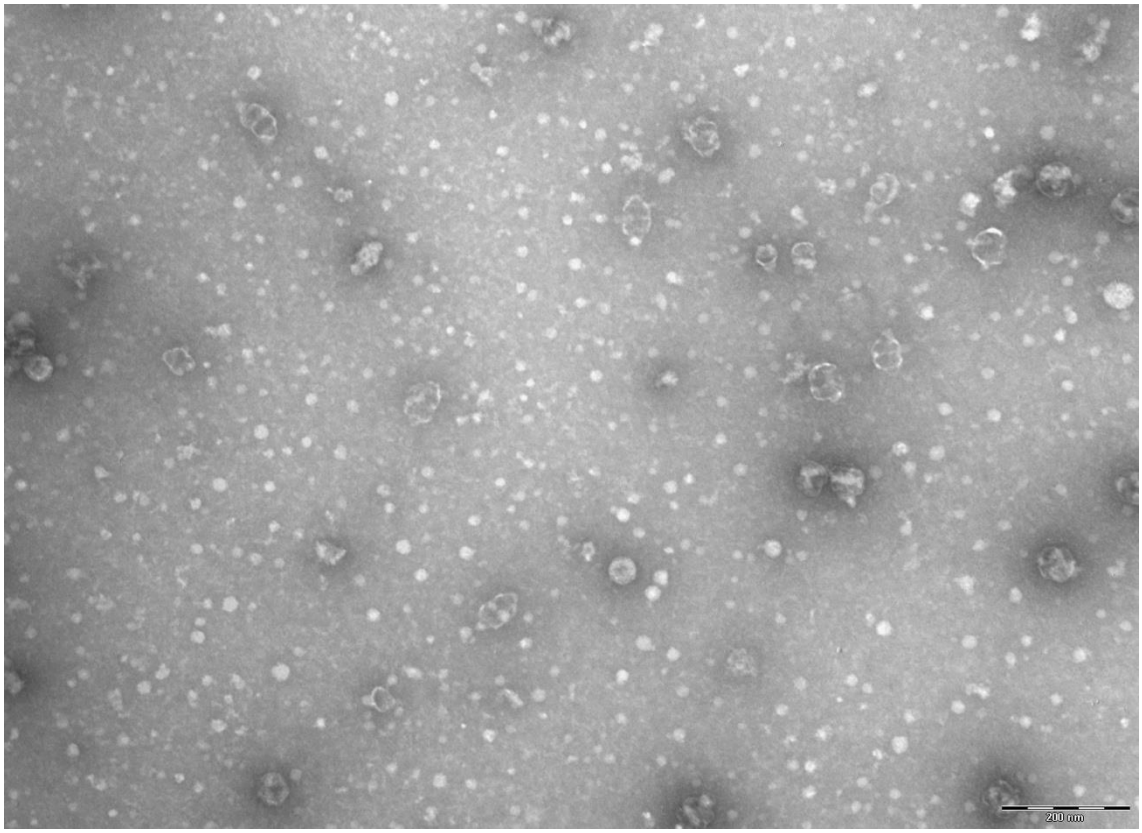

Figure 2 Annex. MVPβ-myc mutant construct analysis: virus titration, purification of vaults by co-infection of MVPα-rBV with MVPβ-myc mutant rBV. (**A**) R4β-ins-193-194 mutant. (**A'**) Negative staining analysis of the mutant. (**B**) R4β-sus-188-199 mutant. (**B'**) Negative staining analysis of the mutant. (**C**) R5β-ins-241-252 mutant. (**C'**) Negative staining analysis of the mutant. (**D**) R6β-ins-297-299 mutant. (**D'**) Negative staining analysis of the mutant. (**E**) R6β-sus-295-298 mutant. (**E'**) Negative staining analysis of the mutant.

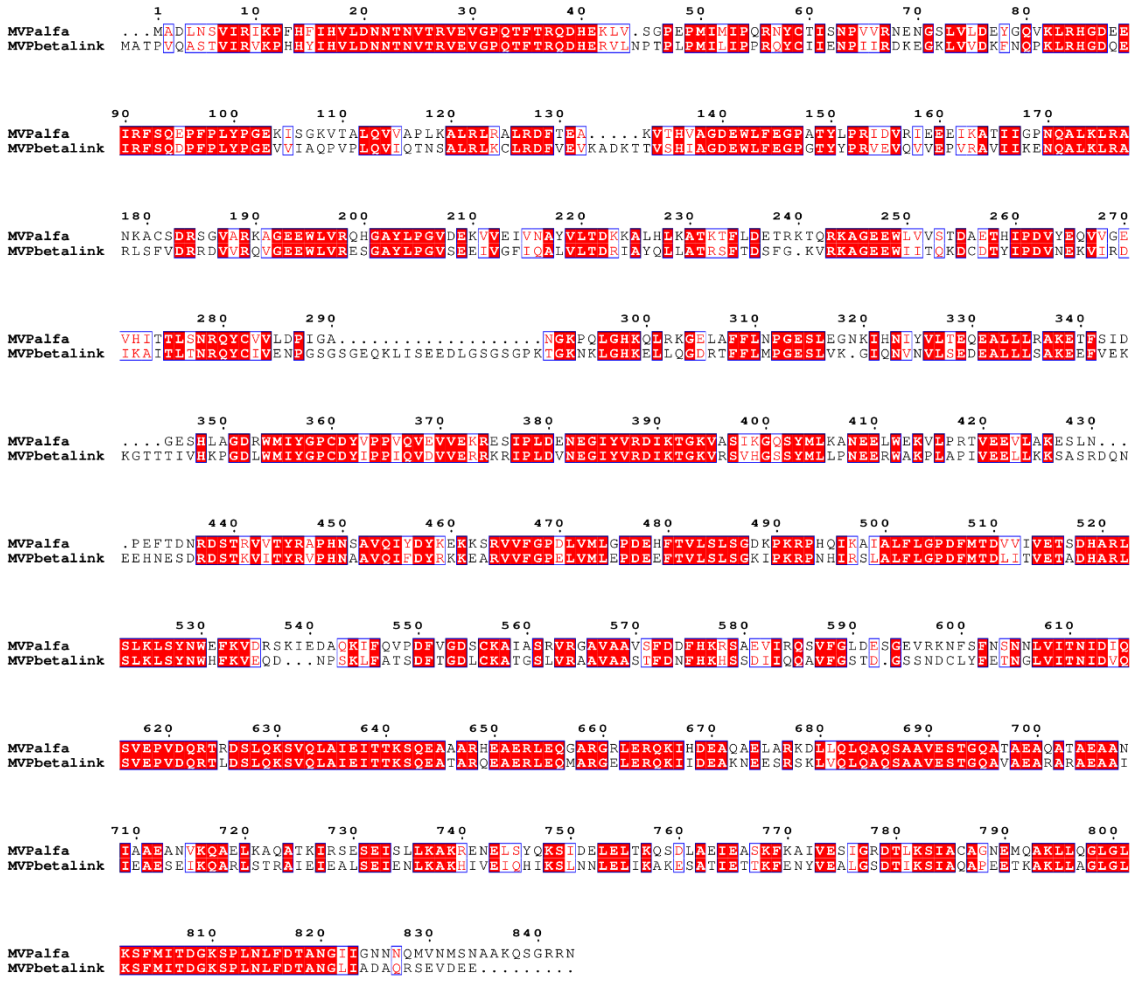

Figure 3 Annex. Sequence alignment of MVPα and MVPβ with the myc-tag flanked by the long link.